

INFORMATION TO USERS

This manuscript has been reproduced from the microfilm master. UMI films the text directly from the original or copy submitted. Thus, some thesis and dissertation copies are in typewriter face, while others may be from any type of computer printer.

The quality of this reproduction is dependent upon the quality of the copy submitted. Broken or indistinct print, colored or poor quality illustrations and photographs, print bleedthrough, substandard margins, and improper alignment can adversely affect reproduction.

In the unlikely event that the author did not send UMI a complete manuscript and there are missing pages, these will be noted. Also, if unauthorized copyright material had to be removed, a note will indicate the deletion.

Oversize materials (e.g., maps, drawings, charts) are reproduced by sectioning the original, beginning at the upper left-hand corner and continuing from left to right in equal sections with small overlaps.

Photographs included in the original manuscript have been reproduced xerographically in this copy. Higher quality 6" x 9" black and white photographic prints are available for any photographs or illustrations appearing in this copy for an additional charge. Contact UMI directly to order.

**ProQuest Information and Learning
300 North Zeeb Road, Ann Arbor, MI 48106-1346 USA
800-521-0600**

UMI[®]

University of Alberta

**A Comparison of Photogrammetrically Determined Astronomical Refraction of
Sunlight at High Zenith Angles with a Ray-tracing Computer Model Employing
Rawinsonde Profiles**

by

Russell D. Sampson



**A thesis submitted to the Faculty of Graduate Studies and Research in partial
fulfillment of the requirements for the degree of Doctor of Philosophy**

Department of Earth and Atmospheric Sciences

and

Department of Civil and Environmental Engineering

Edmonton, Alberta

Spring 2001



**National Library
of Canada**

**Acquisitions and
Bibliographic Services**

**395 Wellington Street
Ottawa ON K1A 0N4
Canada**

**Bibliothèque nationale
du Canada**

**Acquisitions et
services bibliographiques**

**395, rue Wellington
Ottawa ON K1A 0N4
Canada**

Your file Votre référence

Our file Notre référence

The author has granted a non-exclusive licence allowing the National Library of Canada to reproduce, loan, distribute or sell copies of this thesis in microform, paper or electronic formats.

The author retains ownership of the copyright in this thesis. Neither the thesis nor substantial extracts from it may be printed or otherwise reproduced without the author's permission.

L'auteur a accordé une licence non exclusive permettant à la Bibliothèque nationale du Canada de reproduire, prêter, distribuer ou vendre des copies de cette thèse sous la forme de microfiche/film, de reproduction sur papier ou sur format électronique.

L'auteur conserve la propriété du droit d'auteur qui protège cette thèse. Ni la thèse ni des extraits substantiels de celle-ci ne doivent être imprimés ou autrement reproduits sans son autorisation.

0-612-60343-1

Canada

University of Alberta

Library Release Form

Name of Author: **Russell D. Sampson**

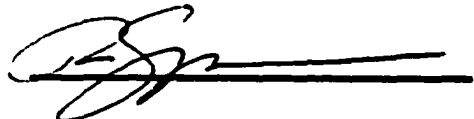
Title of Thesis: **A Comparison of Photogrammetrically Determined Astronomical Refraction of Sunlight at High Zenith Angles with a Ray-tracing Computer Model Employing Rawinsonde Profiles**

Degree: **Doctor of Philosophy**

Year this Degree Granted: **2001**

Permission is hereby granted to the University of Alberta Library to reproduce single copies of this thesis to lend or sell such copies for private or scientific research purposes only.

The author reserves all other publication and other rights in association with the copyright in the thesis, and except as hereinbefore provided, neither the thesis nor any substantial portion thereof may be printed or otherwise reproduced in any material form whatever without the author's prior written permission.



Department of Earth and
Atmospheric Science
University of Alberta
1-26 Earth Sciences Building
Edmonton, Alberta, Canada
T6G 2E3

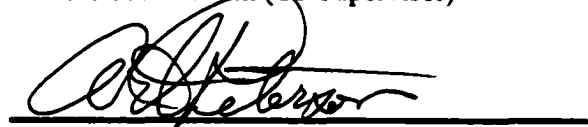
Date: Jan 29, 2001


University of Alberta

Faculty of Graduate Studies and Research

The undersigned certify that they have read, and recommend to the Faculty of Graduate Studies and Research for acceptance, a thesis entitled A COMPARISON OF PHOTOGRAMMETRICALLY DETERMINED ASTRONOMICAL REFRACTION OF SUNLIGHT AT HIGH ZENITH ANGLES WITH A RAY-TRACING COMPUTER MODEL EMPLOYING RAWINSONDE PROFILES by Russell Dean Sampson in partial fulfillment of the requirements for the degree of Doctor of Philosophy.


Edward P. Lozowski (Co-Supervisor)


Arthur E. Peterson (Co-Supervisor)


Waldemar H. Lehn (External Examiner)


Douglas P. Hube (Committee Member)


Gerhard Reuter (Committee Member)


John D. Wilson (Committee Member)

Date: Jan. 26/01

ABSTRACT

Many important areas of science such as geodesy, astrometry, satellite navigation, and remote sensing require accurate understanding of the amount of astronomical refraction. However, very little work has been done to actually compare the observed and modelled astronomical refraction at high zenith angles. In this study, a ray tracing model using atmospheric data from rawinsondes is for the first time compared with the measured astronomical refraction presented by the setting Sun. These measurements were obtained on December 8, 14 and 22, 1998 from the campus of the University of Alberta in Edmonton, and the Stony Plain Upper Air Station, about 25 km west of Edmonton, Alberta. Astronomical refraction values were measured through a theodolite survey (Edmonton) and photogrammetry (Stony Plain). Photogrammetric images were obtained using a Questar 3.5-inch telescopic lens and then scanned on an Agfa Studio Scan II *si* flat bed colour scanner. Before accurate measurements could be extracted from the negatives, the camera and scanner required calibration. The calibration of the scanner found systematic linear and non-linear distortions of less than 0.6%. The calibration of a consumer grade flatbed scanner has so far, not appeared in the literature. Photographs of star fields were used to determine the focal length (1445.3 ± 3.6 mm) and the distortions of the Questar lens. A terrestrial calibration method helped verify these results. Both methods showed no measurable lens distortion. The photogrammetric calibration of a Questar 3.5 inch telescopic lens has not appeared in the literature. The theodolite measurements of astronomical refraction from Edmonton and photogrammetric measurements from Stony Plain

showed good agreement with the refraction model for the December 14 and 22 sunsets. The poorest fit occurred during the December 8 sunset when a substantial horizontal temperature gradient was present. From conversations with Environment Canada employees it is also possible that the VIZ rawinsonde used on December 8 may have been from an old and possibly defective supply. A Modified U.S. Standard Atmosphere (MUSSA) profile produces a better fit between model and observed astronomical refraction than the rawinsonde profiles. The results of this study suggest that the temperature measurements from the rawinsondes may be too inaccurate to improve on a MUSSA model. Nonetheless, both models showed a significant improvement over the Pulkovo Refraction Tables.

Acknowledgements

I would first like to thank my supervisors Ed Lozowski and Art Peterson for providing their leadership, guidance and friendship. Their continued support has made this work possible and made my experience in the graduate program one of the most enjoyable and rewarding of my life. I thank the rest of the committee Doug Hube, John Wilson, Gerhard Reuter and the external examiner Waldemar Lehn for their comments, encouragement and counseling. Even though he was not on the committee Hans Machel's interest in atmospheric optics and his organization of those early morning sessions was greatly appreciated.

There are many fellow students I would like to thank for their friendship and assistance. I thank Brian Crenna for sharing his boundless knowledge of computing, Karen Harper for her understanding of the complex academic system, Julian Brimelow and Neil Taylor for their help with my interpretation of the rawinsonde data. I would especially like to thank Victor Chung for sharing his vast talents in mathematics, experimental design, and computing. His friendship has been one of the most important results of this work.

I have also enjoyed working and socializing with the research associates, Krzysztof Szilder and Tom Flesch. I would also like to thank Roxanne Lalonde for her sage advice.

Many other people supplied valuable assistance in the work. Barry Arnold helped me understand the workings of the Questar telescope. Jerry Funston and the staff at the Stony Plain Upper Air Station were instrumental in providing rawinsonde data and helping me with the photogrammetric set up at the station.

Doug Hube and the Department of Physics provided the Questar telescope. The Department of Earth and Atmospheric Sciences and the Department of Civil and Environmental Engineering also supplied surveying instruments.

I would also like to thank Jennifer and Mark Brockington, Judith Enarson, Micheal Fisher, Judy Fjoser, Paul Greidanus, Lynette Hussain, Isabell Hotchkiss, Fran Metcalf, Randy Pakan and a special thank you to Laura Smith and Terry Thompson.

This research was supported by NSERC, a University of Alberta Dissertation Fellowship, University of Alberta Ph.D. Scholarship, and the Province of Alberta Graduate Fellowship.

Finally and most importantly, I would like to thank my wife Susan for her untiring support throughout this long journey. This work is dedicated to her.

TABLE OF CONTENTS

Introduction	
Importance of Study	Page 1
Thesis Outline	Page 2
Chapter 1: Photogrammetric Calibration of a Consumer Grade Flatbed Scanner.	
Abstract	Page 4
1. Introduction	Page 4
1.1 Previous Work	Page 6
1.2 Experimental Procedure	Page 7
1.3 Distortion Model	Page 8
1.4 Least Squares Analysis and a Residual Atlas	Page 12
1.5 The Target	Page 13
2. Results	Page 16
2.1 Possible Aliasing of the Periodic Distortion	Page 22
2.2 Stability of Scanner Distortion	Page 27
3. Conclusions	Page 28
Appendix A: Sampling Theory: Aliasing	Page 29
References	Page 31

Chapter 2: The Selection and Calibration of an Optical System for High Magnification 0.1 arcminute Photogrammetry.

Abstract	Page 32
1. Introduction	Page 32
2. Selection of the Camera System and Emulsion	Page 33
3. Measurement of Lens Distortion of the Questar 3.5	Page 36
4. Measurement of Focal Length of the Questar 3.5	Page 44
5. Further Calibration of the Questar 3.5	Page 56
5.1 Targets	Page 56
5.2 Object and Camera Orientation	Page 58
5.3 Image Co-ordinates	Page 62
5.4 Calibration Software	Page 63
5.5 Results	Page 64
6. Film Flatness	Page 67
7. Conclusions	Page 67
Appendix A: Object and Image Co-ordinates for Questar Calibration Targets	Page 68
Appendix B: Solution to the Photogrammetric Problem (The Bundle Method)	
B.1 The Collinearity Equation	Page 81
B.2 Self-Calibration	Page 85
B.3 Solution through Least Squares Adjustment	Page 88
References	Page 91

Chapter 3: A Comparison of Photogrammetrically Determined Astronomical Refraction of Sunlight at High Zenith Angle with a Ray-tracing Computer Model Employing Rawinsonde Profiles

Abstract	Page 93
1. Introduction	Page 95
1.1 Current Astronomical Refraction Applications	Page 97
1.2 Historical Background and Literature Review	Page 99
1.2.1 Introduction	Page 99
1.2.2 The Empirical Era	Page 99
1.2.3 The Analytical Era	Page 101
1.2.4 The Meteorological Era	Page 111
1.2.5 Modern Observations of High Zenith Angle Astronomical Refraction	Page 120
1.3 Summary of Astronomical Refraction	Page 123
2. The Astronomical Refraction Model	Page 135
2.1 Introduction to the Model	Page 135
2.2 Construction of the Model	Page 136
3. Experimental Design	Page 145
3.1 Introduction	Page 145
3.2 Instrumentation	Page 145
3.3 Astronomical Refraction Measured from Edmonton	Page 147
3.4 Atmospheric Issues	Page 149

3.5 Times and Azimuthal Location of Sunset	Page 156
3.6 Reference Targets	Page 158
3.6.1 Selection of Reference Targets	Page 159
3.6.2 Estimating Distances to Reference Targets	Page 159
3.6.3 Altitude and Azimuth of the Reference Targets	Page 161
3.6.4 Terrestrial Refraction	Page 163
3.7 Photogrammetric Analysis	Page 166
3.7.1 Scanning and Digitization of Images	Page 167
3.7.2 Correction for Scanner Distortions and Rotation of Image	Page 168
3.7.3 Treetop Reference Targets	Page 171
3.7.4 Exterior Orientation of the Camera	Page 171
3.7.5 Tree Sway Correction	Page 175
4. Results	Page 176
4.1 Sensitivity Analysis ($\delta\theta$)	Page 176
4.2 Comparison of Photogrammetric Data and the Ray Tracing Model	Page 177
4.2.1 Atmospheric Soundings	Page 177
4.2.2 Comparison of Observed and Modelled Astronomical Refraction Using Rawinsonde Profiles	Page 188
4.2.3 Photogrammetric and Theodolite Results	Page 191
5. Analysis	Page 224
5.1 Estimating Uncertainty in the Refraction Model	Page 224

5.2 Using Significant and Mandatory Levels: An Operational Refraction Model	Page 231
5.3 Using a Modified U.S. Standard Atmosphere (MUSSA) in the Refraction Model	Page 234
5.4 The Horizontal Temperature Gradient and Model Sensitivity	Page 237
5.5 Comparison of Refraction Model with Pulkovo Refraction Tables	Page 243
6. Conclusions	Page 251
7. Discussion	Page 254
Appendix A: Calculation of the Refractive Index of Air	Page 256
Appendix B: Derivation of the Fundamental Astronomical Refraction Equations	Page 261
B.1. Introduction to the Geometrical Optics of Refraction	Page 261
B.2. Introduction to Refraction in a Spherically Symmetric Atmosphere	Page 264
B.3. Derivation of the Ray Curvature Equation	Page 270
Appendix C: Refraction Model Fortran 77 Code (Digital Compiler)	Page 274
C.1. Table of Contents	Page 274
Fortran 77 Code	Page 278
Appendix D: Precision and Accuracy of the Bomford Terrestrial Refraction Formula	Page 304
Appendix E: Fortran 77 Code for 3x3 Matrix Inversion	Page 315

Appendix F: Treetop and Reference Target Data	Page 320
Appendix G: Sounding Files for December 8,14 and 22, 1998	Page 324
Appendix H: Astronomical Refraction as a Function of Depth in the Atmosphere	Page 335
References	Page 341

Chapter 4: Final Conclusions and Suggestions for Further Research

1. Photogrammetry: Conclusions	Page 348
1.1 Suggestions for Further Research into the Photogrammetric Utility of Flatbed Scanners	Page 348
1.2 Suggestions for Further Research into the Photogrammetric Utility of the Questar 3.5-inch Telescopic Lens	Page 349
2. Astronomical Refraction: Conclusions	Page 350
2.1 Suggestions for Further Research into the Use of the Astronomical Refraction Model	Page 350
References	Page 352

LIST OF TABLES

Chapter 1: Photogrammetric Calibration of a Consumer Grade Flatbed Scanner.

Table 1: Scanner distortion residuals atlas.	Page 15
Table 2: Estimates of scanner distortions.	Page 22
Table 3: Five longest alias wavelengths.	Page 23

Chapter 2: The Selection and Calibration of an Optical System for High Magnification 0.1 arcminute Photogrammetry.

Table 1: Distortion measurements for the Questar lens.	Page 39
Table 2: Right ascension and declination of target stars in M45.	Page 52
Table 3: Mean focal length using ten star images from M45.	Page 53
Table 4: Object co-ordinates of total station and camera.	Page 60
Table 5: Comparison of tape measure and surveyed distances.	Page 62
Table 6: Computed focal length of Questar lens.	Page 64
Table 7: Results of the mobile focal plane experiment.	Page 66

Appendix A

Table A1: Object co-ordinates for calibration target.	Pages 69-71
Table A2 to A10: Image co-ordinates of calibration target.	Pages 72-80

Chapter 3: A Comparison of Observed High Zenith Angle Astronomical

Refraction with Output from a Ray Tracing Model using Rawinsonde Profiles

Table 1: Seasonal difference in astronomical refraction.	Page 121
Table 2: Surface temperature time series for period around sunset	Page 152
Table 3: Approximate sunset times for observing sites and dates	Page 157
Table 4: Surface meteorological data and terrestrial refraction	Page 166
Table 5: RMS of observed and modelled refraction	Page 235
Table 6: RMS of modelled and Pulkovo refraction	Page 244

Appendix D: Precision and Accuracy of the Bomford Terrestrial Refraction

Formula

Table D1: Observed and corrected altitude of Keephills smokestack	Page 307
Table D2: Geometric and corrected altitude of Keephills smokestack	Page 308
Table D3: Uncertainties in dT/dz and terrestrial refraction	Page 311

Appendix F: Treetop and reference target data

Table F1: Zenith angle measurements of targets	Pages 321-323
---	----------------------

Appendix G: Sounding Files for December 8, 14, and 22, 1998

Table G1: Sounding file for December 8, 1998	Pages 325-326
Table G2: Sounding file for December 14, 1998	Page 327
Table G3: Sounding file for December 22, 1998	Page 328

Appendix H: Sounding Files for December 8, 14, and 22, 1998

Table H1: Cumulative absolute astronomical refraction at selected heights.

Page 336

Table H2: Cumulative fractional astronomical refraction at selected heights.

Page 337

LIST OF FIGURES

Chapter 1: Photogrammetric Calibration of a Consumer Grade Flatbed Scanner.

Figure 1: Schematic of scanner	Page 9
Figure 2: Scanner distortion residual atlas	Page 14
Figure 3: Linear regression bias in periodic distortion	Page 17
Figure 4: Linear fit to the mean of the x -residuals	Page 19
Figure 5: Linear fit to the mean of the y -residuals	Page 20
Figure 6: Linear and modelled sinusoidal fit to the y -residuals	Page 20
Figure 7: An example of a non-aliased signal	Page 24
Figure 8: An example of a non-aliased sampling	Page 24
Figure 9: An example of an aliased signal	Page 25
Figure 10: An example of an aliased sampling	Page 25
Figure 11: Measurements to test for aliasing in the y -distortion	Page 26

Chapter 2: The Selection and Calibration of an Optical System for High Magnification 0.1 arcminute Photogrammetry.

Figure 1: A schematic of a Maksutov telescope.	Page 35
Figure 2: A schematic of a collinear lens and the celestial equator.	Page 38
Figure 3: Star trails from the δ Orionis region.	Page 40
Figure 4: Star trails from the δ Orionis region.	Page 41
Figure 5 to 10: Residuals from least squares fit to star trails.	Page 42
Figure 11: Negative image of M45 star cluster.	Page 47
Figure 12: Schematic of moving principal point.	Page 51

Figure 13: The calculated uncertainty in focal length.	Page 55
Figure 14 and 15: Photographs of Stadium target field.	Page 57
Figure 16: Schematic of calibration target field.	Page 58
Figure 17: Schematic of calibration set up.	Page 60
Figure 18: Schematic of triangulation set up.	Page 61
Figure 19: Graph of image distance versus object distance.	Page 65

Appendix A

Figure A1 to A9: Image co-ordinates from lens calibration.	Pages 72-80
---	--------------------

Appendix B

Figure B1: Schematic of image and object space co-ordinates.	Page 82
Figure B2: Schematic of barrel and pincushion distortion.	Page 85
Figure B3: Orientation of decentering distortion in image space.	Page 87

Chapter 3: A Comparison of Observed High Zenith Angle Astronomical

Refraction with Output from a Ray Tracing Model using Rawinsonde Profiles

Figure 1: A schematic of astronomical refraction.	Page 104
Figure 2: The optical path for identity of $\tan i$.	Page 106
Figure 3: The non-linear behavior of Snell's Law.	Page 124
Figure 4 to 9: Density and density gradient graphs.	Pages 126-131
Figure 10: The straight-line incident angle.	Page 133
Figure 11: A schematic of the ray-travel increment.	Page 138
Figure 12: The geometric configuration of astronomical refraction.	Page 142
Figure 13: The Kern E2 theodolite with solar projection box.	Page 148

Figure 14: A schematic of the balloon and ray trajectory.	Page 150
Figure 15: Horizon markers visible from the Stony Plain site.	Page 160
Figure 16: A schematic of digitization error test images.	Page 169
Figure 17: Object and image co-ordinates in object space.	Page 172
Figure 18: The sensitivity of the refraction model to $\delta\theta$.	Page 178
Figure 19 to 24: Density gradient error analysis graphs.	Pages 179-185
Figure 26 to 28: The sunset photographs.	Pages 189-191
Figure 29a to 43a: Observed and modelled sunsets (rawinsonde).	Pages 192-222
Figure 29b to 43b: Observed and modelled sunsets (MUSSA).	Pages 193-221
Figure 44: Observed minus modelled refraction graphs.	Page 223
Figure 45: Observed and modelled refraction graphs (rawinsonde).	Page 225
Figure 46: Observed and modelled refraction graphs (MUSSA).	Page 226
Figure 47: Refraction model error due to VIZ measurement error.	Page 228
Figure 48: Refraction model error due to RS80 measurement error.	Page 229
Figure 49: Difference due to significant and mandatory profiles.	Page 233
Figure 50: Map of meteorological surface conditions 12/08/98.	Page 238
Figure 51 to 53: Surface temperature time series.	Page 239
Figure 54: The sunset ray path from Stony Plain.	Page 241
Figure 55: Changes in surface temperature and model output.	Page 242
Figure 56a to 58a: Model and Pulkovo refraction (rawinsonde).	Pages 245-249

Figure 56b to 58b: Model and Pulkovo refraction (MUSSA).

Pages 246-250

Appendix B

Figure B1: A schematic illustrating Fermat's principle of least time.

Page 263

Figure B2: Refraction in a spherically symmetric atmosphere

Page 266

Figure B3: The angle ϕ with respect to the x -axis.

Page 270

Appendix D

Figure D1: Altitude measurements of the Keephills smokestack. Page 306

Figure D2 to D5: Sensitivity analysis of terrestrial refraction error. Page 313

Appendix G

Figure G1 to G5: Rawinsonde profiles for December 8, 14, 22, 1998.

Pages 329 - 334

Appendix H

Figure H1: Incremental astronomical refraction.

Page 338

Figure H2: Cumulative absolute astronomical refraction.

Page 339

Figure H3: Cumulative fractional astronomical refraction.

Page 340

LIST OF SYMBOLS

Chapter 1: Photogrammetric Calibration of a Consumer Grade Flatbed Scanner.

x,y	The image co-ordinates of the target (a grid plate) [cm]
X,Y	The object co-ordinates of the target (a grid plate) [cm]
α	Tilt angle of the grid-plate target relative to the y-axis [degrees]. Tilt angle is positive in a counter-clockwise direction (i.e. rotation from the positive x-axis towards the positive y-axis)
γ	The tilt angle of the scanner head [degrees] normal to the direction of motion of the scanner head. Positive in a counter-clockwise direction
ψ,ϕ	Tilt of the axis of the grid plate image with respect to the x and y-axis respectively
f_x	Fractional linear scaling distortion along the axis of the scanner head produced by any difference between the manufacturer's stated resolution and the actual resolution
f_y	Fractional linear scaling distortion along the axis of the scanner track
a,b	Translational distortion (a in the x-direction, b in the y-direction)
s	The average vertical spread of the residuals [pixels]
d	The distance from the origin of the image [pixels]
λ	Wavelength of sinusoidal wave distortion along the axis of the scanner track [cm]
A	Amplitude of the wave [cm]
ϵ	Phase of the wave

σ_x, σ_y	Random measurement error [cm]
k^*	The number of wavelengths of an aliased wave
k	The number of wavelengths of the true signal
J	The number of samples of the true signal
I	The sampling interval
L	The length of the sample [cm]
m	The number of alias frequencies

Chapter 2: The Selection and Calibration of an Optical System for High Magnification 0.1 arcminute Photogrammetry.

f_{\min}	Minimum focal length of the lens necessary to achieve desired resolution [m]
r	The size of a single pixel in the flatbed scanner [μm]
θ	Angular displacement
x, y	The image co-ordinates [m]
δ	The declination angle of the star
α	The right ascension angle of the star
f	Focal length of the lens (at infinite object distance) [m]
η	The angular displacement of a star from the camera's optical axis
c	Image distance [m]
d	Object distance [m]
R	Astronomical refraction angle
z_0	Zenith angle of the star

ϕ	Geographic latitude of the observer
H	Hour angle of the star
LST	Local sidereal time
β	The angular displacement between two stars
ξ, γ	Mean horizontal angles of the terrestrial calibration targets as measured by the total station
j, k, l, m	Sides of the survey triangle for the terrestrial calibration [m]
D	Distance between terrestrial calibration target points [m]

Appendix B: Solution to the Photogrammetric Problem (The Bundle Method)

ω, ϕ, κ	Angles of rotation
X, Y, Z	Object co-ordinates [m]
x, y, z	Image co-ordinates [m]
c	Principal distance of the lens [m]
$M_{\omega, \phi, \kappa}$	Rotation matrices
m_{ij}	Rotation matrix elements
\mathbf{a}	Image vector
\mathbf{A}	Object space vector
k	Scaling factor
f_1, f_2	Total distortion factor of the lens
δr	Radial lens distortion [non-dimensional]
K_i	Coefficients of the radial lens distortion at infinite focus
r	Radial distance from the principle point along the film plane [m]

P_1, P_2	Decentering distortion at infinite focus [non-dimensional]
y_m	Observations (image co-ordinates) [m]
x_m	Object co-ordinates of the targets [m]
a_m	Coefficients of interest (image distance, distortion coefficients, camera orientation, etc.)
v_m	Residuals of observations
V	Residual matrix
B	Object coordinate matrix
δ	Matrix of the coefficients of interest (focal length, distortion, principal point location, etc.)
C	Image coordinate matrix
Q	Exponent of the joint distribution function
σ	Standard deviation of the observations
W	Weight matrix

Chapter 3: A Comparison of Photogrammetrically Determined Astronomical Refraction of Sunlight at High Zenith Angle with a Ray-tracing Computer Model Employing Rawinsonde Profiles

Many different fields of study have been incorporated into the investigation of astronomical refraction. In this chapter the fields of photogrammetry, meteorology, astronomy and optics have been cited. Each field of study has many standard symbols that appear in other fields but represent different values. For example H in meteorology is the scale height, while H in astronomy is the hour

angle. The symbols in Section 1 were adopted from Mahan (1962). In order to remain consistent with the customs of each branch of science and to maintain the historical nature of the derivation given by Mahan, the symbols were not altered from their original sources.

Section 1: Introduction

μ	Index of refraction
i	Incidence angle
e	Refracted angle
r_n	Distance from the centre of the Earth to the end of the light ray [m]
a	Mean radius of the Earth [m]
Z	Apparent zenith angle of the celestial object as seen by the observer
P	Points along the light ray
O	Centre of the Earth
ω	The radial distance traveled by the light ray, with respect to the centre of the Earth [m]
h	The height of the observer above the mean radius of the Earth [m]
R	The astronomical refraction angle
α, A, λ	Bessel's empirical refraction coefficients
B	Barometric pressure used in Bessel's refraction formula [mb]
T	Temperature correction for the barometer used in Bessel's refraction formula [$^{\circ}\text{C}$]
γ	The ambient air temperature used in Bessel's refraction formula [$^{\circ}\text{C}$]

C,D,E Corrective terms for humidity, the colour of the star, and geographic location incorporated in the Pulkovo Refraction Tables

Section 2: The Astronomical Refraction Model

θ	The angle between the lines joining the centre of the Earth and the beginning and the end of a ray path increment
β	The elevation angle of the light ray ($\beta = 90^\circ$ is towards the zenith)
r_e	The radius of the Earth [m]
T	Temperature [K]
p	Barometric pressure [Pa]
z	Height above mean sea level in geometric metres [m]
Z	Height above mean sea level in geopotential metres [gpm]
g	The acceleration due to gravity [ms^{-2}]
g_0	The mean sea level acceleration due to gravity [ms^{-2}]
ϕ	Geographic latitude
H	The scale height of the atmosphere [m]
κ	Curvature of the light ray
n	Average index of refraction of a given layer of atmosphere
η	The complement of the angle of refraction ($90^\circ - e$)
γ, ψ, ξ	The additional angles formed by a curved ray in a spherically symmetric atmosphere
ε	Miss angle of the ray with respect to the Solar disk
a_{sun}	Calculated angular altitude of the portion of the Sun the ray will strike

Section 3: Experimental Design

Q^*	Net radiation flux
Q_H	Sensible heat flux
Q_E	Latent heat flux
Q_G	Sub-surface heat flux
A	Azimuth angle
h	Horizontal angle
r_{Sun}	Angular radius of the Sun
R_t	Terrestrial refraction angle
k	Bomford's ray curvature coefficient
d	Distance to terrestrial target [m]
x,y,z	Image co-ordinates (photogrammetry) [m]
X,Y,Z	Object co-ordinates (photogrammetry) [m]
f	Focal length of the lens at infinite focus [m]
ω, ϕ, κ	Angles of rotation of the image coordinate reference frame
\mathbf{a}	Image vector
\mathbf{A}	Object space vector
\mathbf{M}	Rotation matrix (Image co-ordinates to object co-ordinates)
m_{ij}	Rotation matrix elements

Appendix A: Calculation of the Refractive Index of Air

n	Index of refraction
-----	---------------------

n_{air}	Index of refraction of standard air (15°C, 101,325 Pa, 0% R.H. and 450 ppm CO ₂)
n_{ws}	Index of refraction of pure water vapor at 20°C, 1333 Pa
ρ_a	The density of the dry component of air [kgm ⁻³]
ρ_{air}	The density of standard air (15°C, 101,325 Pa, 0% R.H. and 450 ppm CO ₂) [kgm ⁻³]
ρ_w	The density of the vapor component of air [kgm ⁻³]
ρ_{ws}	The density of pure water vapor [kgm ⁻³]
e_s	Saturation vapor pressure [Pa]
s_0, \dots, s_6	Constants in the saturation vapor pressure equation
T, T_K	Temperature [K]
T_C	Temperature [°C]
σ	Wave number of light (reciprocal of the vacuum wavelength)
k_0, \dots, k_3	Constants in the refractive index of standard air equation
c_f	Empirical correction factor in the refractive index of water vapor equation (under standard conditions)
w_0, \dots, w_3	Constants in the refractive index of water vapor equation (under standard conditions) [non-dimensional]
Z	Compressibility of dry air [non-dimensional]
a_0, \dots, a_2	Constants in the compressibility of dry air equation
b_0, b_1	Constants in the compressibility of dry air equation
c_0, c_1	Constants in the compressibility of dry air equation
d	Constant in the compressibility of dry air equation

e	Constant in the compressibility of dry air equation
R	Universal gas constant ($8.314510 \text{ Jmol}^{-1}\text{K}^{-1}$)
M_w	Molar mass of water vapor [kgmol^{-1}]
M_a	Molar mass of dry air [kgmol^{-1}]
x_c	Concentration of CO_2 [ppm]
x_w	Molar fraction of water vapor in moist air
h	Fractional relative humidity
f	Enhancement factor of water vapor in air [non-dimensional]
α, β, γ	Constants in enhancement factor equation

Appendix B: Derivation of the Fundamental Astronomical Refraction Equations

t	Travel time of a light ray [arbitrary units]
v_i, v_t	Velocity of the incident light ray and the transmitted light ray [arbitrary units]
a, b, h, x	Dimensions of Fermat's triangles describing the path of the light ray [arbitrary units]
θ_i, θ_t	Incidence and refracted angle in Fermat's derivation of Snell's Law
n_i, n_t	Index of refraction of the incidence and refracted medium in Fermat's derivation of Snell's Law
v_j	Velocity of the light ray associated with the j th atmospheric layer [ms^{-1}]
s_j	Path length of the light ray associated with the j th atmospheric layer [m]
c	Speed of light in a vacuum [ms^{-1}]

<i>OPL</i>	Optical path length [m]
<i>r,θ</i>	Polar co-ordinates of the light ray (origin at the centre of the Earth)
<i>β</i>	Complement of the incidence angle
<i>r_e</i>	Radius of the Earth [m]
<i>κ</i>	Curvature of the light ray
<i>φ</i>	Angular deflection of a curving ray
<i>x,y</i>	Cartesian co-ordinates for the curving light ray [m]

Appendix D: Precision and Accuracy of the Bomford Terrestrial Refraction

Formula

<i>a</i>	Altitude angle
<i>r</i>	Distance to the centre of the Earth [m]
<i>z</i>	Height above mean sea level [m]
<i>d</i>	Distance to target [m]
<i>R_t</i>	Terrestrial refraction angle
<i>T</i>	Temperature [K]
<i>p</i>	Barometric pressure [mb]
<i>h</i>	Height above mean sea level [m]
<i>r_e</i>	Radius of the Earth [m]
<i>Z</i>	Zenith angle

Appendix H: Refraction as a Function of Depth in the Atmosphere

R'_i Incremental refraction in the i th layer [°]

R_j Cumulative absolute refraction [°]

R_0 Cumulative absolute refraction observed at the surface [°]

INTRODUCTION

IMPORTANCE OF STUDY

As outlined in Chapter 3, the study of astronomical refraction has a long and distinguished history. The problem has been addressed by such eminent figures in early science as Ptolemy, Tycho, Kepler, Newton, Cassini, Bessel, Laplace and Euler (Mahan, 1962). A better understanding of astronomical refraction would have direct benefits in such fields as astrometry (Gubler and Tytler, 1998), Satellite Laser Ranging (SLR)(Yan and Wang, 1999), satellite navigation (Kireev and Sokolovskiy, 1994), satellite remote sensing (Noerdlinger, 1999), surveying (Anderson and Mikhail, 1998) and archaeoastronomy (Schaefer and Liller, 1990).

Before the invention of computers, researchers attempted to produce semi-analytical solutions to the problem of astronomical refraction (Mahan, 1962). More recently astronomical refraction models, using standard atmospheric profiles, have been run on computers (Garfinkel, 1967, Saastamoinen, 1979, Mikkola, 1979, Yatsenko, 1995, Thomas and Joseph, 1996, Stone, 1996, Yan, 1996, Yan, 1998). However, there has been very little work done evaluating the effectiveness of these models by comparing the calculated refraction values to actual observed refraction (Clemence, 1951). The following study compares the astronomical refraction calculated by a computer ray-tracing model to the astronomical refraction presented by the setting Sun. As outlined in Chapter 3, the amount of astronomical refraction increases with increased zenith angle; therefore refraction at sunset is a severe test of the accuracy of the model. It was also hypothesized that the use of measured atmospheric profiles in the model rather than idealized atmospheric profiles should

improve the quality of the model output. This hypothesis has also never been fully evaluated. In order to do this, astronomical refraction measurements were obtained within 20 minutes of the rawinsonde launch and from a location less than 100 metres from the launch site.

The astronomical refraction was measured photogrammetrically using a consumer grade photographic system. The key components of this system included a Questar 3.5-inch telescopic lens, an Olympus OM-1 35-mm camera body, Kodak Tri-X film and an Agfa Studio Scan II *si* flatbed colour scanner. Since a standard professional grade photogrammetric system was beyond the resources of the project, a major research component of this study was to evaluate the photogrammetric effectiveness of this less expensive system. To date, no published work has appeared on the photogrammetric calibration of consumer grade flatbed scanners or the Questar 3.5-inch telescopic lens. A cost effective and simple photogrammetric system such as the one employed and calibrated here, would have uses in such fields as Geographical Information Systems (GIS) (Ebi et al. 1994), environmental monitoring (Warner, 1994), medicine (Peterson, et al, 1993), forestry (Carson, 1985), soil science (Warner, 1995), surveying (Peterson and Durdle, 1991), and industrial design (Schubert, 2000).

THESIS OUTLINE

The thesis is written in paper format and is divided into three main chapters, each a self-contained manuscript. The order of the chapters represents the order in

which the individual tasks were completed before the astronomical refraction could be measured photogrammetrically.

Chapter 1: Photogrammetric Calibration of a Consumer Grade Flatbed Scanner. A flatbed scanner distortion model is described and used to produce a distortion atlas. Linear and non-linear distortions produced by an Agfa Studio Scan II si colour flatbed scanner are measured.

Chapter 2: The Selection and Calibration of an Optical System for High Magnification 0.1 arcminute Resolution Photogrammetry. The choice of photogrammetric system (lens, camera, and film) is justified according to the desired resolution. The focal length at infinite object distance and lens distortion values of a Questar 3.5-inch telescopic lens are measured using stellar and terrestrial targets.

Chapter 3: A Comparison of Photogrammetrically Determined Astronomical Refraction of Sunlight at High Zenith Angle with a Ray-tracing Computer Model Employing Rawinsonde Profiles. A ray-tracing model is used to simulate the observed refraction presented by sunsets observed on December 8, 14 and 22, 1998 from the Stony Plain Upper Air Station in Alberta. The model uses atmospheric profiles obtained from a rawinsonde launched within 20 minutes and less than 100 metres from the observer. Observed astronomical refraction is also compared with model output using a Modified U.S. Standard Atmosphere profile and with values derived from the Pulkovo Refraction Tables.

Chapter 4: Final Conclusions and Suggestions for Further Research. A summary of the findings and recommendations for further work.

CHAPTER 1: PHOTOGRAMMETRIC CALIBRATION OF A CONSUMER GRADE FLATBED SCANNER

Abstract

The photogrammetric utility of an Agfa Studio Scan II *si* flat bed colour scanner was examined. The scanner has a 400 ppi horizontal and 800 ppi vertical optical resolution with a pixel size of 64 μm by 32 μm . Systematic linear and non-linear distortions in the scanned images were observed, indicating the need for calibration. The calibration was done with the assistance of a distortion model, which produced a scanner distortion atlas. Distortions in the image coordinates were found by directly scanning a glass calibration grid-plate. In the absence of corrective adjustments, the measured distortions produced deviations of 0.6% or less from the object coordinates. For this particular scanner the tilt of the scanner head appears to be about 6.0 arcminutes, with a scaling distortion in the x-direction of 0.9941 and 0.9992 in the y-direction. The periodic distortion appears to have an amplitude of 1.6 pixels, and a wavelength of 4.9 cm. There appears to be no aliasing in the periodic distortion measurements.

1 Introduction

Traditional photogrammetric measurement of negatives or prints usually requires the use of expensive and complex stereoplotters or other similar devices. For less demanding requirements, a simpler and more accessible technique may be desirable. One such application is the measurement of 35 mm negatives taken with a

non-metric or consumer grade camera. Other disciplines with a proven need for inexpensive lower-precision photogrammetry include Geographical Information Systems (GIS) (Ebi *et al.* 1994), forestry (Carson, 1985), soil science (Warner, 1995), medicine (Peterson, *et al.*, 1993) general surveying (Peterson, and Durdle 1991) and environmental monitoring (Warner, 1994). Flatbed scanners have also been successfully used as stereoscopic near-field cameras with application in such areas as printed circuit design and testing (Schubert, 2000).

The original motivation for this study was to scan 35 mm negatives to help determine the astronomical refraction of the setting Sun. Due to the motion of the Sun, traditional survey instruments can only be used to obtain single point measurements at a given time. Telescopic photogrammetry offers an opportunity to measure the near-instantaneous position of the entire disc of the Sun. Image coordinates must be measured to facilitate Sun location computations. However, budget and time constraints made rapid and inexpensive means of obtaining image coordinates from 35 mm negatives desirable.

The calibration described in this paper was performed in order to evaluate the suitability of an Agfa Studio Scan II *si* flat bed scanner for these astronomical refraction studies. The results should also be relevant to other applications. Maximum tolerable experimental error in determining the horizontal coordinates (altitude and azimuth) of the Sun predetermined the required accuracy of the scanner. Exposure timing errors and the accuracy of theodolite reference measurements of stationary reference markers imposed a maximum tolerable experimental error of ± 0.1 arcminute. The telescopic lens used to photograph the setting Sun (a Questar

3.5 inch telescopic lens) had a calibrated focal length of 1445.3 ± 3.6 mm. Thus a 0.1 arcminute error translates into a linear error of $42 \mu\text{m}$ on a 35 mm negative. This is 31% larger than a scanner pixel at 800 ppi. Therefore, to maintain 0.1 arcminute experimental accuracy, it would be necessary to detect and correct any scanner distortion greater than 1 pixel over the length of a 35 mm negative.

The film stock chosen for the experiment was 35 mm Kodak Tri-X black and white film. The film resolution was limited by the emulsion grain size. In order to exploit the full resolution of a black and white film, it is recommended that a scanner should have a pixel size of about 10 by 10 μm (Kölbl and Bach, 1996). Consequently, emulsion grain size was not the limiting factor when scanning at 800 ppi.

Since detailed engineering drawings and specifications of the Agfa scanner used in this study were proprietary information, no information on the exact operation or manufacturing tolerances could be obtained. Consequently, the scanner was treated as a 'black-box' and the cause of each distortion could only be inferred from the calibration data.

1.1 Previous Work

Warner and Andersen (1992) calibrated a Canon Colorlaser Copier (CLC-200). In their work a Pentax 645 and a Pentax 35 mm camera were used to image an outdoor target field. Measurements of the image coordinates of the targets were measured directly from the diapositives using an analytical plotter. The copier enlarged the original 35 mm diapositives and made direct copies of enlargement

prints from the Pentax 645 camera. The resulting photocopies were then measured and compared with the original image coordinates through a least-squares affine coordinate transformation. It appears that no attempts were made to minimize the effects of film buckling in either the camera or the enlarger.

Their results extracted only linear distortions. The 35 mm enlargement showed a 1.023 ± 0.040 mm mean stretch in the x-direction (0.22%) and the 645 image showed a mean stretch of 0.224 ± 0.140 mm. Skewness (nonperpendicularity of axes) was found to be 0.887 ± 0.099 mm for the 35 mm enlargement and -1.663 ± 1.124 mm for the 645. Photographic enlargement of the diapositive prior to copying was most likely the cause of the larger uncertainty in the 645 image.

A major limitation of photocopier technology is that the output is not machine-readable. The image coordinates of the photocopy must still be measured from a digitizing tablet or plotter. Modern flatbed scanners can provide digital output directly to the computer. Image processing software can then be used to extract pixel image coordinates directly from the image file.

1.2 Experimental Procedure

In order to determine the effectiveness of the scanner as a photogrammetric tool, it was necessary to calibrate the device using a target of known dimensions and stability. The x-y image coordinates (in pixels) of the target were obtained by scanning portions of a 25 by 25 cm Zeiss glass stereo-plotter calibration grid-plate. Systematic discrepancies from the precisely known object coordinates of the targets were used to establish a calibration model for the scanner. Prior to conducting the

calibration experiment a computer model of the scanner distortion was developed for use in interpreting the scanning results.

1.3 Distortion Model

The model was designed to simulate the scanner output for a perfect grid-plate by imposing various distortions. The origin of the image coordinates was chosen to be the grid point closest to the lower left corner of the frame. The positive y -axis was taken to lie along the direction of motion of the scanner head, with the x -axis normal to the y -axis. Model input parameters consist of:

- $ppcm$ Manufacturer's stated resolution [pixels per cm]
- α Tilt angle of the grid-plate rulings relative to the x -axis [degrees] (see Figure 1). The tilt angle is considered to be positive in a counter-clockwise direction (i.e. rotation from the positive x -axis towards the positive y -axis).
- γ Tilt angle of the scanner head [degrees] relative to the normal to the direction of motion of the scanner head. Positive in a counter-clockwise direction.
- f_x Fractional linear scaling distortion along the axis of the scanner head produced by any difference between the manufacturer's stated resolution and the actual resolution.
- f_y Fractional linear scaling distortion along the axis of the scanner track
- λ Wavelength [cm] of a sinusoidal wave distortion along the axis of the scanner track.
- A Amplitude [cm] of the wave distortion.

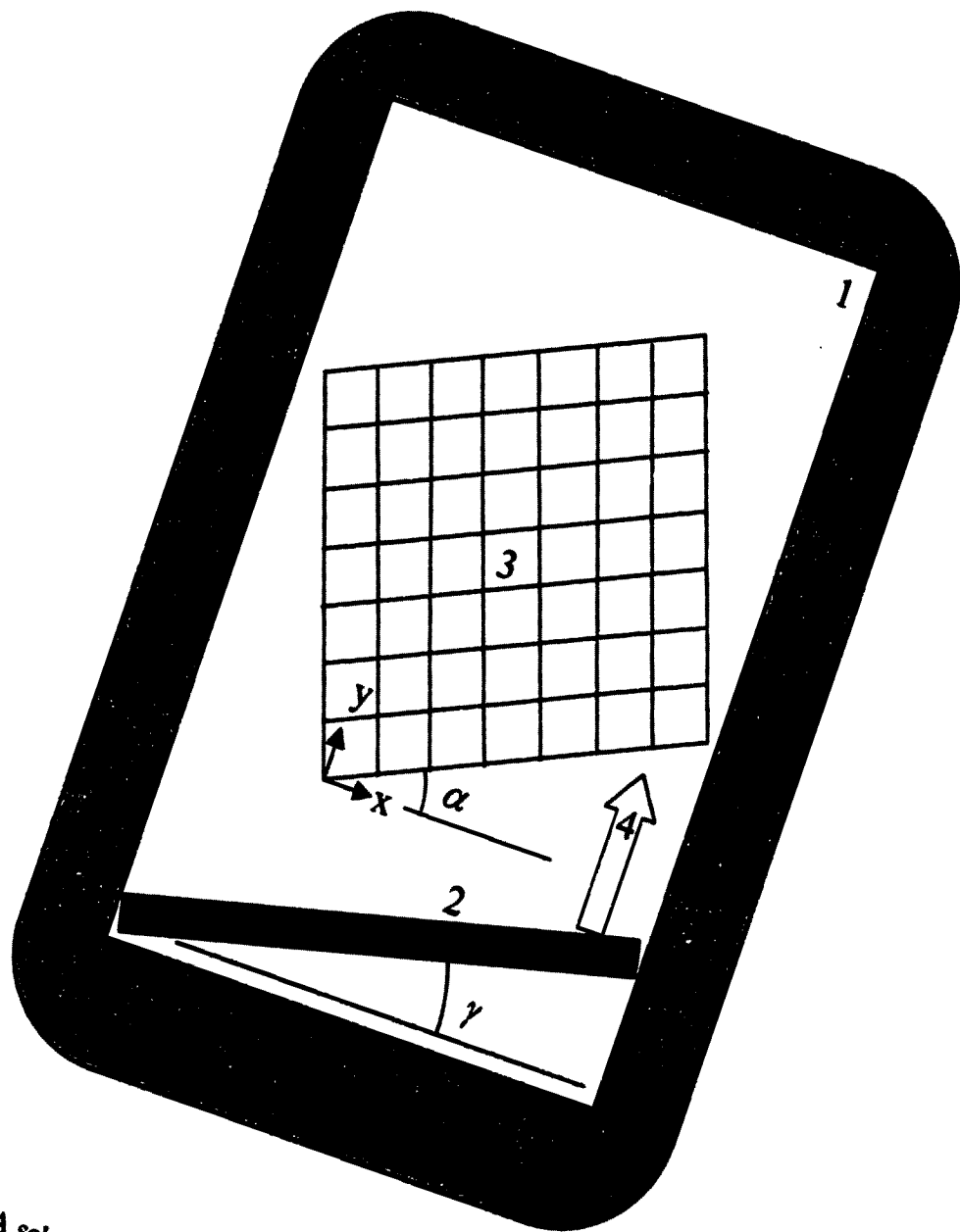


Figure 1: A schematic of the scanner head and grid plate orientation. 1) Scanner platen, 2) scanner head, 3) grid plate target and 4) direction of scanner head motion.

ε Phase of the wave relative to the x,y origin.

σ_x, σ_y Random measurement error [cm].

The modelled image coordinates x and y [cm] were determined from a transformation matrix derived in the following steps. The rotation due to the tilt of the calibration grid-plate is given by the formula:

$$\begin{bmatrix} x' \\ y' \end{bmatrix} = \begin{bmatrix} \cos \alpha & -\sin \alpha \\ \sin \alpha & \cos \alpha \end{bmatrix} \begin{bmatrix} X \\ Y \end{bmatrix}, \quad (1)$$

A

where x' and y' are the rotated co-ordinates and X and Y are the object co-ordinates (i.e. the actual raw measurements). The rotation due to the tilt of the scanner head γ can now be determined through the equation:

$$\begin{bmatrix} x'' \\ y'' \end{bmatrix} = \begin{bmatrix} \sec \gamma & 0 \\ -\tan \gamma & 1 \end{bmatrix} \begin{bmatrix} x' \\ y' \end{bmatrix}, \quad (2)$$

B

where x'' and y'' are twice rotated co-ordinates. The effects of scaling distortions f_x and f_y can now be included through the equation:

$$\begin{bmatrix} x \\ y \end{bmatrix} = \begin{bmatrix} f_x & 0 \\ 0 & f_y \end{bmatrix} \begin{bmatrix} x'' \\ y'' \end{bmatrix}, \quad (3)$$

C

where x and y are the image coordinates. Now:

$$\begin{bmatrix} x \\ y \end{bmatrix} = \mathbf{C} \begin{bmatrix} x'' \\ y'' \end{bmatrix} = \mathbf{CB} \begin{bmatrix} x' \\ y' \end{bmatrix} = \mathbf{CBA} \begin{bmatrix} X \\ Y \end{bmatrix} + \begin{bmatrix} a \\ b \end{bmatrix}, \quad (4)$$

which when expanded, gives the general form for the transformation:

$$\begin{bmatrix} x \\ y \end{bmatrix} = \begin{bmatrix} f_x \sec \gamma \cos \alpha & -f_x \sec \gamma \sin \alpha \\ -f_y \cos \alpha \tan \alpha + f_y \sin \alpha & f_y \cos \alpha + f_y \sin \alpha \tan \gamma \end{bmatrix} \begin{bmatrix} X \\ Y \end{bmatrix} + \begin{bmatrix} a \\ b \end{bmatrix}, \quad (5)$$

where a and b are translational coefficients in the x and y directions. Based on a preliminary calibration of the scanner, it was apparent that a sinusoidal translational distortion was produced along the direction of travel of the scanner head. A probable explanation for such a distortion is the decentering or non-circularity of one or more drive wheels. Consequently, the model includes translational values a and b of the form:

$$a = \sigma_x, \quad (6)$$

and

$$b = A \sin\left(\frac{2\pi Y}{\lambda} + \varepsilon\right) + \sigma_y. \quad (7)$$

Equation 5 was used to produce values of x and y and these were then converted to pixel coordinates and rounded to the nearest pixel.

Distortion values were first entered into the model and a least squares method was used to estimate these distortion values from the modelled image co-ordinates thereby simulating the calibration process and determining how well it works. The first method uses an approximate geometric solution and the second employs a least-squares fit to the distortion measurements.

In the approximate geometric method we compute the tilt angle of the grid-plate and the individual distortion values. This method can be used only when linear distortions are applied. Although this method produces cumbersome correction formulae, it is helpful in allowing a quick assessment of the computer model.

The tilt of the array is estimated from:

$$\gamma = \sin^{-1} \left[\frac{p^2 \tan \phi - \tan \psi}{p(1 - \tan \phi \tan \psi)} \right], \quad (8)$$

where ψ and ϕ are the tilt of the axis of the grid-plate image with respect to the scanner's x and the y -axis image coordinates respectively. The value of p is the ratio of the measured y and x resolutions of the scanner (i.e. the actual ppi of the scanner). Since this ratio is very close to unity, it can be ignored.

The tilt of the plate can then be estimated from the formula

$$\alpha = \tan^{-1} \left(\frac{\tan \psi + \sin \gamma}{\cos \gamma} \right), \quad (9)$$

and finally, f_x and f_y are found from

$$f_x = \frac{x \cos \gamma}{X \cos \alpha}, \quad (10)$$

and

$$f_y = \frac{y \cos \gamma}{Y \cos(\gamma - \alpha)}. \quad (11)$$

1.4 Least Squares Analysis and a Residuals Atlas

In order to reveal the distortions inherent in the scanner, the difference between the measured pixel co-ordinates of the actual grid-plate and the co-ordinates of a hypothetical undistorted and perfectly aligned grid can be plotted against their measured distance from the origin. That is, measured residuals in the x and y -direction ($\hat{\alpha}_x$, $\hat{\alpha}_y$) were plotted against their respective co-ordinates (x or y). The

model was then used to estimate a set of distortion coefficients, which reproduces the behavior of the residuals.

The grid point at the lower left corner of the image was chosen as a common origin for both the measured and the hypothetical perfect grid. Correction formulae were then produced by a linear regression analysis of the residuals.

In order to help interpret the residuals, a schematic distortion atlas was constructed. Figure 2 shows the fundamental distortion types from a hypothetical 4 by 4 grid-plate. A guide to the combinations of these residuals appears in Table 1. It was apparent from the computer model that the tilt of the grid-plate should be kept to less than a degree in order to keep the vertical spread of the data to a minimum and make the linear regression more accurate.

1.5 The Target

The target used was a 1 cm grid etched onto a 25 x 25 cm glass plate. The plate was manufactured by V.E.B. Carl Zeiss Jena and is normally used in the calibration of stereoplotters. According to the manufacturer's specifications, the median absolute error of the grid coordinates is $\pm 0.9 \mu\text{m}$ in the x and y -directions, with a maximum calibrated error of a single grid point of $2.1 \mu\text{m}$. The mean error in the orthogonality of the grid is 2.4 arcseconds, which translates into approximately $0.1 \mu\text{m}$ over 1 cm. Consequently, plate error was ignored since each error is smaller by more than an order of magnitude than the pixel size of the scanner.

Normally, the object co-ordinates of the photogrammetric calibration target must be determined through a painstaking survey. The use of the grid-plate greatly

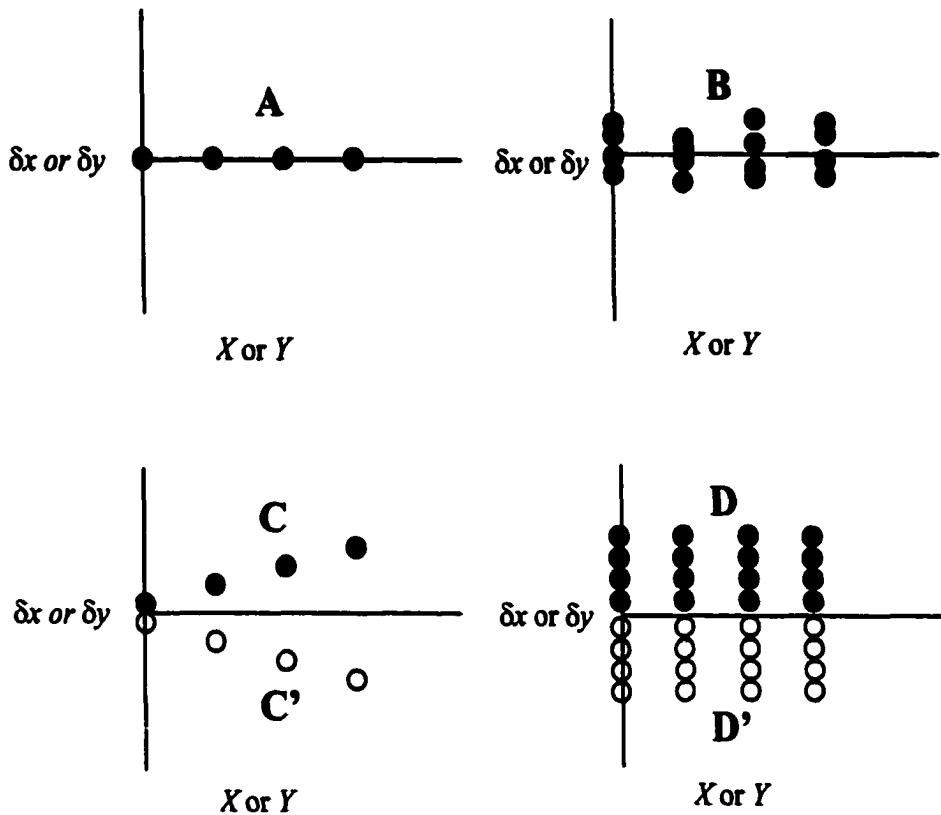


Figure 2: The residuals (differences between the measured and an undistorted grid-plate) produced by the fundamental types of scanner distortion. The ordinate is the object distance along the plate and the abscissa is the residuals. Plot A represents no distortion, B is random measurement error only, C and C' are scaling distortions, and D and D' are distortions due to the tilt of the grid-plate or scanner head.

Distortion Description	δx vs. X Graph	δy vs. Y Graph
No distortion	A	A
Measurement error	B	B
Scaling in X only	(C or C') + B	B
Scaling in Y only	B	(C or C') + B
Tilt of grid-plate only	(D or D') + B	(D' or D) + B
Tilt of scanner head only	B or [(C or C') + B] [†]	(D' or D) + B
X scaling and grid-plate tilt	(C or C') + B + (D or D')	(D' or D) + B
Y scaling and grid-plate tilt	(D' or D) + B	(C or C') + B + (D or D')
X scaling and scan head tilt	(C or C') + B [‡]	(D' or D) + B
Y scaling and scan head tilt	(C or C') + B + (D or D')	(C or C') + B + (D or D')
X and Y scaling only	(C or C') + B	(C or C') + B
X and Y scaling and grid-plate tilt	(C or C') + B + (D or D')	(C or C') + B + (D or D')
X and Y scaling and scanner head tilt	(C or C') + B	(C or C') + B + (D or D')
X and Y scaling and all tilts	(C or C') + B + (D or D') ^{**}	(C or C') + B + (D or D') ^{**}

Table 1: List of graph types from different linear distortions. The letters A, B, C, C', D and D' correspond to the distortion types illustrated in Figure 1. Notes: * δx and δy will be on opposite sides of the X or Y-axis. [†]This condition holds for $-1^\circ < \gamma < 1^\circ$, otherwise the slope also becomes a function of the tilt of the grid-plate. [‡] If $-1^\circ > \gamma > 1^\circ$ then the slope will also become a function of the scanner head tilt. ^{**} The difference between the vertical spread in the data points in the two graphs will depend on the magnitude and sign of the tilt of the scanner head.

simplified the calibration, since the dimensions, geometry and accuracy of the target were predetermined. The simple target geometry and dimensions also allowed for a predictive calibration model to be more easily constructed, verified and interpreted.

2. Results

Limitations in computer memory prevented a full plate scan at maximum resolution. Consequently four initial scans were made of a 9 cm by 9 cm section of the grid-plate producing an 8 by 8 target point field. Image files were stored in Tagged Image File Format (TIF).

The residuals in the first scans suggested that there were distortions of a sinusoidal nature along the y-axis. If the scan area captures only a small number of wavelengths, or a fraction of a single wavelength of the sinusoidal translational distortion, the least-squares fit could deviate from the central axis of the curve and the mean scaling distortion in the y-direction would be poorly determined (see Figure 3). To minimize this risk, the scan area should be as long as possible in the y-direction. As a result, four 2.5 by 25 cm scans were performed, encompassing the full length of the target grid in the direction of travel of the scanner head. This scan area produced a 3 by 24 point target field.

During the scans, the positions of the grid-plate and the scan area were fixed. Pixel image coordinates of the scanned grid-plate intersection points were extracted using the image analysis software Scion Image (1998).

The pixel co-ordinates for the four scans were then averaged. The mean sample standard deviation of the four measurements for each target was 0.05 pixels

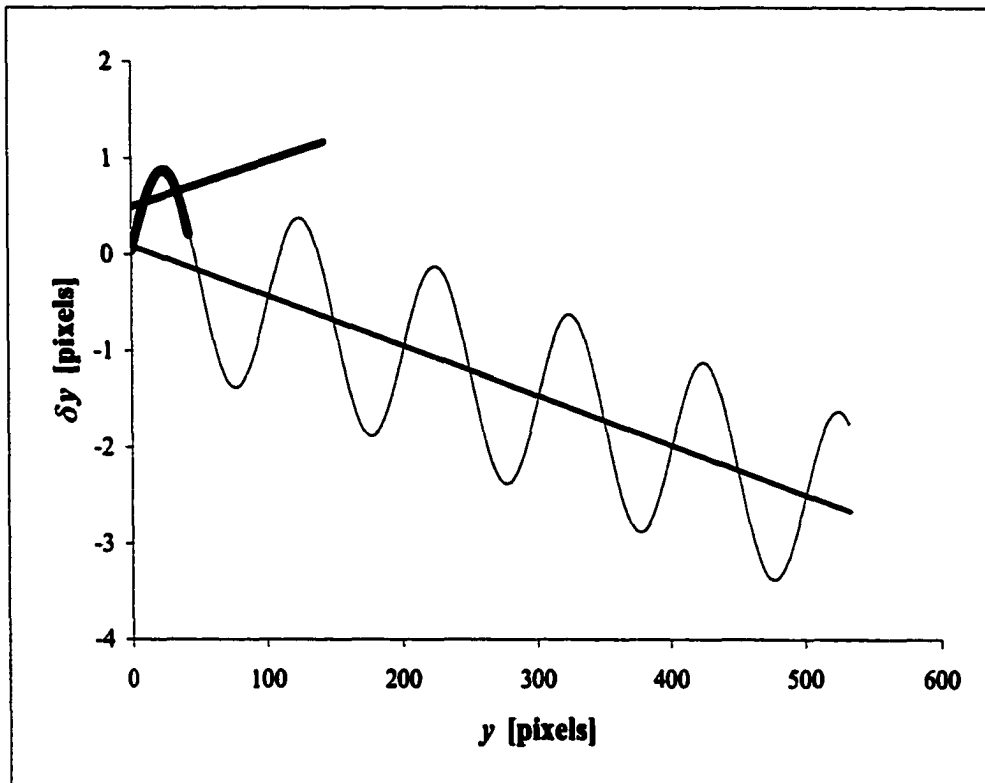


Figure 3: An illustration of why numerous wavelengths must be sampled by the scanner before an accurate measurement of the linear scaling distortion (black line) can be determined. The thick line is a linear fit to the partial wavelength (thick curve).

in the x-direction with a maximum sample standard deviation of 0.58 pixels, while for the y-direction the mean sample standard deviation was 0.11 pixels with a maximum of 0.5 pixels. This suggests that the scanner was consistent (i.e. dimensionally stable) from one scan to the next. The graphs of the residuals appear in Figures 4, 5 and 6.

In Figure 5 the vertical spread of the δy data is much less than the δx data in Figure 4. Using the distortion atlas and the computer model this difference could be explained if the tilt of the scanner head was approximately the same as the tilt of the grid-plate. The tilt of the plate can be estimated from:

$$\alpha \cong \arctan\left(\frac{s}{d}\right), \quad (12)$$

where s is the average vertical spread in Figure 4 (4.75 pixels) and d is the total distance in pixels (2205 pixels). The resulting calculated tilt is 7.4 arcminutes.

The linear regression of the averaged scanner residuals produced the following result:

$$\delta x = -6.1 \times 10^{-3} (\pm 2.0 \times 10^{-4})x - 1.611 (\pm 0.002), \quad (13)$$

where x is the distance from the origin in pixels. Uncertainties in the slope and the intercept were calculated according to methods outlined in Taylor (1982). A linear regression for the averaged scanner residuals in the y-direction yielded:

$$\delta y = -6.54 \times 10^{-4} (\pm 1.7 \times 10^{-5})y - 0.85 (\pm 0.13). \quad (14)$$

Placing values of ψ and ϕ from the image coordinates into Equations 8, 9 and 10 produces a value of 6.2 arcminutes for both α and γ . From Equation 10 the value

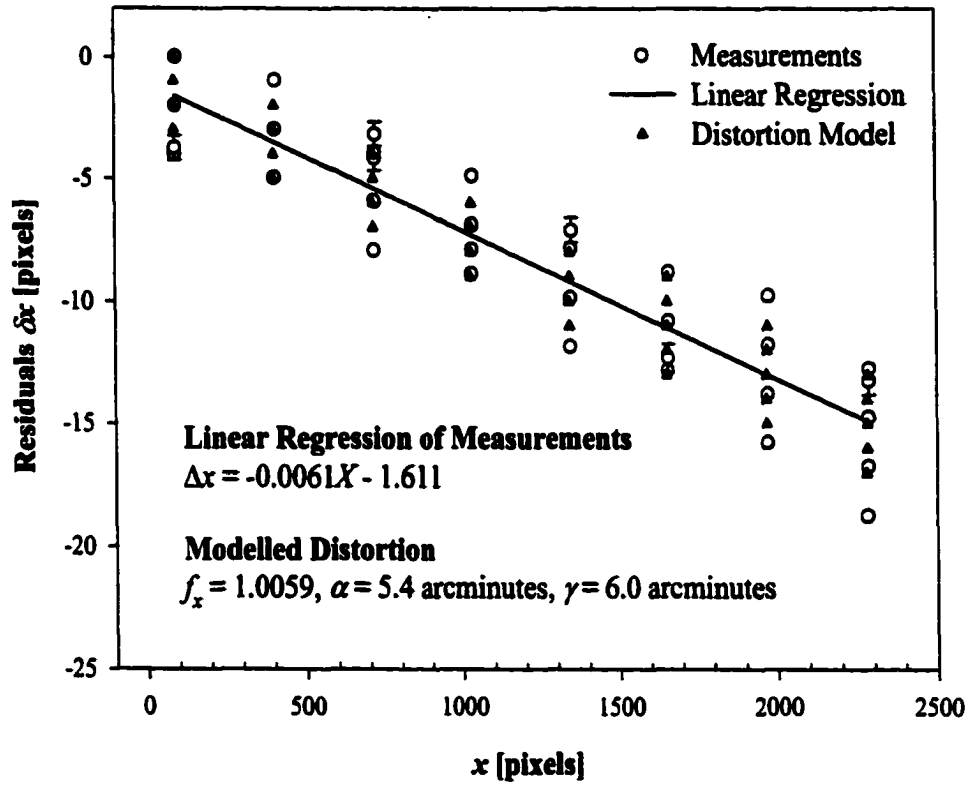


Figure 4: Linear fit to the mean of x -residuals for all four scans of an 8 by 8 target point grid.

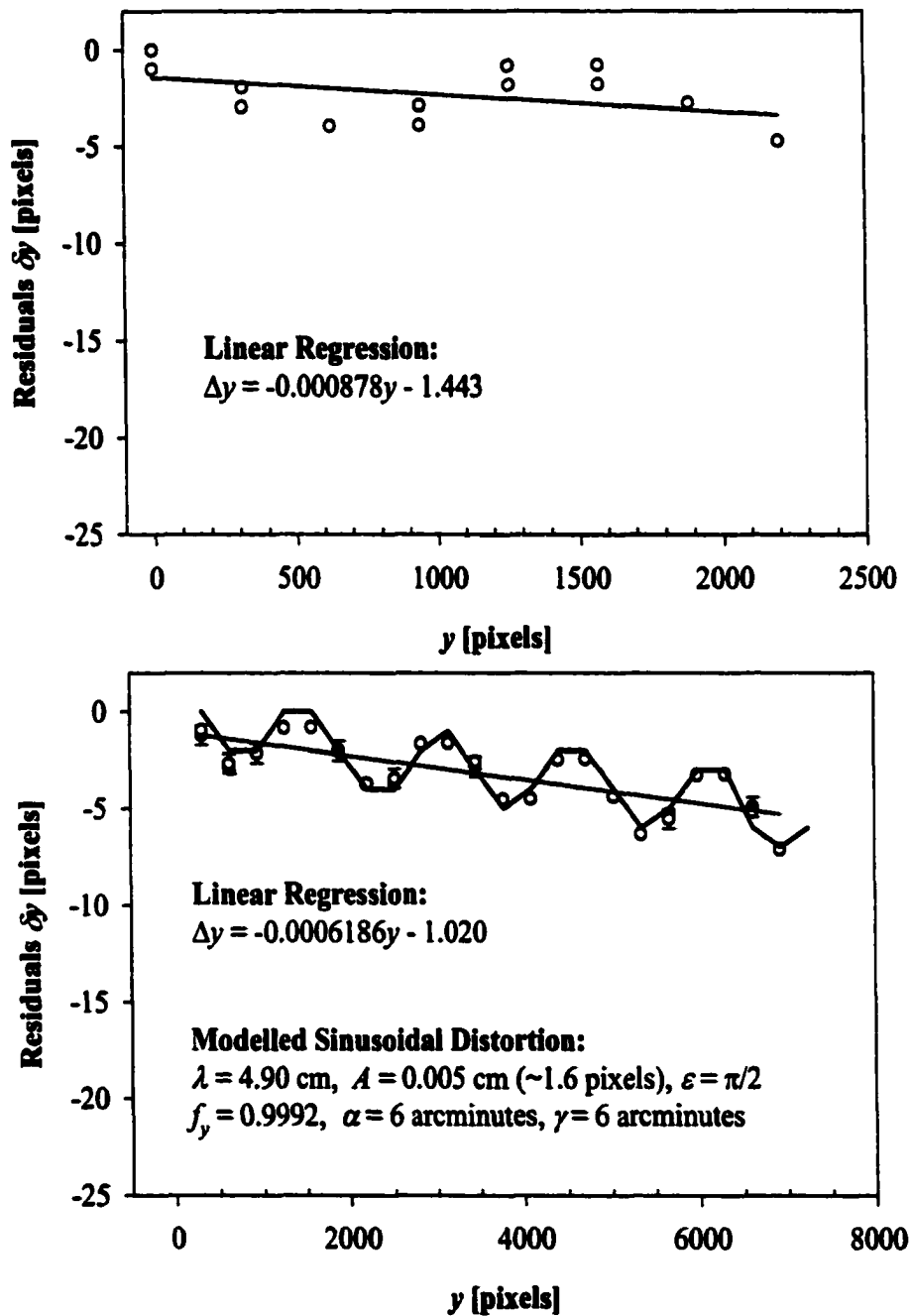


Figure 5: An example of the residuals for an 8 by 8 target point grid in the y-direction. **Figure 6:** The average of four scans of a 3 by 24 cm target point grid in the y-direction. The solid curve represents the modelled residuals, rounded to the nearest pixel. Error bars are the sample standard deviations of the four measurements.

of f_x was found to be 0.9931. Due to the non-linear distortion in the y -direction, f_y could not be calculated directly using Equation 11.

Non-linear distortions in the y -direction appear to be sinusoidal, with a wavelength of approximately 1610 pixels, and amplitude of about 2 pixels. The phase appears to be the same in all the scans. In Figure 6 the amplitude appears to increase slightly with increasing y . This effect was common to all scans and may be due to the discrete sampling of an analogue wave.

The computer model was then used to reproduce the observed residuals. This helped remove any effect a tilted grid-plate would have on the final correction formulae. Starting with the estimated values for scaling distortion ($f_x = 0.9931$), grid-plate tilt ($\alpha = 6.2$ arcminutes), and scanner head tilt ($\gamma = 6.2$ arcminutes) the model was manually adjusted until the output appeared to closely match the measurements in Figures 4 and 6. As a more quantitative test, the model parameters (grid plate tilt, and scaling distortion) were adjusted until the sum of the absolute residuals between the modelled and the measured residuals were minimized. These modelled values could then be used in the final correction formulae, which can be derived from Equation 5. A summary of the results appears in Table 2.

Parameter	Analytic	Graphic	Model	Graphic	Model
f_x	0.9931	0.9939	0.9941		
f_y				0.9994	0.9992
α [°]	6.2	7.2	5.4	-	6.0
γ [°]	6.2			7.2	6.0
A [pixels]				2	1.6
λ [cm]				5.0	4.9
ε				$\pi/2$	$\pi/2$

Table 2: Geometric estimates (Equations 8 through 11), graphically estimated (using Equation 12) and modeled values for the scaling distortions, (f_x and f_y) grid-plate tilt (α), scanner head tilt (γ), periodic distortion amplitude (A), wavelength (λ) and phase (ε).

2.1 Possible Aliasing of the Periodic Distortion

Since the periodic distortion was detected using a periodic instrument (the grid-plate), aliasing may be present in the data. Aliasing may be thought of as high frequencies masquerading as low frequencies. According to (Chapal and Canale, 1985) there must be at least 2 samples per cycle in order that the true frequency is detected. Otherwise, an aliased frequency will be measured. This sampling rate is called the Nyquist frequency.

A theoretical consideration of aliasing (Poularikas and Seely, 1988) is given in Appendix 1A. The expression for the alias wave is given by:

$$F(x) = Ae^{2\pi j\left(\frac{k^*}{J}\right)}, \quad (15)$$

where A is the amplitude, and

$$k = k^* + mJ, \quad (16)$$

where k^* represents the number of wavelengths of the aliased wave produced by J samples of k wavelengths of the true signal. Since there are an infinite number of m

integers there are an infinite number of possible signal waveforms that can produce a given alias as measured by a given sampling frequency.

From the measurements of the y -distortion of the scanner $k^* \approx 4.5$ and $J = 22$. Placing these values into Equation 16 produces a series of possible signal wavelengths; the largest five are listed in Table 3.

m	k	$\lambda = 22/k $ [cm]
-2	-39.5	0.557
-1	-17.5	1.257
0	4.5	4.888
1	26.5	0.830
2	48.5	0.454

Table 3: The five longest wavelengths that can produce a sampled wavelength of 4.888 cm as measured by a 1-cm grid-plate over a sampling distance of 22 cm.

A spreadsheet model was constructed to explore the behavior of aliasing and techniques to detect possible aliases in the periodic distortion. Values of λ found from Equation 16 were entered into the model and aliases were produced with a wavelength of 4.888 cm. If the observed wave is not an alias then a phase shift of the sampling frequency (i.e. where the sampling starts) should not produce a shift in the phase of the observed wave with respect to fixed coordinates. Results from the model can be seen in Figures 7 through 10. It is apparent from these simulations that shifting of the grid-plate by a few millimetres in the y -direction should make it possible to determine the occurrence of aliasing.

In order to test for the possible occurrence of aliasing the grid-plate was moved along the y -axis in increments of about 0.2-cm and then scans were taken of the same

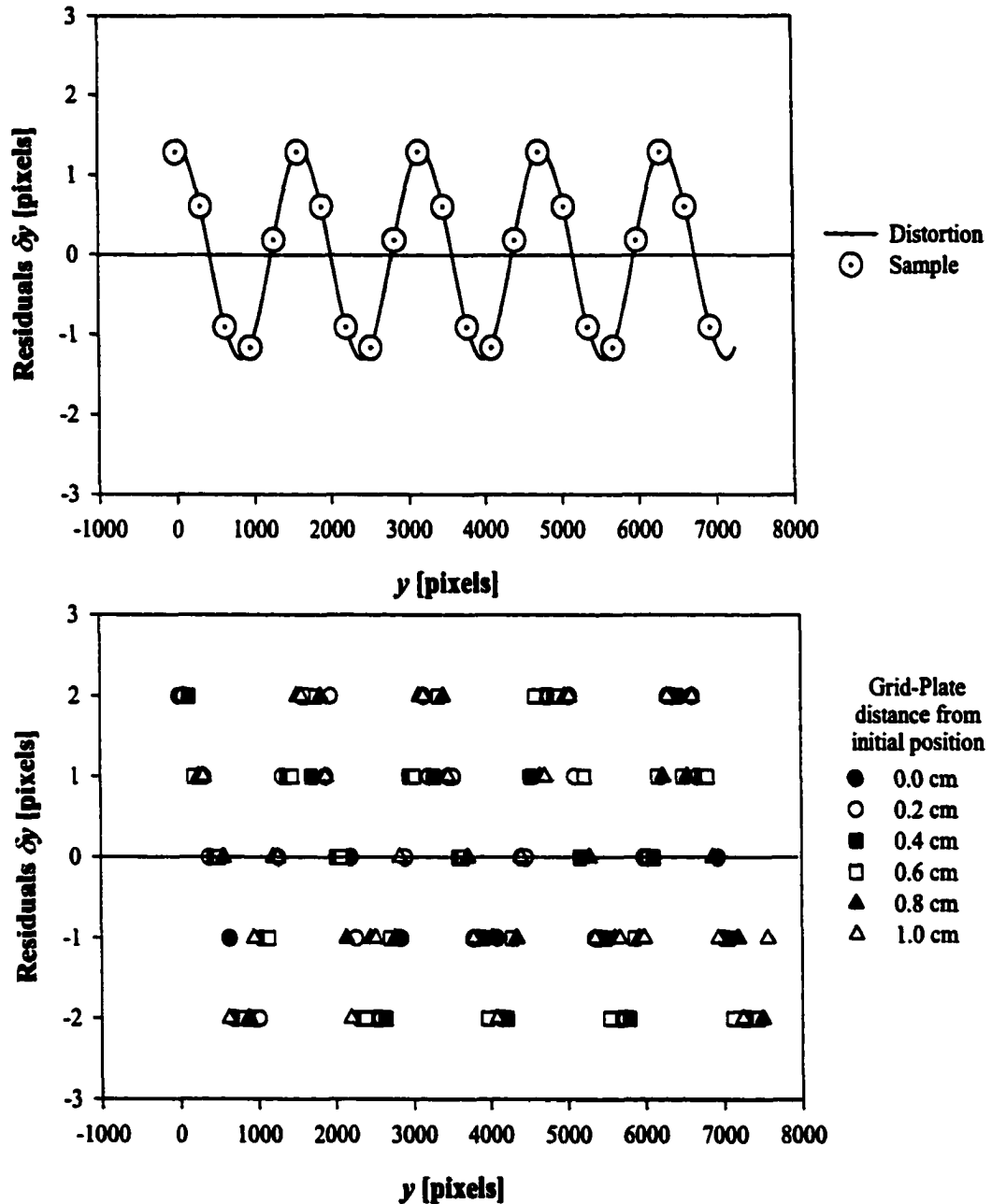


Figure 7: A 1 cm sampling of a $\lambda = 5.0$ cm distortion with a 1.3 pixel amplitude. **Figure 8:** A modelled sampling of the same distortion with a moving grid-plate and ± 0.5 pixel measurement error, with the final values rounded to the nearest pixel. Increase in amplitude from Figure 6 is due to measurement error and round-off error.

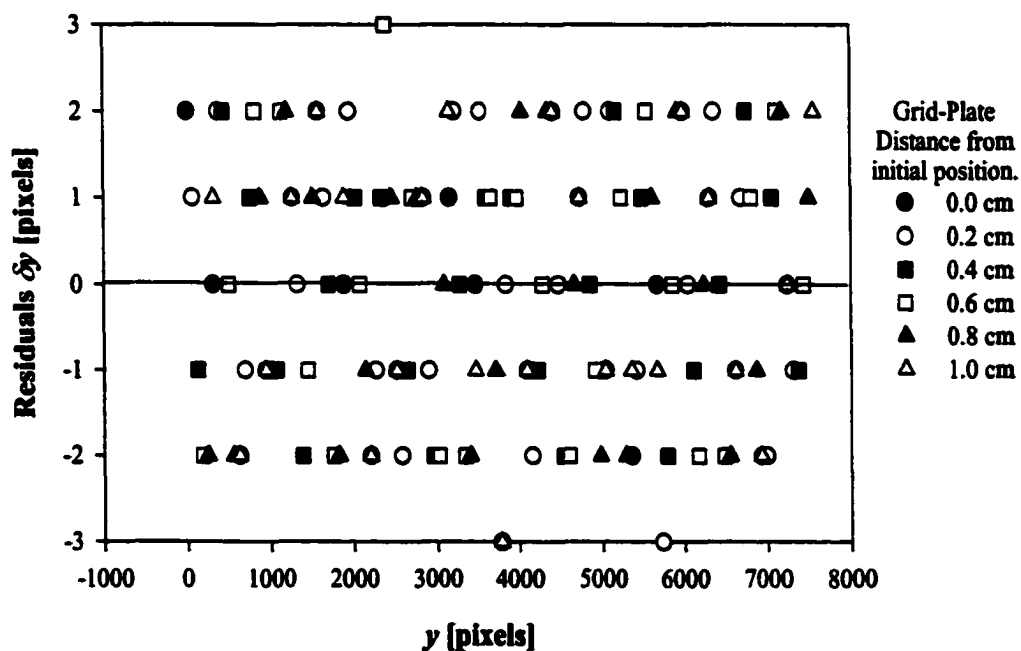
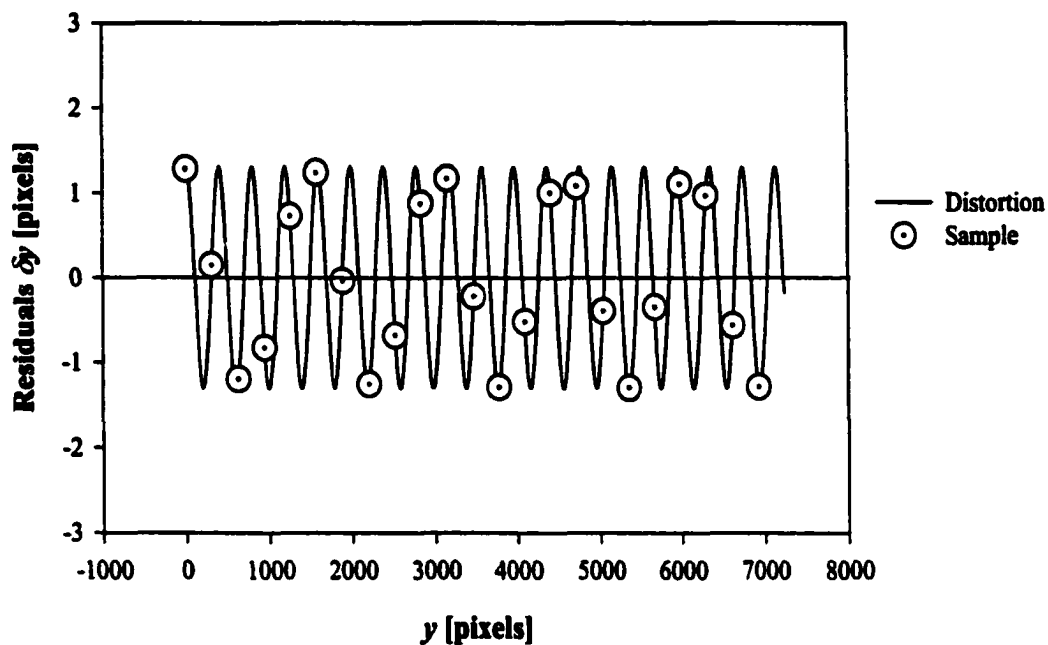


Figure 9: A 1 cm sampling of a $\lambda = 1.257$ cm distortion with a 1.3 pixels amplitude displaying an aliased wave of $\lambda = 5.0$ cm.

Figure 10: A sampling of the same distortion with a moving grid-plate with ± 0.5 pixel measurement error and rounded to the nearest pixel.

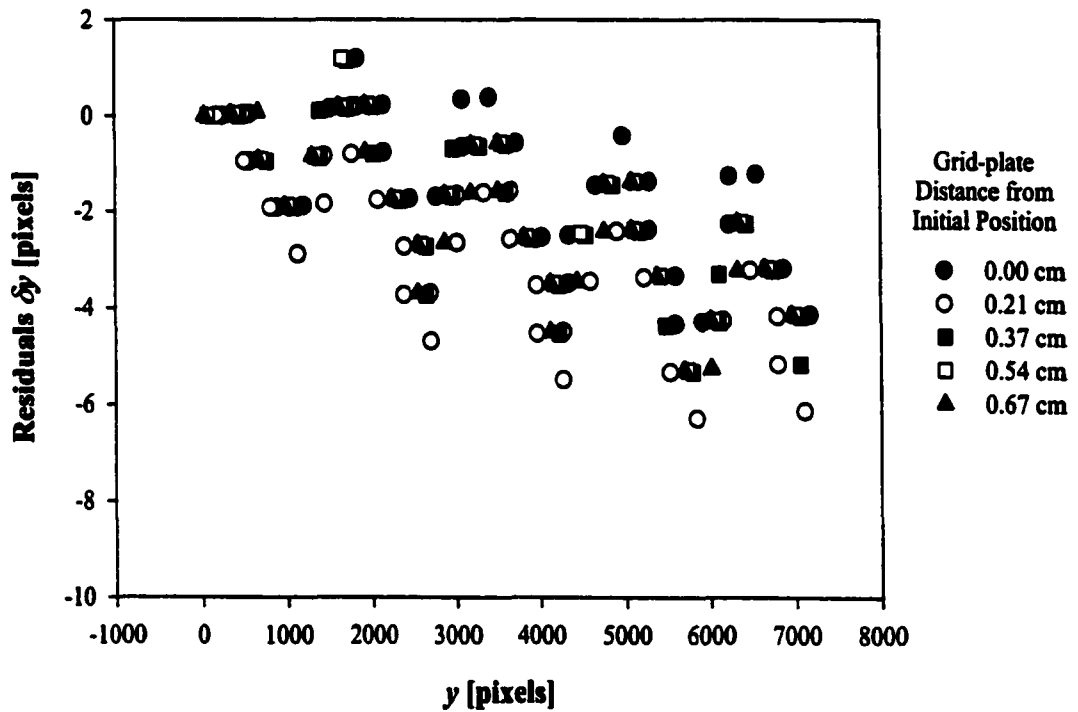


Figure 11: Measured distortion in the y-direction with a moving grid-plate and fixed scanning area. Position of the grid-plate was determined by the difference in pixel coordinates from one scan to the next.

scanner field. Care was taken to ensure the tilt of the plate was constant from one scan to the next by positioning the grid-plate against a straightedge fixed to the scanner platen. The results of these measurements can be seen in Figure 11. The results suggest that aliasing is unlikely since the phase of the measured wave appears to be constant.

2.2 Stability of Scanner Distortion

Due to the mechanical nature of the scanner there may be instability in the relative pixel coordinate produced from one scan to the next. To test the stability of the distortion in the y-direction a series of fourteen 2 by 24 cm scans were done across the full length of grid-plate. The positions of the plate and the scanner field were kept fixed. The average standard deviation of the entire data set was 0.12 pixels with the maximum sample standard deviation of 0.51 pixels. This suggests that the scanner output is stable over the short term (i.e. less than an hour). Continued tests over the lifetime of the machine would be necessary to evaluate the long-term dimensional stability of the scanner.

The grid-plate sat on the scanner platen for more than 29 minutes and was noticeably warmer when removed. This would imply that dimensional instabilities in the scanner or grid plate caused by thermal expansion might not be an issue. However, more detailed measurements would need to be done to firmly establish the absence or presence of any effects.

3. Conclusions

The results suggest the Agfa Studio Scan II *si* can achieve single pixel accuracy once calibrated and appropriate corrections are applied. Linear distortions in both axes appear to be systematic and therefore corrective formulae can be effective.

The non-linear distortions in the y-direction also appear to be systematic and can also be subtracted from the image coordinates. In order to determine the phase of a sinusoidal correction, care should be taken when placing the original image on the scanner.

For this particular scanner the tilt of the scanner head appears to be about 6.0 arcminutes, with a scaling distortion in the x-direction of 0.9941 and 0.9992 in the y-direction. The periodic distortion appears to have an amplitude of 1.6 pixels, and a wavelength of 4.9 cm. There appears to be no aliasing in the periodic distortion measurements.

It is assumed that much of the distortion is a result of manufacturing limitations. As a result, it would be necessary to calibrate each scanner before photogrammetric measurements of single pixel accuracy could be achieved.

APPENDIX A

SAMPLING THEORY: ALIASING

A discrete sampling of a continuous wave may produce a frequency not present in the original wave. This process is called aliasing and the minimum sampling frequency necessary to measure a particular frequency is called the Nyquist frequency.

A theoretical consideration of aliasing (Poularikas and Seely, 1988) starts with the relationship:

$$k\lambda = JI = L, \quad (\text{A1})$$

where λ is the wavelength of the signal being sampled (i.e. the true wavelength), I is the sampling interval, J is the number of sample intervals (the number of samples is $J+1$) in length L and k is the number of wavelengths of the signal in length L .

The aliased wave equation can be derived by starting with the expression for the actual wave:

$$F(x) = Ae^{\frac{i2\pi}{\lambda}x}, \quad (\text{A2})$$

where A is the amplitude, and x is the displacement. Equation A1 can be rearranged into the form:

$$\lambda = \frac{JI}{k} = \frac{L}{k}, \quad (\text{A3})$$

and then combined with Equation A2 to give:

$$F(x) = Ae^{ik\frac{2\pi}{L}x}. \quad (\text{A4})$$

During sampling x becomes discretized taking the form:

$$x = jI, \quad (\text{A5})$$

where $j = 0, 1, 2, 3, \dots$ Substituting Equation A5 into Equation A4 and simplifying produces:

$$F(x) = Ae^{ik\frac{2\pi j}{J}}. \quad (\text{A6})$$

The identity:

$$e^{2\pi i} = -1, \quad (\text{A7})$$

can then be used to derive an equation describing the set of alias waveforms.

Equation A7 can be modified into the form:

$$e^{2\pi m i} = 1, \quad (\text{A8})$$

where m is an integer. Multiplying Equation A8 and A6 gives:

$$F(x) = Ae^{2\pi i m \left(\frac{k^*}{J}\right)}, \quad (\text{A9})$$

where

$$k = k^* + mJ. \quad (\text{A10})$$

In Equation A10, k^* represents the number of wavelengths of the aliased wave produced by J samples of k wavelengths of the true signal. Since there are an infinite number of m integers there are an infinite number of possible signal waveforms that can produce a given alias as measured by a given sampling frequency.

References

- Carson, W. W., 1985: Development of an Inexpensive Image Space Plotter, *Photogrammetric Record*, **11**, 525-541.
- Chapal, S. C., and Canale, R. P., 1985: *Numerical Methods for Engineers*, Second Edition, McGraw-Hill, New York, 839 pp.
- Ebi, N., Lauterbach, B., and Anheier, W., 1994: An image analysis System for Automatic Data Acquisition from Colored Scanned Maps, *Machine Vision and Applications*, **7**, 148-164.
- Kölbl, O. and Bach U., 1996: Tone Reproduction of Photographic Scanners, *Photogrammetric Engineering & Remote Sensing*, **62**, 687-694.
- Poularikas, A. D. and Seely, S., 1988: *Elements of Signals and Systems*, PWS-KENT Publishing Company, Boston, 581 pp.
- Peterson, A. E., and Durdle, N. G., 1991: Surveying Possibilities with 35 mm Cameras, Volume IV (May, 1991). *Proceedings of C.S.C.E. Annual Conference*, Vancouver, British Columbia, 432 - 440.
- Peterson, A. E., Durdle, N. G., Raso, V. J. and Hill, D. L., 1993: Calibration of Video Cameras for Scoliosis Mapping, *Geomatica*, **47**, 29-38.
- Schubert, R., 2000: Using a Flatbed Scanner as a Stereoscopic Near-Field Camera, *IEEE Computer Graphics and Applications*, **20**, 38-45.
- Scion Image, 1998. (Scion Corporation), URL: www.scioncorp.com
- Taylor, J. R., 1982: *An Introduction to Error Analysis*, University Science Books, New York, 270 pp.
- Warner, W. S., 1995: Mapping a Three-dimensional Soil Surface with Hand-Held 35 mm Photography, *Soil & Tillage Research*, **34**, 187-197.
- Warner, W. S., 1994: Evaluating a Low-cost, Non-Metric Aerial Mapping System for Waste Site Investigators, *Photogrammetric Engineering & Remote Sensing*, **60**, 983-988.
- Warner, W. S. and Anderson, Ø, 1992: Consequences of Enlarging Small-Format Imagery with a Color Copier, *Photogrammetric Engineering & Remote Sensing*, **58**, 353-355.

CHAPTER 2: THE SELECTION AND CALIBRATION OF AN OPTICAL SYSTEM FOR HIGH MAGNIFICATION 0.1 ARCMINUTE RESOLUTION PHOTOGRAMMETRY

Abstract

The accurate photogrammetric measurement of atmospheric refraction requires the selection of a lens and emulsion that will provide the necessary angular resolution. This chapter explores the selection and calibration of a Questar 3.5-inch telescopic lens for this purpose. A simplified calibration scheme using star trails is described. The resulting calibration suggests that the lens is free of distortions to the limitations of the measurement method (about $32 \mu\text{m}$ on a 35 mm negative). A more traditional terrestrial calibration method was also used to help verify the star trail results. Both methods showed no measurable distortion. Stellar images were also used to establish the focal length of the lens (1445.3 ± 3.6 mm).

1. Introduction

The original motivation for this study was to obtain photographic images of the setting Sun to help determine the astronomical refraction at high zenith angles. Due to the motion of the Sun, traditional survey instruments can only be used to obtain single point measurements at a given time. Telescopic photogrammetry offers an opportunity to measure the near-instantaneous position of the entire disc of the Sun. Image co-ordinates (i.e. co-ordinates defined by an image reference frame) must be measured to facilitate Sun location computations. However, budget

and time constraints made rapid and inexpensive means of obtaining image coordinates from 35-mm negatives desirable. Digital image files were obtained using an Agfa Studio Scan II *si* while image co-ordinates were extracted using image analysis software by Scion Image.

A critical component in any photogrammetric system is a lens with known focal length and distortion characteristics. Cameras used in photogrammetry are either metric or non-metric. A metric camera often has a flat plate in front of the emulsion with *réseau* marks to help detect and correct for film deformation. The frame of the metric-camera may also have fiducial marks in the corners or the midpoints of the side that can be used to locate the principal point (the centre of the image). Metric cameras are often pre-calibrated with all lens distortion characteristics documented by the manufacturer or a central calibration agency.

Non-metric cameras are typically of a consumer grade quality and do not have these markings or documented distortion characteristics. Therefore, the Questar lens and camera system must be calibrated before photogrammetric measurements can be extracted using known distortion values and focal length.

2. Selection of the Camera System and Emulsion

The selection of the photogrammetric system was, to a high degree, dictated by the desired angular resolution of the measured refraction of the rising or setting Sun. Previous experience with measuring sunrise and sunset refraction (Sampson, 1994) indicated that such things as terrestrial refraction, theodolite measurement accuracy, and atmospheric scintillation restrict the overall accuracy of visual

angular measurements of distant terrestrial or celestial objects near the horizon to about ± 0.1 arcminute.

It seemed intuitively obvious that a highly magnified image of the Sun would be necessary to achieve the desired resolution in a photogrammetric system. However, budget constraints and availability necessitated the use of consumer grade 35-mm photographic technology.

In order to record both the profile of the Sun and the positions of nearby reference markers on the film, it was necessary to use a film that had a high exposure latitude. High-contrast films such as colour diapositive and low speed black and white films would succeed in obtaining an image of the Sun but might fail to record any reference markers. The optimum emulsions appeared to be films such as Kodak Tri-X or T-Max 400. To further reduce the contrast between the horizon reference markers and the disk of the Sun, the exposed film was 'pull' processed at 7 minutes in D-76 developer.

The rms granularity of standard 35-mm Tri-X film is 17 (a dimensionless value) and the resolving power is about 100-line pairs per millimetre (Kodak, 1999). To determine the granularity, a densitometer with a circular window $48 \mu\text{m}$ in diameter is used to repeatedly measure the density of a negative of given exposure. The density is a fractional measurement with 1.0 being perfectly opaque and 0.0 perfectly transparent. Multiplying the standard deviation of the density measurements by 1000 gives the rms granularity (Kodak, 1982). The value of 17 is approximately equivalent to a resolution of $10 \mu\text{m}$. In the refraction research digital image files of the negatives were to be produced using an Agfa Studio Scan

II *si* flatbed scanner with a pixel size of approximately $32 \mu\text{m}$. Consequently, the scanner rather than the film grain limited the resolution of the photogrammetric system. In view of this, the minimum focal length of the lens in millimetres may be estimated by:

$$f_{\min} \cong \frac{r[\text{mm}]}{\theta[\text{rad}]}, \quad (1)$$

where r is the pixel size of the scanner and θ is the desired angular resolution of the experiment (0.1 arcminute). The resulting minimum focal length is 1100 mm.

The current version of the Questar 3.5-inch telescopic lens is advertised to have a focal length of 60 inches (1524 mm). The lens is a Maksutov-Cassegrain design (Maksutov, 1944) (see Figure 1) with an aperture of 3.5 inches (89-mm). This instrument is well-suited for 35-mm photography with high quality optics, a convenient finder with a solar filter, accurate focusing mechanisms and a simple adapter for 35-mm cameras¹.

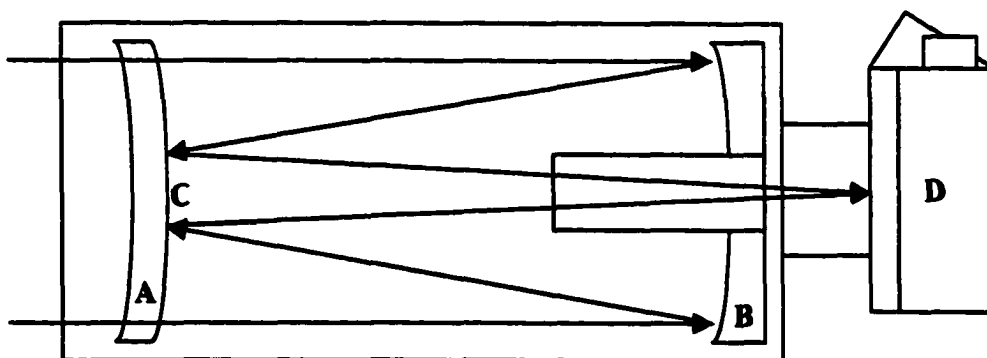


Figure 1: Cut-away schematic diagram of a Maksutov telescopic camera lens. (A) The spherical convex-concave corrector lens, (B) the spherically concave primary mirror, (C) the secondary mirror (an aluminized spot on the back of the corrector lens), and (D) the camera body.

¹ The telescope and tripod were obtained from the University of Alberta's Department of Physics.

3. Measurement of Lens Distortion of the Questar 3.5

All lenses have varying degrees of distortion. Before photogrammetric measurements can be taken, the magnitude of the lens distortion must be ascertained. Radial and decentering distortion tends to curve lines that are originally straight. Parallel lines also tend to lose their parallel nature. If distortions are detected exceeding the desired resolution of the experiment, correction formulae must be derived and applied.

It is well known that lens distortion can vary with object distance (Brown, 1971). Therefore, for this study, it was desirable to measure a target at or near infinite focus. The chosen target field was the star field around the celestial equator near the star δ Orionis. This area of the sky has the largest concentration of bright stars near the celestial equator. The celestial equator was chosen since a stationary camera pointed at this location produces star trails that will exhibit minimum curvature. A hypothetical star on the celestial equator would produce a straight star trail if the camera's horizontal axis lies along the celestial equator. At the latitude of Edmonton the maximum altitude (minimum zenith angle) of the celestial equator is equal to about $36^{\circ} 30'$ ($90^{\circ} - \phi$). In order to reduce the effects of atmospheric refraction, the images were taken when the star field was very near southern culmination (i.e. near the meridian and near maximum altitude).

With the x-axis of the film plane on the celestial equator, the linear distance in the y-direction on the film plane is related to the stellar declination angle as follows:

$$y = \frac{f \tan \delta}{\cos \eta}, \quad (2)$$

where f is the focal length of the lens, δ is the declination of the star and η is the angular displacement of the star from the Y axis (see Figure 2).

The Questar has a 35-mm angular field of view of about $1^\circ 26'$ by $0^\circ 56'$. Through a perfect lens, a certain amount of distortion will occur as an image of the celestial sphere is transferred to the film plane. The maximum deviation from linearity due to this transformation is the difference between the value of y at the corner of the frame (position A in Figure 2) and its value as it crosses the y -axis (position B in Figure 2). For example, if the telescope was pointed at the celestial equator the star at the upper corner would have $\delta = 0^\circ 28'$ (half the width of the field of view), $\eta_a = 43'$, and when it crosses the central axis of the frame $\eta_b = 0^\circ$. Placing these values into Equation 2 gives a difference in y from point A to point B of $1.0 \mu\text{m}$. Therefore, since this value is an order of magnitude less than the resolution of the photogrammetric system, it can be ignored. As well, the approximate resolution of Tri-X film is better than 100 lines per millimetre or about $10 \mu\text{m}$ (Kodak, 1999). Therefore it appears that the experiment should be sensitive enough to detect lens distortion within the limits expressed by the flatbed scanner. If the measured star trails systematically deviate from linearity then the experiment will have detected lens distortion. Conversely, a null result will suggest that the lens distortion is less than the limits of the experiment.

A number of exposures were taken of the star field with the camera in both vertical and horizontal orientations in order to measure distortions in two directions. The exposures were taken when the star field was near the meridian

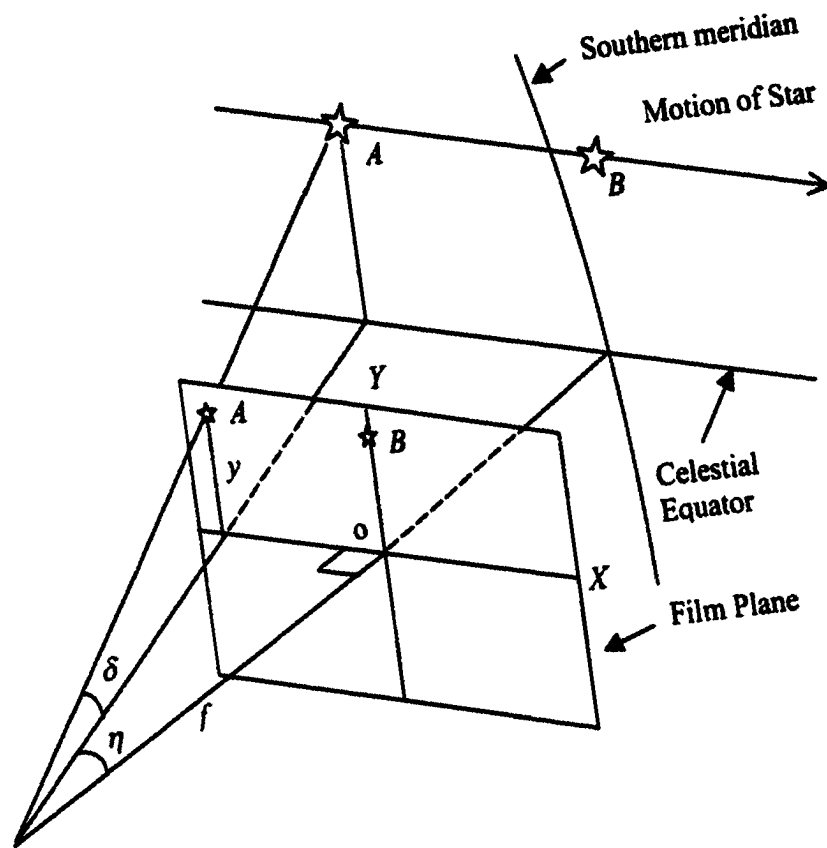


Figure 2: A collinear lens with the celestial equator as the horizon. As the Earth rotates the star moves from location A to B and y will decrease towards the centre of the image.

where the paths of the stars would be nearly parallel with the horizon. This was done to minimize the effects of astronomical refraction.

The negatives were scanned on the Agfa Studio Scan II *si* flatbed scanner. Digital files were transferred to Scion Image (Scion Corporation, 1998) and image coordinates (in pixels) were measured (see Figures 3 and 4). A study of the scanner revealed measurable and systematic linear and non-linear distortions in both axes (Sampson, Peterson and Lozowski, 2000 in-press). Correction protocols derived from this study were applied to each image.

Residuals from a least-squares fit of the image co-ordinates were plotted (see Figures 5 to 10). The results are summarized in Table 1.

Star No.	Camera Format	σ_r [pixels]	Slope	Uncertainty in Slope
1	H	0.52	0.03996	0.00005
2	H	0.53	0.04047	0.00004
3	H	0.56	0.04002	0.00005
4	V	0.26	0.0537	0.0002
5	V	0.36	0.0536	0.0003
6	V	0.35	0.0532	0.0004

Table 1: Distortion measurements of the Questar 3.5 telescopic lens. The first column is the star number from Figures 3 and 4. The second column is the orientation of the camera. The third column is the standard deviation of the residuals of the least squares fit. The fourth column is the slope of the least squares fit and the last column is the uncertainty in the slope (Taylor, 1982). The difference in the uncertainties is due to the difference in length of the star trails.

The uncertainty in the measurements may come from a number of sources. The vertically formatted images all have smaller standard deviations in the residuals than the horizontally formatted images. However, the uncertainty in the

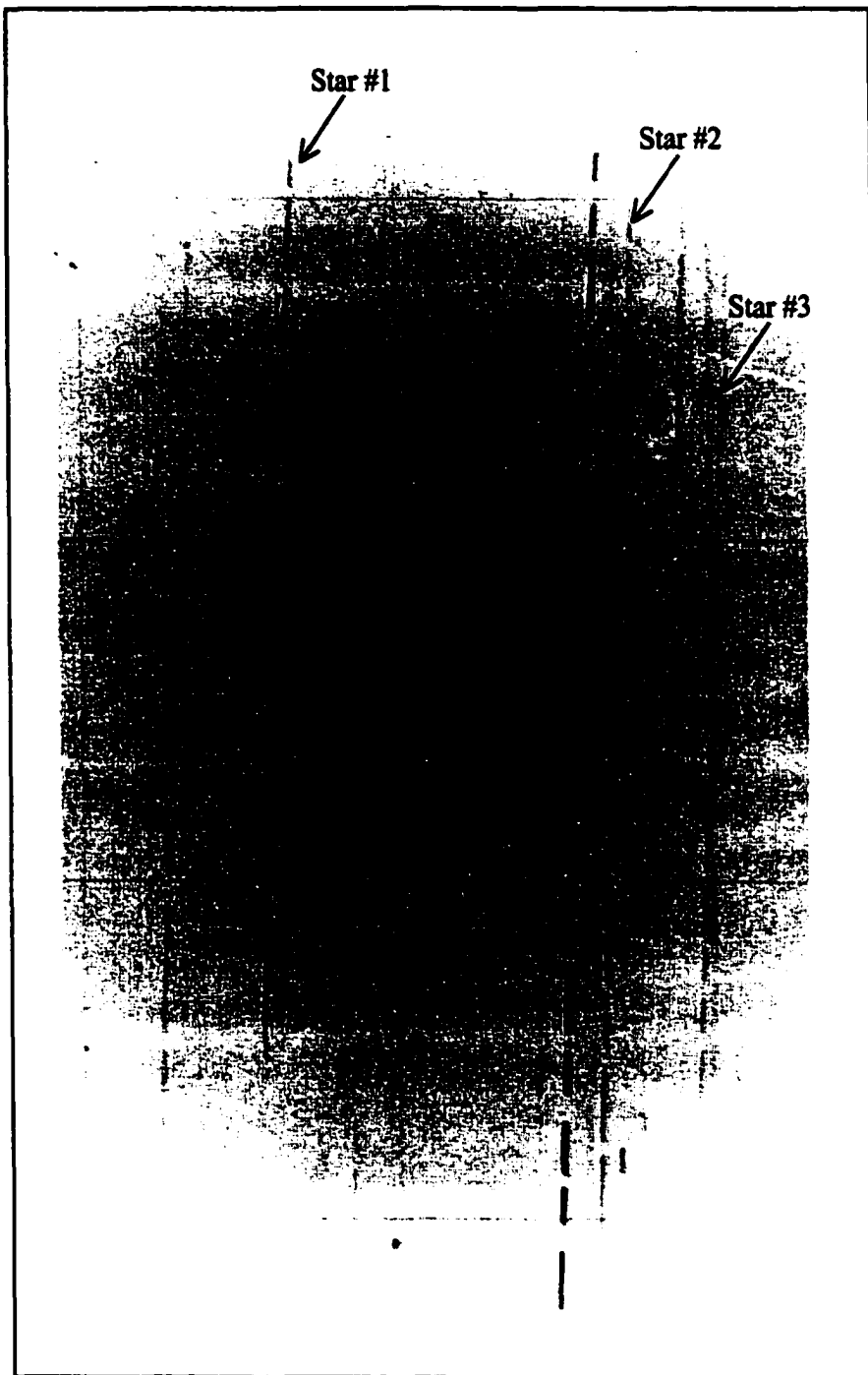


Figure 3: Star trails from the δ Orionis region taken with the Questar 3.5 telescopic lens. Stars used in the lens distortion measurements are labelled. Background grid lines are from a Zeiss 1-cm calibration plate used to hold the negatives flat and determine the phase of non-linear scanner distortions.

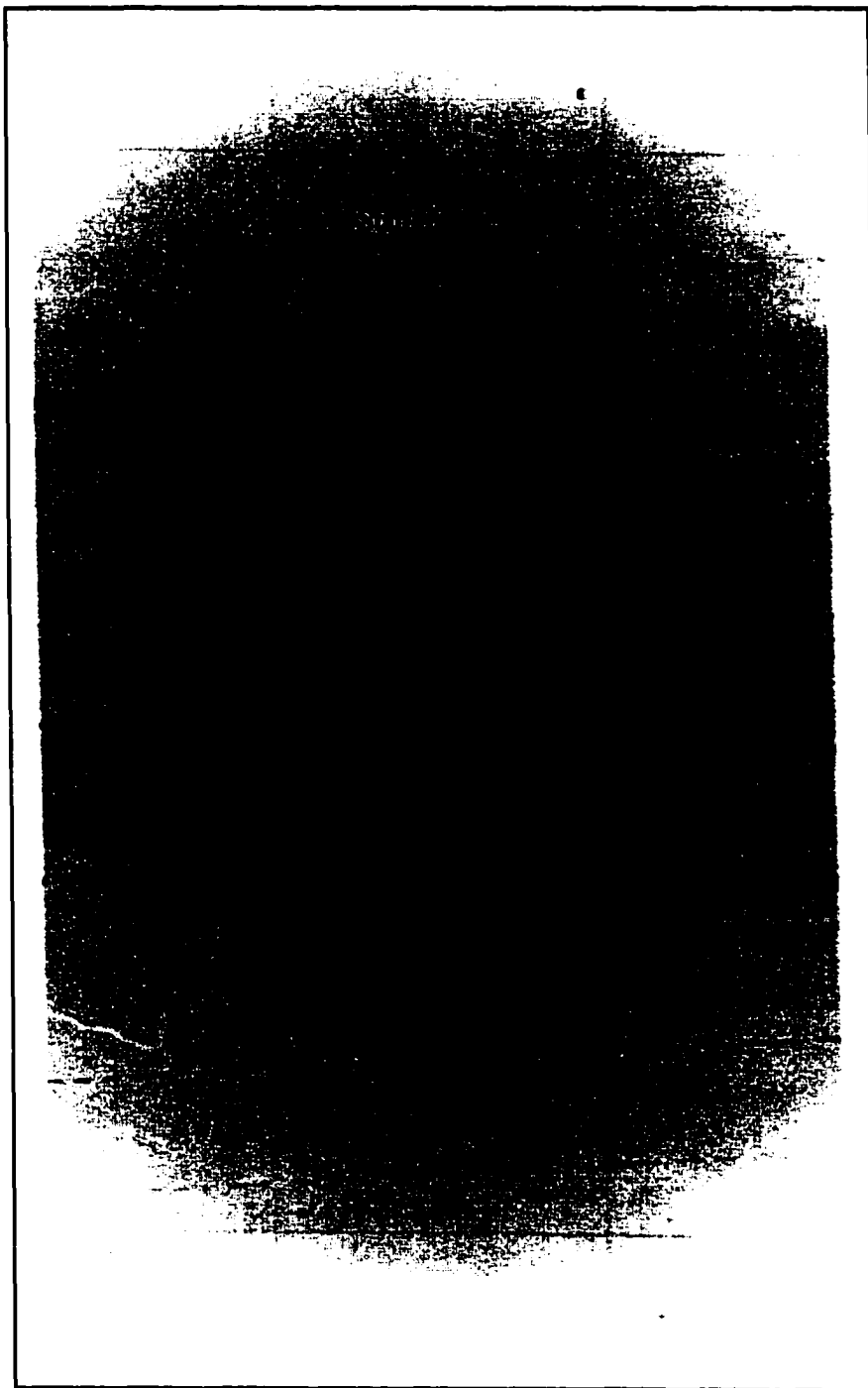


Figure 4: Star trails from the δ Orionis region taken with the Questar 3.5 telescopic lens. Stars used in the lens distortion measurements are labelled.

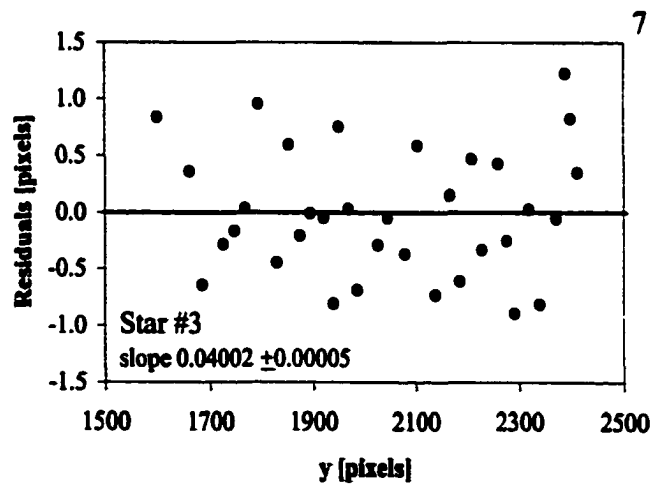
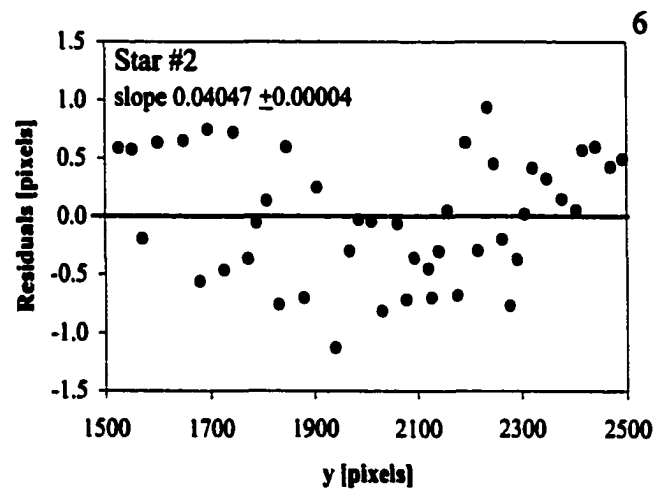
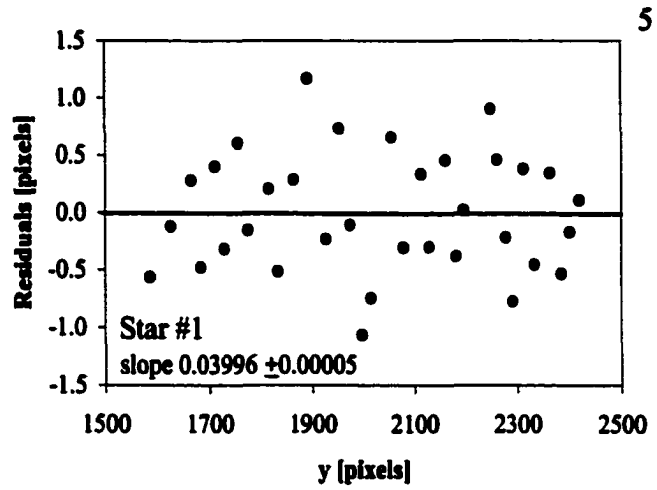


Figure 5, 6 and 7: Residuals of fit from linear least squares fit of star trails from horizontally oriented camera (Figure 3). Note the large difference in axes scales.

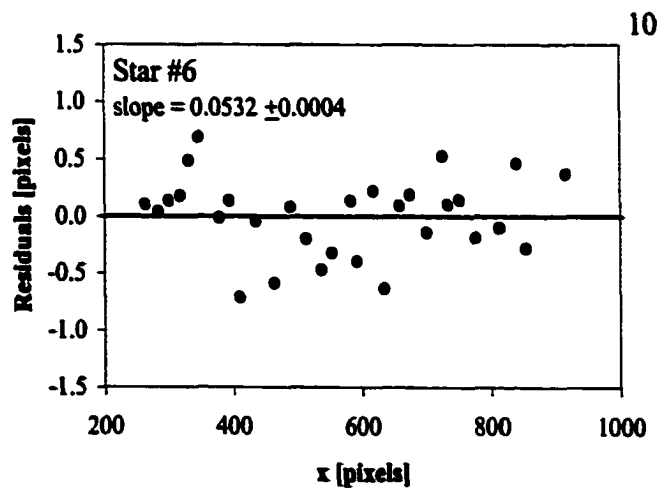
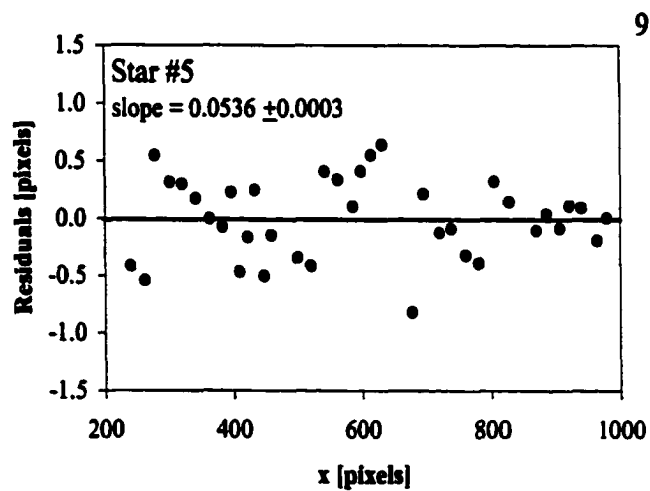
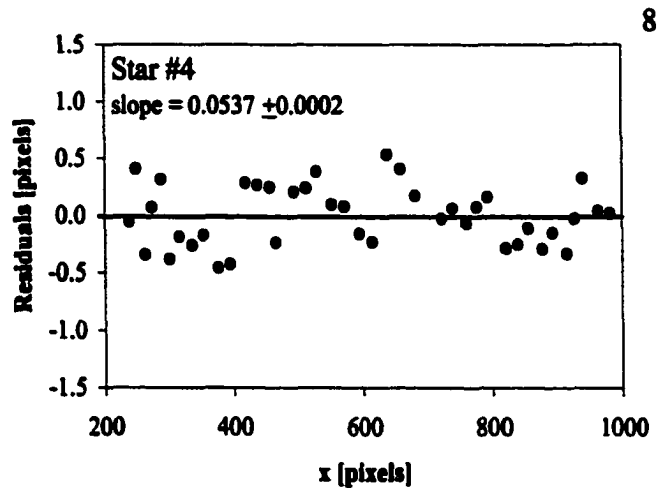


Figure 8, 9 and 10: Residuals of fit from linear least squares fit of star trails from vertically oriented camera (Figure 4). Note the large difference in axes scales.

slope is greater. Since the trails are longer on the horizontally formatted images, it is to be expected that if the random measurement error were the same then the uncertainty in the slope should be less. The difference in the standard deviations of the residuals between the H and the V cases may be possibly due to poorer focusing in the H image. Very faint star trails have a low signal to noise ratio leading to uncertainty in the position of the image. Conversely, if a star is relatively bright then the trails on the negative are expanded making it difficult to visually locate the centre of the star trail.

The largest difference in slope occurs between star trail 1 and 2. This difference in slope is a half pixel over a distance of 1000 pixels (i.e. approximately the full length of the negative). This would suggest that the difference could be ignored for the purposes of the intended experiment.

Therefore, the results appear to suggest that there is no significant deviation from linearity or parallelism at the resolution limits of the scanner. This in turn implies that the Questar lens used here is free of distortions to within the limits of the experiment.

4. Measurement of the Focal Length of a Questar 3.5

In order to calculate the focal length of the lens, a target of known dimensions must be photographed and the image coordinates measured. The image distance c changes with the object distance d as follows:

$$\frac{1}{c} = \frac{1}{f} - \frac{1}{d}, \quad (3)$$

where f is the image distance when the object distance is infinite (i.e. the focal length of the lens).

If the desired accuracy of the final object co-ordinates is a standard deviation of 0.1 arcminute then the accuracy of the focal length measurements can be estimated by calculating the change in focal length produced by a variation of ± 0.1 arcminute over the expected usable distance on the negative. The approximate focal length of the Questar is 1524 mm. From test photos of the Sun, the maximum distance from the centre of the negative to the edge of the field of view is expected to be about 15 mm. The desired accuracy of the focal length measurements can be derived from the error propagation formula (Taylor, 1982):

$$\delta\theta = \frac{\partial\theta}{\partial f} \delta f, \quad (4)$$

where $\delta\theta$ is the uncertainty in the angular measurements in radians (± 0.1 arcminute = 2.91×10^{-5} radians), δf is the uncertainty in the focal length measurements and the partial derivative $\partial\theta/\partial f$ is derived from:

$$\theta = \tan^{-1}\left(\frac{x}{f}\right), \quad (5)$$

where x is the distance from the centre of the negative to the image of the target and f is the focal length of the lens. The partial derivative of θ with respect to f is:

$$\frac{\partial\theta}{\partial f} = \frac{-x}{f^2 + x^2}, \quad (6)$$

placing (6) into (4) and solving for δf gives:

$$\delta f = \frac{\delta\theta(f^2 + x^2)}{x}. \quad (7)$$

Placing the values of $\delta\theta$, x and f into (7) gives a value of ± 4.4 mm for the uncertainty in the measured focal length of the lens.

This uncertainty can now be used to derive the minimum image distance c_{\min} used to determine the focal length:

$$c_{\min} = 1545 - \delta f. \quad (8)$$

Placing this value into (3) gives a minimum object distance of 450 metres. Therefore to find the focal length a calibration target should be more than 450 metres away.

In the refraction study, the object distance to the Sun can be taken to be infinite while the estimated distance to the horizon reference targets is greater than 2 kilometres (in the sunset refraction experiment these targets were treetops used to establish the Sun's horizontal co-ordinates). The most convenient target field would therefore appear to be stars since their positions are known to very high accuracy and they present very well defined images on the negative. The Pleiades star cluster (M45 in the constellation of Taurus) was chosen as a suitable target. This cluster has enough bright members to be easily photographed and it is far enough above the celestial equator (at $\phi = 53^\circ 30' \text{ N}$) to allow for photographs to be taken well above the horizon, thereby minimizing the effects of atmospheric refraction. A 5 second unguided exposure was taken of the cluster. As the Earth rotated the images of the stars were trailed. This provided two data points for each star, one at the beginning of the image and one at the end (see Figure 11).

Scanning the negatives with the Agfa Studio Scan II *si* flatbed scanner produced digital image files. Scion Image software (Scion Corp., 1998) was used to

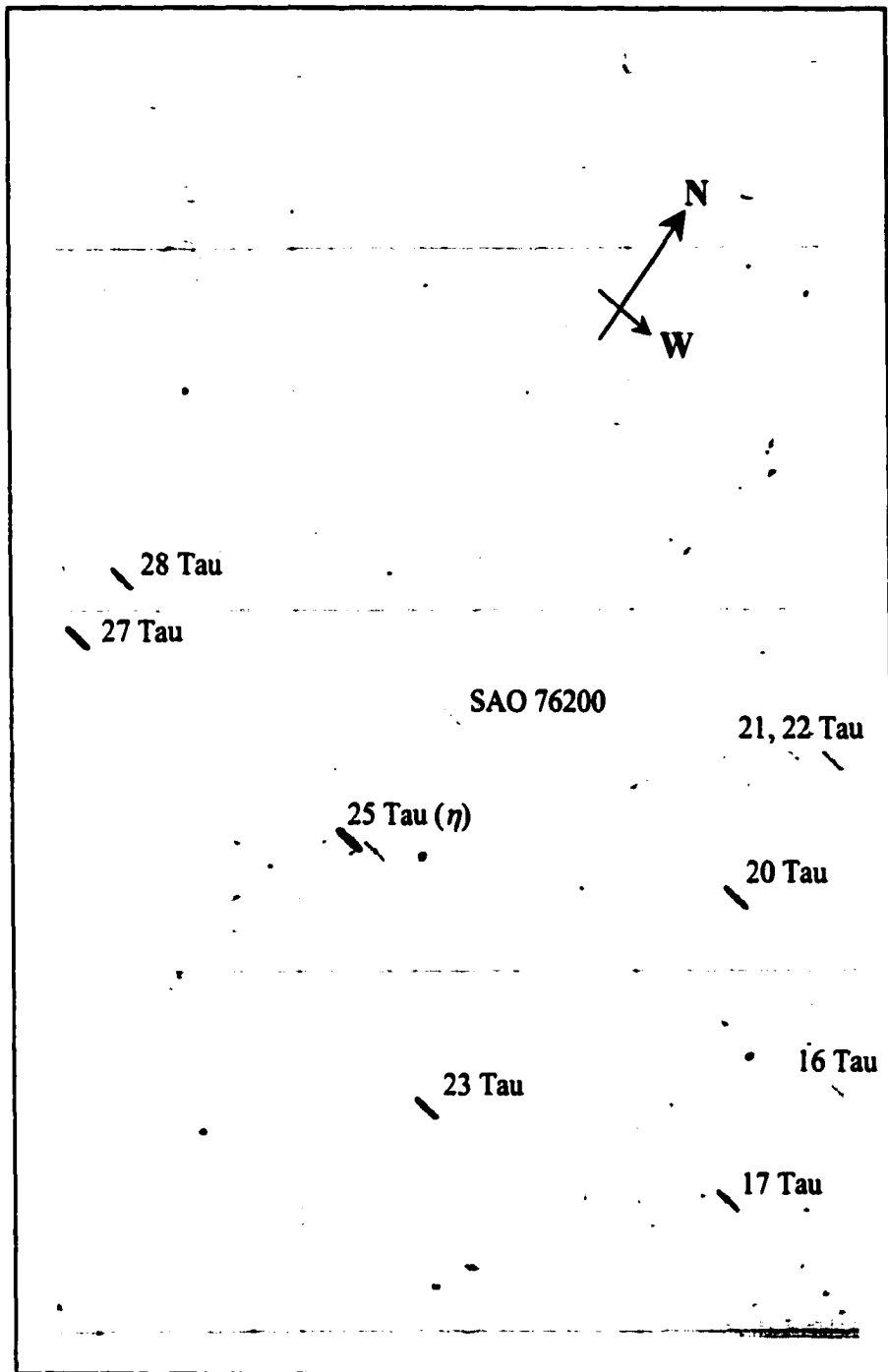


Figure 11: Negative of the M45 star cluster taken with the Questar 3.5 telescopic lens. The grid is produced by a Zeiss 1-cm grid plate used to hold the film flat and establish the phase of the periodic distortion in the flatbed scanner. Stars used to find the focal length are labelled. Unguided 5-second exposure on Tri-X film.

extract the pixel coordinates of the beginning and end points of each star trail. A one-centimetre grid plate was used to flatten the negative on the scanner platen. Image contrast was adjusted to allow both the grid and the star trails to be easily measured. Measurements of the grid points in the y-direction of the scanner (the direction of travel of the scanner head) established the phase of the periodic distortion of the scanner. Corrected pixel coordinates were calculated from scanner distortion correction formula (Sampson, Peterson and Lozowski, in press).

The celestial coordinates of the individual stars are well known to very high accuracy. The annual proper motion of a star in both right ascension and declination is provided in the star catalogue (Hoffleit and Warren, 1991). Using this information, the celestial coordinates were corrected to the date of the exposure. In order to estimate the effects of atmospheric refraction on the positions of the stars the amount of refraction R for objects with a zenith angle less than about 80 degrees was estimated from the formula (Green, 1985):

$$R = 60''.29 \tan z_0 - 0''.06688 \tan^3 z_0, \quad (9)$$

where z_0 is the zenith angle of the star.

The zenith angle z_0 and azimuth A of the star were found from the formulae (Green, 1985):

$$\cos z_0 = \sin \delta \sin \phi + \cos \delta \cos \phi \cos H, \quad (10)$$

and:

$$\cos A = \frac{\sin \delta - \cos z_0 \sin \phi}{\sin z_0 \cos \phi}, \quad (11)$$

where δ is the declination of the star, ϕ is the geographic latitude of the observer and H is the hour angle of the star found from $H = LST - \alpha$, where LST is the local sidereal time (Bishop, 1996) and α is the right ascension of the star.

The apparent right ascension α' and declination δ' of the star due to atmospheric refraction is found from:

$$\sin \delta' = \cos(z_0 - R) \sin \phi + \sin(z_0 - R) \cos \phi \cos A, \quad (12)$$

and:

$$\alpha' = LST - \cos^{-1} \left(\frac{\cos(z_0 - R) - \sin \delta' \sin \phi}{\cos \delta' \cos \phi} \right), \quad (13)$$

where LST is the local sidereal time converted to angular form.

The greatest deviation in the star's published celestial co-ordinates due to its annual proper motion was 0.1 arcsecond in right ascension and 0.2 arcsecond in declination.

The amount of astronomical refraction is directly proportional to the zenith angle of the star. If two stars had the same zenith angle they would experience the same astronomical refraction and the angular distance between the two stars would be unchanged. Therefore stars in the photographic field with the greatest difference in zenith angle will show the greatest effect due to refraction. In the case of the images used in this experiment, the maximum difference in right ascension is 0.1 arcsecond and the maximum difference in declination is 0.9 arcsecond. Since the resolution of the scanner is about 4.4 arcseconds per pixel, the effects of refraction and proper motion can therefore be ignored.

From the corrected right ascension (α'_n) and the declination (δ'_n) an angular displacement β between two stars can be calculated from the formula (Green, 1985):

$$\cos \beta = \sin \delta'_1 \sin \delta'_2 + \cos \delta'_1 \cos \delta'_2 \cos(\alpha'_1 - \alpha'_2). \quad (14)$$

The value β and the linear distance between the star images on the negative can now be used to determine the focal length of the lens.

In shorter focal length lenses, the image coordinates of the principal point are essential in determining the focal length. However, the Olympus OM-1 camera body used in this experiment was non-metric, and therefore did not have fiducial marks indicating the location of the principal point on the negative.

The importance of the position of the principal point to the calculated focal length can be determined through a simple sensitivity analysis. Suppose a target star used to determine the focal length is located in one corner of a 35-mm frame. If the assumed principal point were exactly in the centre of the frame, the distance d to the target star would be 21.6 mm. At a focal length of 1500-mm (the approximate focal length of the Questar) the star produces an angular displacement of $\theta = 49' 30''$ from the principal point. Now suppose the assumed principal point is located at the maximum distance from the true principal point and at the maximum distance from the target star. The assumed principal point is now in the opposite corner of the frame from the target star (see Figure 12). Since the focal length is very long compared to the size of the negative, the measured angular displacement of the star from the principal point would then be almost exactly 2θ or $1^\circ 39'$ (this characteristic of the lens was also demonstrated in Section 3). The

erroneous focal length f' can now be calculated using the linear distance between the assumed principal point and the target star (43.2 mm) and the angular displacement 2θ using the equation:

$$f' = \frac{2d}{\tan 2\theta}. \quad (15)$$

The erroneous focal length is 1499.7 mm, a difference of 0.02%. This produces a maximum angular error of $0.6''$ on a 35-mm image, well below the resolving limits of the photogrammetric system.

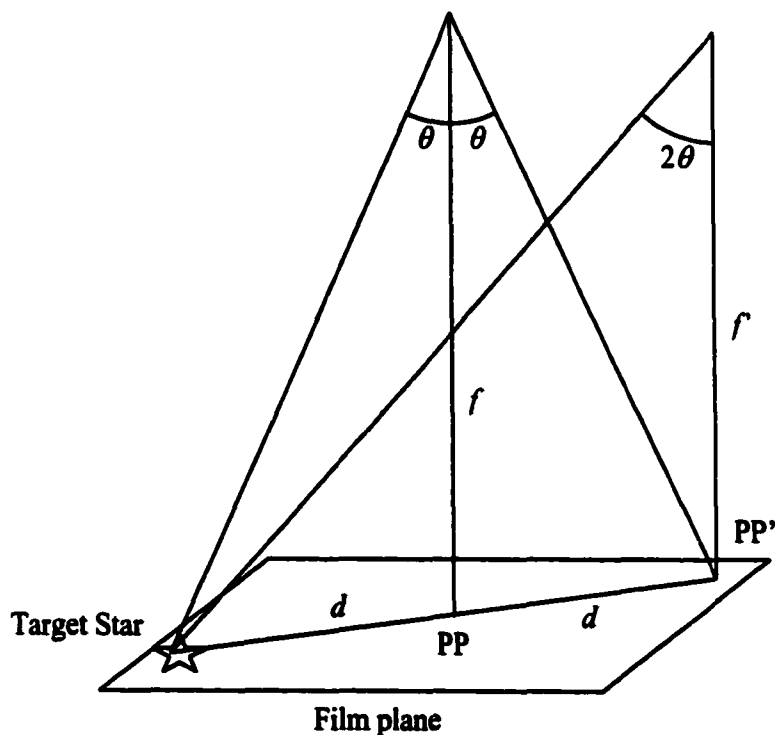


Figure 12: PP is the correct principal point in the centre of the 35-mm frame. PP' is the erroneous principal point.

Therefore, all the stars were used as the principal point since this assumption produces a maximum error that is an order of magnitude smaller than the desired accuracy.

The focal length f of the lens can then be calculated from the equation:

$$f = \frac{d}{\tan \beta_p}, \quad (16)$$

where d is the distance in millimetres from the star used as the assumed principal point to the target star in image coordinates and β_p is the angular displacement between the star used as the assumed principal point and the target star.

Ten stars were selected from the image (see Figure 11 and Table 2). Each of the ten stars was used as an assumed principal point and a focal length was determined from the distance between itself and the remaining nine stars. A total of nine focal lengths were calculated from each star and the mean and population standard deviation of these focal lengths appears in Table 3.

Star Name	RA (2000.0) [h m s]	δ (2000.0) [° ' "]
16 Tau	3 44 50.1	24 18 02.8
17 Tau	3 44 54.3	24 07 29.1
20 Tau	3 45 51.3	24 22 44.6
21 Tau	3 45 56.2	24 33 57.3
22 Tau	3 46 04.7	24 32 57.3
23 Tau	3 46 21.3	24 57 35.2
25 Tau	3 47 30.8	24 06 58.8
27 Tau	3 49 11.4	24 03 52.7
28 Tau	3 49 13.0	24 08 52.7
SAO 76200	3 47 31.2	24 17 59.4

Table 2: Right ascension and declination for the target stars of M45. All values are corrected for precession to the year 2000.0 and have also been corrected for stellar proper motion and atmospheric refraction.

Principal Point Star	Mean focal Length [mm]	Standard Deviation [mm]
16 Tau	1449.1	4.0
17 Tau	1444.2	3.0
20 Tau	1445.1	4.2
21 Tau	1446.8	2.0
22 Tau	1445.9	1.9
23 Tau	1446.2	3.0
25 Tau	1444.6	4.3
27 Tau	1446.0	2.1
28 Tau	1443.5	2.4
SAO 76200	1445.0	4.7

Table 3: Mean focal length using ten Pleiades stars as assumed principal points. The standard deviation is about 0.3% of the focal length. The mean of the all the focal lengths is 1445.6 ± 3.3 mm.

Since the computed focal length is inversely proportional to the tangent of the angle between the chosen principal point star and the target star, the uncertainty of the computed value will also be inversely proportional to this angle. The total uncertainty in the focal length δf can be expressed by (Taylor, 1982):

$$\delta f = \sqrt{\left(\frac{\partial f}{\partial d} \delta d\right)^2 + \left(\frac{\partial f}{\partial \beta_{pp}} \delta \beta_{pp}\right)^2} \quad (17)$$

where δd is the uncertainty in the measurement of the distance between the principal point star and the target star, and $\delta \beta_{pp}$ is the uncertainty in the angular distance between the same two stars. The accuracy of the celestial co-ordinates for modern star catalogues is sub-arcsecond (Monet, 1992) and therefore, the uncertainty in the angular value β_{pp} can be considered negligible. Therefore, Equation 17 is reduced to:

$$\delta f = \frac{\delta d}{\tan \beta_{pp}}. \quad (18)$$

In order to further evaluate the focal length measurements the error estimates derived from Equation 18 were compared with the derived focal length values. Equation 18 produces an uncertainty envelope ($f \pm \delta f$) with input parameters of image distance f , the angular distance between the two stars β_{pp} and the uncertainty in the distance between the two stars δd . The envelope was plotted against the distance between the principal point star and the target star. On the same chart the measurements of the focal length were also plotted. The input values for Equation 18 were adjusted until the uncertainty envelope visually encompassed the measurements (see Figure 13). The final selected value $\delta d = \pm 1.9$ pixels, appears reasonable given the appearance of the stellar images on the negatives. From this analysis the focal length was found to be 1445.0 ± 3.2 mm. The uncertainty was found from the half-width of the envelope at the cluster of measurements furthest from the principal point star (approximately 26 mm). It is apparent that the model and the statistical sample produce very similar values.

Taking the average of the two results suggests that the focal length of the Questar lens is 1445.3 ± 3.3 mm. The uncertainty of these results is 25% better than the ± 4.4 mm focal length uncertainty derived earlier, indicating that the lens is sufficiently well characterized for the proposed astronomical refraction studies.

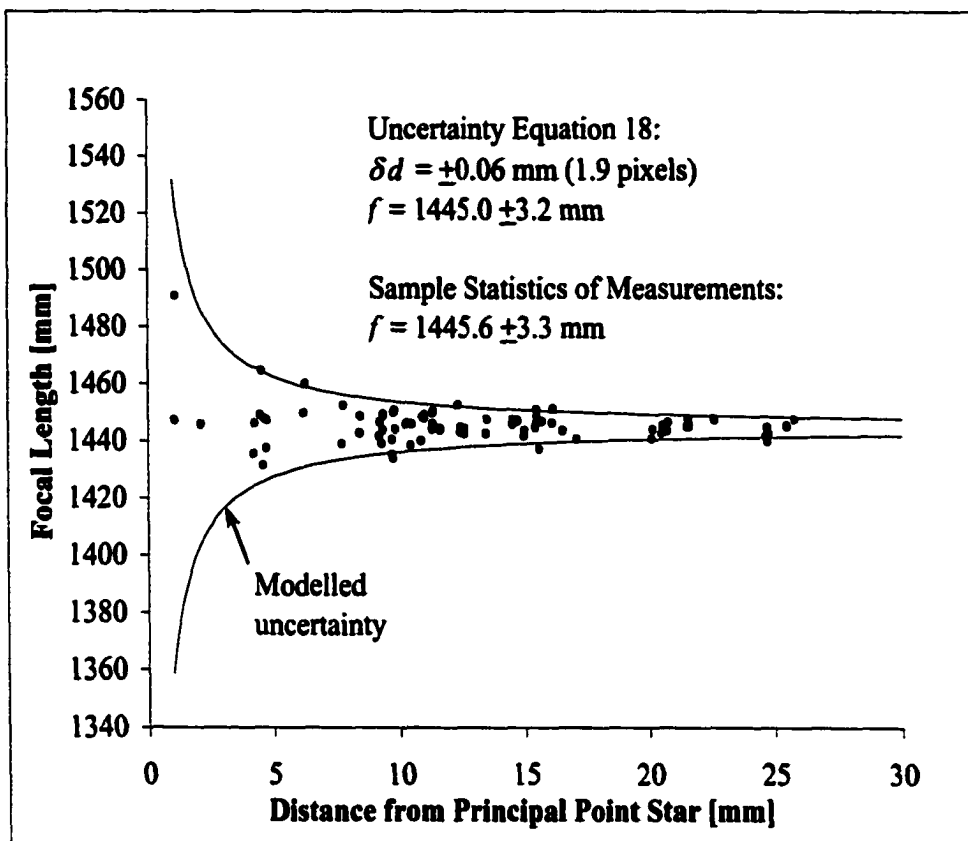


Figure 13: The calculated uncertainty in the focal length of the Questar lens compared to measured focal length. The value δd is the error of the distance between the principal point star and the target star. The scatter plot represents the stellar measurements.

5. Further Calibration of the Questar Lens

In order to help verify the stellar calibration of the lens, a more traditional terrestrial calibration was performed. This consisted of taking photographs of a target field of known location, using a series of camera positions and orientations. The location of the camera and the targets was established by triangulation using a Sokkia total station. The focal length of the lens, its principal point and any lens distortions can be extracted from comparisons between the measured image co-ordinates and hypothetical image co-ordinates created by a perfect lens. With the Questar lens focused at infinity, a terrestrial target field would need to be about a kilometre away and approximately 16 by 25 m in size in order to fill a 35mm frame. Therefore, it was necessary to find a closer and more manageable target field. In order to test the stellar calibration results, a number of calibrations at different distances were taken of the target field. It was anticipated that the focal length and the distortional behavior of the lens could be extrapolated to an infinite focus from these relatively close focal distances.

5.1 Targets

Fifty-four targets were mounted on the north section of the University of Alberta Stadium west side bleachers (see Figures 14 and 15). The targets were Marlboro gummed cloth page reinforcements with 7 mm openings. The targets were positioned to provide three target fields with at least 16 targets in the closest image (see Figure 16). The distances between the camera and the centre of the target field were approximately 25, 50 and 80 metres. Photographs were taken with

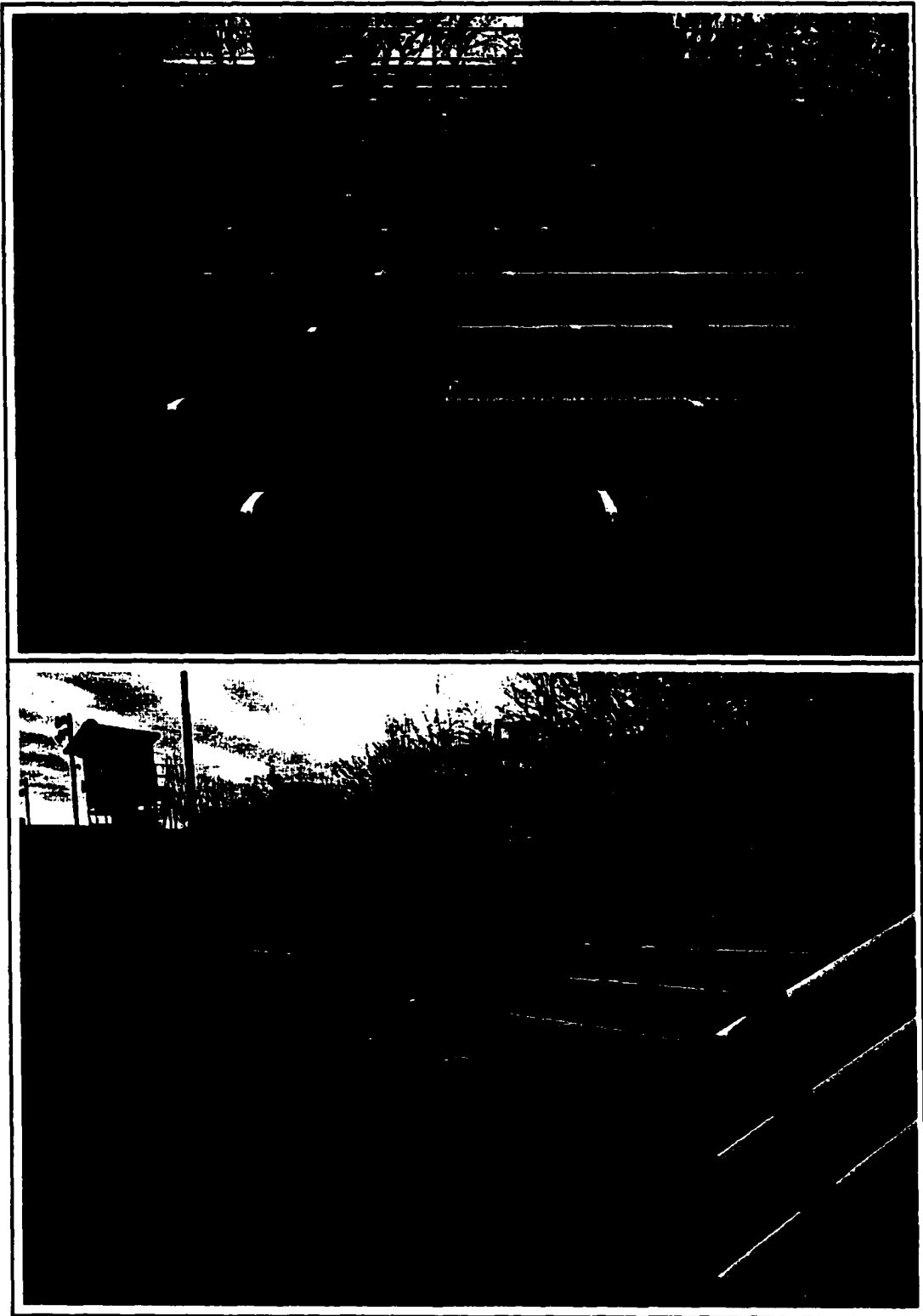


Figure 14 and 15: University of Alberta Stadium target field. The boundaries of each row of targets are marked by white tape.

the camera at three orientations; level and rotated $\pm 90^\circ$. Three exposures at three different shutter speeds were taken in order to obtain the optimum negative density.

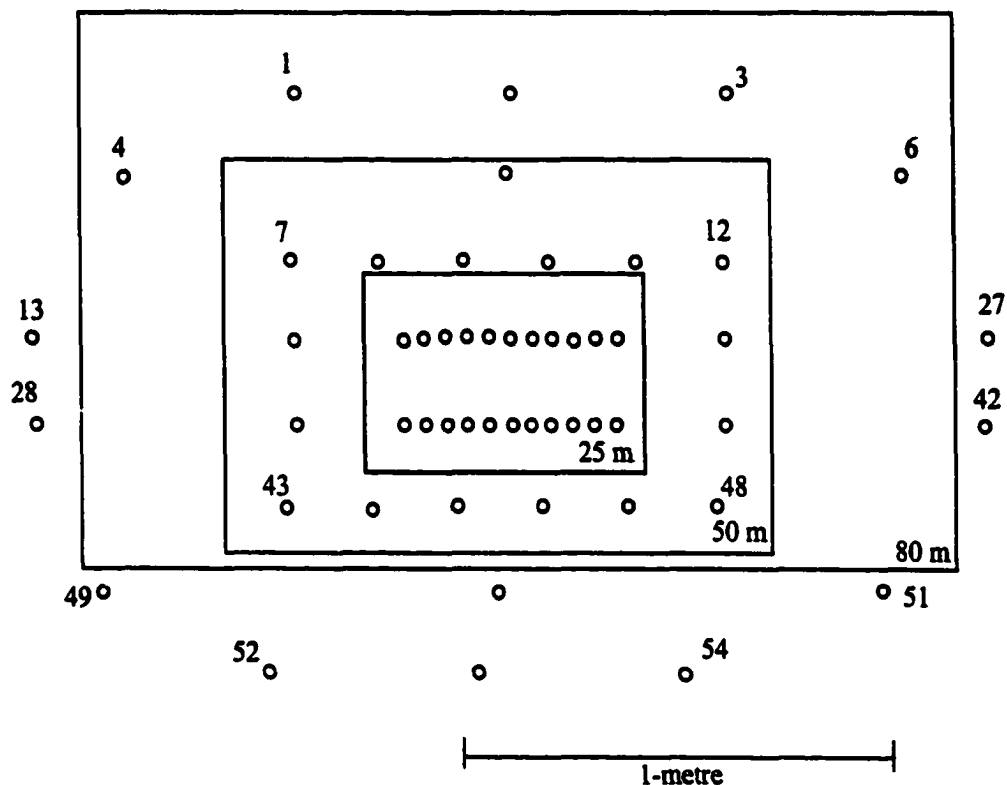


Figure 16: Calibration target field as seen from the camera. Rectangular areas are approximate photographic fields of view from 25, 50 and 80 metres.

5.2 Object and Camera Co-ordinates

A Sokkia total station was used to measure the object co-ordinates of the calibration targets and the camera. The origin of the object space was taken to be the north station of the survey instrument. A plan view of the set-up can be seen in Figure 17. The object co-ordinates of the targets are listed in Appendix A. Each target was measured twice at each station - once with the telescope in the direct

orientation and once with it reversed. The northing, easting and elevation were derived from the raw horizontal and zenith angles of the targets using an in-house least squares survey adjustment routine. The average standard deviation of the co-ordinates was 0.002 m for the northing, 0.004 m for the easting, and 0.001 m for the elevation. The elevation values in Appendix A have the height of the tripod and instrument (1.438 m) subtracted from the original results. The co-ordinates for the south station and the camera positions are listed in Table 4. Since the Questar is a compound lens, which uses a mirror as the primary light gathering element, the effective distance from the target to the film plane was approximately 1.445 m 'behind' the lens. Therefore an additional 1.445 m was added to the northing of the camera position in Table 4. In order to justify this procedure let us assume the Questar was replaced with a single telescope mirror of 1.445 m focal length. The optical configuration would have the camera facing away from the targets. Therefore the distance from the target to the film plane would be $D + f$, where D is the distance from the target to the mirror and f is the focal length.

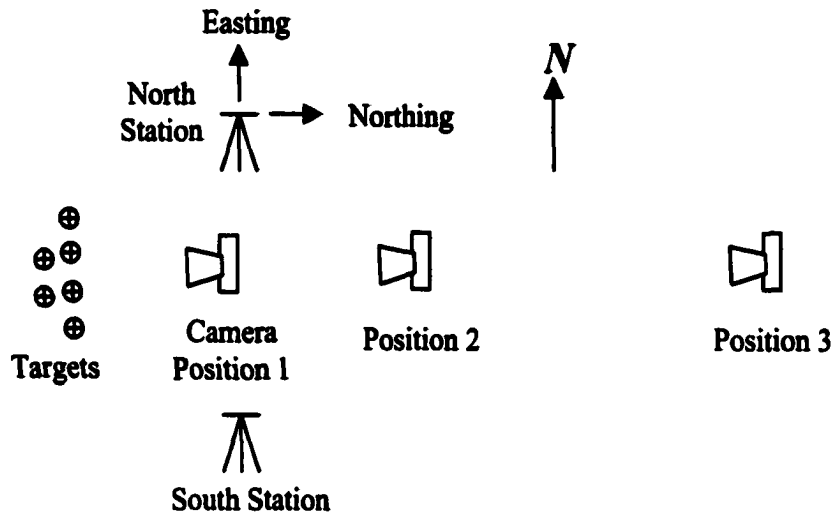


Figure 17: Plan view of calibration set-up. Northing, easting and elevation with the co-ordinate origin at the north station were used as the object co-ordinates.

Target	Northing [m]	Easting [m]	Elevation [m]
South Station	2000.0000	972.9801	99.9416
Cam. Pos. 1	1996.5293	987.4618	99.7568
Cam. Pos. 2	2021.4432	987.0003	99.9391
Cam. Pos. 3	2051.7586	986.3681	99.6167

Table 4: Object co-ordinates for the south station of the Sokkia total station and the camera positions. An additional 1.4 m was added to the northing co-ordinates to compensate for the compound nature of the optical light path.

In order to examine the validity of these optical computations and measurements, three check distances were measured using a tape measure and then calculated independently using the raw angles. The measurement method is illustrated in Figure 18.

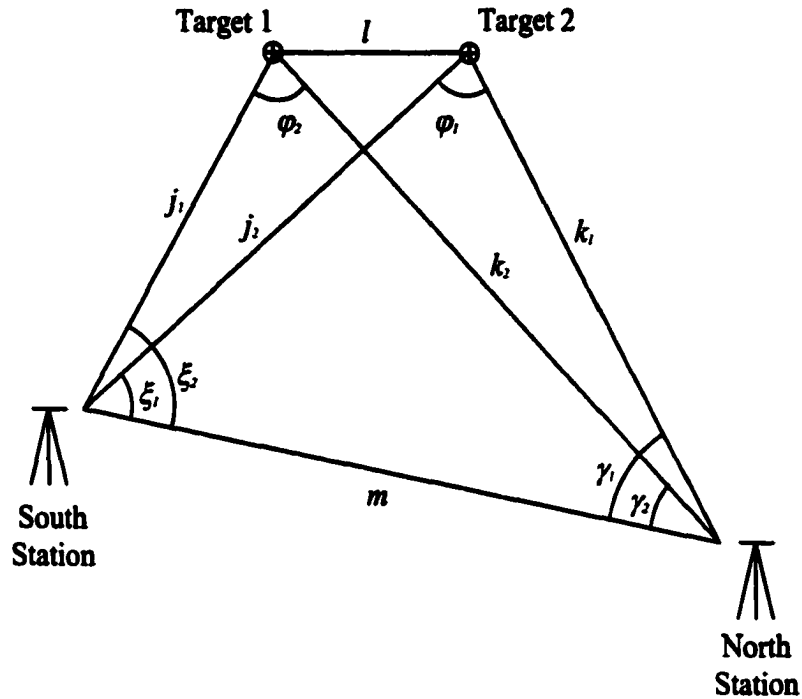


Figure 18: Plan view of triangulation measurement method. Angles ξ and γ are the mean horizontal angles measured from the direct and reversed telescopic position of the Sokkia.

The distance between the two targets l was calculated using the Sine and Cosine Laws. Sides j_1 and j_2 are calculated from the Sine Law:

$$j_{1,2} = \frac{m \sin \gamma_{1,2}}{\sin \xi_{1,2}}, \quad (19)$$

where m is the distance between stations (27.020 m), and angles γ and ξ are the horizontal angles measured by the Sokkia (see Figure 18). The horizontal distance between the targets, l , is found from the Cosine Law:

$$l^2 = j_1^2 + j_2^2 - 2j_1j_2 \cos(\xi_2 - \xi_1). \quad (20)$$

The final distance d is now calculated using the formula:

$$D^2 = l^2(1 + \cot^2(z)), \quad (21)$$

where z is the zenith angle of the south station as measured from the north station.

The results are listed in Table 5. The average residual between the computed distances and the tape measurements is +0.47 mm. Since the estimated measurement accuracy of each target with the Sokkia total station was about ± 1 mm, this residual would appear to be insignificant thus validating the measurement and computational methods.

Targets	Tape Measurement [m]	Computed Distance [m]
1-3	1.005	1.0056
4-6	1.800	1.8003
13-27	2.204	2.2045

Table 5: Comparisons between tape measured distances (± 0.001 m) between target points and calculated distances using angle measurements from the Sokkia total station.

5.3 Image Co-ordinates

Image co-ordinates were obtained by scanning the negatives with an Agfa Studio Scan II *si* flat bed scanner at maximum resolution (800 ppi). Digital files were then imported to image analysis software (Scion Image, 1998) where pixel co-ordinates were obtained of the centre of each target.

The negatives were flattened against the platen by a grid plate normally used for calibrating stereo plotters. This grid plate provided accurate 1 cm grid reference targets to establish the phase of the periodic distortion of the scanner. Scanner

distortion was then removed by applying corrections to the pixel co-ordinates (see Chapter 1).

The corrected image co-ordinates and target field diagrams can be seen in Appendix A.

5.4 Calibration Software

In-house photogrammetric software called TRIPLET was used to estimate the focal length, radial distortion and decentering distortion of the lens. The program requires the input of the known object co-ordinates, along with estimates of the camera orientation, one of the camera locations, and measured image coordinates. Three photographs using three different camera orientations were used to establish the calibration. The calibration routine is based on the Bundle Adjustment method (Slama, 1980, Karara, 1989). The routine solves a series of collinearity equations, which describe the light ray joining each target point with the perspective centre of the lens and the corresponding image on the photograph. A summary of the method appears in Appendix B.

Since good preliminary values of camera orientation were not available, the TRIPLET software was first used to establish accurate orientation values for each image. For this purpose, instead of entering three photographs with three camera orientations from a single station, one photo was entered into the program three times. The computed camera orientation values were then inserted into TRIPLET and the program solved for the focal length, radial lens distortion and decentering distortion.

5.5 Results

The computed focal length appears in Tables 6. Computed values of radial and decentering distortion were found to be smaller than the limits of the experiment thus confirming the results from the stellar method in Section 3.

d [m]	Focal Length [mm]	σ [mm]
25	1456.5	2.5
50	1451.2	1.0
80	1447.6	0.9
∞	1445.3	3.2

Table 6: Computed focal length of the Questar 3.5 telescopic lens. First column is the object distance. Last column is the standard deviation on the determined focal length. First three rows are the results from terrestrial calibration. Last row is from stellar calibration.

The results in Table 6 were then compared to the simple lens formula (Equation 3). A graph of the measured focal length and the focal length as derived from the simple lens formula can be seen in Figure 19.

It is apparent from Figure 19 that the relationship between the image distance and the object distance departs dramatically from that suggested by the simple lens formula as one might expect given the complexities of the Questar lens. The focus of the Questar is achieved by moving the primary mirror rather than moving the focal plane (i.e. the eyepiece). Consequently the eyepiece or camera is stationary.

An experiment was conducted to explore the optical behavior of the Questar focusing system and to determine its influence on the focal length of the lens. The first experiment involved keeping the primary mirror fixed and moving the focal

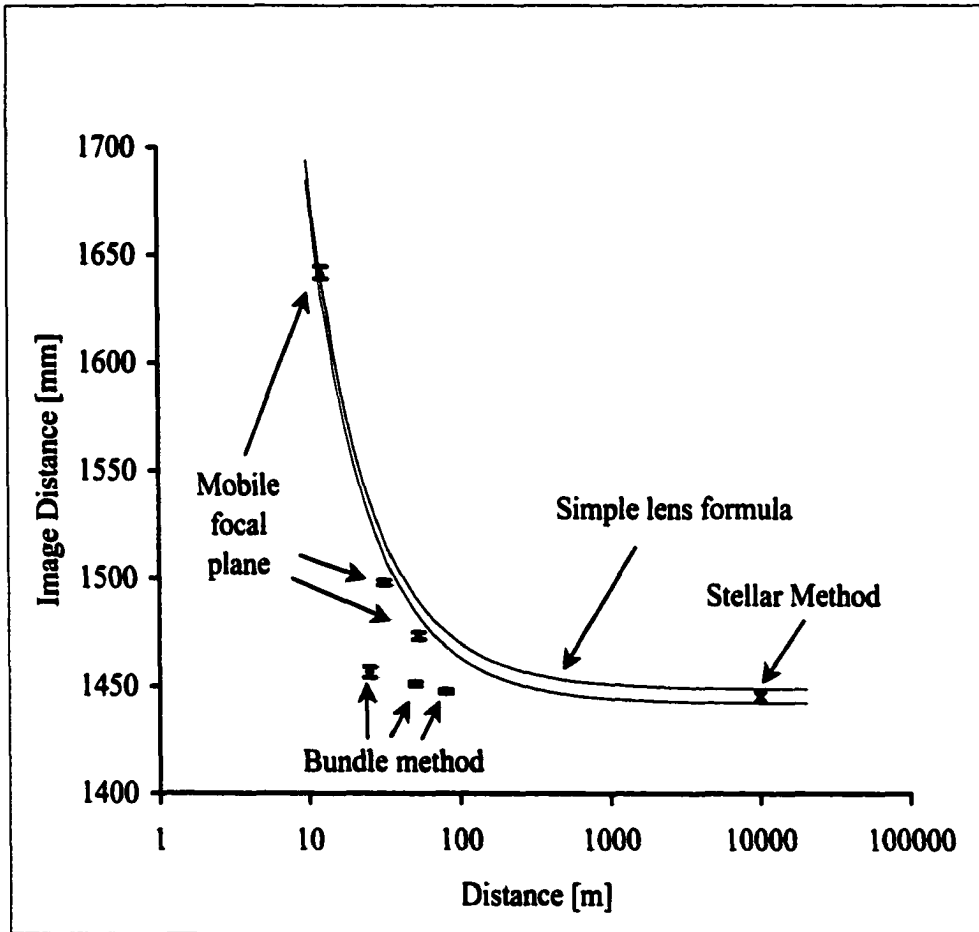


Figure 19: Comparison between various methods for determining the relationship between the image distance and object distance for the Questar lens. The two lines for the simple lens formula represent the limits determined by the uncertainty in f as computed from the stellar method. Error bars on the mobile focal plane data points are the population standard deviation of the measurements. Since the eye can accommodate slightly out of focus optical instruments these error bars do not represent the total uncertainty in the measurement.

plane in order to achieve proper focusing. The telescope was first focused at infinity ($f = 1443$ mm) and then the eyepiece was removed. The telescope was then pointed at a nearby target and the telescope refocused by moving the eyepiece away from the telescope along a graduated straight edge. The telescope was positioned at three distances from the target. Once focus was achieved the distance from the telescope eyepiece holder to the eyepiece was recorded. This was repeated four times for each object distance. The averaged results appear in Table 7 and Figure 19. These values were then added to the focal length at infinity to give the image distance used in Figure 19.

d [m]	c' [mm]	$\sigma(c')$ [mm]
12.37	198.	3.
31.39	54.	1.
53.04	29.	2.

Table 7: Results of the mobile focal plane experiment. The first column is the object distance, column two is the mean of the measured distances from the eyepiece holder to the eyepiece and column three lists the sample standard deviations.

It is apparent from Figure 19 that the Questar lens behaves more like a simple lens when focus is achieved by a mobile eyepiece or film plane. This suggests that the movement of the primary mirror is responsible for the observed departure from the simple lens formula. The uncertainty in the measurements was likely due to inaccuracies in the placement of the eyepiece along the graduated scale. Since the eye can accommodate slightly out of focus optical instruments by refocusing the image, the error bars on the mobile focal plane data point in Figure 19 may not

represent the total uncertainty in the measurement. The uncertainty due to the eye's ability to refocus the image was not measured.

6. Film Flatness

No specific experiment was performed to detect any distortions due to departures from a flat film-plane. Since the flatness of the film is probably different for each exposure, it is impossible to perform a complete calibration. Peterson and Durdle (1991) estimated the magnitude of 35-mm film buckling by measuring the image co-ordinates on a series of eight photographs taken by two remote controlled fixed cameras of a field of 36 targets. Their results found that the standard deviation of the image co-ordinates was approximately $3 \mu\text{m}$ with all residuals less than $10 \mu\text{m}$. This would suggest that the distortions introduced by buckling of the film are smaller by an order of magnitude than the limitations of the photogrammetric system (the pixel size of the scanner is about $32 \mu\text{m}$).

7. Conclusions

The calibration results demonstrate that the Questar 3.5 telescopic lens is well suited for determining astronomical refraction to a resolution of 0.1 arcminute. Star trail photographs reveal no detectable lens distortion at the resolution level of the flatbed scanner. Traditional terrestrial calibrations appear to support the star trail results. Photographs of the Pleiades star cluster gave a mean focal length at infinite object distance of $1445.3 \pm 3.6 \text{ mm}$, ($\pm 0.25\%$). The accuracy of the focal length measurements is within the accuracy required to achieve 0.1 arcsecond resolution.

Appendix A:

Object and Image Co-ordinates for Questar Calibration Targets

The second to fifth columns of Table A1 are the angular measurements of the targets in degrees. The sixth, seventh and eighth columns are the northing, easting and elevation of the targets. By convention, these values start at 2000, 1000 and 100 metres. The origin of these co-ordinates was established at the survey site by sighting a reflector mounted on the opposite station.

Tables A2 to A10 and Figures A1 to A9 show the pixel co-ordinates of the target images taken from the 35-mm negatives. Negatives were scanned with an Agfa Studio Scan II *si* at 800 ppi. The optical resolution of the scanner is 400 ppi horizontal and 800 ppi vertical. The settings of the scanner only allow equal resolution on each axis. A setting of 800 ppi means that the horizontal axis employed the resolution enhancement function of the manufacturer's software and is not the optical resolution. Nonetheless, 800 ppi was chosen since it maximized the optical resolution along at least one axis. Image co-ordinates were extracted using Scion Image, image analysis software. Pixel co-ordinates were corrected for scanner distortions.

Target Number	SOUTH STATION		NORTH STATION		Northing X [m]	Easting Y [m]	Elevation Z [m]
	Zenith Angle	Horizontal Angle	Zenith Angle	Horizontal Angle			
1	89.3721	295.5128	89.2611	67.6203	1969.6067	987.4862	100.4246
2	89.3775	296.2811	89.2556	68.4314	1969.6104	987.9880	100.4246
3	89.3831	297.0489	89.2536	69.2469	1969.6245	988.4907	100.4234
4	89.6907	295.2944	89.5854	66.6092	1970.1480	987.0884	100.2350
5	89.6814	296.6874	89.5697	68.0464	1970.1687	987.9763	100.2418
6	89.6957	298.0689	89.5750	69.5692	1970.1690	988.8885	100.2360
7	90.0186	296.3311	89.9186	66.8382	1970.7171	987.4732	100.0455
8	90.0206	296.6492	89.9192	67.1722	1970.7187	987.6754	100.0447
9	90.0149	296.9615	89.9154	67.5011	1970.7219	987.8741	100.0473
10	90.0219	297.2724	89.9196	67.8382	1970.7211	988.0750	100.0440
11	90.0231	297.5828	89.9224	68.1763	1970.7215	988.2762	100.0429
12	90.0233	297.8903	89.9225	68.5121	1970.7236	988.4756	100.0427
13	90.3358	295.8182	90.2372	65.4479	1971.2748	986.8785	99.8692
14	90.3413	296.7856	90.2471	66.4511	1971.2752	987.4818	99.8648
15	90.3379	297.1828	90.2471	66.8731	1971.2751	987.7326	99.8656
16	90.3343	297.2607	90.2431	66.9583	1971.2739	987.7826	99.8677
17	90.3226	297.3397	90.2329	67.0422	1971.2745	987.8325	99.8737
18	90.3225	297.4200	90.2331	67.1299	1971.2737	987.8840	99.8736

Table A1: Object coordinates. For details see section 5.2.

Target Number	SOUTH STATION		NORTH STATION		Northing X [m]	Easting Y [m]	Elevation Z [m]
	Zenith Angle	Horizontal Angle	Zenith Angle	Horizontal Angle			
19	90.3204	297.5000	90.2292	67.2114	1971.2767	987.9333	99.8753
20	90.3310	297.5700	90.2407	67.3042	1971.2660	987.9836	99.8691
21	90.3321	297.6497	90.2428	67.3899	1971.2665	988.0342	99.8682
22	90.3321	297.7271	90.2442	67.4736	1971.2667	988.0836	99.8678
23	90.3339	297.8072	90.2456	67.5578	1971.2687	988.1338	99.8669
24	90.3315	297.8861	90.2439	67.6426	1971.2696	988.1840	99.8680
25	90.3314	297.9640	90.2433	67.7284	1971.2694	988.2341	99.8682
26	90.3299	298.3522	90.2449	68.1517	1971.2729	988.4827	99.8680
27	90.3161	299.2807	90.2344	69.1847	1971.2830	989.0835	99.8745
28	90.6932	296.2681	90.5981	65.0347	1971.8281	986.8848	99.6759
29	90.6900	297.2460	90.6049	66.0388	1971.8356	987.4840	99.6747
30	90.6883	297.6601	90.6074	66.4536	1971.8514	987.7343	99.6745
31	90.6881	297.7310	90.6094	66.5480	1971.8402	987.7846	99.6739
32	90.6879	297.8110	90.6092	66.6330	1971.8408	987.8345	99.6739
33	90.6850	297.8918	90.6071	66.7201	1971.8409	987.8852	99.6753
34	90.6874	297.9703	90.6115	66.8034	1971.8418	987.9342	99.6734
35	90.6847	298.0582	90.6093	66.8942	1971.8446	987.9881	99.6747
36	90.6839	298.1278	90.6093	66.9694	1971.8449	988.0319	99.6749

Table A1: Object coordinates. For details see section 5.2.

Target Number	SOUTH STATION		NORTH STATION		Northing X [m]	Easting Y [m]	Elevation Z [m]
	Zenith Angle	Horizontal Angle	Zenith Angle	Horizontal Angle			
37	90.6856	298.2029	90.6117	67.0526	1971.8441	988.0798	99.6738
38	90.6860	298.2821	90.6136	67.1393	1971.8440	988.1300	99.6731
39	90.6860	298.3647	90.6136	67.2275	1971.8455	988.1816	99.6731
40	90.6854	298.4422	90.6136	67.3113	1971.8464	988.2304	99.6732
41	90.6807	298.8357	90.6140	67.7467	1971.8469	988.4811	99.6742
42	90.6740	299.7631	90.6174	68.7893	1971.8526	989.0770	99.6747
43	91.0471	297.6833	90.9707	65.5604	1972.4032	987.4593	99.4865
44	91.0458	298.0118	90.9760	65.9019	1972.4077	987.6593	99.4854
45	91.0350	298.3333	90.9667	66.2467	1972.4083	987.8582	99.4907
46	91.0294	298.6526	90.9681	66.5972	1972.4064	988.0583	99.4916
47	91.0233	298.9740	90.9679	66.9456	1972.4094	988.2583	99.4932
48	91.0222	299.2844	90.9743	67.3065	1972.4004	988.4593	99.4914
49	91.4275	297.4675	91.3392	64.3807	1972.9634	987.0358	99.2980
50	91.4090	298.9768	91.3633	65.9822	1972.9634	987.9532	99.2958
51	91.3811	300.3956	91.3661	67.5582	1972.9698	988.8366	99.3017
52	91.7874	298.5811	91.7264	64.5911	1973.5051	987.4150	99.1154
53	91.7717	299.3997	91.7399	65.4590	1973.5114	987.9063	99.1157
54	91.7635	300.1850	91.7579	66.3140	1973.5188	988.3840	99.1128

Table A1: Object coordinates. For details see section 5.2.

Target Number	x [pixels]	y [pixels]	Target Number	x [pixels]	y [pixels]
15	456	-133	30	444	217
16	365	-139	31	349	220
17	274	-147	32	258	220
18	182	-147	33	163	218
19	93	-148	34	71	223
20	1	-137	35	-28	220
21	-91	-134	36	-108	221
22	-179	-133	37	-198	223
23	-271	-131	38	-291	226
24	-362	-132	39	-387	226
25	-454	-132	40	-479	227

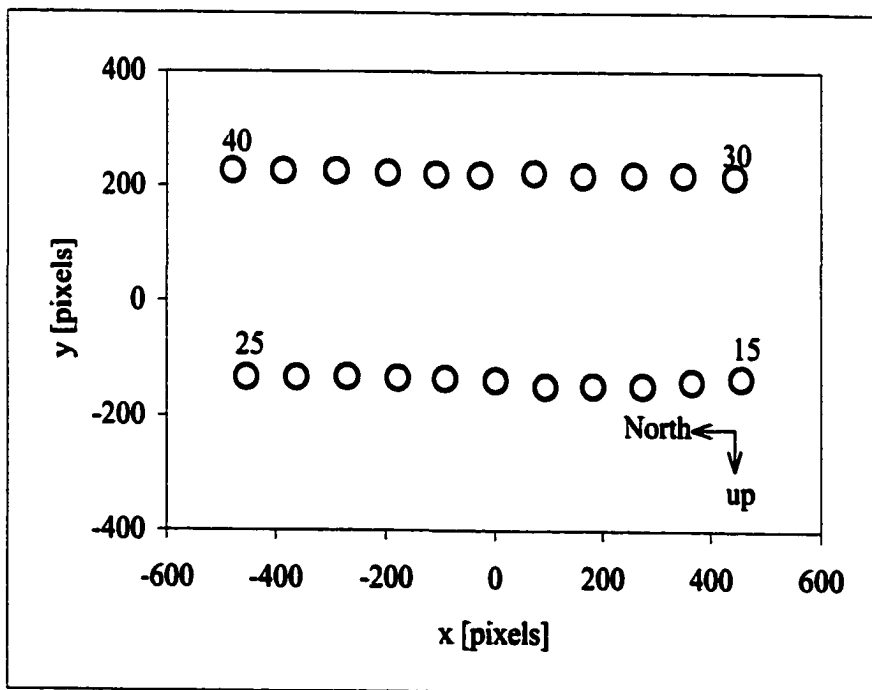


Table A2 and Figure A1: Image co-ordinates from negative #1.

Target Number	x [pixels]	y [pixels]	Target Number	x [pixels]	y [pixels]
9	-465	290	30	203	-294
10	-467	-74	31	205	-199
15	-144	-310	32	204	-106
16	-152	-219	33	200	-12
17	-161	-127	34	203	82
18	-162	-34	35	198	183
19	-167	57	36	197	265
20	-157	150	37	198	355
21	-156	243	45	551	-41
22	-156	333			

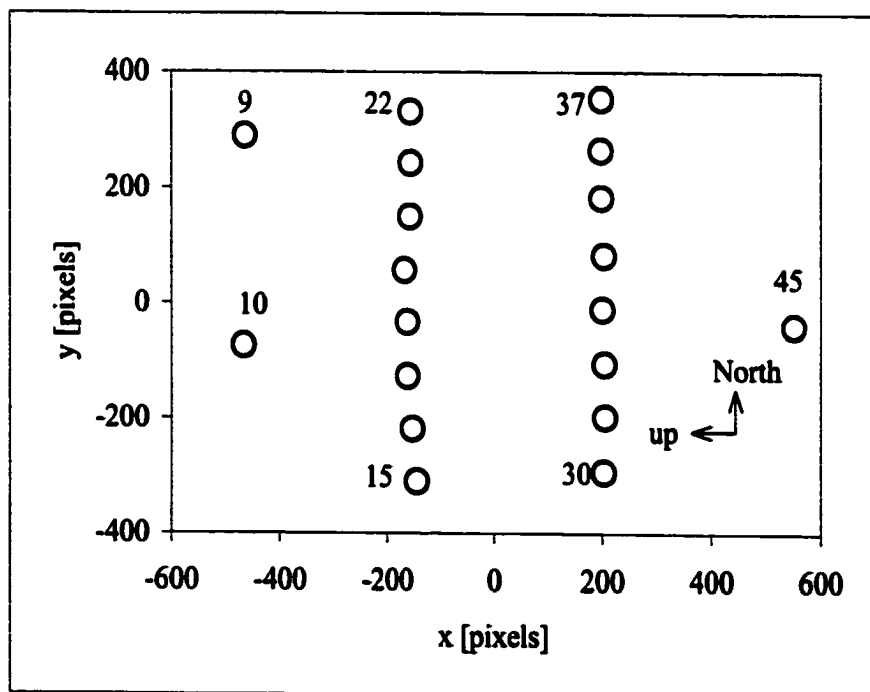


Table A3 and Figure A2: Image co-ordinates from negative # 3.

Target Number	x [pixels]	y [pixels]	Target Number	x [pixels]	y [pixels]
15	-349	195	30	-327	-156
16	-257	201	31	-232	-158
17	-165	211	32	-139	-156
18	-72	211	33	-45	-152
19	21	216	34	49	-155
20	113	207	35	150	-150
21	206	206	36	231	-149
22	295	206	37	321	-150
23	387	206	38	415	-151
24	479	209	39	510	-149

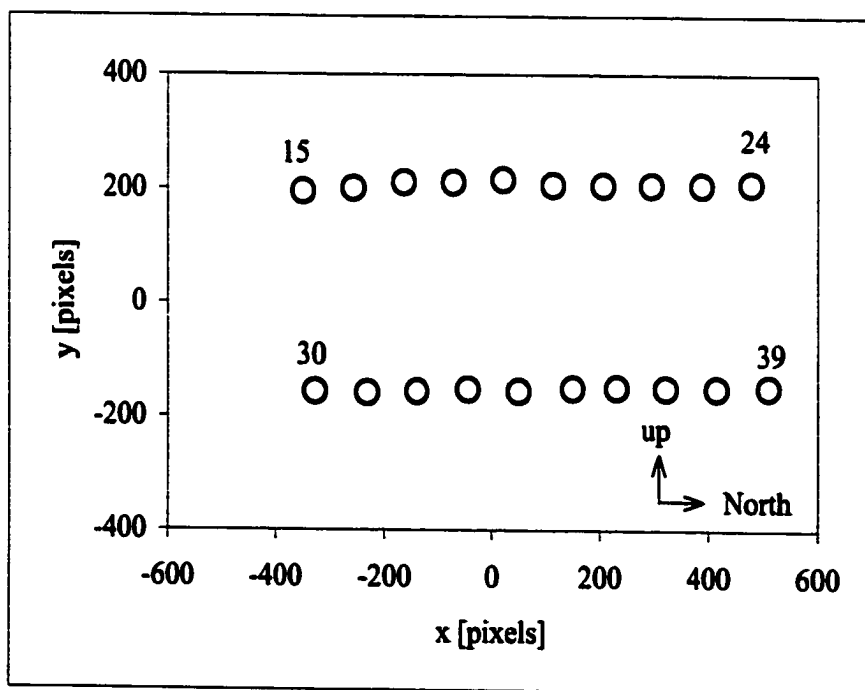


Table A4 and Figure A3: Image co-ordinates from negative # 8.

Target Number	x [pixels]	y [pixels]	Target Number	x [pixels]	y [pixels]
5	-459	3	30	52	-197
8	-290	-259	31	53	-151
9	-288	-80	32	53	-104
10	-285	100	33	53	-58
11	-283	280	34	55	-12
15	-125	-203	35	54	38
16	-127	-157	36	54	79
17	-133	-111	37	55	122
18	-132	-65	38	56	168
19	-133	-20	39	57	216
20	-126	26	40	57	262
21	-125	71	44	230	-259
22	-123	115	45	227	-74
23	-123	161	46	228	113
24	-123	208	47	230	301
25	-123	253	50	417	23

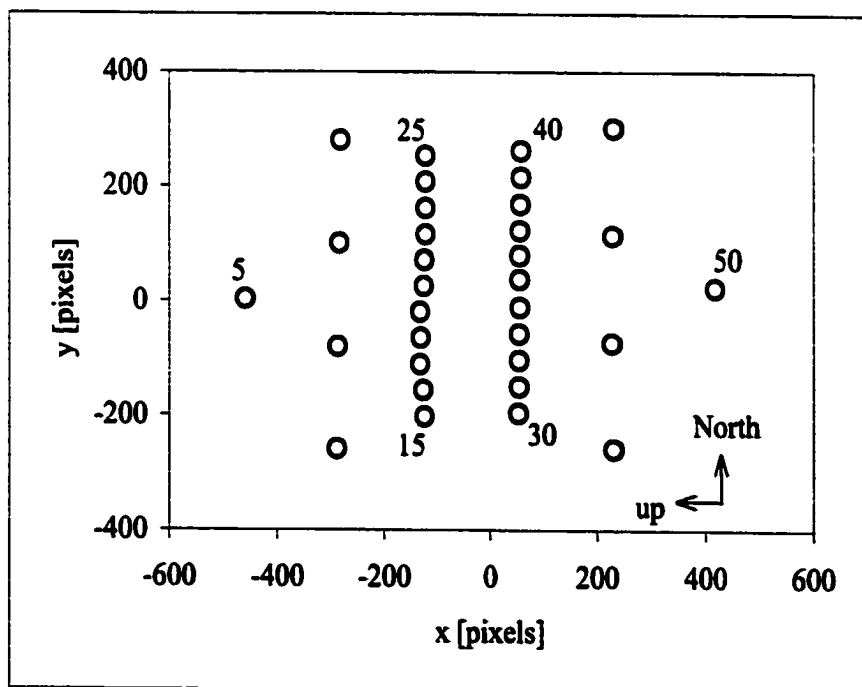


Table A5 and Figure A4: Image co-ordinates from negative # 13.

Target Number	x [pixels]	y [pixels]	Target Number	x [pixels]	y [pixels]
7	-505	266	29	-487	-71
8	-322	268	30	-259	-71
9	-146	268	31	-212	-72
10	34	266	32	-167	-72
11	214	264	33	-121	-71
12	394	264	34	-74	-73
14	-492	106	35	-25	-71
15	-266	106	36	15	-72
16	-220	108	37	60	-72
17	-175	114	38	106	-74
18	-130	113	39	154	-73
19	-84	115	40	198	-73
20	-39	108	41	429	-72
21	7	107	43	-502	-247
22	52	107	44	-319	-249
23	98	106	45	-134	-244
24	143	107	46	52	-245
25	188	107	47	240	-245
26	415	107	48	424	-245

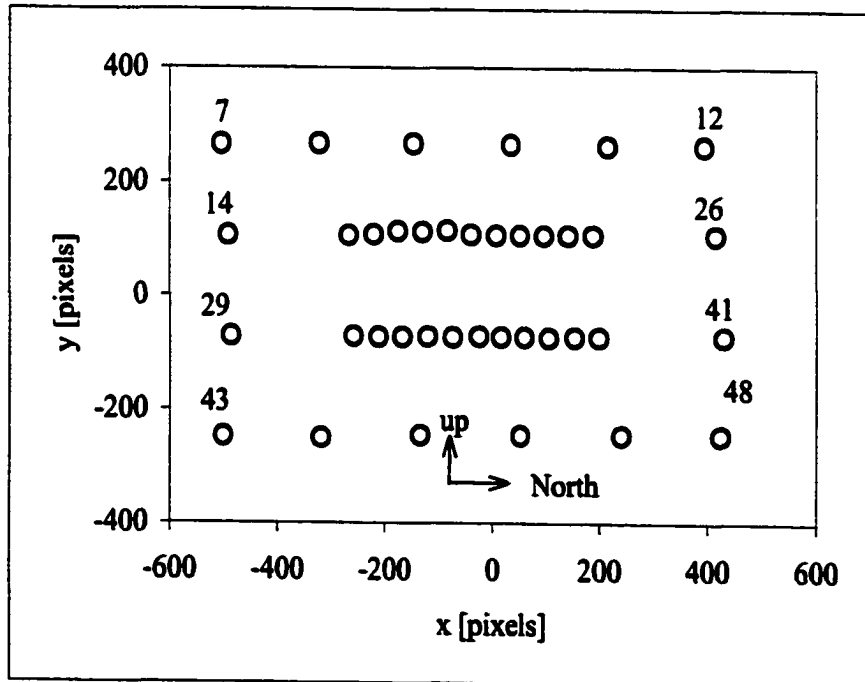


Table A6 and Figure A5: Image co-ordinates from negative # 10.

Target Number	x [pixels]	y [pixels]	Target Number	x [pixels]	y [pixels]
5	5	-367	29	435	138
7	448	-200	30	208	144
8	266	-198	31	161	146
9	90	-195	32	116	147
10	-90	-190	33	69	147
11	-270	-185	34	24	149
12	-451	-182	35	-26	148
14	437	-38	36	-66	149
15	213	-34	37	-109	151
16	166	-35	38	-155	152
17	121	-41	39	-203	153
18	75	-39	40	-249	154
19	31	-40	41	-481	156
20	-14	-32	43	454	316
21	-60	-31	44	270	321
22	-104	-29	45	86	319
23	-150	-27	46	-99	323
24	-196	-27	47	-287	325
25	-242	-27	48	-473	328
26	-470	-24			

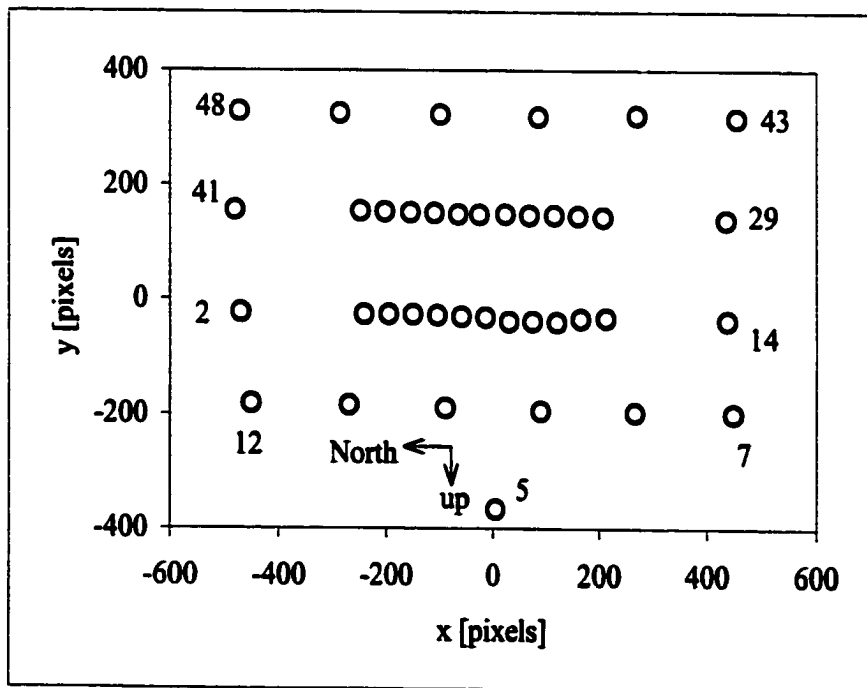


Table A7 and Figure A6: Image co-ordinates from negative # 15.

Target Number	x [pixels]	y [pixels]	Target Number	x [pixels]	y [pixels]
1	291	-206	24	-121	99
2	12	-207	25	-149	99
3	-268	-208	26	-289	99
4	507	-102	29	271	210
5	11	-108	30	129	210
6	-499	-106	31	100	210
7	287	1	32	71	210
8	172	0	33	43	208
9	61	0	34	15	210
10	-52	0	35	-17	209
11	-165	1	36	-42	209
12	-276	1	37	-69	209
14	277	101	38	-98	210
15	135	101	39	-127	210
16	105	99	40	-155	210
17	78	94	41	-297	208
18	50	95	43	280	318
19	22	94	44	166	318
20	-7	99	45	50	314
21	-36	100	46	-65	314
22	-64	99	47	-180	313
23	-92	100	48	-294	313

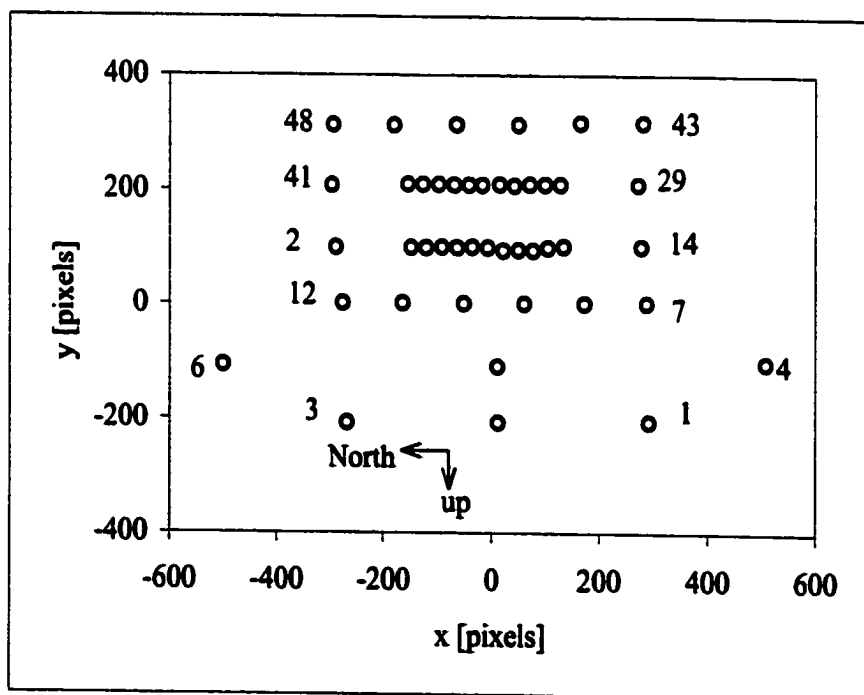


Table A8 and Figure A7: Image co-ordinates from negative # 19.

Target Number	x [pixels]	y [pixels]	Target Number	x [pixels]	y [pixels]
1	267	306	29	-150	287
2	270	27	30	-149	144
3	272	-254	31	-149	115
5	170	26	32	-149	87
7	58	302	33	-147	58
8	59	188	34	-148	30
9	61	76	35	-147	-2
10	60	-37	36	-147	-27
11	61	-148	37	-147	-54
12	62	-263	38	-147	-82
14	-42	292	39	-147	-111
15	-41	150	40	-147	-140
16	-39	121	41	-145	-283
17	-35	93	43	-257	296
18	-35	65	44	-256	180
19	-35	37	45	-252	65
20	-39	8	46	-252	-50
21	-39	-21	47	-250	-165
22	-39	-48	48	-250	-280
23	-39	-76	50	-365	3
24	-38	-105	52	-472	311
25	-38	-133	53	-471	25
26	-36	-275	54	-470	-255

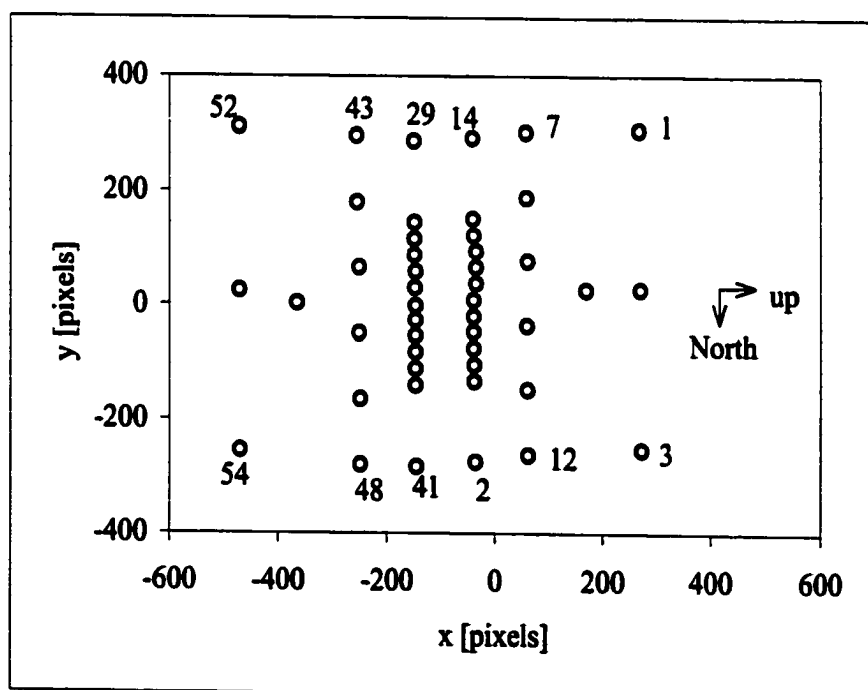


Table A9 and Figure A8: Image co-ordinates from negative # 23.

Target Number	x [pixels]	y [pixels]	Target Number	x [pixels]	y [pixels]
5	2	373	32	-61	57
7	-277	266	33	-31	57
8	-161	267	34	-3	57
9	-49	267	35	29	58
11	178	266	36	53	58
12	291	266	37	81	57
13	64	266	38	110	58
14	-267	166	39	139	57
15	-124	166	40	168	57
16	-95	168	41	312	59
17	-67	173	43	-270	-50
18	-39	172	44	-154	-51
19	-10	172	45	-40	-47
20	19	168	46	77	-47
21	48	167	47	193	-45
22	76	167	48	308	-46
23	104	167	49	-509	-161
24	133	168	50	23	-161
25	162	168	51	536	-155
26	304	169	52	-286	-269
29	-261	57	53	2	-267
30	-118	57	54	283	-268
31	-89	57			

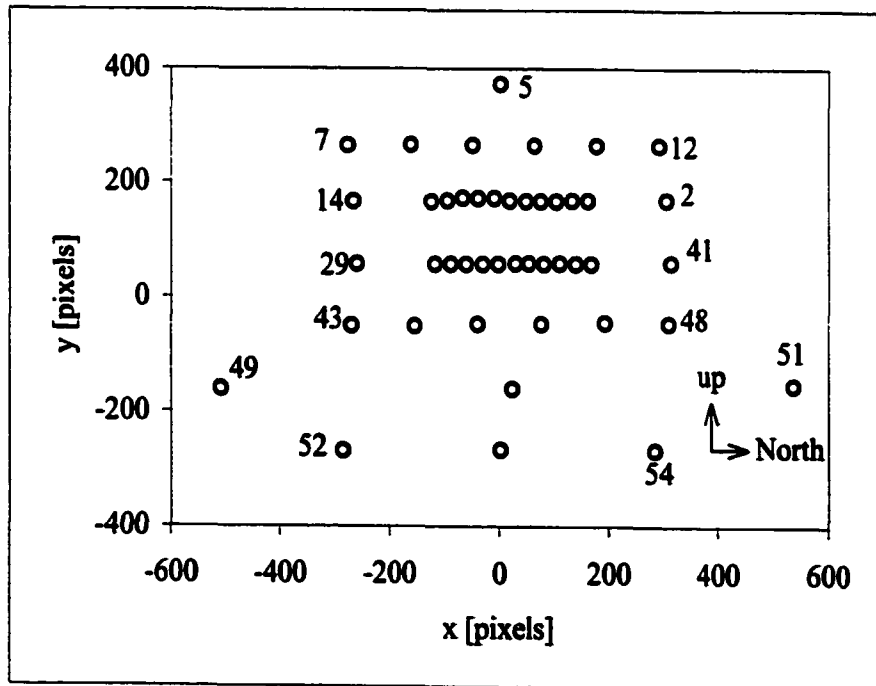


Table A10 and Figure A9: Image co-ordinates from negative # 27.

APPENDIX B

Solution to the Photogrammetric Problem (The Bundle Method)

**Summarized from
Chapters 4 and 5: Karara, (1989)
and Chapter 2: Slama, (1980)**

In a perfect lens the object point, perspective centre of the lens and the image point should be joined by a straight line. This is the essence of collinearity. Unfortunately, only a pinhole 'lens' can guaranteed to be truly collinear. All other lenses deviate to some degree from collinearity. The computer model TRIPLET was used to measure the principal distance, and lens distortions of the Questar 3.5-inch telescopic lens.

B.1 The Collinearity Equation

The first step in the derivation of the collinearity equation is to establish the object and image space coordinate systems. The image and object spaces are both defined as three-dimensional right-handed Cartesian coordinate systems (see Figure B1).

The image space co-ordinates can be transformed into object space co-ordinates through sequential rotation around the X, Y, and Z-axes, thus deriving the exterior orientation of the camera. This is achieved through the multiplication of three 3-by-3 orthogonal rotation matrices whose elements are the cosines of the angles between coordinate axes. The first matrix is:

$$\mathbf{M}_\omega = \begin{bmatrix} 1 & 0 & 0 \\ 0 & \cos \omega & \sin \omega \\ 0 & -\sin \omega & \cos \omega \end{bmatrix}, \quad (\text{B1})$$

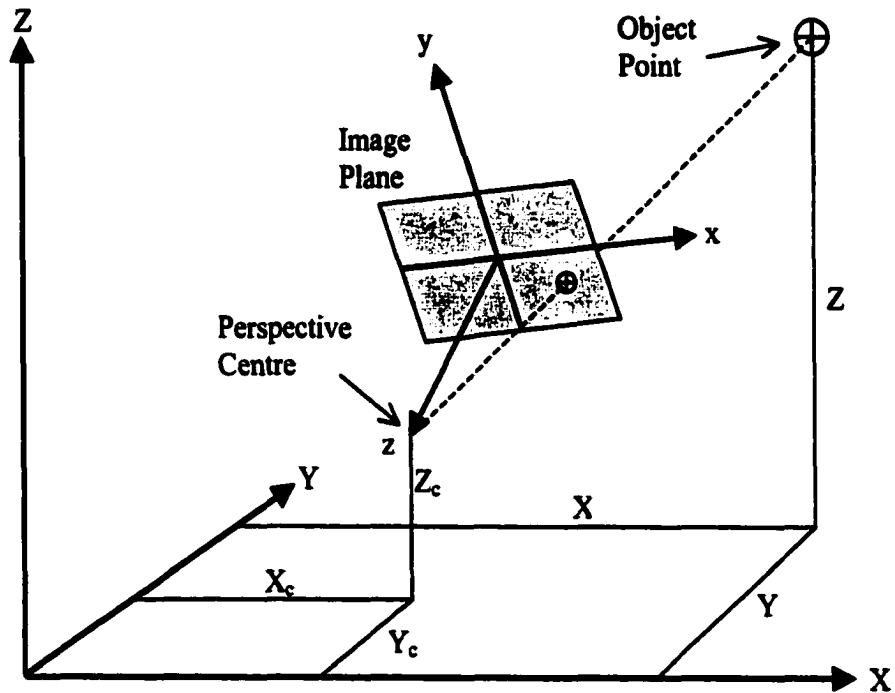


Figure B1: Image space (x, y, z) and object space (X, Y, Z) coordinate systems. Note that the optical system is turned around producing positive image geometry. At an object distance of infinity the position of the perspective centre along the z -axis would be equal to the focal length of the lens. The dashed line represents the collinearity assumption.

where ω is the rotation around the X -axis, taken as positive in the direction that takes the $+Y$ axis towards the $+Z$ axis. The next matrix in the sequence is:

$$\mathbf{M}_\phi = \begin{bmatrix} \cos \phi & 0 & -\sin \phi \\ 0 & 1 & 0 \\ \sin \phi & 0 & \cos \phi \end{bmatrix}, \quad (\text{B2})$$

where ϕ is the angle of rotation about the once-rotated Y' axis (moving the $+Z'$ axis towards the $+X'$ axis). The final rotational matrix is:

$$\mathbf{M}_\kappa = \begin{bmatrix} \cos \kappa & \sin \kappa & 0 \\ -\sin \kappa & \cos \kappa & 0 \\ 0 & 0 & 1 \end{bmatrix}, \quad (\text{B3})$$

where κ is the angle of rotation about the twice-rotated Z'' axis (moving the $+X''$ axis towards the $+Y''$ axis).

These are then multiplied in order giving:

$$\mathbf{M} = \mathbf{M}_\kappa \mathbf{M}_\phi \mathbf{M}_\omega. \quad (\text{B4})$$

which has the following elements:

$$\left. \begin{aligned} m_{11} &= \cos \phi \cos \kappa \\ m_{12} &= \sin \omega \sin \phi \cos \kappa + \cos \omega \sin \kappa \\ m_{13} &= -\cos \omega \sin \phi \cos \kappa + \sin \omega \sin \kappa \\ m_{21} &= -\cos \phi \sin \kappa \\ m_{22} &= -\sin \omega \sin \phi \sin \kappa + \sin \omega \cos \kappa \\ m_{23} &= \cos \omega \sin \phi \sin \kappa + \sin \omega \cos \kappa \\ m_{31} &= \sin \phi \\ m_{32} &= -\sin \omega \cos \phi \\ m_{33} &= \cos \omega \cos \phi \end{aligned} \right\}. \quad (\text{B5})$$

Now the image vector \mathbf{a} can be expressed in image co-ordinates as:

$$\mathbf{a} = \begin{bmatrix} x - x_0 \\ y - y_0 \\ -c \end{bmatrix}, \quad (\text{B6})$$

where x_0 and y_0 are the image co-ordinates of the principal point and c is the principal distance of the lens. It should be noted that only when the lens is focused at infinity is c equal to the focal length of the lens. According to Figure B1 the object space vector \mathbf{A} from the perspective centre to the object point is given by:

$$\mathbf{A} = \begin{bmatrix} X - X_c \\ Y - Y_c \\ Z - Z_c \end{bmatrix}. \quad (\text{B7})$$

The collinearity assumption now requires that once the rotation matrix \mathbf{M} is multiplied by Equation B7, then Equations B6 and B7 should be equal. A scaling factor k can now be applied giving the formula:

$$\mathbf{a} = k\mathbf{M}\mathbf{A}.$$

$$\begin{bmatrix} x - x_0 \\ y - y_0 \\ -c \end{bmatrix} = k\mathbf{M} \begin{bmatrix} X - X_c \\ Y - Y_c \\ Z - Z_c \end{bmatrix}, \quad (\text{B8})$$

where:

$$x - x_0 = k[m_{11}(X - X_c) + m_{12}(Y - Y_c) + m_{13}(Z - Z_c)], \quad (\text{B9})$$

$$y - y_0 = k[m_{21}(X - X_c) + m_{22}(Y - Y_c) + m_{23}(Z - Z_c)], \quad (\text{B10})$$

and:

$$-c = k[m_{31}(X - X_c) + m_{32}(Y - Y_c) + m_{33}(Z - Z_c)]. \quad (\text{B11})$$

To eliminate k , Equations B9 and B10 can be divided by B11 and rearranged to give the final collinearity equations:

$$f_1 = x - x_0 + c \frac{m_{11}(X - X_C) + m_{12}(Y - Y_C) + m_{13}(Z - Z_C)}{m_{31}(X - X_C) + m_{32}(Y - Y_C) + m_{33}(Z - Z_C)}, \quad (\text{B12})$$

and

$$f_2 = y - y_0 + c \frac{m_{21}(X - X_C) + m_{22}(Y - Y_C) + m_{23}(Z - Z_C)}{m_{31}(X - X_C) + m_{32}(Y - Y_C) + m_{33}(Z - Z_C)}, \quad (\text{B13})$$

where f_1 and f_2 are equal to zero if the light path is collinear and non-zero if the lens produces any image distortion.

B.2 Self-Calibration

TRIPLET allows for self-calibration, which is the addition and solution of radial and decentering distortion components in the collinearity equations.

Radial distortion is defined as the deviation from an image position produced by a collinear light path either radially away or towards the principal point of the lens. The term *barrel* (negative) distortion refers to distortion in a direction away from the principal point, while *pincushion* (positive) distortion occurs in a direction towards the principal point axis (see Figure B2).

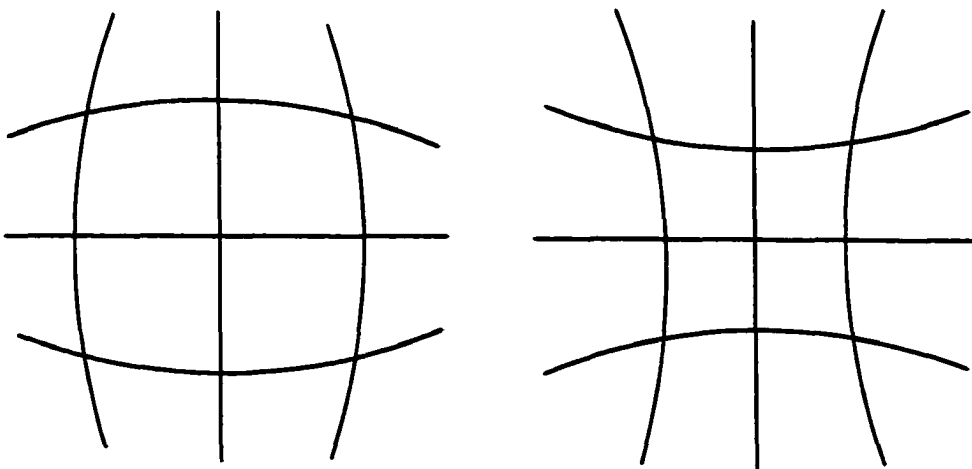


Figure B2: Barrel (left) and pincushion distortion (right) of an orthogonal grid.

The radial distortion δr is represented by the polynomial series (derived from an expansion of the lens ray-tracing formulae)

$$\delta r = K_1 r^3 + K_2 r^5 + K_3 r^7 + \dots, \quad (\text{B14})$$

where the K 's are the coefficients of distortion (at infinite focus) while r is the radial distance from the principal point and is determined from the equation

$$r^2 = (x - x_0)^2 + (y - y_0)^2, \quad (\text{B15})$$

where x and y are the image point co-ordinates and x_0 and y_0 are the co-ordinates of the principal point.

For non-metric camera lenses using small format film (35-mm or 70-mm formats) the first coefficient is usually sufficient to describe the distortional behavior.

Decentering distortion is produced by the misalignment of lens elements where the centre of curvature of the lens elements is not collinear with the optical axis. The effect on the image is the same as that produced by a thin prism placed in front of the lens. There is both a radial and a tangential component to the decentering distortion. The tangential component reaches a maximum at a position angle of ϕ_0 originating from the principal point and measured counter-clockwise from the positive x-axis (see Figure B3). Along this axis the radial component is zero. At right angles to this axis there exists another axis where the radial distortion reaches a maximum and the tangential distortion is zero. The angle ϕ_0 is found from the formula (Slama, 1980):

$$\phi_0 = \tan^{-1} \left(\frac{P_1}{P_2} \right), \quad (\text{B16})$$

where P_1 and P_2 are the values of the decentering distortion at infinite focus.

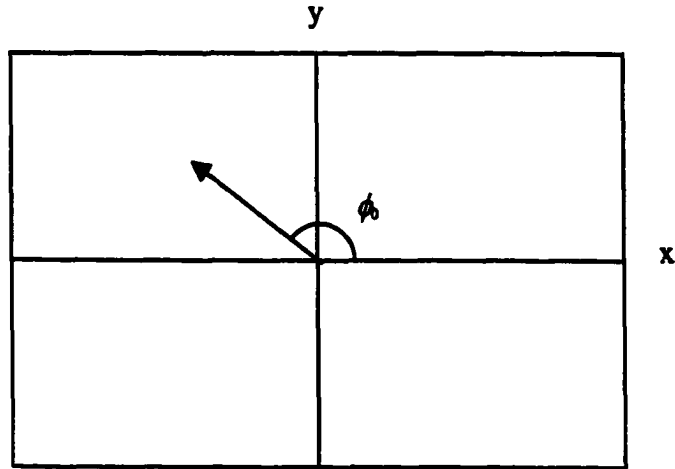


Figure B3: Orientation of decentering distortion in image space.

The decentering distortion Δx and Δy can be represented by the polynomials:

$$\Delta x = \left(1 - \frac{c}{s}\right) \left[P_1(r^2 + 2(x - x_0)^2) + 2P_2(x - x_0)(y - y_0) \right], \quad (\text{B17})$$

and

$$\Delta y = \left(1 - \frac{c}{s}\right) \left[P_2(r^2 + 2(y - y_0)^2) + 2P_1(x - x_0)(y - y_0) \right], \quad (\text{B18})$$

where s is the distance from the object plane to the camera (i.e. the plane of focus).

The radial and decentering distortions can now be added to the collinear equations, which are expressed as:

$$f_1 = (x - x_0) + \frac{(x - x_0)}{r} \delta r + \Delta x + c \frac{m_{11}(X - X_c) + m_{12}(Y - Y_c) + m_{13}(Z - Z_c)}{m_{31}(X - X_c) + m_{32}(Y - Y_c) + m_{33}(Z - Z_c)}, \quad (\text{B19})$$

and

$$f_2 = (y - y_0) + \frac{(y - y_0)}{r} \delta r + \Delta y + c \frac{m_{21}(X - X_c) + m_{22}(Y - Y_c) + m_{23}(Z - Z_c)}{m_{31}(X - X_c) + m_{32}(Y - Y_c) + m_{33}(Z - Z_c)}, \quad (\text{B20})$$

where δr is the radial distortion derived in Equation (B14) and Δx and Δy are the decentering distortions from Equations (B17) and (B18).

B.3 Solution through Least Squares Adjustment

Equations (B19) and (B20) are non-linear and therefore are linearized for least squares adjustment. Taking their partial derivatives can linearize the equations into the form:

$$y_m + v_m = x_{m1}a_1 + x_{m2}a_2 + x_{m3}a_3 + \cdots + x_{mn}a_n, \quad (\text{B21})$$

where y_m is the observation (in this case the image co-ordinates x, y), v_m is the residual of the observations, x_{mn} are the independent variable (the object co-ordinates of the targets X, Y, and Z) and a_n are the coefficients of interest (image distance, distortion coefficients, camera orientation, etc.).

A series of observation equations with y_m placed on the right hand side of Equation (B21) forms the matrix:

$$\mathbf{V} = \mathbf{B}\delta - \mathbf{C}, \quad (\text{B22})$$

$$\begin{bmatrix} v_1 \\ v_2 \\ \vdots \\ v_m \end{bmatrix} = \begin{bmatrix} x_{11} & x_{12} & \cdots & x_{1n} \\ x_{21} & x_{22} & \cdots & x_{2n} \\ \vdots & \vdots & & \vdots \\ x_{m1} & x_{m2} & \cdots & x_{mn} \end{bmatrix} \begin{bmatrix} a_1 \\ a_2 \\ \vdots \\ a_n \end{bmatrix} - \begin{bmatrix} y_1 \\ y_2 \\ \vdots \\ y_m \end{bmatrix}, \quad (\text{B23})$$

The least squares principle states that the exponent of the joint distribution function must be minimized in order to maximize the probability of the value in question, in this case the elements in the δ matrix. The exponent of the joint distribution function can be expressed as:

$$Q = \sum_{i=1}^n \left(\frac{v_i}{\sigma_i} \right)^2. \quad (\text{B24})$$

from this definition it follows that:

$$Q = \sum_{i=1}^n \left(\frac{v_i}{\sigma_i} \right)^2 = \mathbf{v}^T \mathbf{W} \mathbf{v} \quad (\text{B25})$$

where \mathbf{W} is the weight matrix (Davis, et al 1981):

$$\mathbf{W} = \sigma_0^2 \begin{bmatrix} 1/\sigma^2 y_1 & & & & 0 \\ & 1/\sigma^2 y_2 & & & \\ & & 1/\sigma^2 y_3 & & \\ & & & \ddots & \\ 0 & & & & 1/\sigma^2 y_n \end{bmatrix}, \quad (\text{B26})$$

where σ_0 is the variance of unit weight and for most applications it is equal to unity, σ is the standard deviation of the observations and y_n are the observations.

Placing equation (B22) into (B24) gives:

$$Q = (\mathbf{B}\delta - \mathbf{C})^T \mathbf{W} (\mathbf{B}\delta - \mathbf{C}), \quad (\text{B27})$$

or

$$Q = (\delta^T \mathbf{B}^T - \mathbf{C}^T) (\mathbf{W} \mathbf{B} \delta - \mathbf{W} \mathbf{C}), \quad (\text{B28})$$

which can be expanded into the form:

$$Q = \delta^T \mathbf{B}^T \mathbf{W} \mathbf{B} \delta - \delta^T \mathbf{B}^T \mathbf{W} \mathbf{C} - \mathbf{C}^T \mathbf{W} \mathbf{B} \delta + \mathbf{C}^T \mathbf{W} \mathbf{C}. \quad (\text{B29})$$

The solution requires finding the matrix δ , which minimizes Q . Therefore the partial derivative with respect to δ of Equation (B29) should be equal to zero. Therefore, from Equation (B29):

$$0 = 2\mathbf{B}^T \mathbf{W} \mathbf{B} \delta - 2\mathbf{B}^T \mathbf{W} \mathbf{C}, \quad (\text{B30})$$

which can be simplified into the form:

$$(\mathbf{B}^T \mathbf{W} \mathbf{B}) \delta = \mathbf{B}^T \mathbf{W} \mathbf{C}. \quad (\text{B31})$$

Equation (B31) is referred to as the normal equations for the model. Letting:

$$\mathbf{N} = \mathbf{B}^T \mathbf{W} \mathbf{B}, \text{ and } \mathbf{K} = \mathbf{B}^T \mathbf{W} \mathbf{C}, \quad (\text{B32})$$

Equation (B31) can be written:

$$\begin{array}{ccc} \mathbf{N} & \delta & = & \mathbf{K} \\ (n,n) & (n,1) & & (n,1) \end{array} \quad (\text{B33})$$

The solution for δ is the solution of the above normal equations.

The input values for TRIPLET are the image co-ordinates (x, y) , object co-ordinates (X, Y, Z) , camera object space co-ordinates (X_c, Y_c, Z_c) , image coordinate uncertainty, approximate principal distance c , and the approximate camera orientation (ω, ϕ, κ) which are contained in the values of m_{ij} . The program then attempts to solve for $c, \omega, \phi, \kappa, K_1, K_2, P_1$ and P_2 through a least squares adjustment.

References

- Bishop, R. L. (Ed.), 1996: *The Observer's Handbook*, University of Toronto Press, Toronto, 288 pp.
- Brown, D. C., 1971: Close-Range Camera Calibration, *Photogrammetric Engineering*, **37**, 855
- Davis, R. E., Foote, F. S., Anderson, J. M. and Mikhail, E. M., 1981: *Survey Theory and Practice*, McGraw Hill, New York, 992 pp.
- Green, R. M. 1985: *Spherical Astronomy*, Cambridge University Press, Cambridge, 520 pp.
- Hoffleit, D., Warren Jr., W. H., 1991: *The Bright Star Catalogue*, 5th ed. (preliminary version) Yale Univ. Observatory, New Haven, Conn. (on-line catalogue: <http://adc.gsfc.nasa.gov/adc-cgi/cat.pl?catalogs/5/5050>)
- Karara, H. M., ed., 1989: *Non-Topographic Photogrammetry*, 2nd Edition, American Society for Photogrammetry and Remote Sensing
- Eastman Kodak Company, 1982: *Kodak Data for Aerial Photography*, M-29
- Eastman Kodak Company, 1999: *On-line Technical Data*, <http://www.kodak.com/global/en/professional/support/techPubs/f9/f9.shtml>
- Maksutov, D. D., 1944: New Catadioptric Meniscus Systems, *Journal of the Optical Society of America*, **34**, 270
- Monet, D. G., 1992: *Astrometry, Techniques and Telescopes*, in Maran, S. P. *The Astronomy and Astrophysics Encyclopedia*, Van Nostrand Reinhold, New York, 1002 pp.
- Peterson, A. E. and Durdle, N. G., 1991: Surveying Possibilities with 35 mm Cameras, *Proceedings for the Canadian Society for Civil Engineering*, 10th Canadian Hydrotechnical Conference, May 29 – 31, 1991, Vancouver, Volume IV, 432 - 440.
- Sampson, R. D., 1994: *Atmospheric Refraction and its Effects on Sunrise and Sunset*, Master of Science thesis, Department of Geography, University of Alberta, 123 pp.
- Sampson, R. D., Peterson, A. E., and Lozowski, E. P., 2000: *Photogrammetric Calibration of a Consumer Grade Flat-bed Scanner*, *Journal of Photogrammetric Engineering and Remote Sensing*, submitted June 2000

Scion Image, 1998: Scion Corporation, www.scioncorp.com

Slama, Chester C., ed., 1980: Manual of Photogrammetry, 4th Edition, American Society of Photogrammetry, Falls Church, Va. 1056 pp.

Taylor, John R., 1982: An Introduction to Error Analysis, University Science Books, Mill Valley California, 270 pp.

**CHAPTER 3: A COMPARISON OF OBSERVED HIGH ZENITH ANGLE
ASTRONOMICAL REFRACTION OF THE SUN WITH OUTPUT FROM A
RAY TRACING MODEL USING RAWINSONDE PROFILES**

Abstract

Numerous research areas, such as astrometry, navigation and remote sensing require accurate predictions of astronomical refraction through the Earth's atmosphere. Much work has been done to model astronomical refraction, However, very little has been done to compare the observed and modelled astronomical refraction at high zenith angles, where astronomical refraction is at a maximum. In this study, a ray tracing model using atmospheric data from VIZ and Vaisala rawinsondes is compared with the observed astronomical refraction presented by the setting Sun as observed from Edmonton and Stony Plain Alberta on December 8, 14 and 22, 1998. Refraction values were photogrammetrically extracted from images of the setting Sun taken with a calibrated Questar telescopic lens of 1445.3 ± 3.6 mm focal length. The negatives were scanned with a calibrated Agfa scanner. Exposures were taken within 20 minutes of the time of the rawinsonde launch and within 100 metres of the launch location (Stony Plain Upper Air Station in Alberta, Canada). Theodolite measurements of the astronomical refraction taken during the same sunsets, but from a site 25 kilometres to the east of the upper air station, were also obtained. The theodolite and photogrammetric measurements showed good agreement with the model for the December 14 and 22 sunsets. The poorer modelled results for the December 8 sunset used data from a VIZ rawinsonde. According to David Carlsen of Environment Canada (2000),

these instruments were from an old and possibly defective stock. The results produced by the rawinsonde profiles were also compared with the astronomical refraction produced by a Modified U.S. Standard Atmosphere (MUSSA). These profiles start with the observed surface temperature and apply a linear temperature gradient for the major atmospheric layers (troposphere, stratosphere, etc.). The MUSSA profile appears to produce a better fit between modelled and observed astronomical refraction than the rawinsonde profiles. The results of this study suggest that the temperature measurements from the rawinsondes may be too inaccurate or too unrepresentative of the conditions in the optical path to improve on a MUSSA model. Nonetheless, both models showed an improvement over the Pulkovo Refraction Tables.

1. Introduction

The motivation of this project was to explore the possibility of using astronomical refraction as remote sensing technique to measure the temperature profile of the atmosphere. The objective of this work was to test the predictive ability of an astronomical refraction model by comparing its output with observed refraction values. As outlined in the following section, a better understanding of astronomical refraction has applications in such fields as astrometry, remote sensing, satellite navigation, laser ranging, geodesy and archaeoastronomy. To date, there has been very little work comparing observed high zenith angle astronomical refraction with model output (Clemence, 1951).

In an attempt to verify the model accuracy, meteorological data from rawinsondes were used. Since the rawinsonde was launched within a few minutes of the refraction measurements and only a few tens of metres from the observer, it was hypothesized that these measured atmospheric profiles would produce better results than refraction tables (Pulkovo Observatory, 1930, 1956, and 1985) or using a standard atmosphere. The rawinsonde used by Environment Canada is the Vaisala RS80, which has improved sensor resolution and a sampling interval of 10 seconds (Vaisala, 1998). This improved resolution also suggested that an improvement in model output would be expected. However, the horizontal gradients in the atmosphere were not measured by the rawinsonde and therefore were not included in the model.

Photogrammetric measurements of the setting Sun provided the values for the observed refraction. Photographs were taken with a photogrammetrically

calibrated consumer-grade system with a Questar 3.5-inch telescopic lens ($f = 1445.3 \pm 3.6$ mm) coupled to an Olympus OM-1 camera body. The observed horizontal co-ordinates (altitude and azimuth) of the setting Sun were found from the measured horizontal co-ordinates of distant treetops captured in the same image. An orbital model using accurate exposure timings (± 0.2 s) and geographical co-ordinates as input provided the horizontal co-ordinates (zenith angle and azimuth) of the geometric Sun (i.e. unrefracted Sun).

Much of the following model was based on the work of Bruton (1996). Bruton's did not try to simulate the appearance of specific sunset or sunrise events, but was used to simulate the appearance of generic sunrise and sunset phenomena such as blank strips and the Green Flash.

Our model inputs are the time, date, geographic coordinates of the observer, wavelength, and the nearby sounding profiles of the altitude, pressure, temperature, and humidity taken within a few minutes of the time of sunset. From the time and geographic co-ordinates, the model finds the position and apparent diameter of the Sun. The model guesses an initial angle of the light ray from the observer. The path of the ray is then determined from refraction indices calculated from the sounding file produced by rawinsonde balloons launched from Stony Plain, Alberta. Once the ray leaves the atmosphere, its miss-angle with respect to the Sun is calculated. The initial angle is then adjusted and the process repeated until the miss-angle is within 0.1 arcminute of the intended point on the profile of the Sun. The model has also been compared with theodolite observations made at the same time in Edmonton, approximately 25 kilometres east of the primary observation site.

1.1 Current Astronomical Refraction Applications

The visible light from some celestial sources may travel virtually unaffected for many light years only to be distorted by our atmosphere in the last few kilometers of its journey. Much of the reason for placing astronomical instruments into space was to eliminate this problem. However, the accurate ground-based measurement of objects beyond the atmosphere is critical in many physical science disciplines. Therefore, a better knowledge of astronomical refraction may lead to improvements in these areas.

The recent discovery of extrasolar planets has renewed interest in high accuracy ground-based relative astrometry. Relative astrometry is the measurement of angular distances between stars in the same instrument field. An accuracy of 100 microarcseconds (μas) or better, would be necessary to detect stellar movement caused by large extrasolar planets. At this level of accuracy, refraction must be incorporated into the solutions (Gubler and Tytler, 1998). Differential astronomical refraction must also be considered when conducting integral-field (i.e. two-dimensional) spectroscopic observations (Arribas, et. al, 1999). The atmosphere not only refracts light from astronomical sources, but the amount of refraction is a function of the wavelength.

Spacecraft in low earth orbit (LEO) use stellar tracking systems for autonomous navigation. Accurate measurement of the positions of stars near the limb of the Earth requires a correction for astronomical refraction (Kireev and Sokolovskiy, 1994).

The light originating from the Earth and passing through the atmosphere experiences the same refraction as that from celestial objects. Remote sensing from LEO also requires a correction for astronomical refraction (Noerdlinger, 1999).

Satellite Laser Ranging (SLR) is now being used to obtain measurements of such things as: global tectonic plate motion; regional crustal deformation near plate boundaries; the Earth's gravity field; and the orientation of its polar axis and its rate of spin (NASA, 2000). As this technology approaches millimeter accuracy, compensation for astronomical refraction must be included (Yan and Wang, 1999).

Astronomical and terrestrial refraction studies have also been applied to problems in the defense industry. Long distance target tracking – especially ballistic and tactical missiles – can be affected by astronomical or terrestrial refraction (Thomas and Joseph, 1996 and Lehn, 1997).

Many claims in archaeoastronomy – the study of the connection between the ancient structures and astronomy – are dependent on detailed knowledge of astronomical refraction. For instance, the claims of Thom (1971) that Neolithic stone monuments were used to measure the tilt of the Earth's rotational axis have been disputed through the application of astronomical refraction studies (MSc. Thesis Sampson, 1994, Schaefer and Liller, 1990). As well, the mean alignment of the Great Pyramids of Egypt with the cardinal points (Zaba, 1953 and Haack, 1984) appears to be consistent with the bisection of the angle between the summer sunrise and sunset, once differences in seasonal and diurnal astronomical refraction are included (Sampson, 1994).

1.2 Historical Background and Literature Review

1.2.1 Introduction

The long history of astronomical refraction science can be divided into three eras. The first is the empirical era, which is dated from the 1st C A.D. until end of the seventeenth century. At this time, astronomical refraction was observed and measured but lacked a coherent theory. The second is the analytical era which started with the application of the law of refraction (Snell's Law) and was characterized by a mathematical or analytical approach to the problem. At the start of the nineteenth century, primitive physical theories of the atmosphere were first included in the solutions. The current 'meteorological' era began at the start of the twentieth century, when atmospheric profiles were coupled with numerical ray tracing techniques to model astronomical refraction.

1.2.2 The Empirical Era

Possibly the earliest reference to astronomical refraction comes from the 1st C A.D. Greek mathematician Cleomedes. In his work *Circularis Inspectioinis Meteororum*, he states;

"Just as a ring in a glass of water appears to be elevated towards the rim, in the same way the sun will be seen, because of refraction, when in reality it is still below the horizon." (Mahan, 1962)¹

¹ Much of the historical outline up to the 1950's, is from Mahan's 1962 paper: *Astronomical Refraction – Some History and Theories*, *Applied Optics*, 1, 497.

The early astronomer Claudius Ptolemy of Alexandria, in the 2nd C A.D., found that the rising and setting points of celestial objects were deflected towards the north (Smith, 1996, 1999). Ptolemy correctly deduced that this deflection was caused by refraction². Ptolemy also concluded that the amount of refraction would decrease with increasing altitude, reaching zero at the zenith. However, both Cleomedes and Ptolemy believed the atmosphere to be of homogeneous density, and the interface between the air and the ether (i.e. interplanetary space) to be abrupt.

According to O'Connor and Robertson (2000), the dates of Cleomedes' work are still in disagreement by as much as a century. However, it is apparent that Cleomedes was not familiar with the work of Ptolemy. Therefore, it is highly likely that Cleomedes' treatise on refraction predates Ptolemy.

The Persian scholar, Abu Ali Hasan Ibn Al-Haitham (Alhazen) (approx. 965 – 1040) appears to have been the first to suggest that atmospheric refraction was responsible for the flattened shape of the rising or setting Sun (Mahan, 1962). Al-Haitham also deduced the height of a homogeneous atmosphere to be 89-km by noting that twilight ceases when the Sun is 19° below the horizon (Zahoor, 2000).

The first quantitative measurements of astronomical refraction have been attributed to the Danish astronomer Tycho Brahe (Mahan, 1962). In 1587, Tycho measured refraction by observing the solar transit zenith angles (the zenith angle when the Sun crosses the meridian) at the summer and winter solstices. Once again, Tycho believed the refraction occurred at a discrete interface at the top of a

² For a quantitative analysis of this rising and setting point deflection of the Sun due to astronomical refraction see Sampson (2000).

homogeneous atmosphere. Tycho was also the first to publish astronomical refraction tables in his book *Astronomiae Instrauratae Progymnasmata*. At an apparent zenith angle of 90° (i.e. the observed zenith angle which includes the effects of refraction) Tycho observed the amount of astronomical refraction to be $34'$ ($0^\circ.57$).

It was during this era that anomalous astronomical refraction was first observed. In the winter of 1597 a group of Dutch explorers were wintering on the island of Novaya Zemlya in the Russian arctic. At their latitude the Sun should have been constantly below the horizon until about February 9. On January 24, two weeks before the Sun was to reappear, one of the explorers saw the sunrise. The astronomical refraction was calculated to be more than 4° , about eight times the normal amount (Visser, 1956, Lehn 1979). The German astronomer Johannes Kepler (1571 – 1630) deduced that an internal reflection of the sunlight occurred in the atmosphere (Kepler, 1604, Visser, 1956)

Early studies into astronomical refraction were hampered by two fundamental shortcomings – an incomplete knowledge of the law of refraction and a poor understanding of the nature of the atmosphere. Ptolemy stated that the ratio of the incident and refracted angles should be constant. Johannes Kepler (1571 – 1630) later concluded that a corrective term should be added to Ptolemy's theory.

1.2.3 The Analytical Era

The first major leap forward occurred with the discovery of the geometric equation for refraction in 1621. As outlined by the Dutch mathematician Willebrord van Roijen Snell (1580 – 1626) his form of the law remained

unpublished until it appeared in Christiaan Huygen's 1690 treatise on light (Hecht, 1990). The now familiar trigonometric equation was formalized by René Descartes in 1637 (Mahan, 1962). This equation takes the form:

$$\mu_n \sin i_n = \mu_{n+1} \sin e_n. \quad (1)$$

where i_n is the incident angle, e_n is the refracted angle, μ_n is the index of refraction of the incident layer and μ_{n+1} is the index of refraction of the refracting layer (see Figure 1).

The Italian astronomer Gian Domenico Cassini (1625 – 1712) may have been the first to apply Snell's Law to astronomical refraction (Mahan, 1962). Assuming a homogeneous atmosphere of refractive index 1.000284, of height 6.82 km, with the radius of the Earth estimated to be 6377 km, Cassini computed the astronomical refraction for an object of apparent zenith angle 90° (the horizontal refraction) to be $32' 20''$ ($0^\circ.539$).

Observations of astronomical refraction at the horizon by the Royal Professor of Hydrography, Pierre Bouguer (1698 – 1758) and later by the French astronomer Pierre Charles LeMonnier (1715 – 1799) found values significantly different from those measured by Tycho Brahe (Mahan, 1962). Bourguer observed horizontal refraction as low as $22' 50''$ while LeMonnier observed horizontal refraction greater than $34'$. It was obvious from these observations that the refractive behavior of the atmosphere was more complex than had been theretofore believed.

The next major advance was the discovery of the vertical structure of the atmosphere and the subsequent development of the concentric spherical shell model. With this model, an integration of Snell's Law, coupled with the vertical

refractive index profile of the atmosphere, can be used to determine the astronomical refraction. Isaac Newton, Bouguer and Thomas Simpson (Mahan, 1962) independently derived the refraction integral. Since this integral is the foundation of most subsequent investigations, we are justified in presenting the details here (for clarity and consistency, the symbols adopted by Mahan will be used in this derivation). In Figure 1 let P_n and P_{n+1} be points along a light ray path and at the interfaces between atmospheric layers. The point O defines the centre of radius of a spherical earth and spherically concentric atmospheric layers. The sine law can be used for the triangle $O P_{n+1} P_n$ to give the equation:

$$\frac{\sin e_n}{r_{n+1}} = \frac{\sin i_{n+1}}{r_n} \quad (2)$$

where r_n is the distance from the centre of the Earth to the end of the ray at point P_n and r_{n+1} is the distance at point P_{n+1} . Equation 2 can be substituted into Equation 1 to eliminate $\sin e_n$ giving the relationship:

$$\mu_n r_n \sin i_n = \mu_{n+1} r_{n+1} \sin i_{n+1} \quad (3)$$

By extension, it follows that:

$$\mu_n r_n \sin i_n = \mu_{n+1} r_{n+1} \sin i_{n+1} = \dots = \mu_e a \sin Z, \quad (4)$$

where a is the mean radius of the Earth, and Z is the apparent zenith angle of the celestial object as seen by the observer. Therefore, from Equation 4 it is apparent that:

$$\mu r \sin i = \text{constant}, \quad (5)$$

at all points along the ray. Equation 5 can now be differentiated to give the equation:

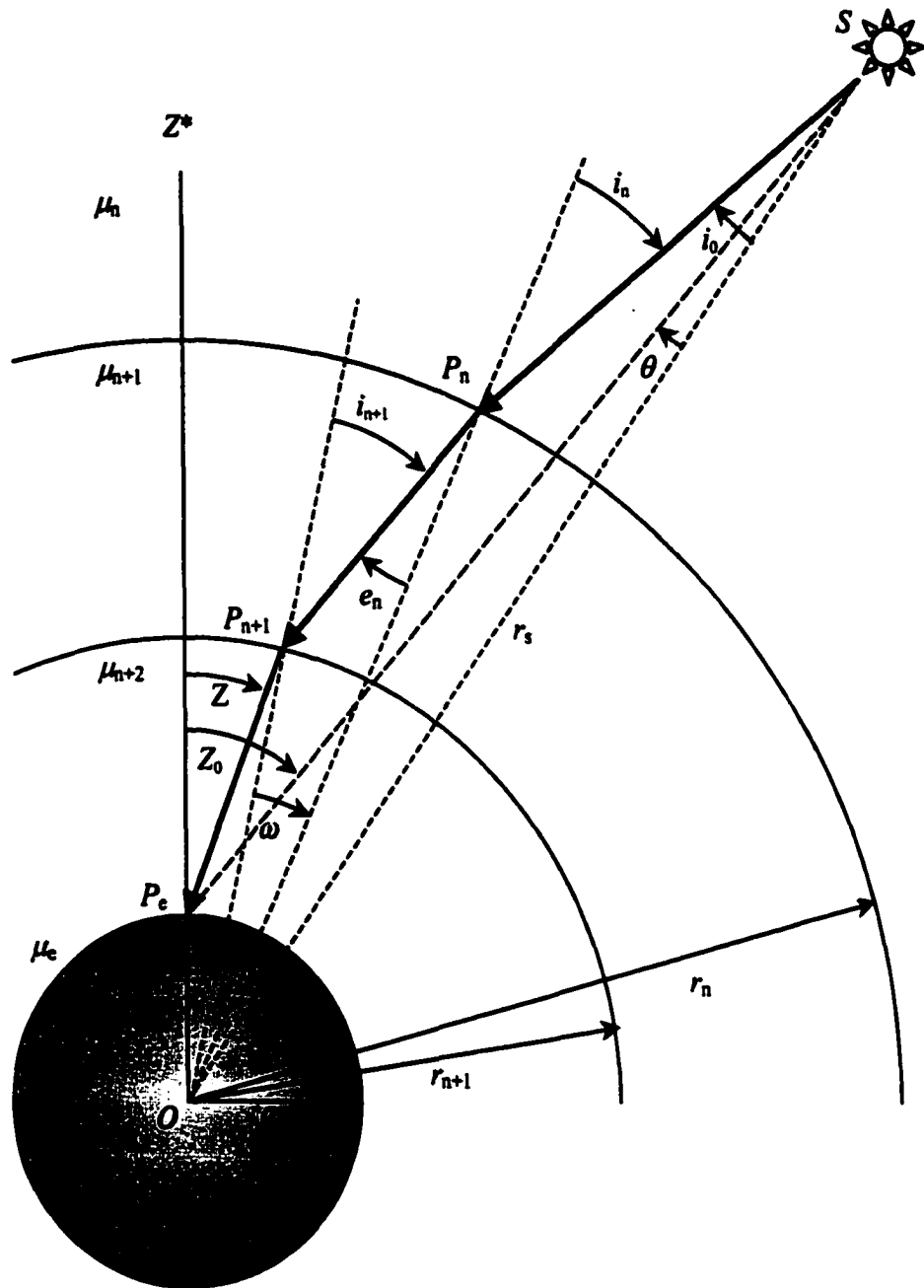


Figure 1: The concentric spherical shell model for astronomical refraction (after Mahan, 1962). P_n and P_{n+1} are points along a light ray path at the interfaces between atmospheric layers. Point O is the centre of a spherical Earth of radius a and the centre of concentric atmospheric layers of radius r_n and r_{n+1} . Angles i_n and e_n are the incident and refracted angles, angle Z is the apparent zenith angle and Z_0 is the unrefracted zenith angle. The angle ω is the angular distance traveled by the ray with respect to the centre of the Earth.

$$di = -\tan i \frac{d\mu}{\mu} - \tan i \frac{dr}{r}. \quad (6)$$

Equation 6 can now be integrated over the complete ray path to give:

$$\int_Z^i di = -\int_{\mu_e}^{\mu_s} \tan i \frac{d\mu}{\mu} - \int_a^{r_s} \tan i \frac{dr}{r}. \quad (7)$$

The last integral can be transformed using the identity (see Figure 2):

$$\tan i = \frac{rd\omega}{dr}, \quad (8)$$

to give:

$$\int_Z^i di = -\int_{\mu_e}^{\mu_s} \tan i \frac{d\mu}{\mu} - \int_0^{\omega_0} d\omega. \quad (9)$$

The first and last integrals are straightforward to evaluate. From Figure 1 it is apparent that $Z_0 = \omega_0 + \theta$. From Equation 4 it is also apparent that:

$$\tan i = \frac{\mu r \sin i}{\mu r \cos i}, \quad (10)$$

where h is the distance the observer is above the mean radius of the Earth. Using a trigonometric identity $\cos x = \sqrt{1 - \sin^2 x}$, Equation 10 becomes:

$$\tan i = \frac{\mu r \sin i}{\sqrt{\mu^2 r^2 - \mu^2 r^2 \sin^2 Z}}. \quad (11)$$

Using Equation 4, Equation 11 can be written:

$$\tan i = \frac{\mu_e a \sin Z}{\sqrt{\mu^2 r^2 - \mu_e^2 a^2 \sin^2 Z}}. \quad (12)$$

Now from Equation 9 the final general form of the integral for the refraction $R = (Z_0 - Z)$, can be written:

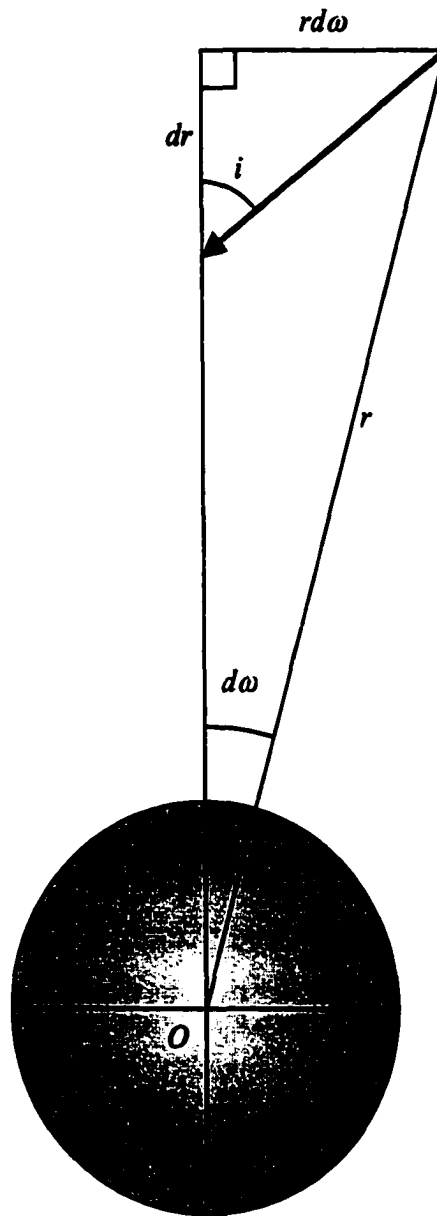


Figure 2: Optical path for identity of $\tan i$. The dark arrow represents the light ray. O is the centre of the Earth, r is the distance of the ray with respect to O , i is the incident angle, and $d\omega$ is the angular distance the ray travels with respect to O .

$$R = (Z_0 - Z) = \int_{\mu_n}^{\mu_e} \frac{\mu_e a \sin Z}{\sqrt{\mu^2 (a+h)^2 - \mu_e^2 a^2 \sin^2 Z}} \frac{d\mu}{\mu} - (i_0 - \theta), \quad (13)$$

where h is the height the observer is above the mean radius of the Earth.

For most astronomical refraction applications, the source is considered to be very distant and in a vacuum. Therefore, we assume $\mu_n = 1$ and $i_0 = \theta$ and the final term in Equation 13 disappears giving the final form of the astronomical refraction integral:

$$R = \int_1^{\mu_e} \frac{\mu_e a \sin Z}{\sqrt{\mu^2 (a+h)^2 - \mu_e^2 a^2 \sin^2 Z}} \frac{d\mu}{\mu}, \quad (14)$$

Early studies of the refraction integral involved mathematical solutions of Equation 14. It was noted by Pierre Bouguer (1698 – 1758) and Thomas Simpson (1710 – 1761) that Equation 14 resembles the integral for an arcsine³ (Mahan, 1962). The value of μ was replaced by the relationship:

$$\mu = \mu_e \left(\frac{a}{a+h} \right)^{1/(m+1)}, \quad (15)$$

where m is an empirical coefficient. Equation 15 is substituted into Equation 14 and integrated producing the relationship:

$$R = \frac{1}{m} \left[Z - \arcsin \left(\frac{\sin Z}{\mu_e^m} \right) \right]. \quad (16)$$

Assuming a constant surface refraction index of $\mu_e = 1.0002927$, a value of $m = 6.0$ in Equation 16 produces a horizontal astronomical refraction of 33' 57", while a

³ $\int \frac{dx}{\sqrt{a^2 - x^2}} = \arcsin \frac{x}{a} + C$

value of $m = 4.0$ produces $41' 35''$. Astronomers used this type of solution until the beginning of the nineteenth century.

The greatest challenge to accurate use of Equation 14 was an exact knowledge of the refractive index profile of the atmosphere. Newton assumed an isothermal atmosphere (Mahan, 1962). In the eighteenth and nineteenth centuries, instruments and methods were developed to measure the vertical structure of the atmosphere. Early thermodynamic theories applied to the problem included the Boyle-Gay-Lussac law, which assumed that the air behaved as an ideal gas, and research done by Laplace, which showed the relationship between the density of air and its index of refraction (Mahan, 1962). The French optical scientist, Jean Baptist Biot (1774 – 1862) and the director of the Paris Observatory, François Jean Dominique Arago (1786 – 1853), experimentally determined that the influence of water vapor on refraction was not significant. Further developments arose from research into the relationships between atmospheric pressure, density and temperature with height. These early model or 'standard' atmospheres were constructed by numerous researchers including; Baeyer, Bessel, Laplace, Svanberg, Bauernfeind, Euler, Gylden, Newton, Schmidt, Ivory, Kowalski, Oppolzer, Radau, Lubbock, Pizzetti, and Young (Mahan, 1962).

Barnabé Oriani (1752 – 1832), director of the Observatory of Brera in Milan, was one of the first to evaluate the refraction integral using the new atmospheric theories. Oriani expanded Equation 14 into a second order power series in terms of $\tan Z$, assuming the thickness of the atmosphere to be small compared with the radius of the Earth. Oriani also assumed that the Boyle-Gay-Lussac law was valid,

and that standard conditions prevailed.⁴ From these assumptions Oriani found the astronomical refraction in arcseconds to be (Mahan, 1962):

$$R = 60.''3826 \tan Z - 0.''00579953 \tan^3 Z. \quad (17)$$

In 1893 Lord Rayleigh (Humphreys, 1940) using a similar mathematical method but slightly different standard values (The scale height of the atmosphere $H = 7.9900$ km) found the astronomical refraction to be:

$$R = 60.''29 \tan Z - 0.''06688 \tan^3 Z. \quad (18)$$

More recently Smart (1965) determined R to be approximated by:

$$R = 58.''3 \tan Z - 0.''067 \tan^3 Z, \quad (19)$$

These formulae were found to be sufficiently accurate for zenith angles less than 70° or in the case of the Rayleigh formula 75° . This type of formula is still found in the literature. For example, Green (1985) used the Rayleigh formula while Allan (1973) used the Smart formulation.

At the start of the nineteenth century, tables compiled by James Bradley (1673 – 1762), the third Astronomer Royal, were the most commonly used source for values of astronomical refraction. Around 1805, the French mathematician Pierre-Simon Laplace (1749 – 1827) attempted to improve the refraction integral by applying a more gradual density decay to the atmosphere. In 1818, the German mathematician and astronomer Friedrich Wilhelm Bessel (1784 – 1846) developed a semi-empirical method that included local meteorological conditions. Bessel's equation for the astronomical refraction R is:

$$R = \alpha(BT)^4 \gamma^2 \tan Z, \quad (20)$$

⁴ Surface atmospheric density $\rho_e = 1.2926 \text{ kgm}^{-3}$, index of refraction $\mu_e = 1.0002927$, and the height

where α , A and λ are empirical functions of Z , B is the measured surface barometric pressure, T is a temperature correction for the barometer (expansion of the mercury column), and γ is the ambient air temperature. For values of Z greater than 85° , Bessel used the stellar positions measured by the German astronomer Friedrich Wilhelm August Argelander (1799 – 1875) to improved the formula (Mahan, 1962). It was argued that geographic variability produced significant discrepancies in the results of Equation 20. Equation 20 served as the foundation for the twentieth century Pulkovo Refraction Tables (Mahan, 1962, Pulkovo Observatory, 1930).

In 1823 the English mathematician Sir James Ivory (1765 – 1842) attempted to improve on the results of Bessel by re-evaluating the vertical density characteristics of the atmosphere. These attempts at improving Equation 20 through the modification of the density function were continued in 1828 by Schmidt⁵, and in 1867 by the Swedish astronomer Johan August Hugo Gylden (1841 – 1896). In 1882 the French astronomer Rodolphe Radau (1835 – 1911) published a comparison of the astronomical refraction derived from the Laplace, Ivory and Schmidt equations. At an apparent zenith angle of 90° , with a surface temperature of 0°C and surface pressure of 760 mmHg, the Laplace scheme produced a refraction of $35' 06''$ ($0.^\circ5850$), while Ivory's gave $36' 41''$ ($0.^\circ611$), and Schmidt $36' 48''$ ($0.^\circ613$).

Gylden later went on to produce the Pulkovo Refraction Tables, based on Bessel's Equation 20. The Pulkovo Tables were derived from the equation:

of the homogeneous atmosphere $l_e = 7.9933$ km.

⁵ Mahan does not give any biographical information on this person nor an original reference.

$$R = \alpha(BT)^4 \gamma^{\lambda} \tan Z(C \cdot D \cdot E), \quad (21)$$

where C , D and E are corrective terms for humidity, the spectral type of the star (i.e. colour), and geographic location (altitude and latitude). These tables are still in use today but are rather cumbersome to use.

All these improvements still did not incorporate the behavior of the real atmosphere, which included such features as diurnally varying vertical temperature gradients, the stratospheric temperature inversion and horizontal density gradients.

1.2.4 The Meteorological Era

The first measurements of the vertical temperature profile of the atmosphere were done in the 18th century. Between 1757 and 1759 the Russian scientist M. V. Lomonosov noted that frost layers on the mountains of Tibet and Ecuador implied a lapse rate of 6°C per kilometre. In 1788 the Swiss natural scientist Horace Benedict de Saussure (1740 –1799) spent 17 days obtaining meteorological data from a high mountain pass near Mont Blanc. From these observations De Saussure estimated the lapse rate to be 6.5°C per kilometre (Khrigian, 1970).

The first atmospheric measurements from a balloon were performed by the French physicist Jacques A. C. Charles who ascended over Paris on December 1, 1783 (Khrigian, 1970). According to the barometric pressure measured, Charles reached an altitude of 3467 metres. On September 16, 1804 the French physicist Joseph-Louis Guy-Lussac (1778 – 1850) ascended to nearly 7 kilometres. Data from this flight were used to check Laplace's theory of astronomical refraction.

Laplace determined that the observed amount of astronomical refraction would require a drop of 46° C at an altitude of 7 kilometres. Guy-Lussac measured a drop of 37° C, but his data may have been affected by radiation error since the importance of shielding the thermometer from direct sunlight had not been fully recognized (Khragian, 1970).

The French aeronaut Gaston Tissandier observed the first temperature inversion during a flight in 1873. However, at the time the meteorological community treated inversions as exceptional and unusual events (Khragian, 1970).

In the late nineteenth century American meteorologists at the Blue Hill Observatory near Boston started to use box kites to measure the vertical temperature structure of the atmosphere. On July 19, 1900 a kite launched from Blue Hill reached a record height of 4.82 kilometres (Khragian, 1970). In Europe the French meteorologist Teisserenc de Bort (1855 – 1913) began using kites in 1897 and paper balloons in 1898.

The French scientist H. Hermite first launched unmanned meteorological balloons in 1892 (Khragian, 1970). Primitive thermographs were attached to these early launches. Soon after the application of these unmanned balloons it was observed that during high altitude flights the temperature would start rising near maximum altitude. In 1902, Teisserenc De Bort and the German meteorologist Richard Assmann (1845 – 1918) announced the discovery of the stratosphere, which is described by this inversion (Khragian, 1970, Friedman, 1989). In 1927 the Soviet meteorologist Pavel A. Molchanov invented the first radiosonde, a balloon borne suite of temperature, humidity and pressure instruments (Wallace and Hobbs,

1977). As the balloon ascends the radiosonde transmits the measurements to a ground station.

In 1896 the German astronomer Julius Bauschinger (1860 – 1935) determined that a high altitude temperature inversion would have very little influence on astronomical refraction for apparent zenith angles less than 80° . At an apparent zenith angle of $87^\circ 56'$ the influence of this high altitude inversion was calculated by Bauschinger to be $16''.36$ (Mahan, 1962).

At the beginning of the twentieth century, the German mathematician Paul Harzer (1857 – 1932) pioneered the use of meteorological observations in astronomical refraction modelling. Harzer used balloon measurements of the atmosphere up to a height of 25 km. Harzer assumed the tropospheric gases were completely mixed except for water vapor. The refractive index was computed from the partial pressure for dry air and the partial pressure for water vapor. The stratosphere was assumed to be in thermal equilibrium with no water vapor present. It was also assumed that the stratosphere would be differentiated, with the heavier components settling to the bottom. With these theoretical assumptions, the refractive index was calculated to a height of 84 km. Harzer then divided the atmosphere into sixty-one optical surfaces and ray traced light from various zenith angles. Using five place logarithm tables, it took sixteen uninterrupted days to complete the tracing of one ray (Mahan, 1962). From his analysis, Harzer found a difference of $28''$ between horizontal refraction (i.e. $Z = 90^\circ$) towards the north and towards the south. It was also found that the stratosphere contributes $3' 12.7''$ of the total horizontal refraction (about 9%). Harzer continued his work by formulating

first order corrections for changes in surface pressure, temperature, water vapor, wind velocity, wavelength, time of year and time of day.

In 1931 F. Wunschmann explored the effects of optical surface deformation on the Harzer model. The ray tracing results were then compared with the concentric shell model. Wunschmann found a maximum deviation of only $-0.027''$ for apparent zenith angles of 80° . Wunschmann concluded that for the atmosphere over Kiel, the concentric spherical shell model appeared to be quite adequate.

During the Second World War the need for better weather forecasts resulted in a dramatic increase in meteorological data. The Yale astronomer, Boris Garfinkel continued to refine the mathematical description of the atmospheric profile (1944). Garfinkel employed the refraction theory developed originally by Radau in 1889. His model was extended to apparent zenith angles up to 116° . Corrections due to station pressure, temperature, height and surface vertical temperature gradient were added. However, the output was not tested against actual refraction observations.

In 1948 the Japanese astronomer Chikara Sugawa of the International Latitude Observatory of Mizusawa used 323 radiosonde measurements over Sendai Japan to calculate the refractive index profile. Sugawa based his numerical integration technique on the work by astronomer Yusuke Hagiwara (1936) of the Astronomical Institute of the Imperial University of Tokyo. Sugawa found the astronomical refraction was consistently less than the values of Radau. Sugawa applied a maximum apparent zenith angle of 85° and found the difference from Radau ranged from $-27.4''$ to $-66.0''$. Sugawa's results also suggested a seasonal variation in the astronomical refraction (Sugawa, 1955). The minimum occurred in

the summer (At $Z = 85^\circ$, June: 08' 34".09) and maximum in the winter (At $Z = 85^\circ$, December: 09' 40".68).

Actual in situ measurements of the refractive index of the atmosphere have been few. In the summer of 1952 Arthur S. G. Grant working for the Geodetic Survey of Canada measured 151 radio wave refractive index profiles of the atmosphere over the Northwest Territories, eastern Quebec and southern Labrador (Grant, 1954). Grant used aircraft soundings from approximately 100 to 600-m above the surface – depending on cloud conditions – to between 4600 and 6100-m. Measurements were taken at 300-m intervals. Grant observed significant change in the radio-refraction index profile during a synoptic scale frontal passage. It was also observed that in the lower 1800-m of the sampled atmospheres the radio-refraction index displayed more variability by an order of magnitude.

In the 1960's Garfinkel employed the 1962 U.S. Standard Atmosphere within a FORTRAN routine based on his 1944 model (Garfinkel, 1967). Garfinkel used a piecewise linear representation of the atmosphere based on the U.S. Standard Atmosphere. The geophysical constants (i.e. the radius of the Earth, standard sea level index of refraction, etc.) were also revised from his 1944 model. The model output was not compared with observed refraction.

Fraser (1975) suggested that certain refraction phenomena like the green flash might be due to atmospheric gravity waves. Atmospheric gravity waves only occur under stable stratification – for example during an inversion. Under these conditions a vertically displaced parcel of air will experience restorative forcing, thus producing an oscillation (Holton, 1979). Since the atmosphere is no longer spherically concentric, Fraser showed that light originating from the same point on

the Sun can take more than one path to the observer. Fraser developed a theorem proving this conjecture but did not attempt to model the effect. The conjecture suggested that gravity waves could also explain the Chinese Lantern effect – when grooves appear symmetrically on both flanks of the rising or setting Sun. Waldemar Lehn, of the University of Manitoba along with Wayne Silvester and David Fraser incorporated this conjecture in their modelling of terrestrial refraction mirages (Lehn, et al, 1994). As Fraser had predicted, Lehn's terrestrial refraction ray-tracing model produced multiple image mirages, including horizontal banding. Lehn tested their model by attempting to reproduce a mirage observed near Tuktoyaktuk in the Canadian Arctic. The mirage features produced by the model were similar to those observed on the same peak.

Lehn and El-Arini (1978) pioneered the use of computer graphics to model atmospheric refraction and simulate actual terrestrial mirages. Lehn also investigated the replacement of standard circular curvature of the ray increments with parabolic arcs. (Lehn, 1985). This was done to better map the ray path over the curved surface of the Earth. Although Lehn's interests were mainly in terrestrial refraction, he did investigate the anomalous astronomical refraction observed by the 1597 Willem Barentz expedition on the island of Novaya Zemlya (Lehn, 1979).

J. Saastamoinen (1979) used an extensive binomial expansion to represent the refraction integral. The scheme was extended to zenith angles up to 90° by inserting a damping factor into the binomial formula and truncating the expansion at a "proper point". The atmosphere was divided into two spherically concentric layers – the troposphere and stratosphere. Each layer had a constant temperature gradient.

The Finnish astronomer Seppo Mikkola of the University of Turku may have been the first to use continuous fractions to represent the refraction integral (Mikkola, 1979). Hao-jian Yan of the Shanghai Observatory appears to have independently rediscovered the continuous fraction expansion for astronomical refraction (Yan, 1996). Yan developed his scheme for a standard atmosphere, based on the U.S. Standard Atmosphere. The uncertainty in the model was determined by finding the range of results produced by the expected range in atmospheric conditions. Once again, no attempt was made to compare the results with actual refraction measurements.

The Russian astronomer A.Yu Yatsenko of the Engelhard Astronomical Observatory has produced a refraction model based on a meridional-latitudinal model of the atmosphere (Yatsenko, 1995). This is possibly the most comprehensive and complex refraction model to date. The model can accommodate optical surfaces of arbitrary configuration. Yatsenko inserted three-dimensional atmospheric data from the 1975 Atlas of Climate Characteristics (Issue 3, Part 2) published by the Hidrometeoizdat of Moscow. From this model Yatsenko found the astronomical refraction varied with azimuth for a hypothetical observer in the city of Kazan. At an apparent zenith angle of 70° and surface temperature of -14°C and pressure of 1020.0 hPa, the maximum azimuthal variation in vertical astronomical refraction was found to be $0''.068$ at 0° and 120° azimuth. The lateral refraction was found to vary from $0''.019$ at an azimuth of 0° to $-0''.026$ at an azimuth of 180° . The model varied from the more traditional concentric spherical shell model by no more than $0''.01$ at apparent zenith distances of 80° or less. The computational time necessary to run the model was relatively

extreme, taking 90 minutes to compute one value of refraction at an apparent zenith angle of 70° on an IBM PC-AT/386 DX25 (25MHz clock speed)⁶.

Michael Thomas and Richard Joseph of the Johns Hopkins Applied Physics Laboratory applied a Gauss-Chebyshev quadrature numerical integration to the standard refraction integral (Thomas and Joseph, 1996). From this scheme Thomas and Joseph simulated the setting Sun using surface temperatures, a troposphere with a constant gradient of -8K/km and an isothermal stratosphere. Comparisons were made between photographed sunset images and simulated solar rim produced by the numerical integration. However, only the shape of the high zenith angle solar rim was compared since no zenith angle measurements were made. It appears the purpose of this work was to support infrared target search and tracking technology in anti-missile defense research.

Ronald C. Stone of the U.S. Naval Observatory in Flagstaff Arizona modified Oriani's tangent power series expansion of the refraction integral (Stone, 1996). Stone compared his results with the Pulkovo refraction tables and found a difference of less than $0''.01$ for apparent zenith angles of less than 65° . At a zenith angle of 85° the difference increased sharply and ranged from $-28''.5$ to $-25''.1$ depending on the surface temperature chosen.

⁶ The ray-tracing model outlined in the next chapter ran on a Pentium II 350 MHz processor. According to Intel's web site (<http://www.intel.com/intel/museum/25anniv/hof/moore.htm>), the 386 processor is about 50 times slower. It took the ray tracing model 27 seconds to complete a full solar disc at a zenith angle of about 70° . At an apparent zenith angle of about $85^\circ.7$ the model takes 61 seconds due to the increase in the optical path length and the greater uncertainty in the initial ray angle. Each solar disc is comprised of 180 points. Therefore, the Pentium II processor will require approximately 13 hours of processing time with this model. Even with an order of magnitude increase in processing speed the computation time is still relatively lengthy. It should be noted that the current ray-tracing algorithm contains a total of 3 cosines at about 100 clock cycles each, 20 divisions at 41 each and 161 additions, subtractions and multiplications at 5 clock cycles each (Brockington, 2000). If the current model uses 10^4 layers and requires three iterations to produce

Using his previous mathematical scheme Hao-jian Yan (Yan, 1996) compared the results produced by a standard atmosphere model with those from radiosondes measurements (Yan, 1998). The radiosondes were launched from West Palm Beach, Florida between February 10 and 14, 1990. Yan found the greatest discrepancy produced by the two atmospheres appeared at the highest zenith angles. At a zenith angle of $87^{\circ}.5$ the difference between the two ranged from about $-0^{\circ}.7$ to $-2^{\circ}.8$. Although not mentioned in the paper, the time and geographic location of the sounding launches (11:15 and 23:15 UTC) were coincidental with the times of local sunrise (11:58 to 12:01 UTC) and sunset (23:10 to 23:13 UTC). This author also noted that the greatest discrepancy between Yan's standard atmosphere and radiosonde refraction results appears during the sunrise events.

The related study of mirages of the Sun and Moon and the famous green flash have also spawned a lengthy scientific and literary history (Minnaert, 1993, O'Connell, 1958). Although it is slightly beyond the scope of this investigation, much work has been done to simulate the appearance of sunset mirages and the green flash (Bruton 1996, Young et al, 1997, Young, 1999). Bruton and Young successfully recreated the general appearance of the green flash and certain solar mirages, however no effort was made to simulate specific events using measured temperature profiles.

each successful ray trace, then the model should take about 30 seconds to complete a solar outline if the processor is dedicated to the task.

1.2.5 Modern Observations of High Zenith Angle Astronomical Refraction

In the bulk of the literature it is apparent that many of these models have never been tested against actual refraction measurements at apparent zenith angles approaching 90° .

In the early 1950's G. M. Clemence of the U. S. Naval Observatory, compiled a statistical study of observed astronomical refraction of the high zenith angle Sun (Clemence, 1951). Clemence received 315 sextant observations from navigators aboard 33 ocean going vessels. The measured refraction was then compared with the Garfinkel model. At an apparent zenith angle of $89^\circ 45'$ the mean deviation was $-0'.7$. However, at this zenith angle the probable error of a single observation was estimated to be $2'.1$. One observation at this zenith angle showed a deviation from Garfinkel's model by $12'$.

One of the few modern attempts to measure astronomical refraction at very high apparent zenith angles was conducted by Bradley Schaefer of the Goddard Space Flight Center and William Liller of the Instituto Isaac Newton (Schaefer and Liller, 1990). The researchers measured astronomical refraction of the setting Sun and Moon. A total of 144 measurements were made from various locations. The averaged amount of astronomical refraction near the horizon was found to be $0^\circ.551$. This is in close agreement with the values found in the twentieth century literature. Frequently cited values for horizontal refraction (i.e. refraction at an apparent zenith angle of 90°) under standard atmospheric conditions are $0^\circ.590$ (Allan, 1973), $0^\circ.583$ (Humphreys, 1940) and $0^\circ.567$ (Green, 1985, Meeus, 1988). The astronomical refraction was also found to be highly variable with a RMS deviation of $0^\circ.16$ and a range from $0^\circ.234$ to $1^\circ.678$, although no compensation

was made for terrestrial refraction of the horizon. Schaefer and Liller applied their results to such topics, as the time of sunrise and sunset, solar eclipses near the horizon, and archaeoastronomy.

The author has done additional work in this area (Sampson, 1991, Sampson, 1994, Sampson, 1997). From 244 sunrise and 125 sunset observations from Edmonton, the mean astronomical refraction for all observations was found to be $0^{\circ}.669$. This was considerably larger than Schaefer's and the more commonly cited values. However, the mean for sunrise events was $0^{\circ}.714$, while the mean for sunset events was $0^{\circ}.579$ – much closer to the accepted value. From this analysis it appeared that the standard horizontal refraction values were assumed to be for sunset conditions. These observations also confirmed Schaefer's findings of high variability in the astronomical refraction at sunrise and sunset.

The author also observed the seasonal differences in astronomical refraction predicted by Sugawa (1955). There was an obvious increase in the amount of refraction in the colder months. However, this trend was observed to be more obvious for sunsets than sunrises (see Table 1).

	May – Aug.	Nov. – Feb.
Sunrise refraction	0.708 (43)	0.763 (95)
Sunset refraction	0.510 (23)	0.699 (30)
Population Standard Deviation (sunrise)	0.11	0.20
Population Standard Deviation (sunset)	0.027	0.10

Table 1: Seasonal difference in astronomical refraction of the rising and setting Sun as observed from Edmonton. Numbers in parentheses are the total number of observations.

The astronomer L. Györi of the Heliophysical Observatory of the Hungarian Academy of Science measured differential astronomical refraction by imaging the solar disc (Györi, 1993). This is the difference in refraction from one point to another on the observed celestial sphere. The most visually obvious effect of differential refraction is the apparent flattening of the solar or lunar disc at large zenith angles. Györi found that the mean of the measurements was in good agreement with values determined by the U.S. Naval Observatory's Almanac for Computers. However, Györi also found that individual cases showed significant deviation – up to a maximum of about ± 1 arcminute for true zenith angles between 82° and 89° . For the same range in zenith distance, the mean deviation was $-3''.6$ and the RMS deviation was $22''.9$.

From all these observations it is apparent that the mean of a number of sunset measurements appears to approach the published values found in tables or from the standard empirical formulae. However, the prediction of individual cases of high zenith angle astronomical refraction still appears to present a challenge and has been generally ignored. In the next section a ray-tracing model will be described and then employed in an attempt to reproduce the high zenith angle astronomical refraction photogrammetrically measured from a series of observed sunsets.

1.3 A Summary of Astronomical Refraction

The following somewhat qualitative argument will help illustrate why much of the variation in astronomical refraction is controlled by the vertical temperature gradient in the boundary layer. The strong relationship between the surface vertical temperature gradient and the amount of refraction can be illustrated through geometric optics and basic thermodynamics.

Snell's law states that the angle of refraction r is a function of the ratio of the index of refraction of the refracting medium n_r to the index of refraction of the incident medium n_i , namely:

$$r = \sin^{-1}\left(\frac{n_i \sin i}{n_r}\right). \quad (22)$$

The greater the ratio between the indices of refraction for the two media, the greater the difference between the incidence angle and the refraction angle.

Snell's Law is non-linear in the sense that the angle of refraction does not increase linearly with the angle of incidence. In the refraction model used in this study, the atmosphere is divided into many thin layers. The difference in refractive index between successive layers is very small. Assuming a very small difference between the two indices of refraction, the relationship between the incident and refracted angle appears almost linear for low incidence angles (i.e. low zenith angles of the Sun). However, just before reaching the critical angle where total reflection occurs, the angle of refraction increases sharply. (see Figure 3).

The index of refraction n is a function of the density of the medium. From Cidor (1996):

$$n - 1 = (\rho_a / \rho_{axs})(n_{axs} - 1) + (\rho_w / \rho_{ws})(n_{ws} - 1), \quad (23)$$

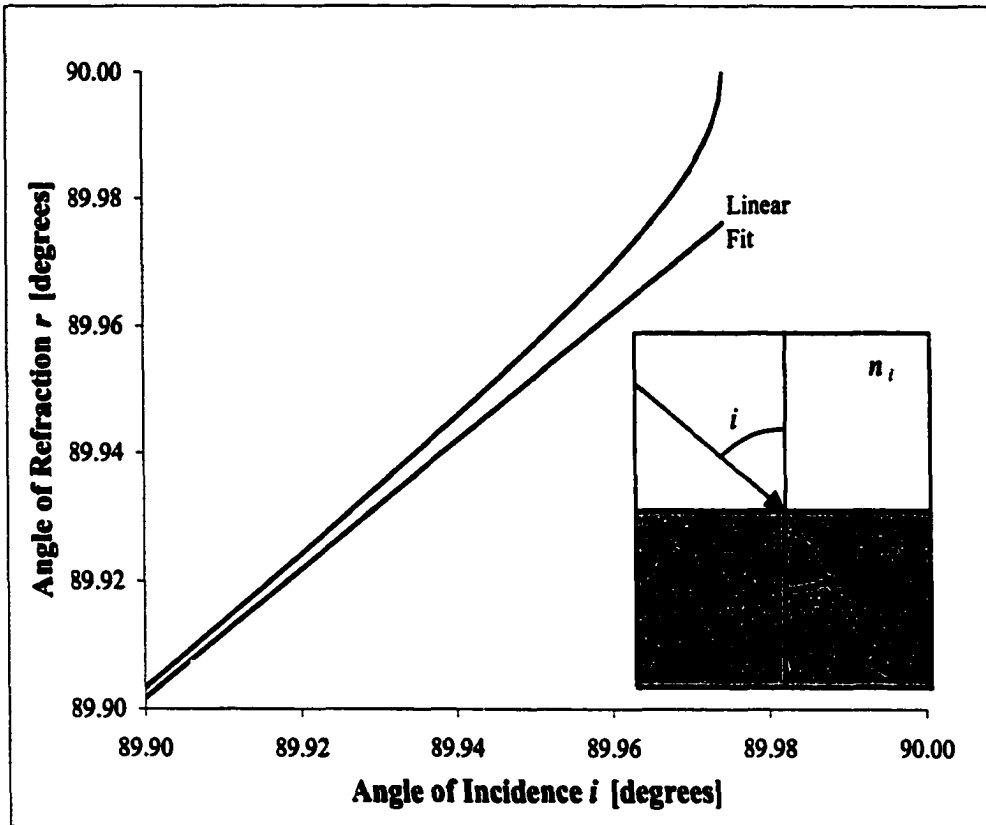


Figure 3: The non-linear behavior of Snell's Law at high refraction angles. The refractive indices are 1.0002766 for n_i , for the incident layer ($\lambda = 580$ nm, $T = 15^\circ$ C, $p = 1013.25$ hPa)(CRC Handbook, 1974), and 1.0002767 for n_r , in the refracted layer. At the maximum angle of refraction (i.e. at the critical angle of $89^\circ.9744$) total internal reflection occurs. The straight line is from a linear fit of the section of the curve from 0° to $89^\circ.90$.

where ρ_{std} is the density of dry air under standard conditions (15° C, 1013.25 hPa, 0% R.H. and 450 ppm of CO₂), ρ_a is the density of the dry air under the observed conditions, n_{std} is the index of refraction of dry air for a particular wavelength under standard conditions, ρ_{ws} is the density of pure water vapor under standard temperature and pressure, ρ_w is the density of vapor under observed conditions and n_{ws} is the index of refraction of pure water vapor for a particular wavelength under standard conditions.

For a given medium the greater the density the greater the index of refraction.

The density of the air ρ is determined by:

$$\rho = \frac{p}{R_a T}, \quad (24)$$

where T is the temperature [K], p is the pressure [Pa] R_a is the specific gas constant for air and given by the formula $R_a = R_d (1 + 0.61q)$, where R_d is the gas constant for dry air and q is the mixing ratio which is equal to the ratio of the mass of the water vapor and the mass of dry air in a given volume of air.

The vertical density profile and vertical density gradient profile of the atmospheres measured in this study can be seen in Figures 4 through 9. The gradients for the U.S. Standard Atmosphere are also shown for comparison. It is apparent from these graphs that the mean density gradient is steepest near the surface. The source of the fine scale variability is explored in Section 5.

The amount of refraction in Snell's law is determined by the ratio of the two refraction indices. Therefore, it is the ratio between the densities of the successive

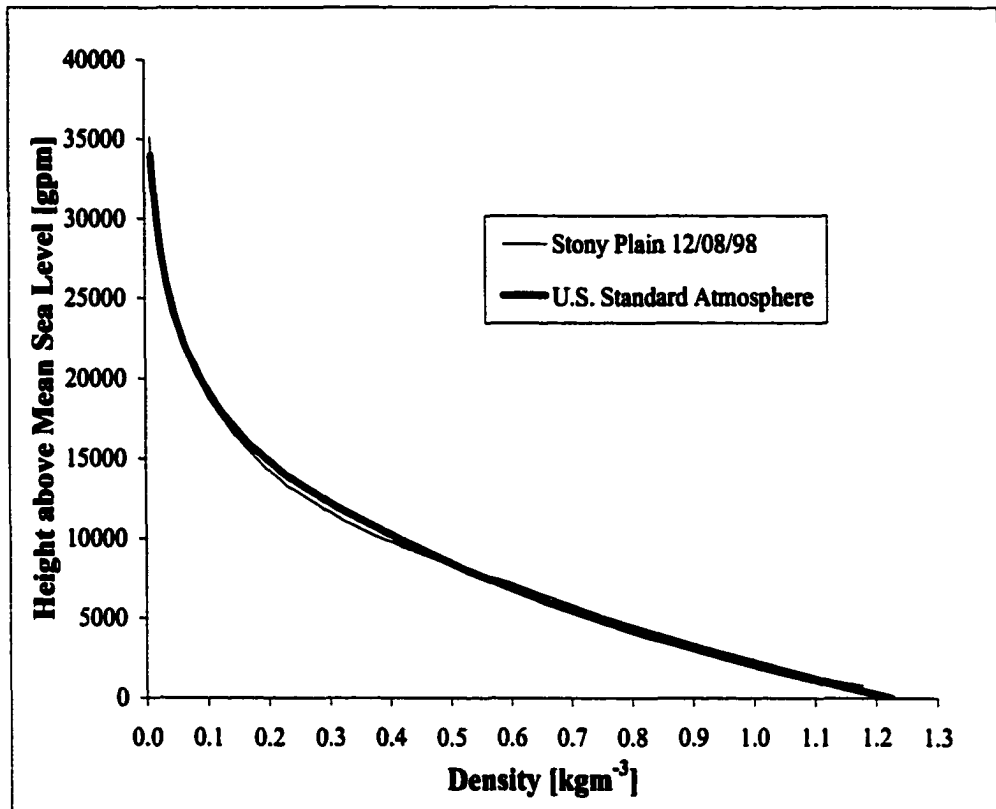


Figure 4: Density profile for December 8, 1998, 23:15 UTC sounding. U.S. Standard Atmosphere is shown for comparison. Elevation of Stony Plain Upper Air station 766 metres above mean sea level.

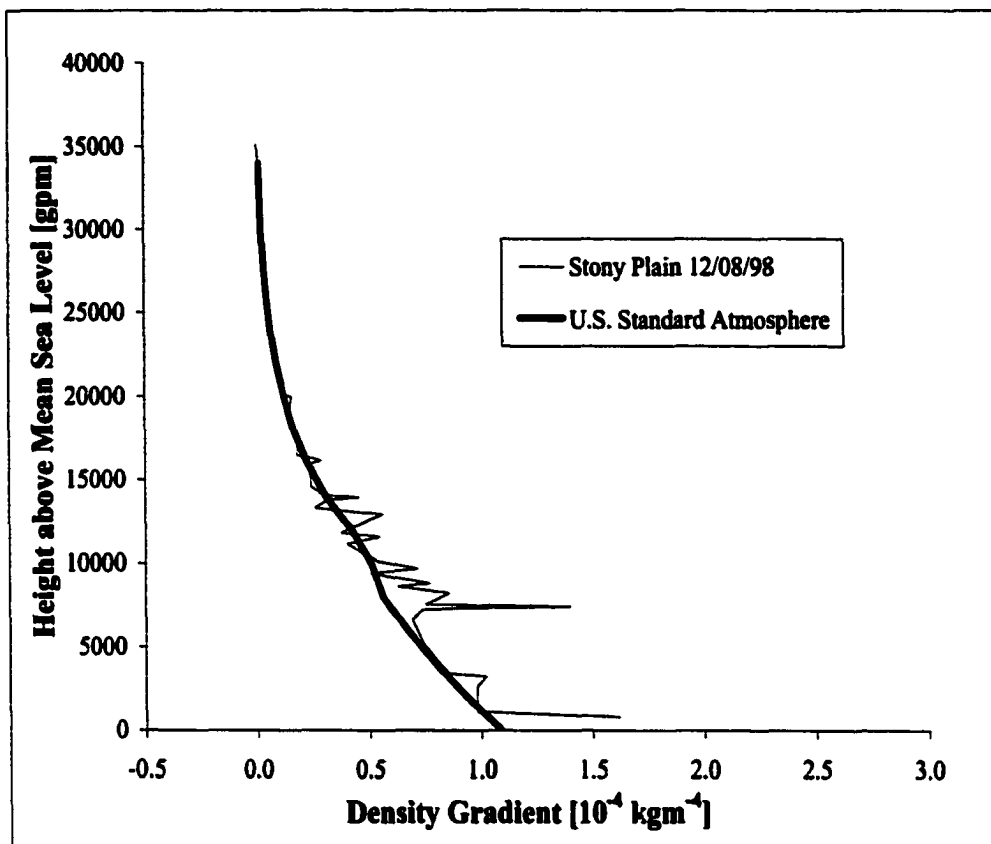


Figure 5: Observed density gradient profile for the Stony Plain, Alberta, December 8, 1998, 23:15 UTC sounding compared to the U.S. Standard Atmosphere. Meteorological data collected with a VIZ rawinsonde system. Altitude of Stony Plain Upper Air station is 766 metres above mean sea level.

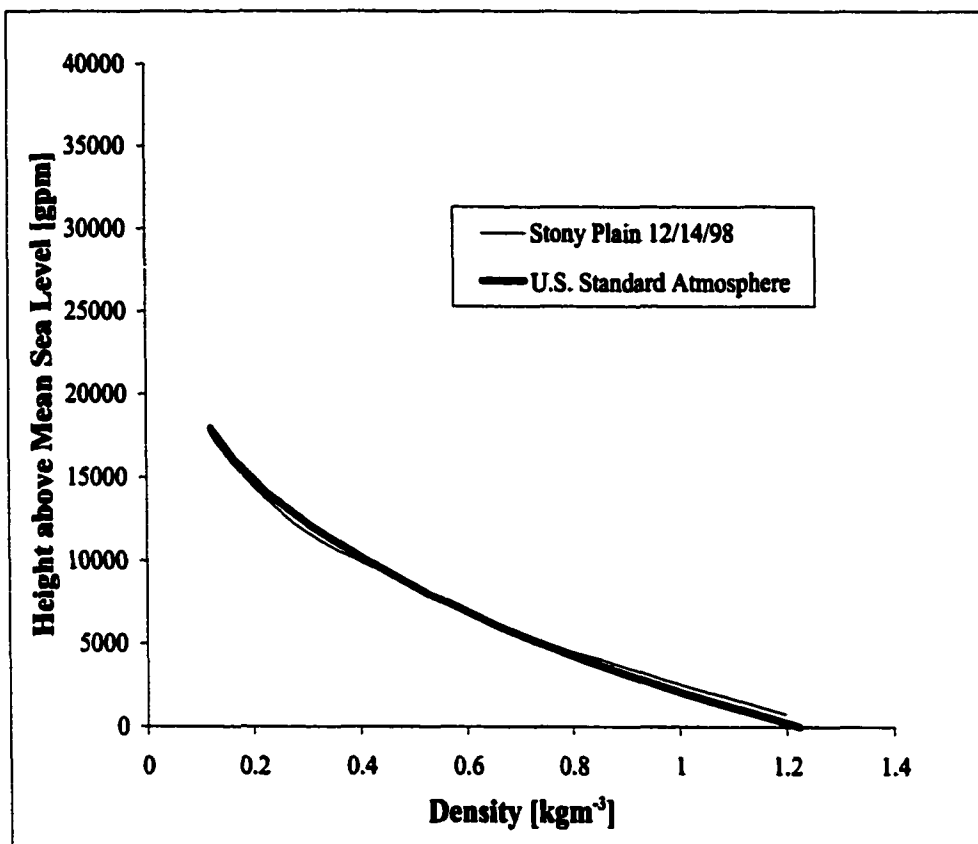


Figure 6: The density profile for December 14, 1998, 23:15 UTC sounding. The U.S. Standard Atmosphere is shown for comparison.

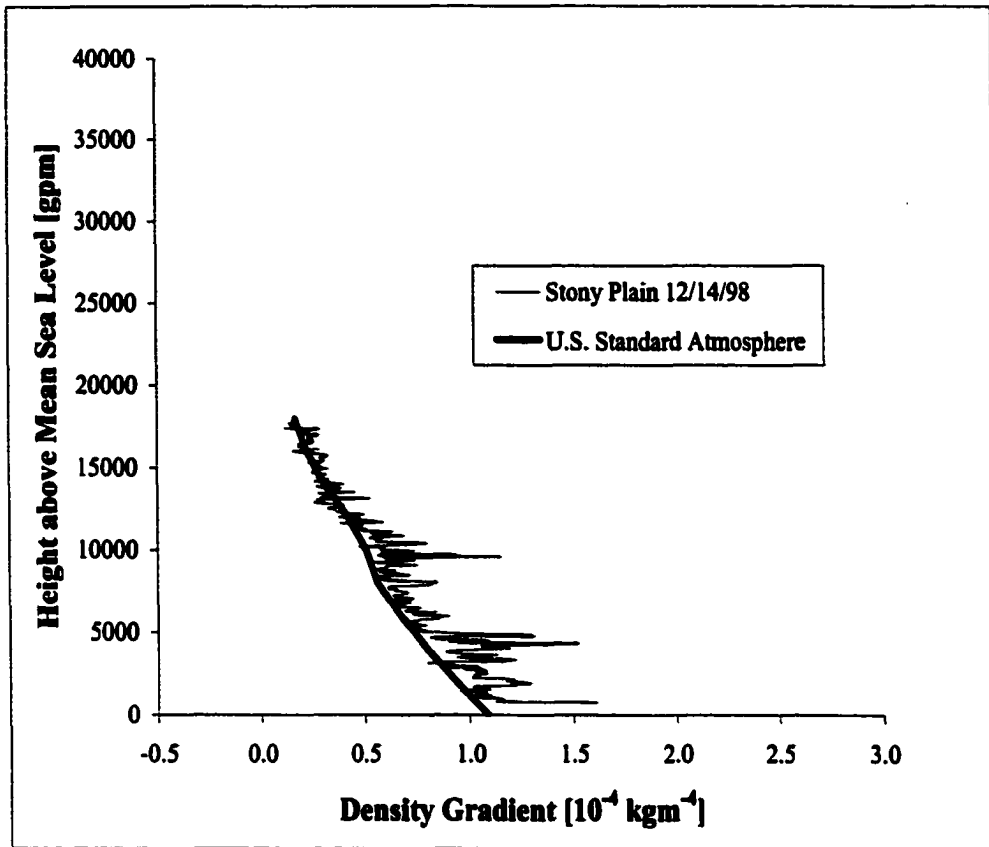


Figure 7: Density gradient profile for the December 14, 1998, 23:15 UTC sounding from Stony Plain Upper Air station (766 metres above mean sea level). U.S. Standard Atmosphere is shown for comparison. Data for the observed profile was collected using a Vaisala RS80 rawinsonde system which samples every 10 seconds. On this day the balloon appears to have burst prematurely.

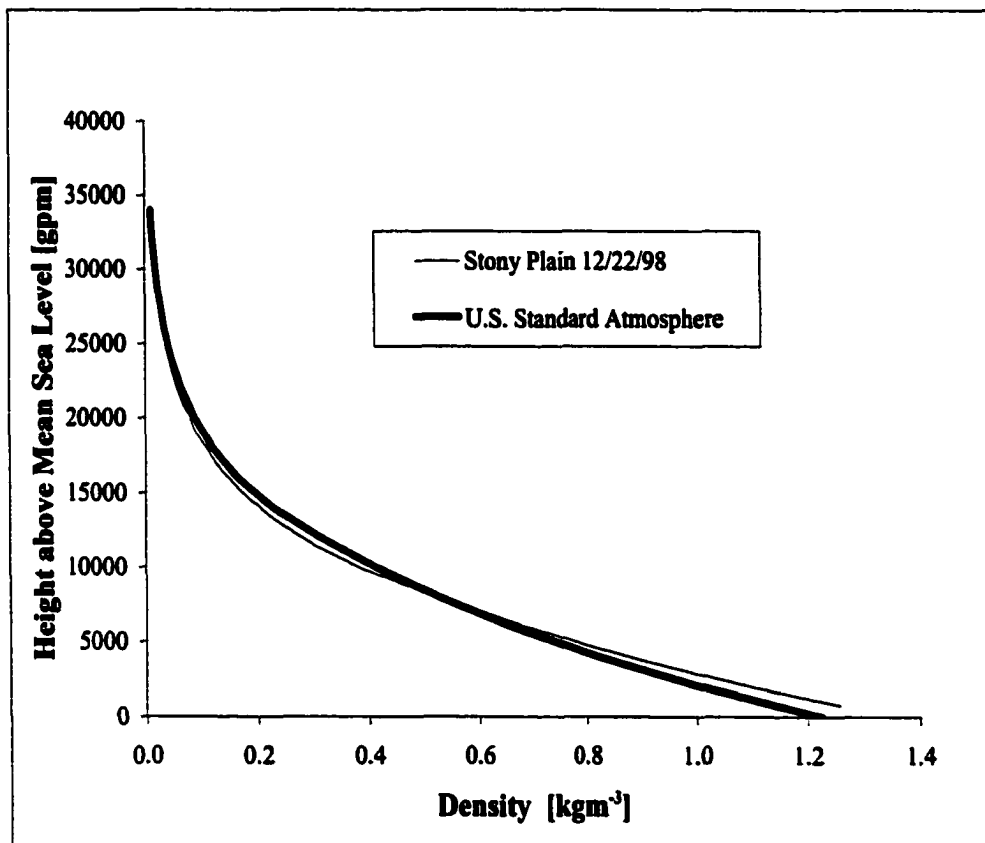


Figure 8: Density profile for December 22, 1998 sounding from Stony Plain Upper Air station (766 metres above mean sea level). U.S. Standard Atmosphere is shown for comparison.

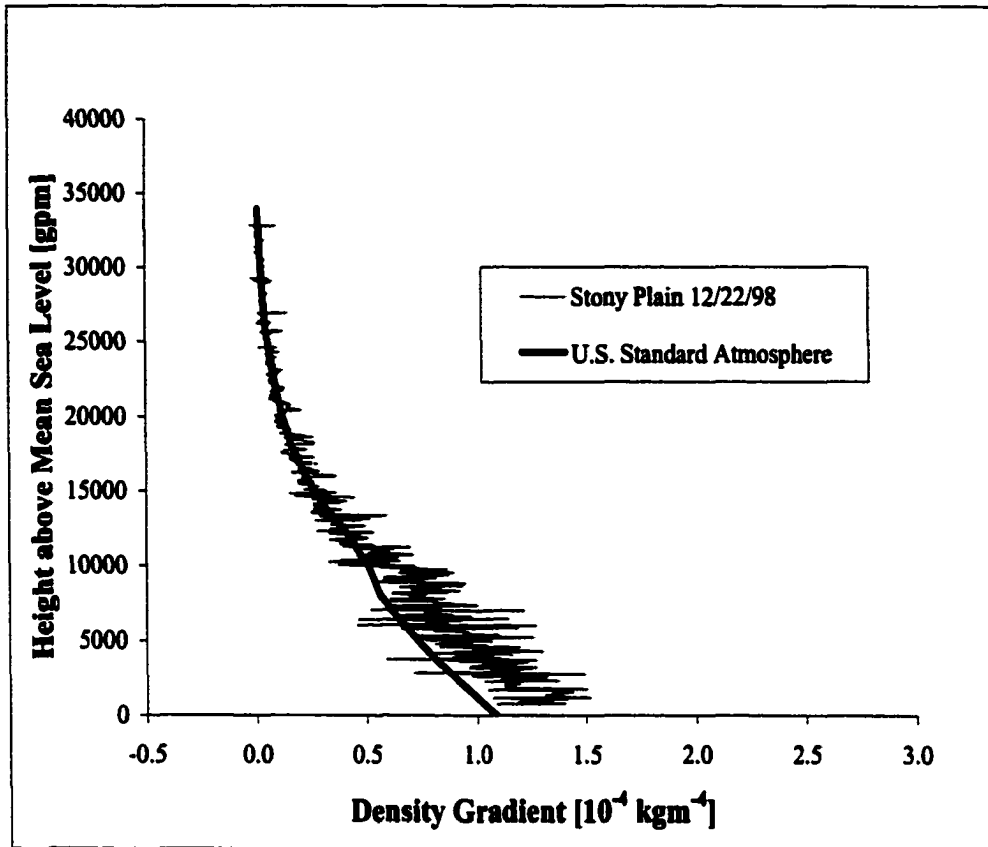


Figure 9: Density gradient profile for December 22, 1998 sounding from Stony Plain Upper Air station (766 metres above mean sea level). U.S. Standard Atmosphere is shown for comparison.

layers, rather than the absolute density of a particular layer that determines the amount of refraction (i.e. the difference between the incident and refracted angles).

Even without refraction, the angle the descending incident ray makes with the constant altitude surfaces of a spherically symmetric atmosphere increases during its descent to its minimum altitude. At sunrise and sunset, the angle of incidence (again without refraction) is 90° at the observer. This unrefracted incidence angle i' can be calculated from the trigonometric formula

$$\sin i' = \frac{r_e}{r_e + z}, \quad (25)$$

where r_e is the mean radius of the Earth, and z is the height of the ray above the mean surface of a spherical Earth (see Figure 10). A plot of this unrefracted incidence angle with respect to height above the surface can be seen in Figure 10.

In the boundary layer of the Earth's atmosphere, the variations in the vertical density gradient are controlled, for the most part, by the variations in the vertical temperature gradient. This is due to the fact that the vertical pressure gradient is nearly constant, while the vertical temperature gradient can vary considerably. For example, it is impossible for the hydrostatic pressure to increase with altitude, while it is very common for the temperature to either sharply increase or sharply decrease just above the surface.

To help illustrate this in a more quantitative fashion, one can compare the changes in density produced by the typical changes in vertical pressure gradient versus the typical changes in the vertical temperature gradient. Using the chain rule Equation 24 can be differentiated with respect to height to produce the formula

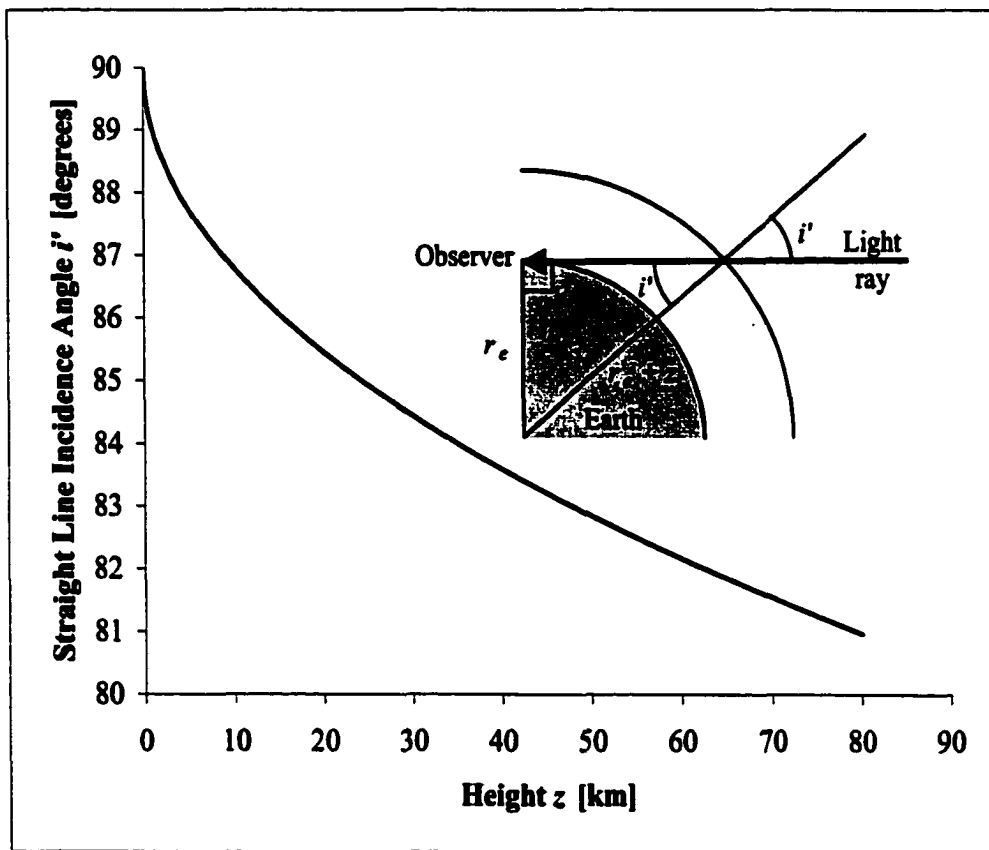


Figure 10: Straight line incidence angle of a line tangent to the surface of the Earth.

$$\Delta \frac{d\rho}{dz} = \Delta \frac{1}{R_a T} \frac{dp}{dz} - \Delta \frac{p}{R_a T^2} \frac{dT}{dz}. \quad (26)$$

Equation 26 is now evaluated assuming $dp/dz = 0$ or $dT/dz = 0$.

First, consider an isothermal atmosphere ($dT/dz = 0$). The pressure p as a function of altitude z may be determined from the hydrostatic equation for an isothermal atmosphere:

$$p = p_0 e^{\frac{-gz}{R_a T}}, \quad (27)$$

where g is the gravitational acceleration, R_a is the gas constant (for simplicity $R_a = R_d$), and T is the temperature. The density, as a function of height, may be determined from Equation 24 with $R_a = R_d$. The temperature range for Edmonton was assumed to be approximately 233 to 303 K (-40 to 30° C). Assuming an isothermal atmosphere of temperature 233 or 303 K, the difference between the two vertical density gradients at $z = 760$ m (Stony Plain) was found to be $7.8 \times 10^{-5} \text{ kgm}^{-4}$.

At Stony Plain, the surface vertical temperature gradient has been observed to vary from $-0.0369 \text{ K}\cdot\text{m}^{-1}$ (superadiabatic) to $0.1818 \text{ K}\cdot\text{m}^{-1}$ (inversion) between the surface to the first sounding level (Sampson, 1994). Assuming an isobaric atmosphere, the difference in the density gradient between these two extreme temperature profiles was found to be $9.8 \times 10^{-4} \text{ kgm}^{-4}$, twelve times that produced by the expected changes in pressure. Since the index of refraction is a function of the density, and the difference between the incidence angle and the refracted angle is a function of the ratio of the two refractive indices, it follows that the temperature profile of the atmosphere is the dominant factor in astronomical refraction.

In summary, the incidence angle and the ratio of the two refraction indices control the amount of refraction. The unrefracted incidence angle increases with proximity to the surface and, according to Snell's Law the refracted angle also increases with increasing incidence angle. Since the density gradient increases with proximity to the surface and since the refractive index is a function of density, it follows that the refractive index gradient should also increase with proximity to the surface. Finally the density gradient is controlled mainly by the temperature gradient. From this argument, it is apparent that the surface layer temperature gradient should have the greatest control over the amount of sunrise and sunset refraction. Further studies into this relationship are covered in Appendix H.

2. The Astronomical Refraction Model

2.1 Introduction to the Model

The historical background and fundamental behavior of astronomical refraction has now been outlined. The motivation of the following experiment was to compare an astronomical refraction model with the observed apparent positions of the setting Sun, and therefore to test the accuracy of a ray tracing astronomical refraction model. The following refraction model was chosen because it uses the fundamental geometrical optics rather than empirical or semi-analytical solutions to the refraction integral. It was also the goal of the experiment to explore the use of observed atmospheric profiles produced by rawinsondes rather than a standard atmosphere. Therefore, a ray-tracing solution was considered the most appropriate strategy.

The model chosen is a time-reversed ray-tracing scheme. Therefore the rays originate from the observer and are aimed towards the Sun. The model takes an initial guess as to the amount of refraction. The atmosphere is divided into layers determined by the end point of the incremental ray path. The index of refraction is calculated for each layer from the temperature, pressure and humidity measured from the rawinsonde. When the ray leaves the atmosphere, the final trajectory of the ray is compared with the position of the Sun. The miss angle is computed and if necessary, a new ray is sent from the observer with an adjustment to the initial angle determined from the amount of this miss angle. The routine is repeated until the miss angle is less than $0'.1$. The process is repeated until a full image of the Sun at a given wavelength is constructed. Another visible wavelength is chosen and the entire process is repeated.

The modelled solar image in three wavelengths (red, yellow and green) is then plotted against the observed position of the Sun and the geometric (unrefracted) Sun.

2.2 Construction of the Model

The initial input values of the model constructed for this experiment were the date, time, and geographical co-ordinates of the location where the images of the Sun were obtained. A celestial mechanics subroutine calculates the celestial co-ordinates of the Sun (RA and dec.) and its semi-diameter. The geographic co-ordinates are then used to determine the altitude and the azimuth of the centre of the Sun (Meeus, 1988). The accuracy of the astronomical subroutine was then

compared with values at 00:00 UTC published in the *Astronomical Ephemeris* (U.S.N.O. 1999) and was found to be in agreement to within $\pm 0''.1$ in right ascension and $\pm 0''.3$ in declination.

An array of radially symmetric points defining the solar disk is then computed. In this model the image of the setting or rising Sun is assumed to be symmetrical about a vertical axis. Therefore, it was necessary only to find the refraction of a series of points along half the circumference of the Sun. The perimeter of the disk is divided into increments of 1° .

The fine scale atmospheric sounding file ($\Delta z \sim 50$ m) for the date chosen is then read and all temperature and pressure values are converted to SI units. The humidity is converted to fractional units.

A ray-travel increment $\delta\theta = 0^\circ.001$ was selected to minimize the computation time and maximize the accuracy (see Section 4.1 for details on the selection of this value). This is the angular distance, with respect to the centre of the Earth, which the light ray travels through a layer of the atmosphere of constant density (see Figure 11). At mean sea level this increment translates to a distance of about 111 metres along the surface of the Earth.

The thickness of the first atmospheric layer Δr_1 is found from the sine law (see Figure 11)

$$\Delta r_1 = r_e \left[\frac{\cos \beta_0}{\cos(\beta_0 + \delta\theta)} - 1 \right], \quad (28)$$

where β_0 is the initial elevation angle of the light ray at the observer, and r_e is the radius of the Earth at point O .

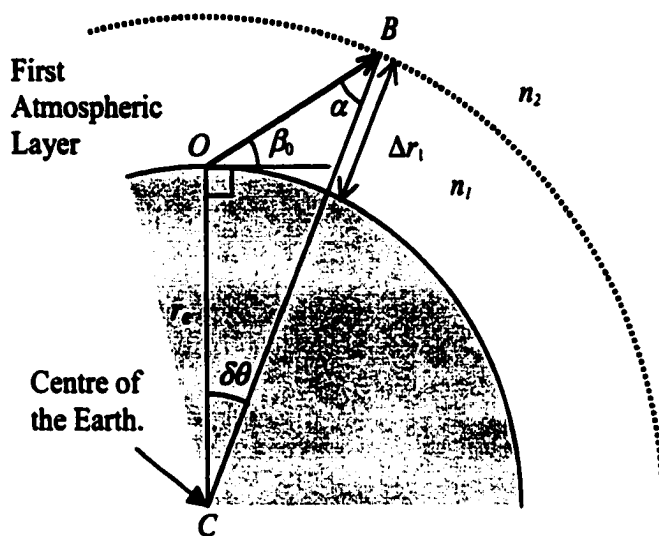


Figure 11: Schematic of the ray-travel increment and the atmospheric layer where the ray path increment is located. The sine law is used on the triangle COB to find Δr_1 the thickness of the first atmospheric layer given an initial incidence angle β_0 , ray travel increment $\delta\theta$, and mean radius of the Earth r_e .

An interpolation is then performed on the rawinsonde data to find the values of the meteorological parameters at point *B*. For temperature and relative humidity, a simple linear interpolation is performed. The temperature T' at point *B* is found from the formula

$$T' = T_i + \left(\frac{\Delta r_i - z_i}{z_{i+1} - z_i} \right) (T_{i+1} - T_i), \quad (29)$$

where T_i , T_{i+1} , z_i , and z_{i+1} are the sounding temperature and height measurements immediately below and above point *B* respectively (in the case of the first layer $i = 1$). Height measurements from the sounding are given in geopotential metres Z and are converted to geometric metres z using a third degree polynomial fit to the geopotential height integral (Wallace and Hobbs, 1977)

$$Z = \frac{1}{g_0} \int_0^z g(\phi, z) dz, \quad (30)$$

where g_0 is the mean sea level acceleration due to gravity. The value of $g(\phi, z)$ is the latitude and geometric height-dependent value of the gravitational acceleration and is found through the formula (Iribarne and Godson, 1981)

$$g_{\phi, z} = g_{45,0} (1 - a_1 \cos 2\phi) (1 - a_2 z), \quad (31)$$

where $g_{45,0}$ is the mean sea level gravitational acceleration at a latitude of 45° , a_1 is 2.59×10^{-3} and a_2 is $3.14 \times 10^{-7} \text{ m}^{-1}$, ϕ is the latitude and z is the geometric elevation above mean sea level. Plotting the expanded integral and fitting a third degree polynomial to the curve produces the expression for the difference δz (added to Z to give z)

$$\delta z = c_1 Z^3 + c_2 Z^2 + c_3 Z + c_4, \quad (32)$$

where $c_1 = 5.23658 \times 10^{-14} \text{ m} \cdot \text{gpm}^{-3}$, $c_2 = 1.566195 \times 10^{-7} \text{ m} \cdot \text{gpm}^{-2}$, $c_3 = -7.08293 \times 10^{-4} \text{ m} \cdot \text{gpm}$, and $c_4 = -8.2 \times 10^{-3} \text{ m}$. The pressure between sounding levels is found from an exponential interpolation scheme. Assuming each layer is isothermal, the scale height H was found from the hydrostatic equation

$$H = \frac{Z_i - Z_{i+1}}{\ln\left(\frac{p_i}{p_{i+1}}\right)}, \quad (33)$$

where Z_i and Z_{i+1} are the geopotential heights of the lower and upper consecutive sounding levels and p_i and p_{i+1} are the pressure measurements at those levels. From the hydrostatic equation the barometric pressure at the height of the ray p' is determined by the formula (Wallace and Hobbs, 1977)

$$p' = p_i \exp\left[-\frac{(Z' - Z_i)}{H}\right], \quad (34)$$

where p_i is the pressure at the sounding level below the ray, Z' is the height of the ray and Z_i is the height of the sounding level below the ray, both in geopotential metres.

The index of refraction is now determined for the top and bottom of the layer described by the initial ray. A scheme developed by Cidor (1996) was employed that uses the separate refraction indices for dry air and water vapor (see Appendix A for details). The amount of carbon dioxide can also be varied in Cidor's algorithms but the need for this is confined to indoor measurements of the refractive index where concentrations can vary considerably. Cidor suggested that the concentration of carbon dioxide be set to 450 ppm.

Snell's law of refraction can now be employed to trace the light ray through each layer. While travelling through a medium with constant density, the ray would be straight. However, as outlined above, the atmosphere has a continuous density gradient. Therefore, the light path has a curvature, which has been introduced to address the density gradient in each layer. The curvature is assumed to be constant in each layer. Once the refractive indices for the top and the bottom of the layers are determined, the ray path can be found from the curvature κ of the ray (see Figure 12) which is calculated from the formula (Bruton, 1996)

$$\kappa = -\frac{\cos \beta \Delta n}{n \Delta r}, \quad (35)$$

where β is the initial angle (at the bottom of the layer), n is the average index of refraction of the layer, Δn is the difference between the indices of refraction at the top and bottom of the layer, and Δr is the thickness of the layer. A full derivation of this formula is found in Appendix B.

The angle η is now calculated from the Cosine Law of the two triangles that share side CM (see Figure 12). For the triangle CMO

$$|\overrightarrow{CM}|^2 = r_e^2 + 1/\kappa^2 - (2r_e/\kappa)\cos \beta_0, \quad (36)$$

while for the triangle CMZ :

$$|\overrightarrow{CM}|^2 = (r_e + \Delta r)^2 + 1/\kappa^2 - 2/\kappa(r_e + \Delta r)\cos \eta. \quad (37)$$

Combining Equations 36 and 37 and simplifying produces the relationship:

$$\cos \eta = \frac{r_e}{r_e + \Delta r} \cos \beta_0 + \frac{\kappa}{2} \left(r_e + \Delta r - \frac{r_e^2}{r_e + \Delta r} \right). \quad (38)$$

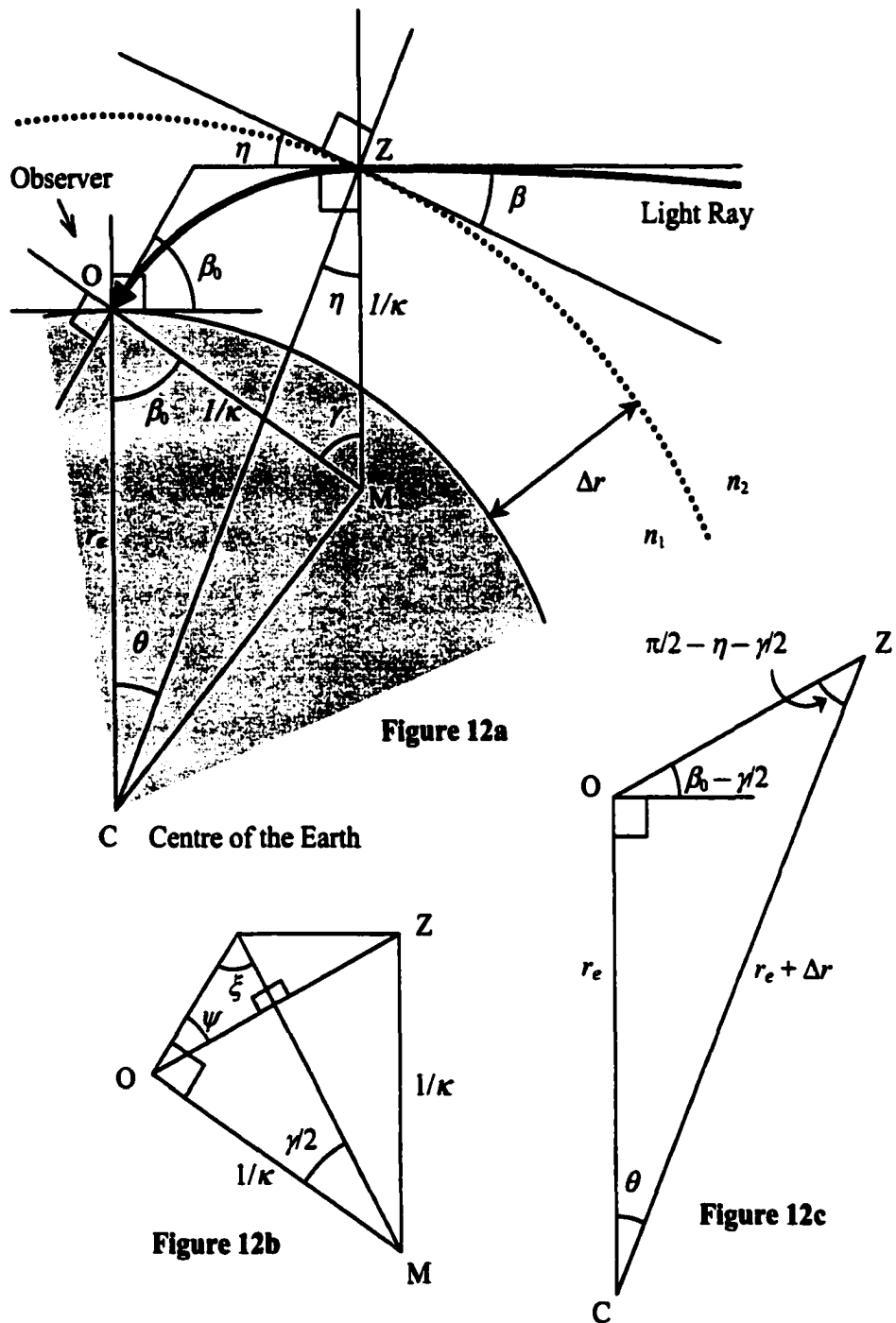


Figure 12: Geometric configuration of astronomical refraction. In Figure 12b since the two right angle triangles share angle ξ , angle $\psi = \gamma/2$. From this result, the angles labeled in Figure 12c can be derived.

The angle β for the next layer is then set equal to the angle η of the previous layer (see Figure 12). The model also checks for total internal reflection by comparing the value of η with the critical angle computed from the formula

$$\cos \eta_{critical} = \frac{n_2}{n_1}. \quad (39)$$

In a time-reversed ray tracing model in a spherically symmetrical atmosphere, if the critical angle is achieved the ray will retrace its path and hit the ground, unless the observer is elevated above the surrounding topography (for example on an island surrounded by the sea). At an initial angle greater than this the observer will still see the Sun, while below this angle the observer will see the horizon. The angle γ is now derived from an application of the Sine Law to the triangle *CZO* in Figure 12c.

$$\frac{\sin\left(\frac{\pi}{2} + \beta_0 - \frac{\gamma}{2}\right)}{r_e + \Delta r} = \frac{\sin\left(\frac{\pi}{2} - \eta - \frac{\gamma}{2}\right)}{r_e}, \quad (40)$$

which can be simplified to:

$$\frac{\cos\left(\beta_0 - \frac{\gamma}{2}\right)}{r_e + \Delta r} = \frac{\cos\left(\eta + \frac{\gamma}{2}\right)}{r_e}. \quad (41)$$

Using the trigonometric identities:

$$\cos(x - y) = \cos x \cos y + \sin x \sin y, \quad (42)$$

$$\cos(x + y) = \cos x \cos y - \sin x \sin y,$$

Equation 41 can now be rewritten as:

$$\tan \frac{\gamma}{2} = \frac{\cos \eta - \frac{r_e}{r_e + \Delta r} \cos \beta_0}{\sin \eta + \frac{r_e}{r_e + \Delta r} \sin \beta_0}. \quad (43)$$

From Figure 12c the value of θ can be found from the equation:

$$\theta = \eta - \beta_0 + \gamma. \quad (44)$$

The value of θ is greater than the initial value $\delta\theta$ due to the introduction of the curvature term.

The ray tracing proceeds until the ray reaches an altitude of 80 km, at which point it is assumed that the amount of further refraction is negligible (Bruton, 1996). The amount the ray misses the target point on the Sun shall be called the miss-angle ε and is calculated from the formula:

$$\varepsilon = \eta_{exit} - \left(\sum_i \theta_i + a_{sun} \right), \quad (45)$$

where η_{exit} is the final value of η as it leaves the atmosphere, and a_{sun} is the calculated altitude of the portion of the Sun the ray is attempting to strike. If the value of ε is greater than 6" (the accuracy of the photogrammetric measurements), then the model adjusts the initial angle by subtracting half of the miss-angle and starts again. Typically, it takes less than 10 iterations before the routine converges on a miss-angle less than 6". The number of iterations increases with increasing zenith angle.

The FORTRAN code for the refraction model can be seen in Appendix C.

3. Experimental Design

3.1 Introduction

Since the greatest astronomical refraction was observed to occur during sunrise (Sampson, 1993), it was decided that the first step in modelling astronomical refraction would be to simulate refraction under the simpler conditions during sunsets. Due to daytime heating and boundary layer mixing caused by convection, the daytime temperature profile of the planetary boundary layer is often close to dry adiabatic (except within a very shallow surface layer). An inversion layer near the surface, which is often present in the morning, can cause anomalous refraction events such as blank strips, Novaya Zemlya mirages (very early sunrises), and the Chinese Lantern effect (Lehn, 1979, Minnaert, 1993, Lynch and Livingston, 1995, Young, et al, 1997).

Since it is well known that the temperature profile of the lower atmosphere can change substantially throughout the day (Arya, 1988, Stull, 1988), it is critical that the sunset observations be conducted at about the same time as the sounding. It is also desirable to conduct the measurements from the same location as the sounding. These requirements will be explained in more detail in a later section.

3.2 Instrumentation

A photogrammetric technique was chosen as the primary method for measuring the astronomical refraction of the setting Sun. The photogrammetric system was used to determine the horizontal coordinates (altitude and azimuth) of the profile of the setting Sun. The component of the photogrammetric system with

the poorest resolution set the limits of the experiment. Horizon reference markers were measured with a theodolite to an accuracy of about 6". This established the limiting resolution criterion for the photogrammetric system.

A Questar 3.5-inch telescope with an Olympus OM-1 35-mm camera body and a super-telephoto focusing screen was found to achieve the resolution criterion of the experiment. The lens was calibrated using photographs of star trails and a more traditional terrestrial calibration target and was found to show no measurable distortions to within the limits of the measuring system. Distortions were found to be less than the pixel size of the scanner (32μ) over a full 35-mm frame.

The lens allowed no control over its aperture. The film used was Tri-X, which was 'pull' processed by one stop in order to reduce the contrast as much as possible. This was necessary to ensure that reference targets on the horizon would not be washed out by the glare of the solar disk. The developed negatives were then scanned on a photogrammetrically calibrated Agfa Studio Scan *si* flat bed scanner. Exposures of 0.001 s were found to be adequate to record both the solar profile and the nearby horizon reference markers (treetops).

In order to record the times of the exposures, a short-wave radio was set up next to the camera and tuned to WWV (5, 10 or 15 MHz). This radio station broadcasts an atomic clock time signal with minute announcements and second ticks. A small tape recorder was held next to the camera, which simultaneously recorded the sound of the camera shutter and the time signals. Timing inaccuracies were estimated to be ± 0.1 second.

3.3 Astronomical Refraction Measured from Edmonton

A simultaneous experiment to measure the sunset refraction was carried out in Edmonton in order to check the validity of the model results and to determine its dependency on geographic proximity to the soundings. To measure the sunset astronomical refraction a Kern E2 theodolite was set up on the roof the Henry Marshall Tory Building on the campus of the University of Alberta (38.9-km east and 2.1-km south of the upper air station). A solar projection box was constructed for the theodolite. This projection box eliminated the possibility of accidental viewing of the Sun which could cause serious vision damage (see Figure 13).

Numerous factors may conspire to degrade the agreement between the observed and the modeled refraction. Inaccuracies in the measurement of the horizontal co-ordinates of the reference markers will cause a systematic error in the calculated co-ordinates of the solar profile. Instrument error in the photogrammetric system such as film buckling, grain, thermal expansion of the lens, and pixel size in the scanner all limit the accuracy of the system. Finally, the difference between the measured atmospheric parameters and those actually experienced by the light ray as it traverses the atmosphere to the observer is also a major source of uncertainty. In order to reduce the differences between these two atmospheres, it would appear to be necessary to match the time and the location of the photogrammetric observation to that of the atmospheric sounding. However, it would also be desirable to explore the dependence of the error in the modelled refraction to geographic distance from the launch of the sounding.

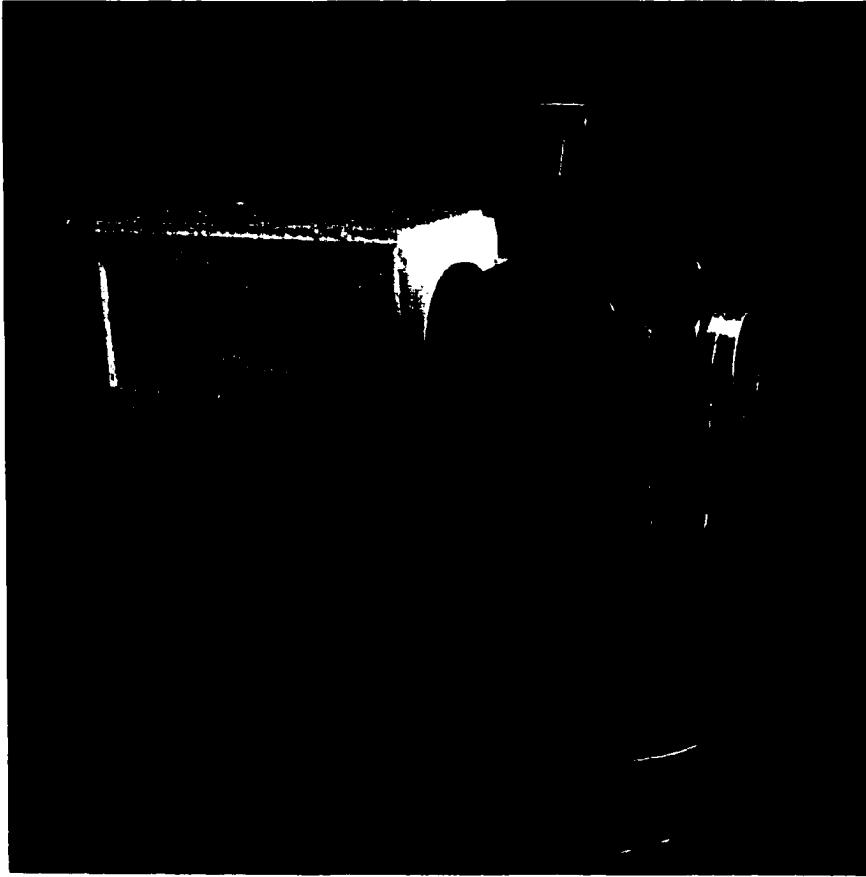


Figure 13: Kern E2 theodolite with solar projection box. A simulated solar image can be seen through the viewing window.

The theodolite was set up at the same location for each sunset event. High frequency vibrations from nearby ventilation fans caused the compensator (self-leveling) mechanisms in the theodolite to become unstable. As a result, the compensator was switched off during sunset measurements. Therefore, extra care was taken to ensure the theodolite was level before observations were obtained. This was done by ensuring the spirit levels were accurately centred and a standard reference marker was measured before and after each set of observations.

During sunset observations, the theodolite was held stationary and the solar image was allowed to drift across the cross hairs. The timing of the transit of the upper limb of the solar disk across the horizontal crosshair was recorded using a digital watch calibrated to the WWV (a radio station broadcasting atomic clock time and time intervals). The accuracy of the times was estimated to be between 0.1 to 3 seconds depending on the scintillation of the solar limb and reduced visibility caused by intervening haze and cloud. The accuracy of the timing generally decreased with increased zenith angle⁷.

3.4 Atmospheric Issues

Using atmospheric soundings from the Stony Plain Upper Air Station in the refraction model implies a fundamental assumption: that the sounding is representative of the air column that the sunlight passes through. In the refraction model, the temperature resolution of the sounding is taken to be $\pm 0.2^{\circ}\text{C}$ (Vaisala,

⁷ Low temperatures and high winds also interfered with the observers' ability to concentrate and accurately record transit times.

1999). It was also an objective of the study to minimize the difference between the measured profile and the air column the ray passes through.

An ideal sounding would be instantaneous and coincidental with the time of the sunset or sunrise observation. As well, the path of this ideal sounding should follow a trajectory identical to the ray-path of the sunlight. This, of course, cannot be the case. Since the time of the balloon launch is fixed (23:15 and 11:15 UT), and the time of sunrise and sunset varies by nearly 5 hours, the two can not always be the same. As well, the atmospheric profile the ray encounters is a near instantaneous profile while the balloon takes almost two hours to measure the atmospheric profile to an altitude of about 30 kilometres. Finally, the position of the observer and the trajectory of the light path are not the same as the starting position and trajectory of the sounding balloon (see Figure 14).

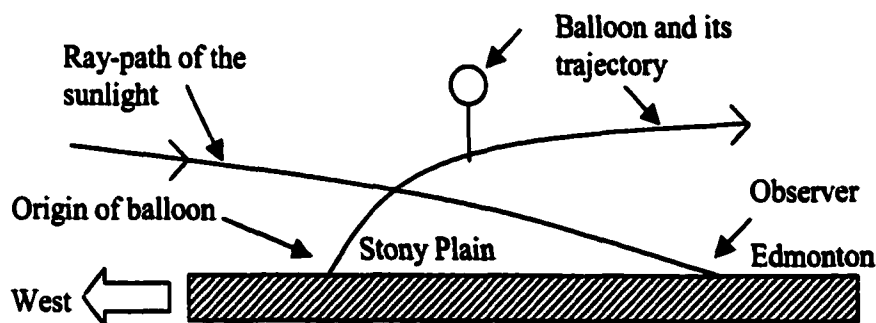


Figure 14: A schematic of the position of the observer, ray-path of the sunlight and the trajectory of the balloon. Here the observer located in Edmonton is watching a sunset. The sounding is launched from Stony Plain west of Edmonton and the prevailing winds are assumed to be westerly.

Temporal changes in the tropospheric temperature profile can occur in two ways. The first is radiative cooling and heating of the surface. Short-term (i.e. less than a day) changes in solar insolation typically produce changes in the temperature profile only in the lowest kilometre of the atmosphere (the planetary boundary layer or PBL). The ground is heated by downward direct and diffuse radiation (both incoming shortwave $K\downarrow$ and incoming longwave $L\downarrow$). We denote by Q^* the difference between the sum of the incoming radiative fluxes and the sum of the outgoing fluxes ($K\uparrow$, reflected shortwave; and $L\uparrow$ emitted longwave). The surface energy balance equation can be written (Oke, 1987)

$$Q^* = Q_H + Q_E + Q_G, \quad (46)$$

where Q_H is the sensible heat flux, Q_E is the latent heat flux and Q_G is the subsurface heat flux. The sign convention is that Q^* is positive when incoming radiation fluxes exceed outgoing radiation fluxes; Q_H and Q_E are positive when directed upward; and Q_G is positive when directed downward into the soil. During a normal sunny day, Q_H is directed upward thus contributing to the heating of the lower atmosphere. Around sunset, Q^* decreases and in the absence of cloud cover will go negative (attaining a magnitude of up to about -100 Wm^{-2}). Now the surface cools rapidly, driven by this upward longwave radiation ($L\uparrow$). Air in contact with the surface is consequently cooled by conduction, and vertical exchange through turbulent convection mixes these cooled parcels aloft. The consequence is a strong downward heat flux ($Q_H \ll 0$) near ground, with a weakening downward heat flux at greater distances from ground ("heat flux divergence"). The equation expressing heat conservation in a horizontally-uniform

and dry air mass shows that any heat flux divergence ($\partial Q_H / \partial z$ is non-zero) implies warming or cooling. In the present instance, $Q_H < 0$ but $\partial Q_H / \partial z > 0$, and a given layer near ground will experience a strong loss of heat out across its bottom boundary, but a weak gain in heat downwards across its top boundary: thus the layer will progressively be cooling. As a result, a temperature inversion is formed in the boundary layer of the atmosphere. This so-called nocturnal inversion layer can start to form in a clear atmosphere about an hour before sunset, depending on the season (Stull, 1988, Arya, 1988).

The temperature profile of the surface layer of the PBL changes with time as the solar irradiance is reduced. Although only two soundings are launched each day, one can get a sense of the rate of cooling of the PBL at the onset of the nocturnal inversion by observing the surface temperature changes over time. Table 2 shows surface temperature time series from the Stony Plain Upper Air Station for three sunsets used in the testing of the refraction model.

Time [UTC]	Temp. [°C]	Temp. [°C]	Temp. [°C]
	Dec. 8-9, 1998	Dec. 14-15, 1998	Dec. 22-23, 1998
sunset times:	23:18	23:17	23:17
20:00	0.0	-1.3	-13.3
21:00	1.1	-1.5	-13.3
22:00	1.5	-1.7	-13.7
23:00	0.3	-2.3	-14.4
00:00	-1.5	-3.5	-15.2
01:00	-2.1	-3.3	-15.8
02:00	-2.3	-4.3	-16.0

Table 2: Surface temperature time series for time around sunset. Those temperatures nearest the time of sunset are in bold. Sunset times are determined for a horizon with $z = 90^\circ$. Temperatures were taken at screen height, approximately 1.5 metres above the ground. The skies were clear for all events. Winds were strong.

From an examination of the values in Table 2 it appears that the surface temperature was changing by -1.5 °C/hr on December 8-9 during the hour that sunset occurred, -0.9 °C/hr on December 14-15, and -0.8 °C/hr on December 22-23. Consequently, a 20-minute (or less) difference between the time of the sounding and the time of the sunset photography would probably have introduced an error of less than half a degree in the surface temperature.

More important than the change in the surface temperature is the change in the vertical temperature profile. The diurnal range in temperature decreases rapidly with height and virtually disappears at the top of the PBL (typically about one kilometre above the surface). From an experiment done during the month of December in southern England, it appears that the rate of change in temperature at an altitude of 17 metres can be about a quarter the rate at the surface (Arya, 1988). Since the balloon sounding records a temperature about every 50 metres, it would be expected that the change in the temperature at the second sounding level would be less than a quarter of the change experienced at the surface. A 20-minute difference between launch and sunset observation would therefore imply a change of less than -0.2 °C, which is approaching the specified resolution limit of the temperature sensor on the sounding.

The other process that can cause the temperature profile to change over time is temperature advection. Frequently in a continental climate like Alberta's, large changes in temperature are produced by the passage of a cold or warm front. Cold air advection can also occur with arctic outflow under the influence of a high-pressure system. Smaller scale advection can occur from such things as

thunderstorm gust fronts, lake breezes and urban heat islands (Wallace and Hobbs, 1977). In this experiment, sunset images were avoided during times of obvious temperature advection.

The amount of advection produced by typical synoptic-scale disturbances can be estimated as follows. The greatest horizontal temperature gradients in a synoptic-scale disturbance are located across the fronts. It is not unusual to have horizontal surface temperature gradients of the order of 10°C over a distance of 100km (Wallace and Hobbs, 1977). The frontal zones are also typically the location of the greatest amount of cloud cover and the highest surface winds (typically around 5 to 10 m/s and rarely exceeding 20 m/s). From this, it can be argued that sunrise and sunset observations could not normally be made during the passage of a front. This would imply that sunsets are typically observable only relatively far from the centre of a low or the frontal zones and under conditions of only modest horizontal temperature gradients and wind speeds.

Nevertheless, taking the worst case scenario of a sunrise or sunset observation occurring during the passage of a frontal zone, the advective temperature change can be estimated. If the horizontal temperature gradient is assumed to be $0.1^{\circ}\text{C}/\text{km}$ and the wind speed is 10m/s (parallel to the gradient), then a stationary observer would measure a rate of temperature change of $0.001^{\circ}\text{C}/\text{s}$ or $0.06^{\circ}\text{C}/\text{min}$. A 20-minute interval would therefore produce a change of 1.2°C . Since the balloon requires 30 minutes to reach the tropopause, it appears the tropospheric profile would change by at least 1.0°C during the time of the ascent. Therefore, it appears

that observations of sunrises and sunsets taken during the passage of a frontal zone may require some adjustment to the measured temperature profile.

A more typical temperature change due to advection can be estimated from the climate normals for the area. The annual mean horizontal surface temperature gradient between the Edmonton International Airport and Vegreville Alberta is $0.0064\text{ }^{\circ}\text{C}/\text{km}$ (Environment Canada, 1999). Vegreville is about 110 km east of Edmonton, in the approximate direction of the prevailing winds. The mean annual wind speed for the Edmonton International Airport is 3.6m/s giving a rate of temperature change of 0.03°C over a 20-minute interval. This is within the specified error of the rawinsonde temperature sensor ($\pm 0.2\text{ K}$).

Therefore, in order to ensure that the vertical temperature profile used in the refraction model is representative of the actual profile at the time of sunset, it would appear reasonable to observe the sunset or sunrise within 20 minutes of the launch of the balloon. Since the total flight time can be as long as two hours, and the boundary layer is the most important refractive component of the atmosphere (see Appendix H), it seems appropriate to plan for sunrise or sunset observations to be timed with the beginning of the balloon launch. Since the balloon ascends at a rate of about 5 metres per second, the sounding should reach the top of the boundary layer (approximately 1-kilometre in height) about 3.3 minutes after launch.

The regions of the world where the summer and winter solstice sunrises and sunsets coincide with the launch times of rawinsondes are Southern Alaska and the Yukon Territory, northern British Columbia, central Alberta, central Montana, northeast Wyoming, northeast Colorado, western Nebraska, central Oklahoma,

eastern Texas, the Yucatan region of Mexico, most of Central America, western Peru, northern Chili, northern Argentina, Singapore, Cambodia, southern Vietnam, southeastern China, North Korea and the extreme eastern regions of Russia (Ahlgren, 1997).

3.5 Times and Azimuthal Location of Sunset

From previous observations of winter sunset (Sampson, 1994), it requires about one or two months to obtain at least 3 useful sunset image sets taking into account cloud cover and an estimated 50-percent failure rate due to the complex nature of the experiment. The upper air station at Stony Plain, launches balloons twice daily at 11:15 and 23:15 UT. Near the winter solstice, the sunset occurs at approximately the same time and the same location on the horizon for many days. Coincidentally, this time also corresponds to the afternoon launch of the rawinsondes. Therefore, near the solstice there occur a maximum number of opportunities to observe sunsets at approximately the same time as the soundings. Table 3 lists standard sunset times (horizontal refraction of 30') for the two locations.

Date 1998-1999	Time[UT] Stony Plain	Azimuth Stony Plain	Time [UT] H. M. Tory	Azimuth H. M. Tory
Nov. 11	23:46	240° 54'	23:43	240° 44'
Nov. 21	23:31	236° 13'	23:29	236° 15'
Dec. 1	23:21	232° 35'	23:19	232° 39'
Dec. 11	23:16	230° 09'	23:14	230° 14'
Dec. 21	23:18	229° 23'	23:16	229° 28'
Dec. 31	23:26	230° 12'	23:24	230° 16'
Jan. 10	23:39	232° 29'	23:37	232° 33'

Table 3: Approximate sunset times and azimuths for Stony Plain Upper Air Station and the H. M. Tory Building at the University of Alberta, in Edmonton. Sunset times obtained from the planetarium and telescope control software: Earth Centred Universe (Lane, 1998).

At these locations, the period from mid-November to the first week of January provides a window with a maximum difference of ± 20 minutes between sunset and the time of balloon launch. Under conditions of substantial temperature advection dates closer to the winter solstice would still be usable since the time difference between sunset and the balloon launch is minimized at this time.

Sunsets viewed from the centre of a city may also be effected by a horizontal temperature gradient produced by the urban heat island effect. Oke (1987) found a roughly linear relationship between the log of population versus the ΔT_{u-r} (max) (the maximum temperature difference between the urban and rural areas). Using this relationship, Edmonton (approximate population 700,000) should experience a maximum surface temperature difference of about 10°C between the centre of the city and the surrounding rural areas.

Depending on such factors as the wind speed and cloud cover, the maximum difference between the urban and rural temperatures occurs at night. The two

temperatures are closest during the daylight hours, with the difference starting to increase just before sunset.

Light rays from the setting Sun, as observed from the city, would therefore traverse this temperature difference⁸. Since the balloon sounding is launched from a rural site, the difference in the vertical temperature profile produced by the urban heat island would be unrecorded. Therefore, in order to ensure that the temperature profile used in the model is representative of the temperature profile experienced by the light ray, it appears to be necessary to make the sunset observations outside the city and near the site of the balloon launch. The astronomical refraction measurements from the Tory building would also supply important evidence regarding these conclusions.

3.6 Reference Targets

Extracting altitude and azimuth values of the solar disk from a photographic image can be achieved in two ways. In the first method it is necessary to have prior knowledge of the camera's orientation and the optical properties of the lens. The object co-ordinates are extracted from the image by knowing exactly where the camera is pointed and the scale and orientation of the final image. In the second method, it is necessary to have a number of targets of known horizontal co-ordinates (altitude and azimuth) in the same image as the Sun. The first method

⁸ The influence of the urban heat island effect on horizontal astronomical refraction can be estimated using a simple cylindrical lens model. The shape of the urban heat island was assumed to be a section of a cylinder with radius 500-km, a maximum depth of 0.1 km and horizontal dimensions of 20 km. The temperature difference of 10°C is assumed to be at the surface. If the air inside the lens is isothermal and at a temperature of 1°C then the maximum additional astronomical refraction measured within the city is between 10" to 20" depending on the location of an observer.

was deemed unsuitable since the orientation of the instrument could not be easily and accurately determined during the time of each exposure.

3.6.1 Selection of Reference Targets

From the rooftop observation deck of the Stony Plain weather station a distant stand of conifer trees was located on the winter solstice sunset horizon. Their large number and sharply defined silhouettes made them suitable reference targets. Difficulties in distinguishing individual trees during the moments after sunset, and movements produced by wind were factors that made these targets less than ideal. Moreover, any delay in measurement of the co-ordinates of the treetops longer than a few months could cause their height to change due to seasonal growth. Consequently, all measurements were taken in the winter and early spring of 1998-1999 before the spring thaw. During the measurements, the wind speed ranged from 10 to 20 kph. Under such conditions the tops of similar nearby conifer trees appeared to move by 0.2 to 0.5 m. In order to help in their identification, images of the targets were taken with the Questar telescopic lens and then labelled (see Figure 15).

3.6.2 Estimating Distances to Reference Targets

It is important to know the distance to the reference targets in order to estimate the amount of error produced by such factors as terrestrial refraction, and parallax error associated with the misplacement of the instruments.



Figure 15: Horizon markers visible from the roof of the Stony Plain Upper Air Station. The photographs were taken with same lens and camera as the sunset images (Questar 3.5-inch telescopic lens and OM-1 camera body). The treetops used in the photogrammetric reduction are labelled. Field is 2° 48' wide and 0° 57' high.

Examination of aerial photographs and topographic maps plus trips to the area suggested that the trees were 2 to 3 km from the Stony Plain weather station. Triangulation measurements using the theodolite showed a considerable uncertainty due to the relatively short baseline afforded by the small observing platform. However, these values did agree with the more qualitative methods described above, giving an average distance of 2.5 km to the treetops.

3.6.3 Altitude and Azimuth of the Reference Targets

Altitude measurements of the treetops were taken with the theodolite placed at the same height as the camera. The uncertainty in the placement of the theodolite, with respect to the height of the camera was estimated to be ± 0.01 m. During a period of about 30 minutes after the sunset photographs, altitude measurements of the reference targets that were in the frame of the photographs were obtained on December 8, 14 and 22.

Limited light, high winds and low temperatures prevented measurements of the reference targets immediately after the photographs were taken. As a result, a full survey of all the trees that appeared in the field could not be done immediately after the photographs were taken. Horizontal coordinate measurements (horizontal angles between reference targets) were taken on the December 8, 10, 14, and 22 with a Wild Heerbrugg, optical-mechanical theodolite with one-arcminute gradations. Measurements taken on March 19 and 31 were taken with the Kern E-2 electronic theodolite with an automatic index compensator. The digital display of the Kern theodolite shows angles to the nearest arcsecond. The self-leveling and

indexing system of the Kern theodolite eliminated the need for reversing the telescope. Differences in the altitude measurement between direct and reversed telescopes were smaller than the errors due to uncertainties in sighting the target. A summary of the altitude data can be seen in Appendix F.

Azimuth values for the treetops were obtained from solar positions using the Kern theodolite. The theodolite's horizontal circle can not be independently oriented towards geographic north so the azimuth of a target can only be determined by the comparison with a target of known azimuth, for example the Sun at a given time. When the theodolite is set up the orientation of the zero-point of the horizontal circle is arbitrary. Therefore the azimuth of a target is its horizontal angle plus some constant.

The azimuthal measurements were performed in the early afternoon when the Sun was high in the southern sky. Since astronomical refraction primarily affects the altitude of an object it can be ignored in azimuthal measurements. Before and after horizontal angles of the treetops were measured, the projected image of the Sun was allowed to transit across the vertical crosshairs of the stationary theodolite. The time of the transit and the horizontal angle were recorded. The stopwatch used for the timings was calibrated with the radio station WWV prior to each set of observations. From the U.S. Naval Observatory's online version of the Multiyear Interactive Computer Almanac (U.S.N.O. 1999), the altitude and azimuth of the centre of the Sun and its angular diameter were obtained for each transit timing. The azimuth of the treetops A_t could then be calculated from the equation:

$$A_t = h_t + [(A_{Sun} - r_{Sun} \cos a_{Sun}) - h_{Sun}], \quad (47)$$

where h_t is the horizontal angle of the treetop, A_{Sun} is the azimuth of the centre of the Sun, r_{Sun} is the apparent radius of the Sun [degrees], a_{Sun} is the altitude of the centre of the Sun, and h_{Sun} is the horizontal angle of the trailing edge of the Sun.

3.6.4 Terrestrial Refraction

Since the light from the reference targets must pass through the atmosphere, the altitude measurements can also be affected by refraction. In general, if the light passes through a density gradient it will be refracted and the measured altitude will be different from the true altitude. In order to simplify the computations, a simple empirical expression for terrestrial refraction was used rather than the numerical model outlined in Chapter 1. It was also felt that since the overall purpose of the present experiment was to test the validity of the atmospheric ray-tracing model, it would be inappropriate if this test was somehow dependent on the use of the model itself.

Many empirical expressions have been developed (Thom, 1958; Bomford, 1980; Brinker and Wolf, 1984) to correct the observed altitude of a terrestrial object with a zenith angle close to 90°. In previous work (Sampson, 1994) a formula for terrestrial refraction, R_t , in radians was selected from Bomford (1980):

$$R_t = \frac{kd}{r_e}, \quad (48)$$

where d [m] is the distance, r_e is the radius of the Earth [m] and k is the refraction coefficient of the light ray found, through the expression

$$k = \frac{252p}{T^2} \left(0.0342 + \frac{dT}{dz} \right), \quad (49)$$

where p is the barometric pressure in millibars, T is the surface temperature [K] and dT/dz is the vertical temperature gradient in degrees per metre (positive for an inversion). The amount of terrestrial refraction is also a function of the zenith angle of the target. For example, a target at the horizon will exhibit more refraction than a target at the same distance but nearer to the zenith. Equations 48 and 49 are not functions of zenith angle presumably because these formulae were intended for geodetic surveys of distant features on the Earth's surface from a station located on the ground, the zenith angle of the targets would most likely be close to 90° . As can be seen in Appendix F, zenith angles of all the treetops were no more than 2 arcminutes from 90° . Consequently, Equation 48 and 49 were considered to be appropriate for this study.

From Equations 48 and 49 the terrestrial refraction was estimated assuming $d = 2500$ m. Reference target measurements taken in December were obtained within a half-hour of the time of the sounding launch. Therefore, surface lapse rates (surface to first rawinsonde observation) for December were taken from fine-scale sounding data⁹. Since the horizontal coordinate measurements made in March were done in the late morning and early afternoon, the sounding data could not be used directly. Since the winds were moderate the boundary layer was most likely relatively well mixed and, therefore, the surface vertical temperature gradient should have been close to dry adiabatic (-0.0098 °C/m).

Archived hourly surface meteorological data from the Stony Plain Upper Air Station were unavailable. Consequently, surface meteorological data were obtained

⁹ Meteorological parameters measured every 10 seconds during the ascent of the rawinsonde. These are available only upon special request at a cost of \$200 per sounding and are not archived.

from the Edmonton International Airport (YEG) about 47 km southeast of Stony Plain. From these data the rate of change of the surface temperature at Stony Plain was established for the time of the observations. The surface temperature provided by the 23:15 UTC (17:15 MST) sounding was then used to determine the surface temperature at the time of the treetop measurements. A simple linear extrapolation in height was used to determine the temperatures. Significant and mandatory¹⁰ levels were used to establish the surface lapse rate for December 10, March 19 and March 31.

A distant reference target was measured at the beginning and end of each set of observations. The target was a tall smokestack at the Keephills power plant. These measurements established the overall terrestrial refraction behavior for the observing interval. Since the smokestack was found to be more distant than the reference target treetops, it was assumed that the terrestrial refraction would be more exaggerated on the smokestack. For details on its location and height see Appendix D. The results are listed in Table 4.

¹⁰ Mandatory levels are meteorological parameters measured by the sounding balloon at the surface and the following barometric pressure levels: 1000, 850, 700, 500, 400, 300, 250, 200, 150, 100, 70, 50, 30, 20, 10, 7, and 5, hPa (1 hPa = 10² Pa). The final levels may not be measured if the balloon bursts before ascending to these heights. Significant levels are additional levels that permit the reconstruction of temperature and humidity profiles to within specified criteria. For the temperature sounding, significant levels are added to the mandatory levels between the surface and 300 hPa. This is to permit a linear interpolation between mandatory levels that will differ by no more than 1° C from the complete sounding data set. Beyond this altitude the difference can not exceed 2° C (Weather Services Directorate, 1987).

Date	T [° C]	p [mb]	dT/dh [° /m]	R_t trees ["]	R_t stack [']	a [']	$a - R_t$ [']
12/08/98*	-0.5	924.6	0.008	11	1 49	11 22	9 33
12/10/98	6.0	918.0	-0.005	7	1 11	10 39	9 28
12/14/98*	-2.5	931.3	0.002	10	1 35	10 54	9 19
12/22/98*	-14.3	934.3	-0.011	7	1 07	10 34	9 27
03/19/99	2.0	933.0	-0.010	6	1 02	10 24	9 22
03/31/99	-1.0	926.0	-0.006	7	1 13	10 31	9 18

Table 4: Surface meteorological data and estimated terrestrial refraction (Equation 48). Photographs of the setting Sun were obtained on the dates marked with an asterisk. The other dates are when the reference targets were measured. Surface vertical temperature gradients for December 10, 1998, March 19, 1999 and March 31, 1999 are estimates from the mandatory and significant sounding levels. The sixth column is terrestrial refraction calculated from Equation 48 for the reference target (the smokestack at the Keephills power plant). The seventh column is the measured altitude of the top of the smokestack and the last column is the altitude of the smokestack, corrected for terrestrial refraction.

An analysis of the precision and accuracy of the Bomford formulation (Equation 48 and 49) can be found in Appendix D. It was determined that the Bomford formulation could be successfully employed in eliminating systematic error introduced by the terrestrial refraction of the reference targets. Using the Keephills smokestack as a reference target of known location and height, it was found that Bomford's formulation improved both the precision and the accuracy of the observations to within the uncertainty limits of the experiment.

3.7 Photogrammetric Analysis

Once the film was developed, the image co-ordinates were transformed to object co-ordinates (zenith angle and azimuths). The extremely long focal length of

the Questar lens (about 1445 mm) presented unique challenges in the extraction of the object co-ordinates. These will be discussed in the following sections.

3.7.1 Scanning and Digitization of Images

The negatives were scanned at 800 ppi, the maximum optical resolution of the machine. A glass calibration plate was used to flatten the negatives. This plate was manufactured by Zeiss and is used in the calibration of stereo plotters. It is etched with a 1-cm grid that, according to the manufacturer's specifications, has a median absolute error in each grid coordinate of $\pm 0.9 \mu\text{m}$ in the x and y-directions, with a maximum error of $2.1 \mu\text{m}$ for a single grid point. The mean error in the orthogonality of the grid is 2.4 arcseconds, which translates into approximately $0.4 \mu\text{m}$ over the maximum dimensions of a 35-mm negative. Plate error could therefore be ignored, since each error is smaller by more than an order of magnitude than the pixel size of the scanner.

The contrast and brightness of the scanned image were adjusted until the calibration grid lines, format of the frame (the edge of the frame), the profile of the Sun and the treetop reference targets were easily visible on the same image. If all four features of the image could not be made visible on the same frame, then the same scanned image was saved in multiple files with different contrast and brightness settings that allowed the identification of the necessary features.

The pixel co-ordinates were extracted using image analysis software: Scion Image (1999). The images were magnified until individual pixels were visible on a screen display. The location of the targets (format lines, calibration grid points,

treetops or the solar limb) were identified and selected using the computer's mouse. The software created an ASCII file of the x,y pixel co-ordinates of the selected pixel. Four separate files were created for the format, grid intersection points, treetop reference targets and solar profile.

In order to estimate the measurement error of the digitization process, an experiment was devised using two independent observers to measure the same locations on the solar limb. This was necessary since parts of the solar profile exhibited continuous, rather than discrete, changes in the pixel gray-scale values between the solar disk and the surrounding sky. These gradations could cause ambiguity in locating the solar profile on the image.

A solar image was selected and guide marks were then placed directing the observer to the area on the limb along a single axis. A second image was then used to direct the observer to the same area along the other axis (see Figure 16). For the purposes of this uncertainty experiment a total of 12 points were compared between the two observers. The result showed a mean error in the x -direction of 0.00 pixels with a RMS error of 0.87 pixels and a mean error in the y -direction of 0.88 pixels with an RMS error of 1.8 pixels. This experiment suggested that measurement error from one observer to the next is probably of the order of a single pixel or better.

3.7.2 Correction for Scanner Distortions and Rotation of Image

A full photogrammetric calibration of the flatbed scanner was performed using the Zeiss calibration grid plate. From this analysis, linear distortions in both

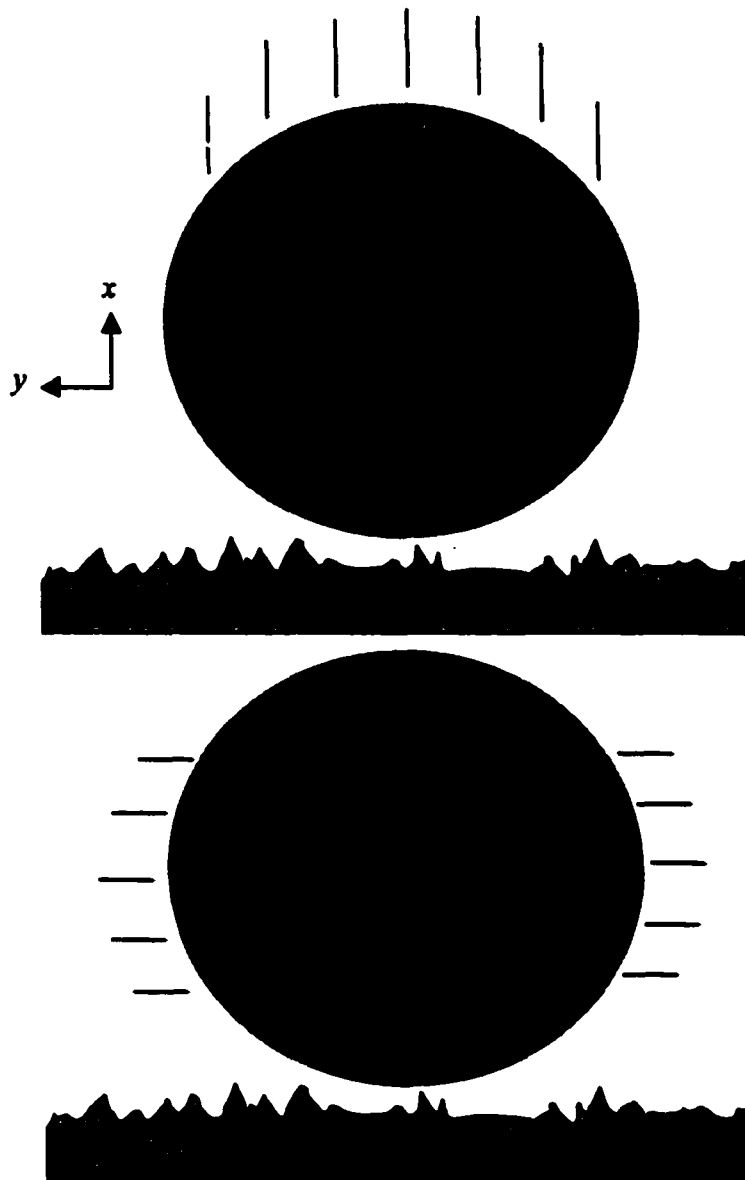


Figure 16: Schematic of test images used to estimate the measurement error from digitization of the solar profile. Single pixel wide, guidelines near, but not touching, the solar limb were used to direct the observers to the measurement area. The intersection points of the guidelines with the solar limb are positions deduced by the first observer.

axes were discovered. As well, a sinusoidal distortion was also found in the direction of travel of the scanner head (the y-axis). Corrections were then applied to the raw pixel co-ordinates using empirical formulae derived from this analysis.

The linear distortion in the x-direction was found to be (for 800 ppi):

$$\Delta x = -0.0061(\pm 0.0002)x - 1.611(\pm 0.002), \quad (50)$$

while the linear distortion in the y-direction was:

$$\Delta y = -0.00065(\pm 1.7 \times 10^{-5})y - 0.85(\pm 0.13). \quad (51)$$

The sinusoidal component of the distortion had a wavelength of 4.90 cm, an amplitude of 0.005 cm. The phase of the sinusoidal distortion was constant in the scanner reference frame. However, since individual negatives were placed in different parts of the scanner, the measured phase of the sinusoidal distortion in each image could vary. The Zeiss calibration plate was used to flatten the film against the scanner platen and provide reference points to determine the image-relative phase of the sinusoidal distortion.

The approximate centre of the frame was then found from the format image co-ordinates. The centre was found from half of the difference between the mean x and y co-ordinates of the opposite sides of the format. The image was then rotated to a standard orientation and the origin of the pixel co-ordinates was translated to the approximate centre of the frame. The origin of the pixel co-ordinates is the lower left of the raw scanned image.

3.7.3 Treetops Reference Targets

Once reference targets of known position are identified in the image a transformation can be performed to convert the image co-ordinates of the Sun and the treetops into object co-ordinates.

Treetop reference targets were identified in the images and their pixel image co-ordinates transformed into object co-ordinates (metres). The solar image and the treetop reference targets were far enough away that there appeared no appreciable focus difference in the image. Therefore, the Sun and the treetops were considered to be at the same distance from the camera. Therefore, for the purposes of this transformation the distances to the Sun and the treetops were set at 2.5 km – the approximate distance of the treetops. Since a photogrammetric calibration of the Questar lens revealed no measurable distortions, the object co-ordinates Y, Z of the treetops could be easily calculated using the relationship:

$$Y = \frac{X(x)}{f}, \text{ and } Z = \frac{X(y)}{f}, \quad (52)$$

where $X = 2,500$ m, x, y are the image co-ordinates, and f is the focal length of the lens in the same units as the image co-ordinates (1445.3-mm or 45521 pixels at 800 ppi). Once values for Y and Z are found it is a simple trigonometric process to convert to horizontal co-ordinates (altitude and azimuth).

3.7.4 Exterior Orientation of the Camera

The exterior orientation of the camera is the position of the camera when the image was taken. More specifically, it is the angular relationship between the image and object space coordinate systems (see Figure 17). The values of ω, ϕ and

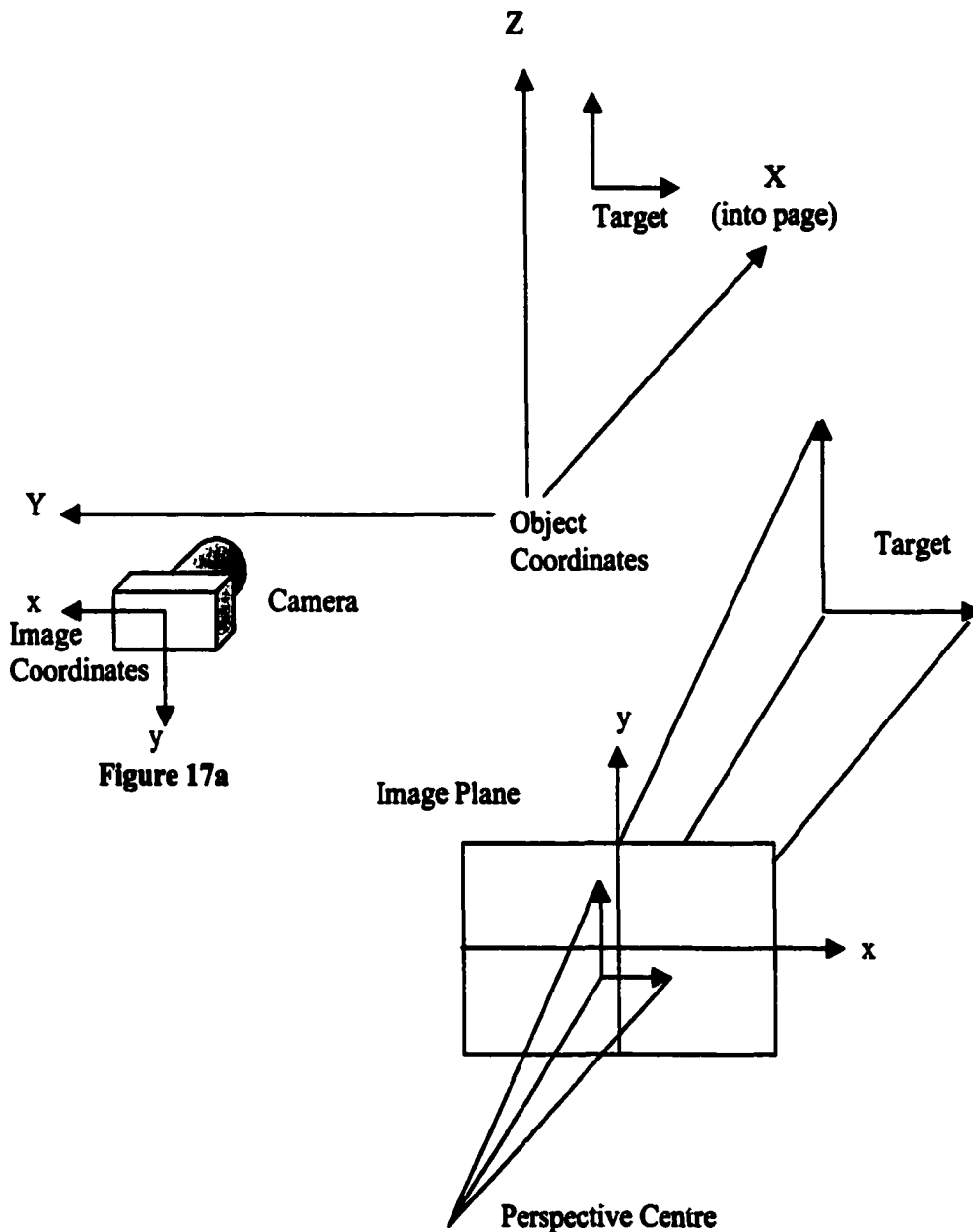


Figure 17b

Figure 17a: Object coordinates and image coordinates in object space. The origin of the object coordinate frame is arbitrary but for this experiment was placed at the perspective centre of the camera. **Figure 17b:** Image space coordinates oriented with a positive image. The perspective centre is point of perspective, and in a positive image orientation the image is located between the perspective centre and the object. In the more intuitive negative image orientation the perspective centre is between the image and the object.

κ must be calculated in order to derive the final object co-ordinates of the solar image. Photogrammetric software like TRIPLET (in-house software) is designed to extract these values out of image co-ordinates.

The extremely long focal length of the lens tends to destabilize photogrammetric software like TRIPLET. To help the computer routine converge on a solution, estimates of the values of ω, ϕ and κ were derived from a computer model based on the three dimensional rotational matrix (Karara, 1989):

$$\mathbf{a} = \mathbf{MA}$$

$$\begin{bmatrix} x \\ y \\ z \end{bmatrix} = \begin{bmatrix} m_{11} & m_{12} & m_{13} \\ m_{21} & m_{22} & m_{23} \\ m_{31} & m_{32} & m_{33} \end{bmatrix} \begin{bmatrix} X \\ Y \\ Z \end{bmatrix}, \quad (53)$$

where x, y, z are the image co-ordinates, X, Y, Z are the object space co-ordinates and

$$\left. \begin{aligned} m_{11} &= \cos \phi \cos \kappa \\ m_{12} &= \sin \omega \sin \phi \cos \kappa + \cos \omega \sin \kappa \\ m_{13} &= -\cos \omega \sin \phi \cos \kappa + \sin \omega \sin \kappa \\ m_{21} &= -\cos \phi \sin \kappa \\ m_{22} &= -\sin \omega \sin \phi \sin \kappa + \cos \omega \cos \kappa \\ m_{23} &= \cos \omega \sin \phi \sin \kappa + \sin \omega \cos \kappa \\ m_{31} &= \sin \phi \\ m_{32} &= -\sin \omega \cos \phi \\ m_{33} &= \cos \omega \cos \phi \end{aligned} \right\}. \quad (54)$$

In the rotation matrix computer model the input values were the object space co-ordinates (in metres) of the treetops and the image space co-ordinates (in pixels).

The values of ω, ϕ and κ for Equation 54 were manually adjusted until the sum of the squares of the residuals between the original image co-ordinates and the calculated image co-ordinates was minimized. The adjustment to ω, ϕ and κ was aided by a graph showing the position of the modelled and the original image co-ordinates. Success was achieved when the modelled image coordinate points were on top of the original points.

After this procedure, these estimates of the object co-ordinates, image co-ordinates, focal length and values for ω, ϕ and κ were input to TRIPLET. Final values were then re-computed with convergence occurring significantly more quickly and with far fewer situations with solution divergence. Once the manual conditioning of the data is performed TRIPLET converges very rapidly and with very small residuals of usually less than a pixel. For a review of the underlying principals of the TRIPLET software (a Bundle Adjustment method) see Chapter 2 Appendix B.

The TRIPLET computed values of ω, ϕ and κ were then substituted into Equation 54 to produce a final rotation matrix (Equation 31). Given the image co-ordinates, to solve for the object co-ordinates requires the inversion of the rotation matrix (Equation 53). This was done using a FORTRAN program that performed a Gauss-Jordan Elimination method with full pivoting (Press, 1992). The FORTRAN code for this routine is listed in Appendix E.

The inverse rotation matrix was then used to directly convert the image co-ordinates of the solar profile into object co-ordinates (in metres). It is then a

simple matter of trigonometry to translate these values into altitude and azimuth angles.

3.7.5 Tree Sway Correction

It was found that all the sunset images were shifted towards the west relative to a theoretical azimuth by a fraction of an arcminute. Since all the images were taken during high winds it appears reasonable to assume that the treetop reference targets were systematically deflected towards the East.

Under windy conditions, it is not unreasonable to have 15 to 20 metre tall trees sway as much as 0.6-metres (Flesch and Wilson, 1998). Turbulent winds could cause the amount of sway to vary from tree to tree in a single photograph. In order to estimate the amount of azimuthal deflection of the treetops, the differences in horizontal angles were measured between a set of treetops and a distant high-tension transmission tower during high wind and calm conditions. Moderate westerly winds were experienced on all three occasions. From Stony Plain the hourly mean velocity was 13 km/h from the southwest on December 8, 1998, 28 km/h from west on December 14, 1998 and 28 km/h from the west on December 22, 1998. The average azimuthal deflection was found to be -12 ± 8 arcseconds (i.e. a deflection to the east) with a minimum deflection of -2 arcseconds and a maximum deflection of -22 arcseconds. At a distance of 2500 metres, this represents an average of 0.14 metres with a maximum value of 0.27 metres.

Once the azimuth of each sunset image was determined the final image was moved eastward to line up with the modelled image. Although it would be difficult

or impossible to measure the mean deflection due to tree sway in each photograph, the small correction (-1.3 to 0") applied to each image appears justified given the preceding argument. Correction values are listed with each image (see Figures 29a to 43a).

4. Results

Before proceeding with the comparison of the observed and the modelled astronomical refraction the choice of ray path increment was investigated as well as some details regarding the meteorological data obtained from sounding.

The measured refraction was also compared to the model values using a Modified U.S. Standard Atmosphere (MUSSA) rather than the measured atmosphere from the rawinsonde. The use of publicly accessible sounding files (the significant and mandatory level files) is also explored with the intent of investigating the effectiveness of the model with the large archived database of soundings. The possible sensitivity of the model to horizontal temperature gradients is also discussed. Finally the model output is compared with the Pulkovo Refraction Tables – long considered the standard for astronomical refraction values at high zenith angles.

4.1 Sensitivity Analysis ($\delta\theta$)

The refraction model was optimized with respect to the ray path increment $\delta\theta$. This is done in order to ensure the model produces the best possible results but with the minimum amount of computation time. The sensitivity of the

model to the selection of a value of $\delta\theta$ may depend on the particular sounding characteristics or the altitude of the Sun.

In order to determine a suitable value of the ray path increment $\delta\theta$, the value was changed until no further change in the modelled refraction output was observed. To test the effect of altitude and sounding characteristics on the model response, two times from each date were selected to represent the Sun at its highest and lowest observed altitude. The model was then run with different values of $\delta\theta$. The results appear in Figure 18.

It is apparent that the model produces unrealistic astronomical refraction at values of $\delta\theta$ greater than about $0^\circ.05$ and no apparent improvement occurs with values less than about $0^\circ.001$. Therefore, a value of $0^\circ.001$ for $\delta\theta$ is a reasonable compromise between computational speed and model stability.

4.2 Comparison of Photogrammetric Data and the Ray Tracing Model

4.2.1. Atmospheric Soundings

During the experiment Environment Canada used both the VIZ Mark II rawinsonde system and the Vaisala RS80. At this time Environment Canada was converting to Vaisala RS80 and the surplus VIZ rawinsondes were being used for training purposes. The December 8 sounding was produced using a VIZ rawinsonde. This VIZ rawinsonde produces a coarser vertical temperature resolution. During the summer of 2000, more than half of a sample of about 24 used at the Winnipeg office of the Environment Canada were found to be faulty during preflight calibration and rejected before launch (Personal communication,

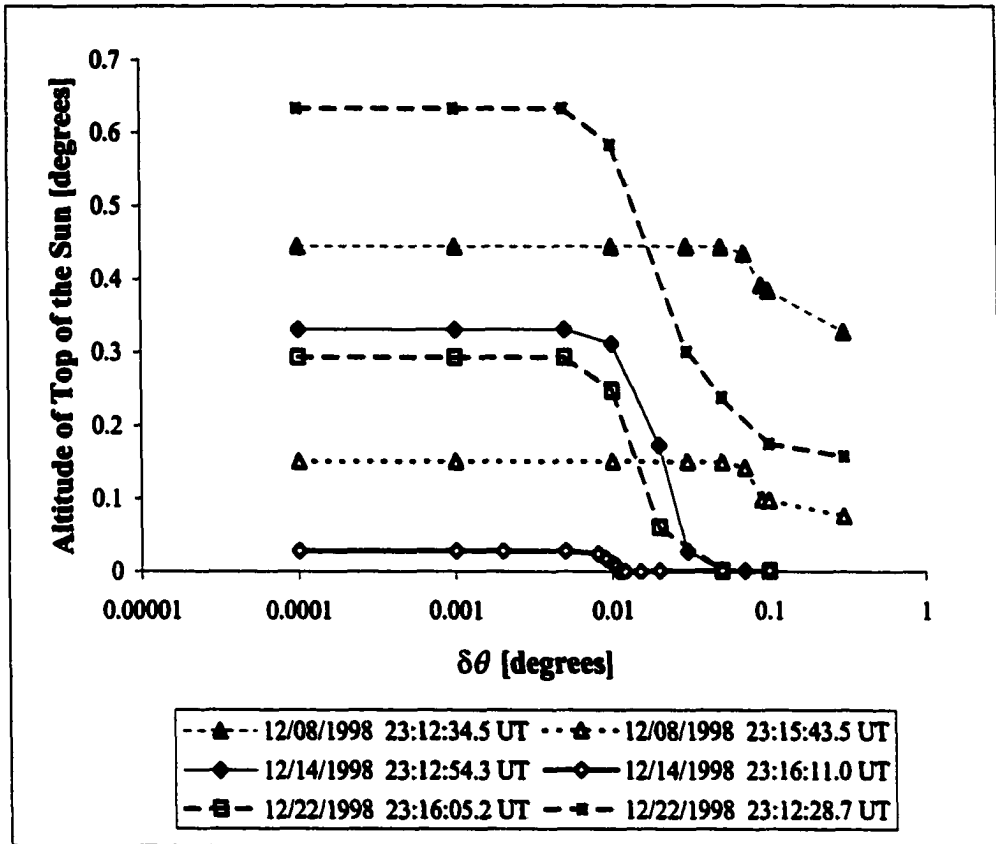


Figure 18: The variation in modelled altitude of the refracted Sun (upper-most point on the solar profile) as a function of the ray path increment $\delta\theta$. All three sunset cases are represented with one higher and one lower altitude value. From this graph it is apparent that values of $\delta\theta$ less than about $0^\circ.05$ produce no significant difference in the value of the refracted solar altitude.

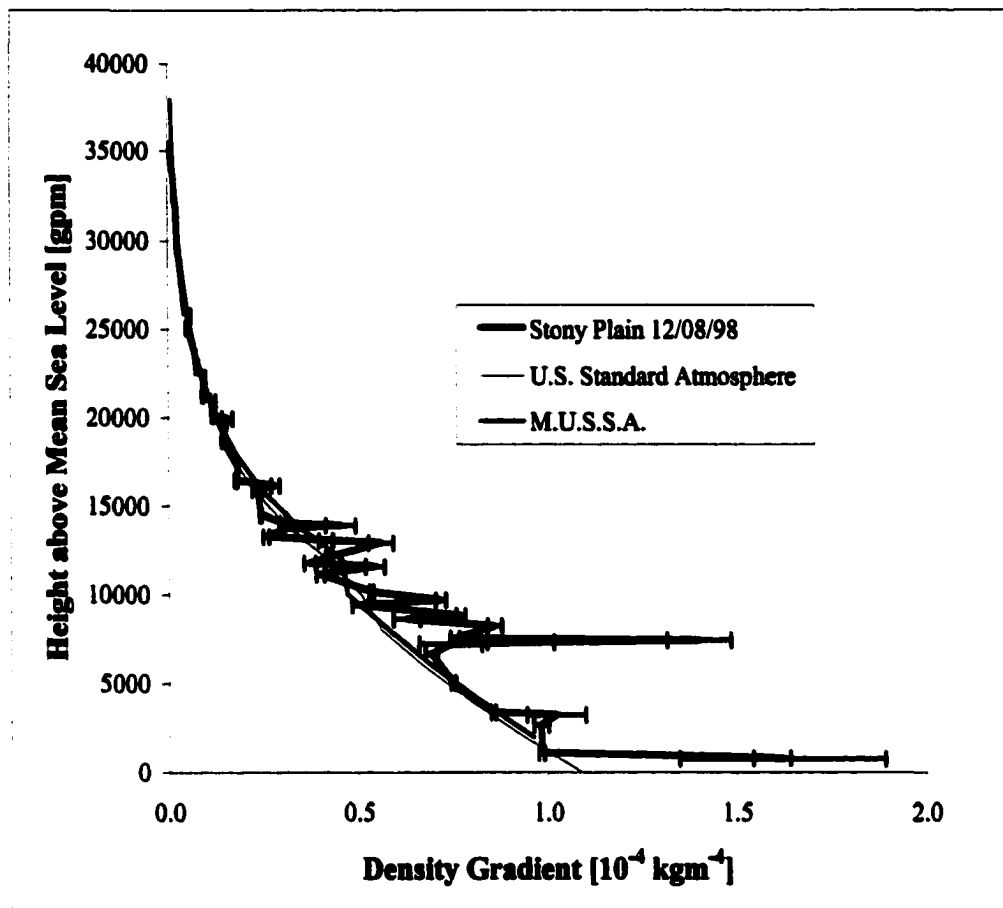


Figure 19: Observed density gradient profile for the Stony Plain, Alberta, December 8, 1998, 23:15 UTC sounding compared to the U.S. Standard Atmosphere and MUSSA profile. Meteorological data collected with a VIZ rawinsonde system. The altitude of the Stony Plain Upper Air station is 766 metres above mean sea level. The error bars indicate the uncertainty in the density gradient produced by error propagation of the meteorological parameters through the equation for density. Magnified portions of the graph (Figures 20 and 21) help illustrate the relationship between gradient error and proximity to the U.S. Standard Atmosphere profile and a MUSSA profile.

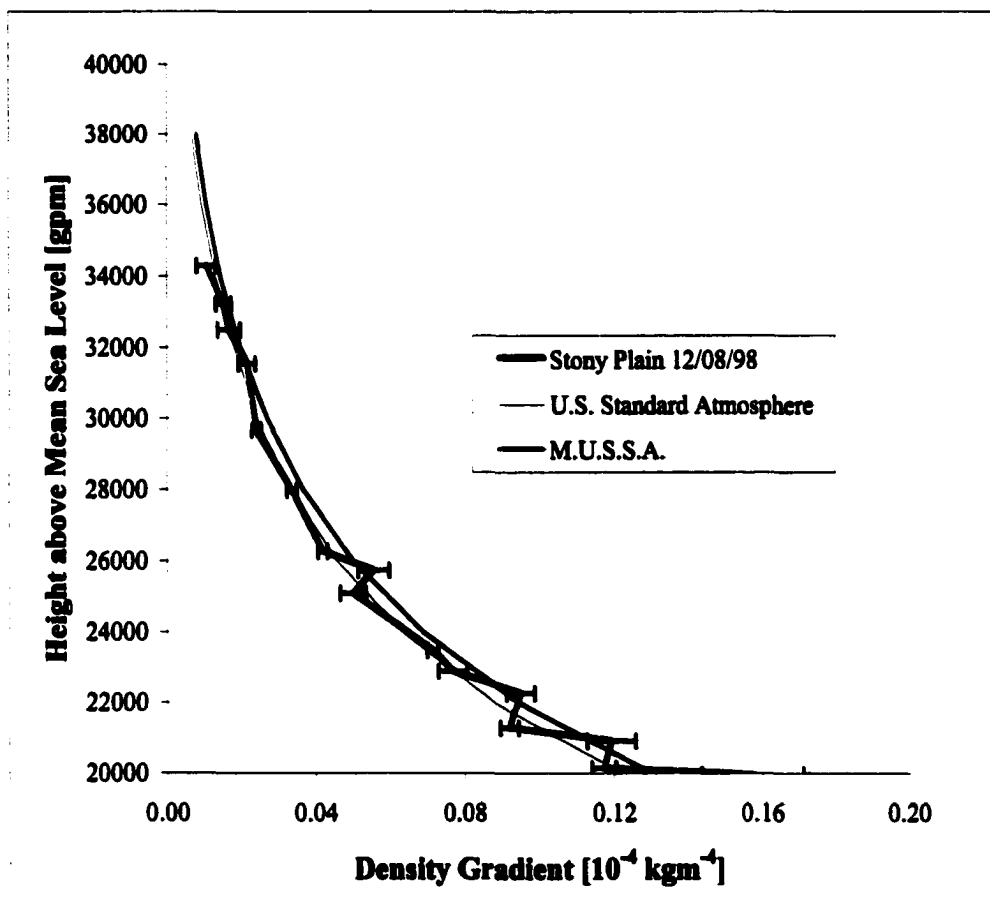


Figure 20: Upper portion of the density gradient profile for the Stony Plain, Alberta, December 8, 1998, 23:15 UTC sounding (VIZ rawinsonde).

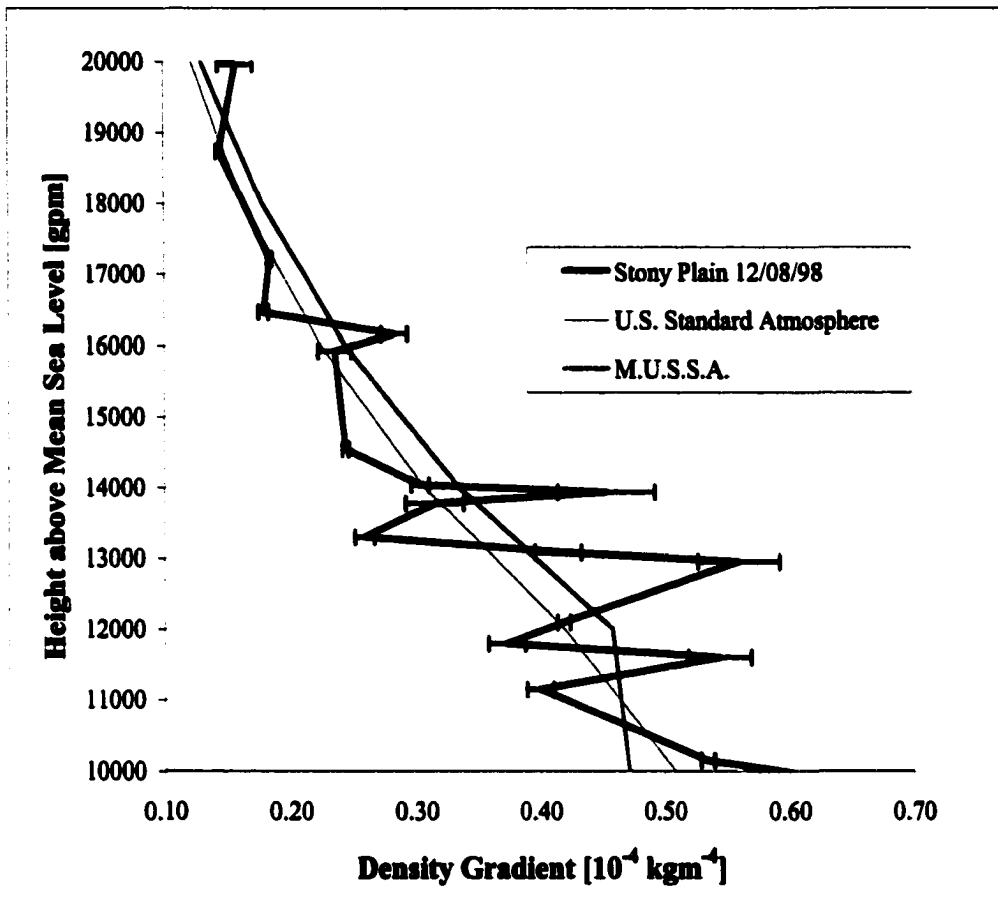


Figure 21: Middle portion of the density gradient profile for the Stony Plain, Alberta, December 8, 1998, 23:15 UTC sounding (VIZ rawinsonde).

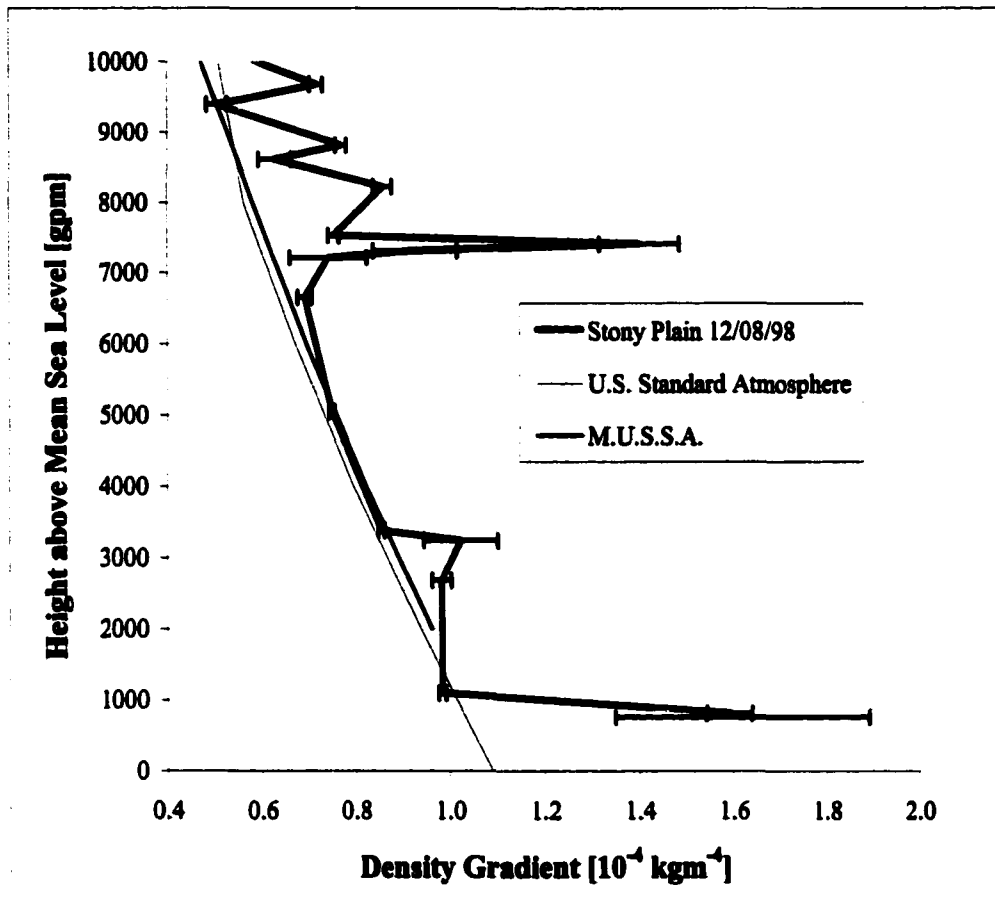


Figure 22: Lower portion of the density gradient profile for the Stony Plain, Alberta, December 8, 1998, 23:15 UTC sounding (VIZ rawinsonde).

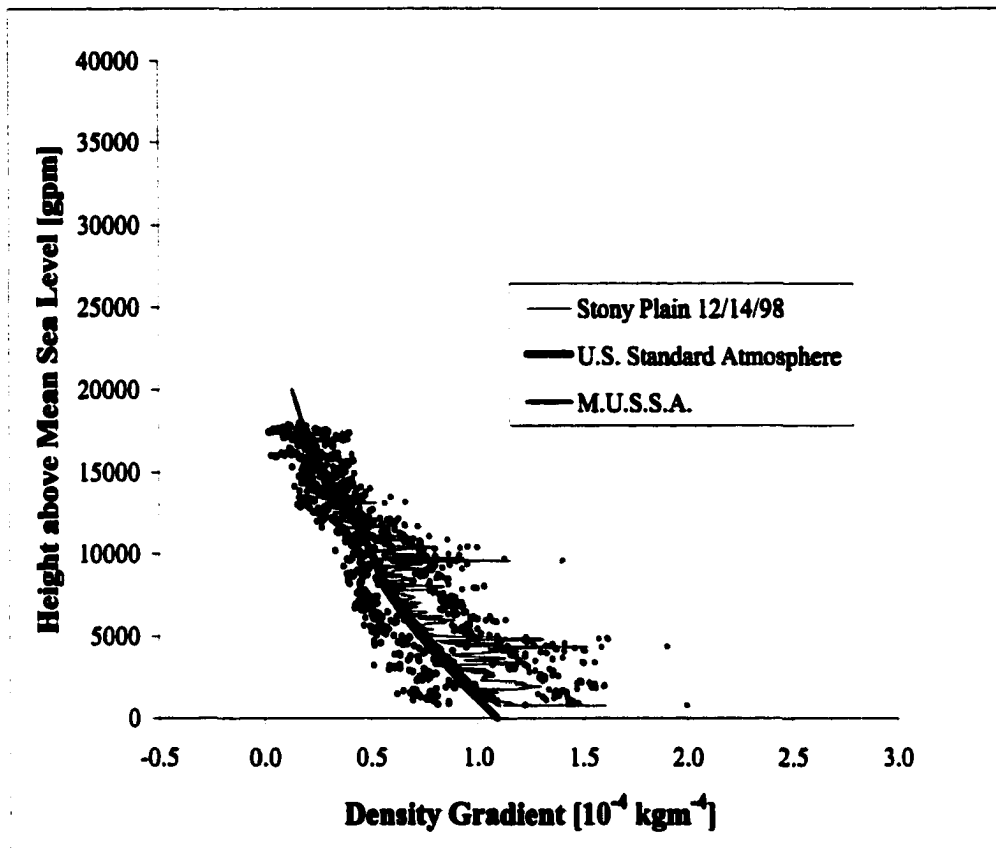


Figure 23: Density gradient profile for the December 14, 1998, 23:15 UTC sounding from the Stony Plain Upper Air station (766 metres above mean sea level). The U.S. Standard Atmosphere and MUSSA profile is shown for comparison. Data for the observed profile were collected using a Vaisala RS80 rawinsonde system which samples every 10 seconds. On this day the balloon appears to have burst prematurely. The red and blue dots represent the positive and negative uncertainties due to instrument error in the observed profile (± 0.2 K, ± 0.1 hPa, $\pm 2\%$ R.H., and ± 3 gpm). These values were calculated using the error propagation method outlined in Taylor (1982).

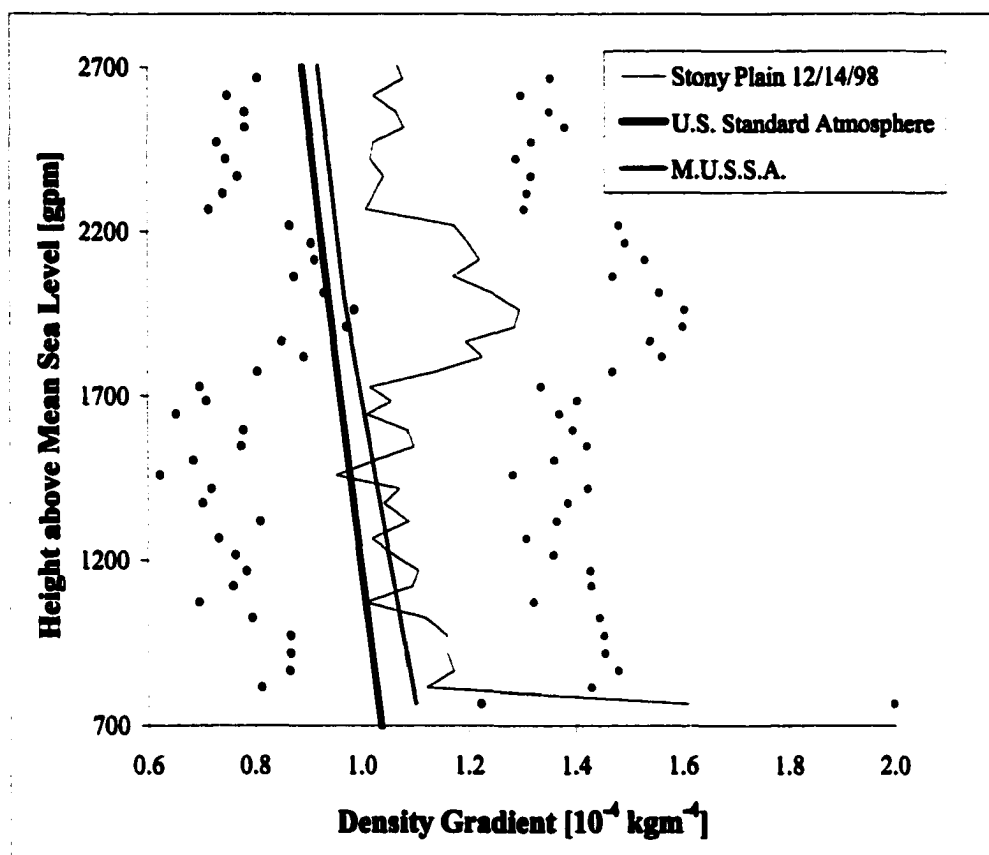


Figure 24: The planetary boundary layer density gradient profile for the December 14, 1998, 23:15 UTC sounding from the Stony Plain Upper Air station (766 metres above mean sea level). The U.S. Standard Atmosphere and MUSSA profiles are shown for comparison. Data for the observed profile was collected using a Vaisala RS80 rawinsonde system which samples every 10 seconds. On this day the balloon appears to have burst prematurely. The red and blue dots represent the positive and negative uncertainties due to instrument error in the observed profile (± 0.2 K, ± 0.1 hPa, $\pm 2\%$ R.H., and ± 3 gpm). These values were calculated using the error propagation method outlined in Taylor (1982).

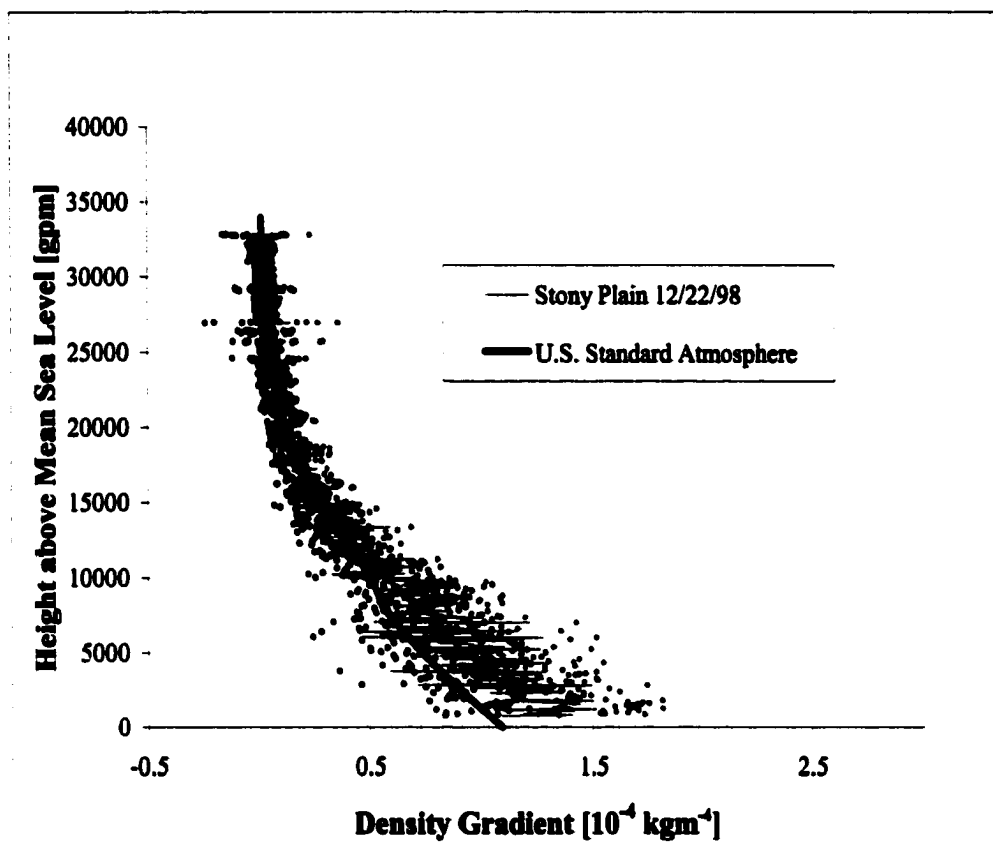


Figure 25: Density gradient profile for the December 22, 1998, 23:15 UTC sounding from the Stony Plain Upper Air station (766 metres above mean sea level). The U.S. Standard Atmosphere profile is shown for comparison. Data for the observed profile were collected using a Vaisala RS80 rawinsonde system which samples every 10 seconds. The red and blue dots represent the positive and negative uncertainties due to instrument error in the observed profile (± 0.2 K, ± 0.1 hPa, $\pm 2\%$ R.H., and ± 3 gpm). These values were calculated using the error propagation method outlined in Taylor (1982).

David Carlsen, Meteorological Service of Canada, 2000). It was assumed that these defects were due to their state of deterioration from prolonged storage.

Portions of the sounding files can be seen in Appendix G. The Vaisala RS80 rawinsonde (December 14 and 22) transmits every 10-seconds or approximately every 50 metres. It was assumed that this increased data rate would improve the refraction modelling, since the crucial boundary layer density gradient would be more finely resolved.

As mentioned in Appendix D, the measurement uncertainty from a Vaisala RS80 rawinsonde as specified by the manufacturer is ± 0.2 K for temperature, ± 0.1 hPa (hectopascals) for pressure and $\pm 1\%$ for relative humidity (Vaisala online technical specifications, 1998). The VIS Mark II rawinsonde has the same specified accuracy except for humidity, which is stated to be $\pm 2\%$ (Sippican Inc, 1998). Comparisons between different rawinsonde models suggest that the manufacturer's stated temperature accuracy may be overoptimistic. The range of temperatures between rawinsonde models shows a range of about ± 0.4 K near the surface and ± 3.0 K at 10 hPa (Schmidlin and Finger, 1987). Much larger errors can occur due to faulty observation, data reduction and archiving of sounding data (Schartz and Doswell, 1991). A common error is not allowing the temperature sensor to reach equilibrium before launch. Sounding balloons are assembled in heated or air-conditioned shelters and the sensor may retain a thermal memory of the indoor environment. Thermal lag of the temperature sensor also causes the temperature values to lag a few seconds behind the ascent of the balloon (Mahesh, et al, 1997). Vaisala claims that the thermal lag of the RS80 temperature sensor is 2.5 seconds at

1000 hPa. It should also be noted that the surface temperature value for all soundings is not derived from the temperature sensor in the rawinsonde, but from a surface meteorological station. These stations are not always in the same location as the launch site of the rawinsonde.

The height of the sounding levels is determined from an integration of the hydrostatic equation. The absolute error of the height increases with increased height. The RS80 has a height error of less than a metre at pressures of 900 hPa or less (i.e. below a kilometre above mean sea level) and increases to about 20 metres at 10 hPa (about 31 km) (Antikainen and Hyvönen, 1983). Similar height errors were found in other rawinsonde models, with a slight increase in the error at low levels during daytime launches (Schmidlin and Finger, 1987). This increase is due to solar radiation, and in the RS80 is corrected using a standard algorithm (Luers and Eskridge, 1995). The radiation error during sunset is very low near the surface.

The ascent rate of the balloon is about 5 ms^{-1} and the duration of the sounding is about 100 minutes. At a height of about 32,000 gpm the balloon bursts and the detection of an increase in pressure stops the data transmission.

From the density gradient profiles (Figures 5, 7 and 9), it is apparent that the observed profiles have a considerable amount of fine-scale variability. To help determine whether this variability could be real or due to instrument noise, an error propagation analysis was performed on the density gradient data. The error bars in Figures 19 to 22 and the red and blue points in Figures 23, 24 and 25 indicate the uncertainty in the density gradient found through a propagation of the uncertainties in humidity, pressure, temperature and height through the density gradient formula.

The error propagation method is outlined in Taylor (1982). It is apparent from this analysis that much, but certainly not all, of the fine scale variations in the density gradient may be due to instrument noise since the calculated error is larger than the measurement fluctuations. The majority of the error appears to originate from the uncertainty in the temperature measurements. It is also interesting to note that in the December 8 profile, those rawinsonde density gradient values in the troposphere with the smallest uncertainties consistently fall very near the Modified U.S. Standard Atmosphere density gradient profile. This suggests that the density gradient in this case may have been very similar to a MUSSA profile.

4.2.2 Comparison of Observed and Modelled Astronomical Refraction Using Rawinsonde Profiles

Successful photographs from Stony Plain, along with theodolite measurements at the University of Alberta, were obtained on December 8, 14 and 22, 1998 (see Figures 26 through 28). The model was run for three wavelengths of visible light: 660 nm (red), 580 nm (yellow) and 530 nm (green). Blue (470 nm) was not included since very little light of this wavelength is directly transmitted through the atmosphere at high zenith angles (Lynch, and Livingston, 1995). Output values included altitude and azimuth for points on the limb of the geometric (i.e. unrefracted) Sun and the modelled Sun. The results were then plotted against the co-ordinates of the observed sunset extracted from the photographs (see Figures 29a to 43a).

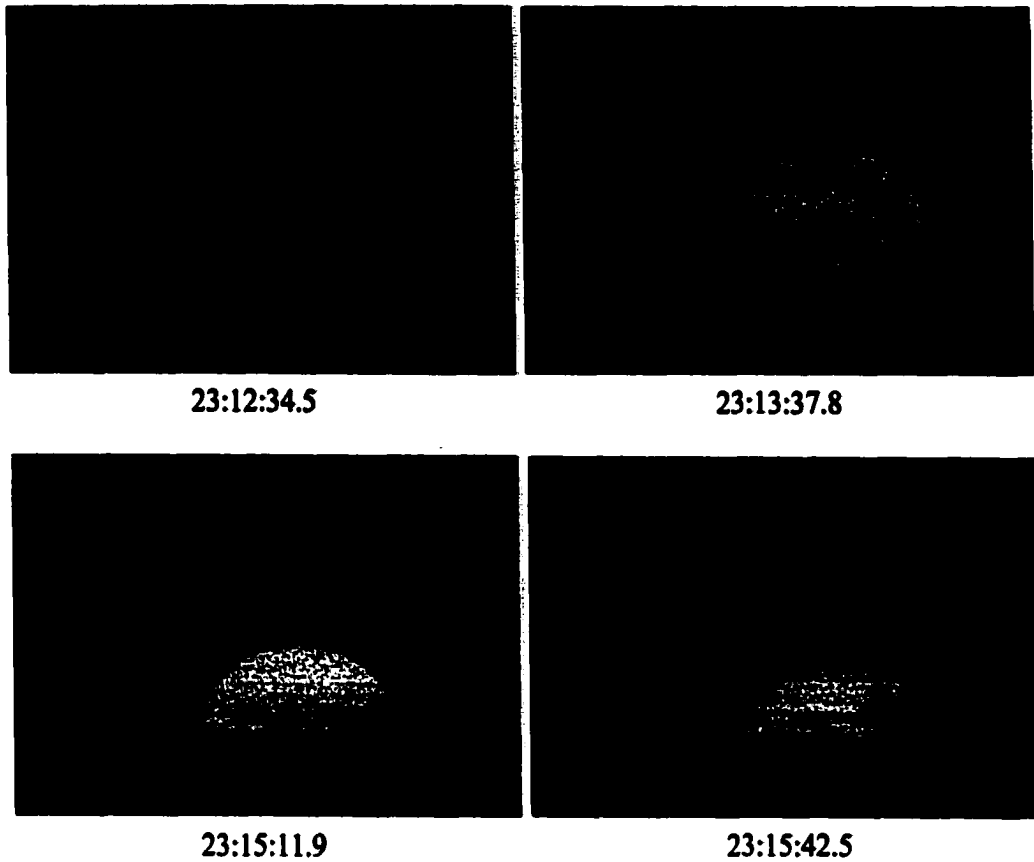


Figure 26: Stony Plain sunset sequence used in the ray-tracing comparison for December 8, 1998. All images are full frame. All times are in UT. Rawindsonde launch 23:15 UT.

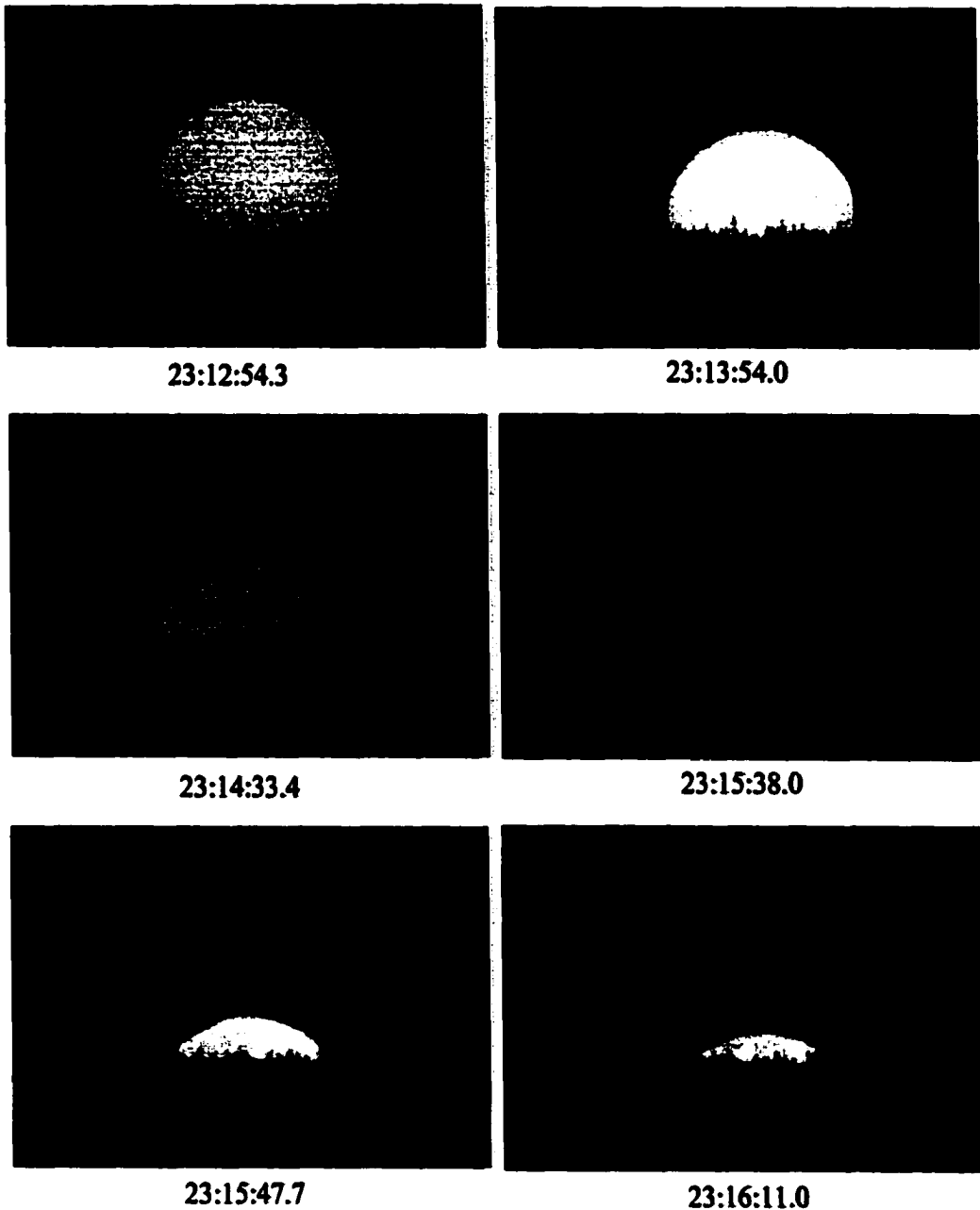


Figure 27: Stony Plain sunset sequence used in the ray-tracing comparison for December 14, 1998. All images are full frame. All times are in UT. Rawindsonde launched at 23:15 UT.

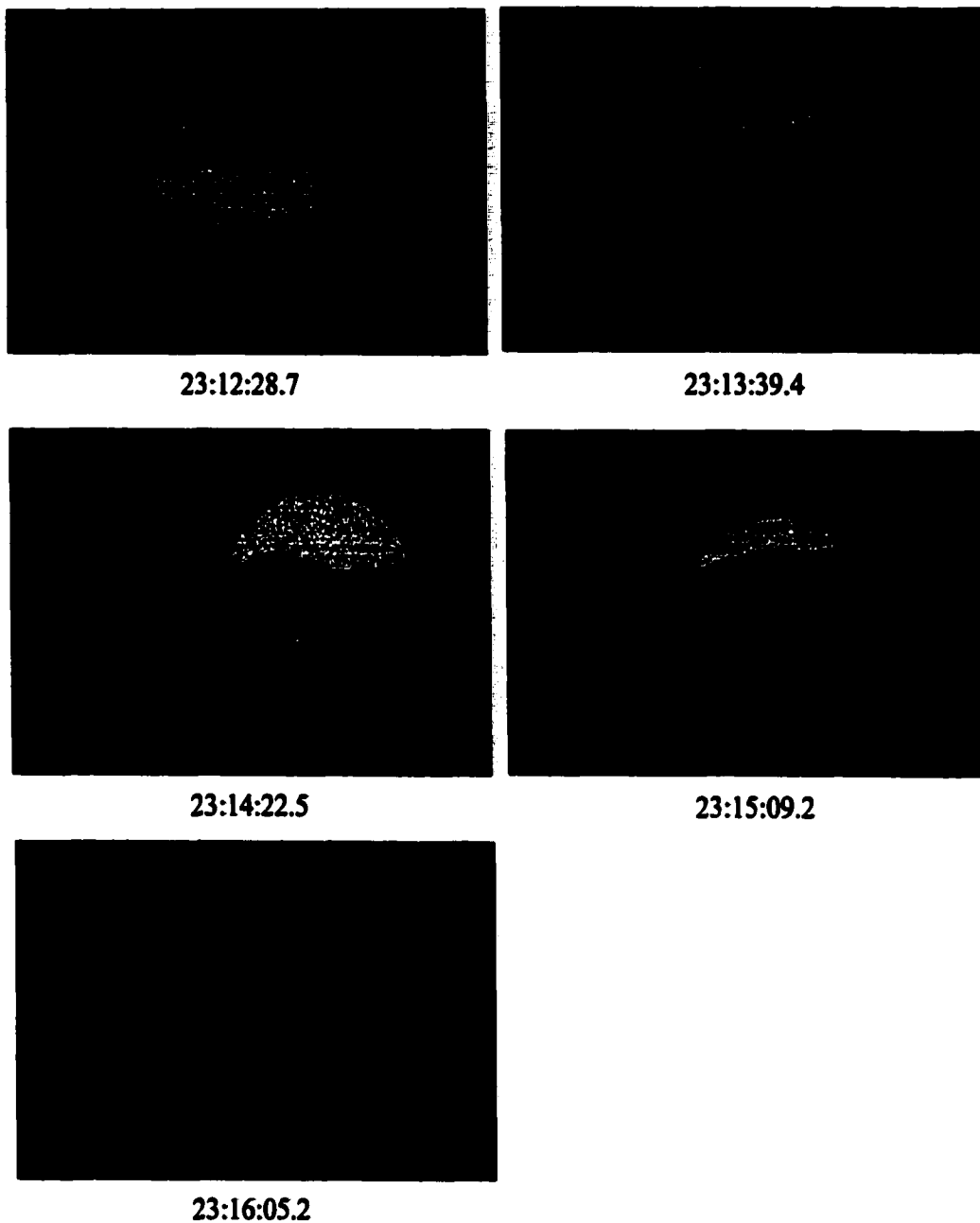
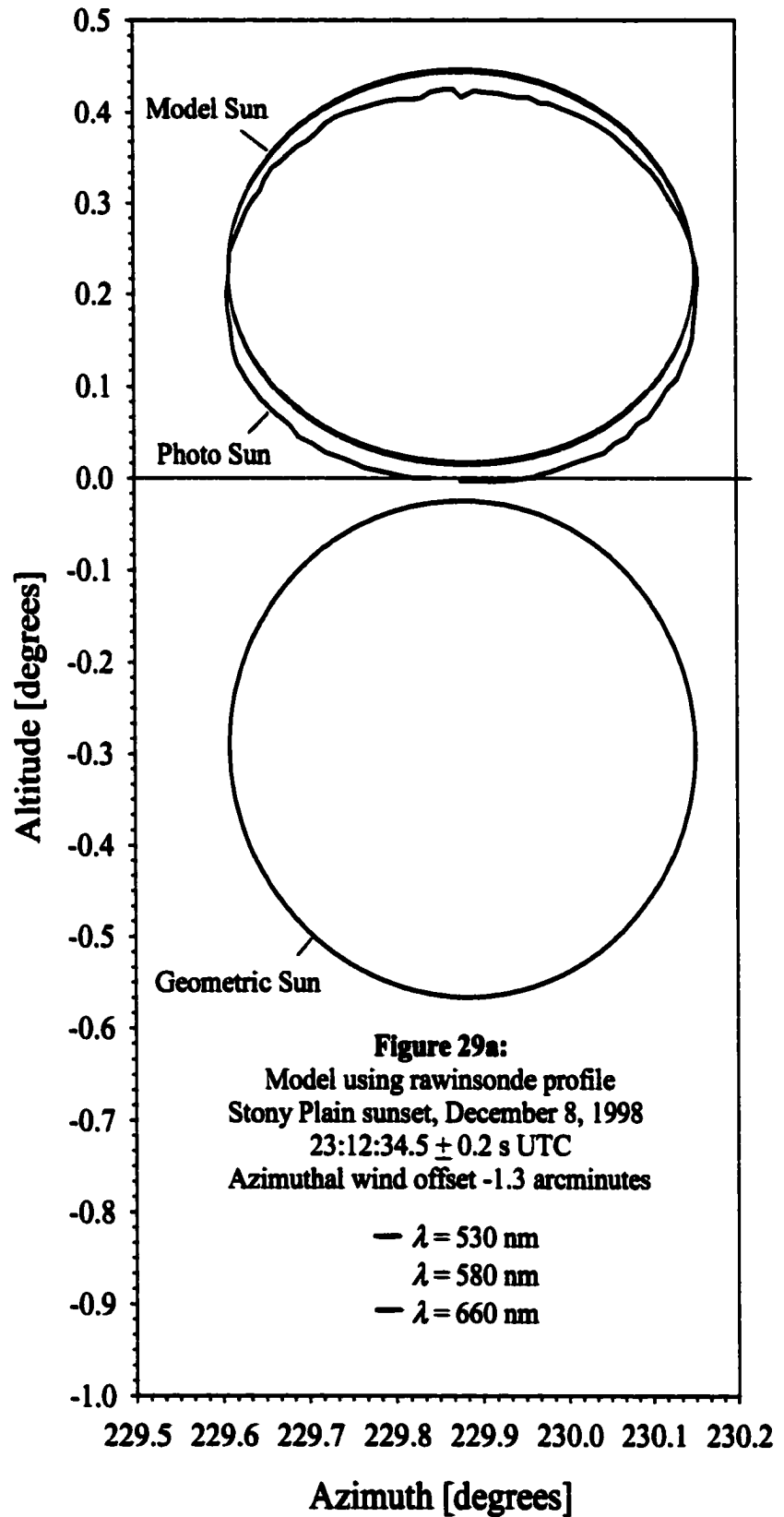


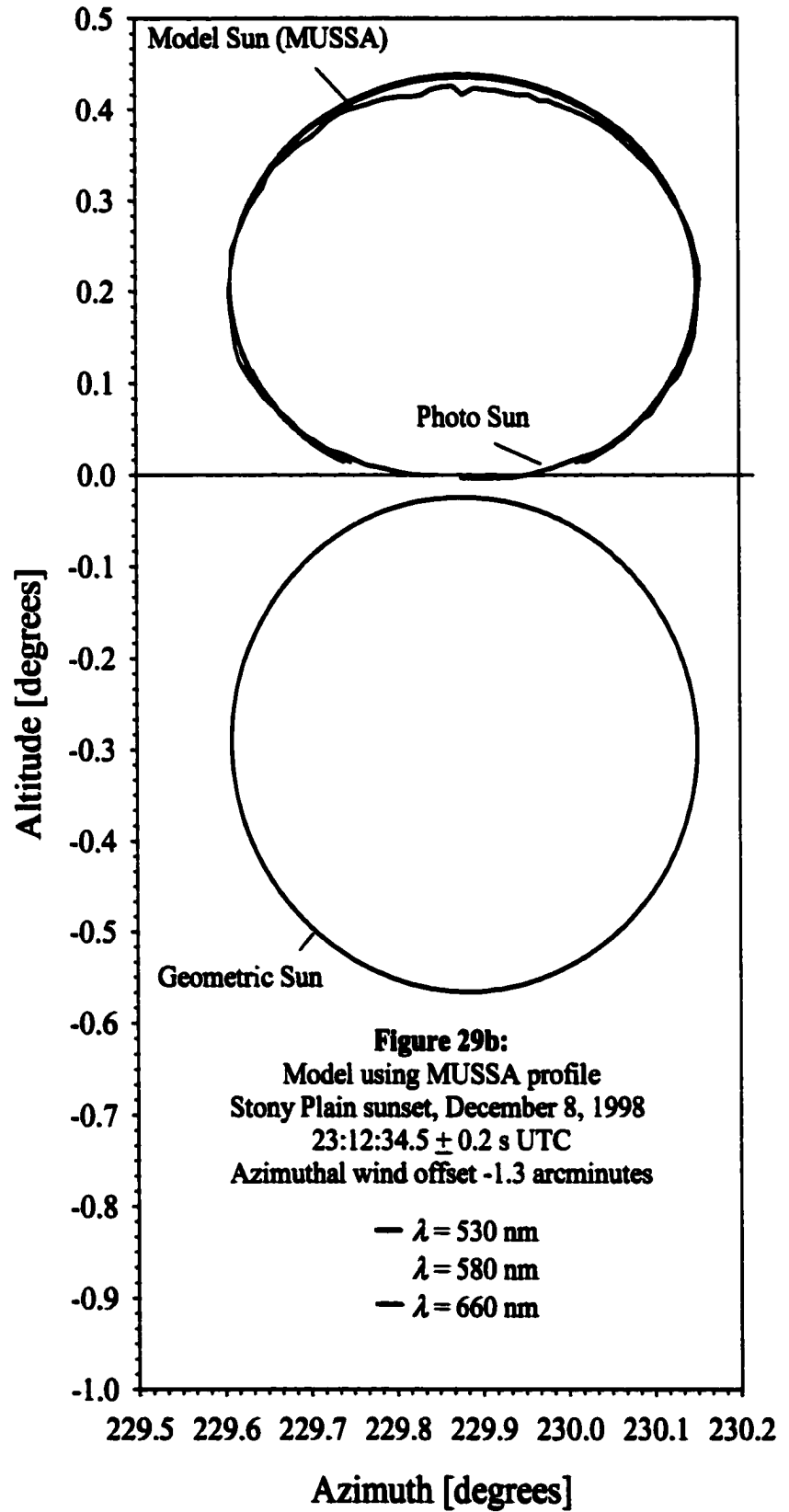
Figure 28: Stony Plain sunset sequence used in the ray-tracing comparison for December 22, 1998. All images are full frame. All times are in UT. Rawindsonde launched at 23:15 UT.

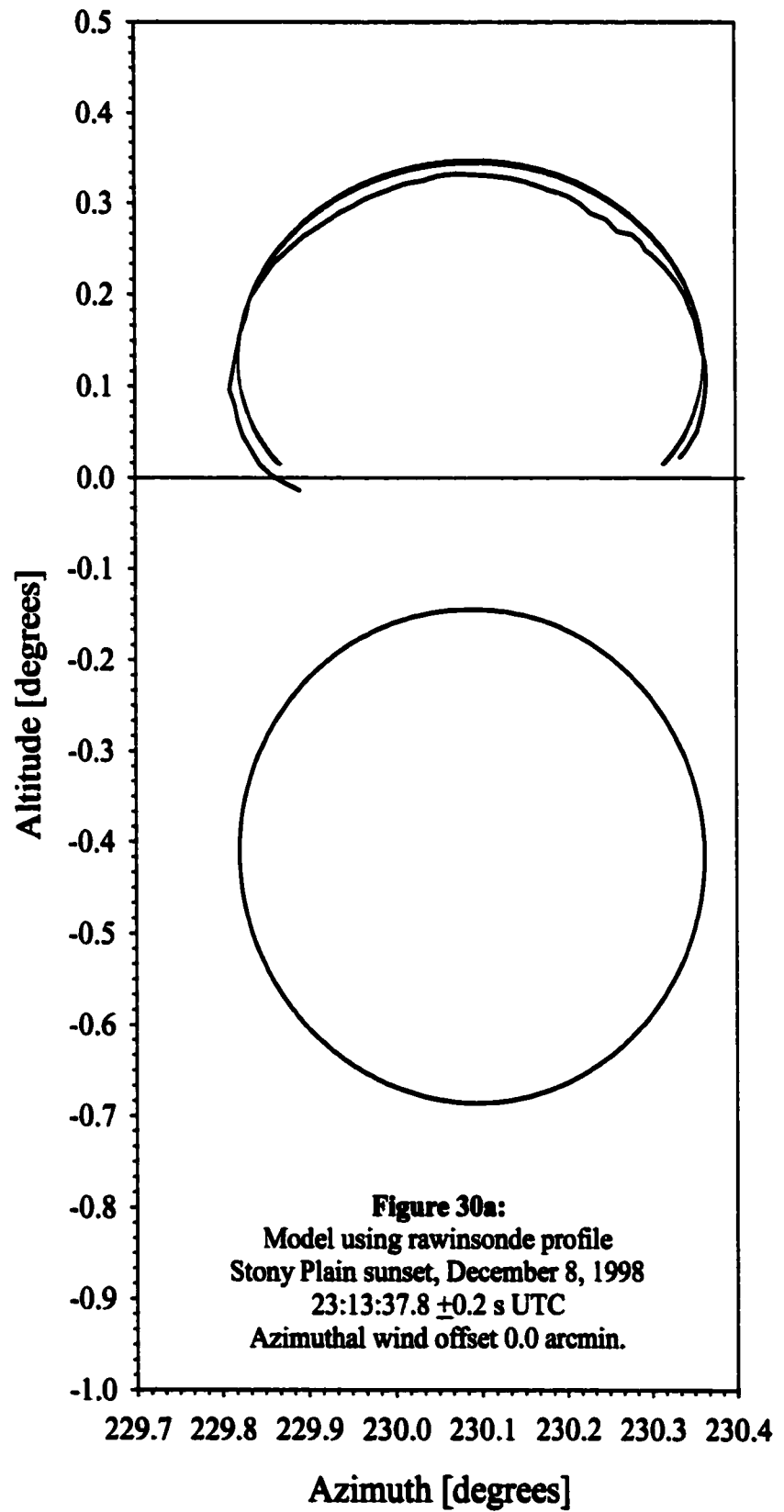
4.2.3 Photogrammetric and Theodolite Results

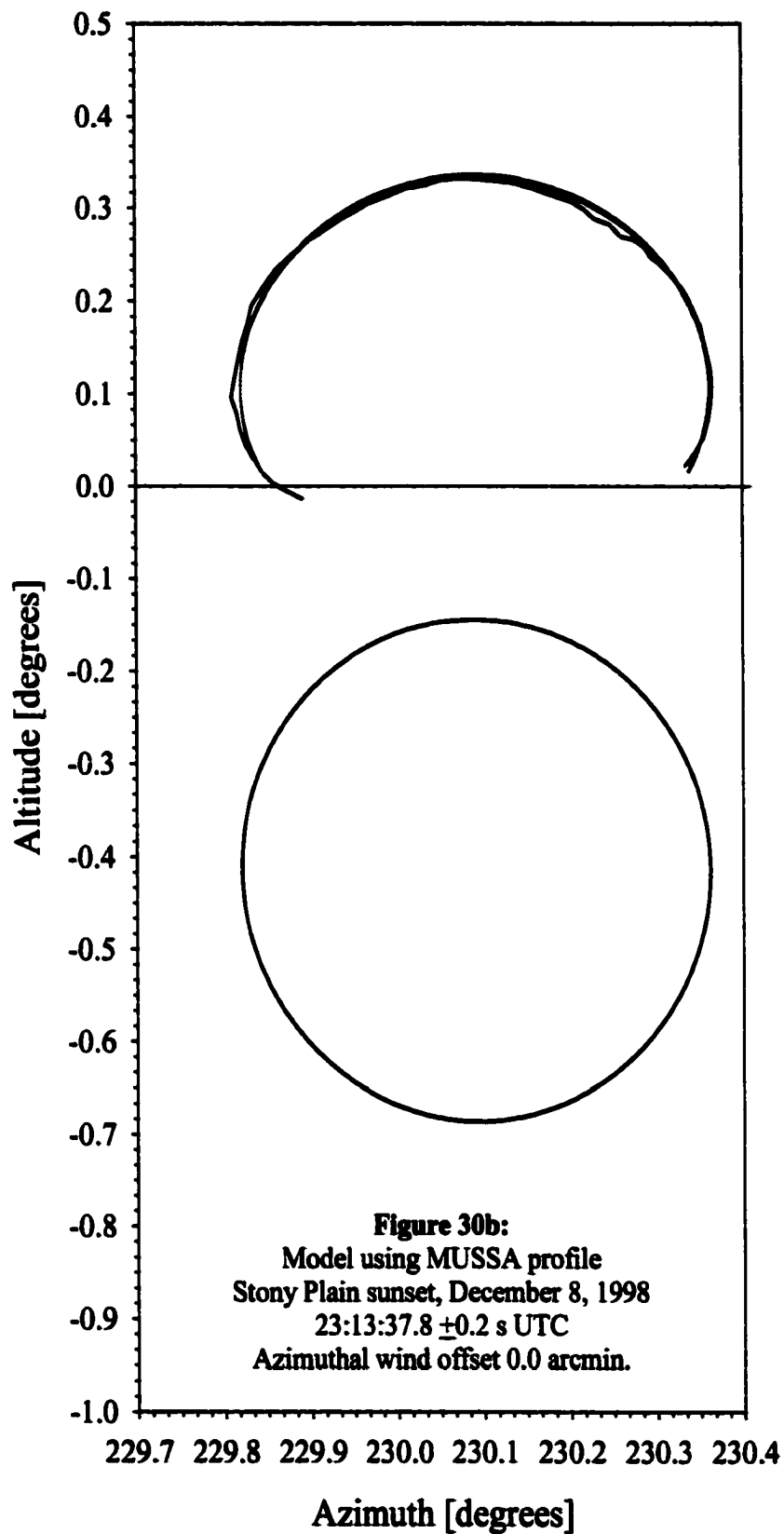
From a qualitative examination of Figures 29a to 43a the agreement between the model and the photogrammetric measurements appears to be better for the December 14 and 22 sunsets. On the December 14 graphs, the lines for the model and the observations overlap for altitudes greater than about $0^{\circ}.1$. This suggests that the difference between the model and the observed refraction is approaching the uncertainty of the model and the observations. The same may be true for altitudes above $0^{\circ}.4$ in the graphs of the December 22 sunset. During the December 8 sunset, the difference between the model and the observed refraction is greater than the estimated error.

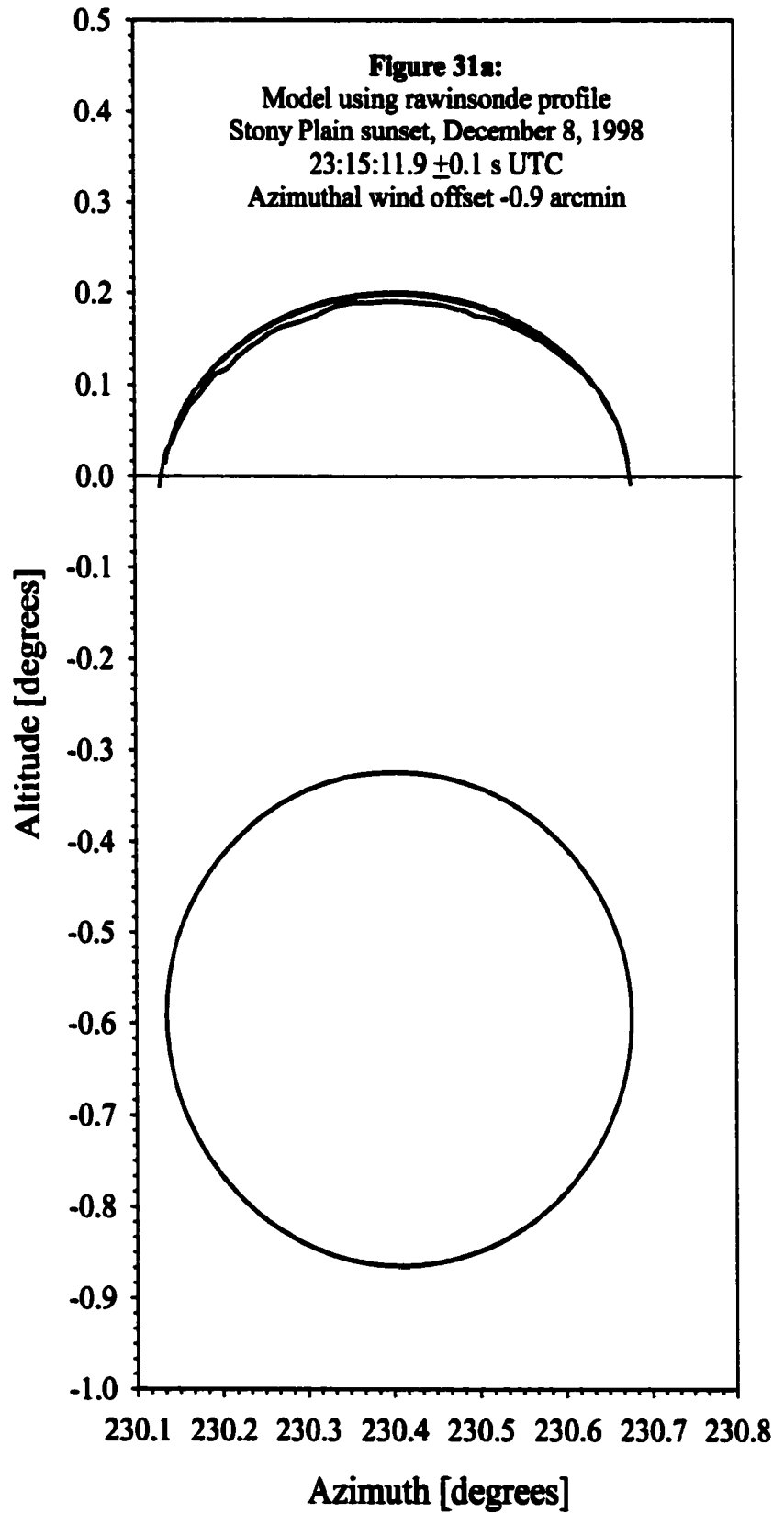
A quantitative comparison between the modelled and observed refraction, including results from the theodolite measurements, was performed by subtracting the altitude of the top of the observed solar profile (i.e. maximum observed altitude) from that of the highest point produced by the model (see Figure 44). Since astronomical refraction is primarily vertical, the analysis becomes ambiguous when points along the 'side' of the observed solar image are compared with values produced by the model. The modelled (yellow light) and observed refraction from the theodolite (Tory rooftop) can be seen in Figure 44. The minimum timing error with the theodolite was estimated to be about 1 second, while the maximum error (due to the increasing scintillation of the image as it approached the horizon) was estimated to be about 3 seconds. These timing error estimates were established from discussions with the observer and can be considered only intuitive measures rather than quantitative. The maximum error occurred just before sunset due to the

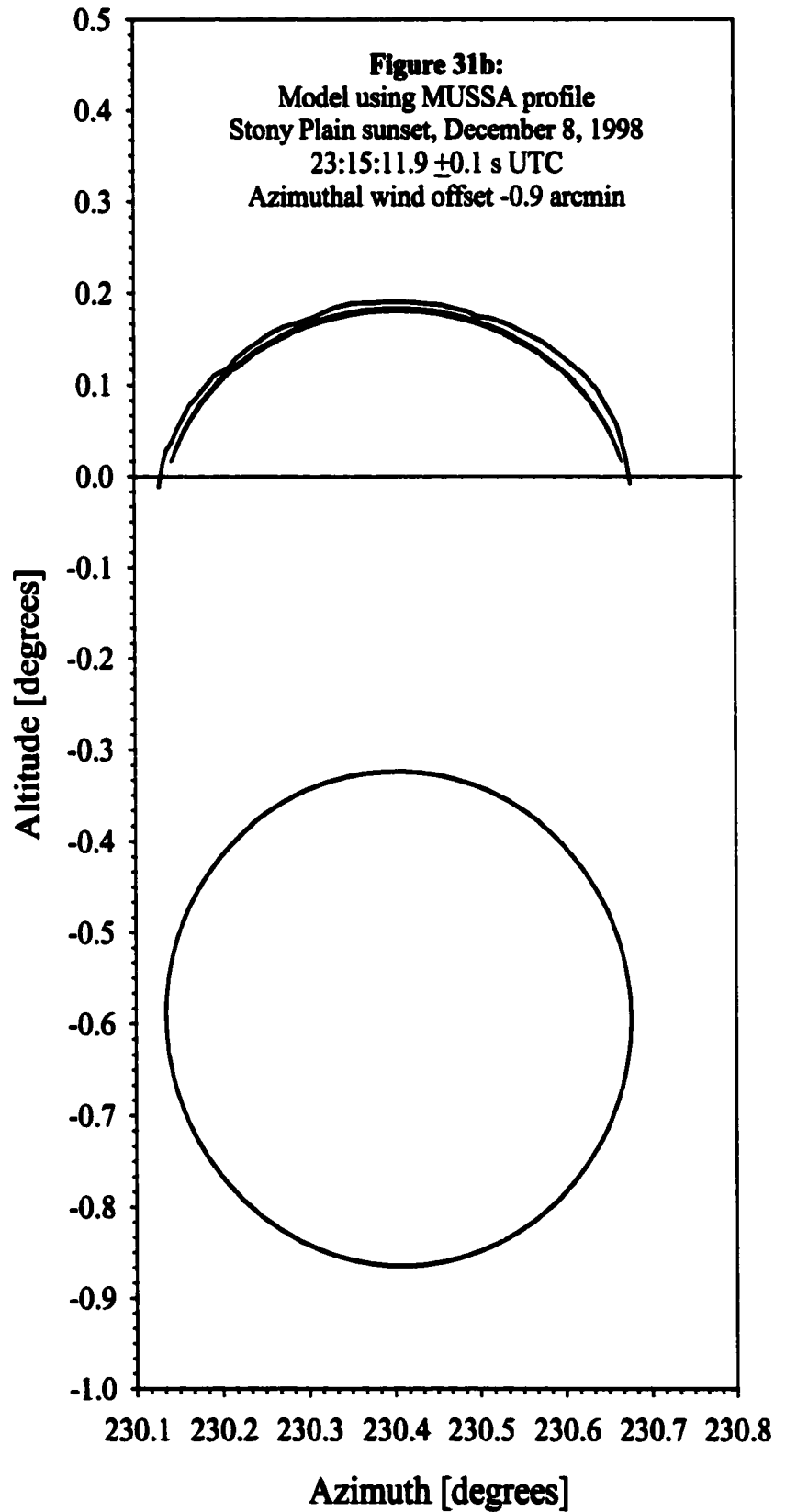


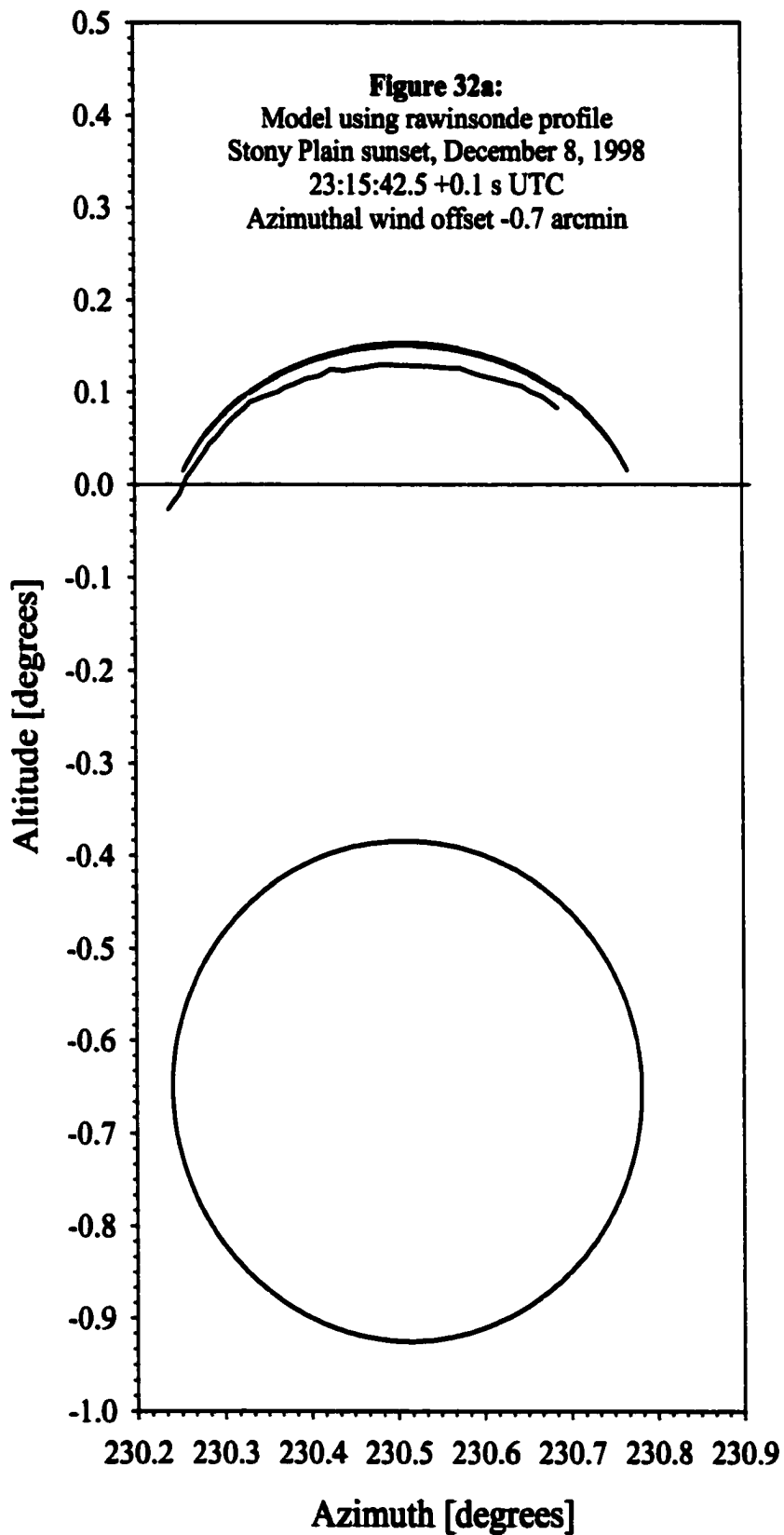


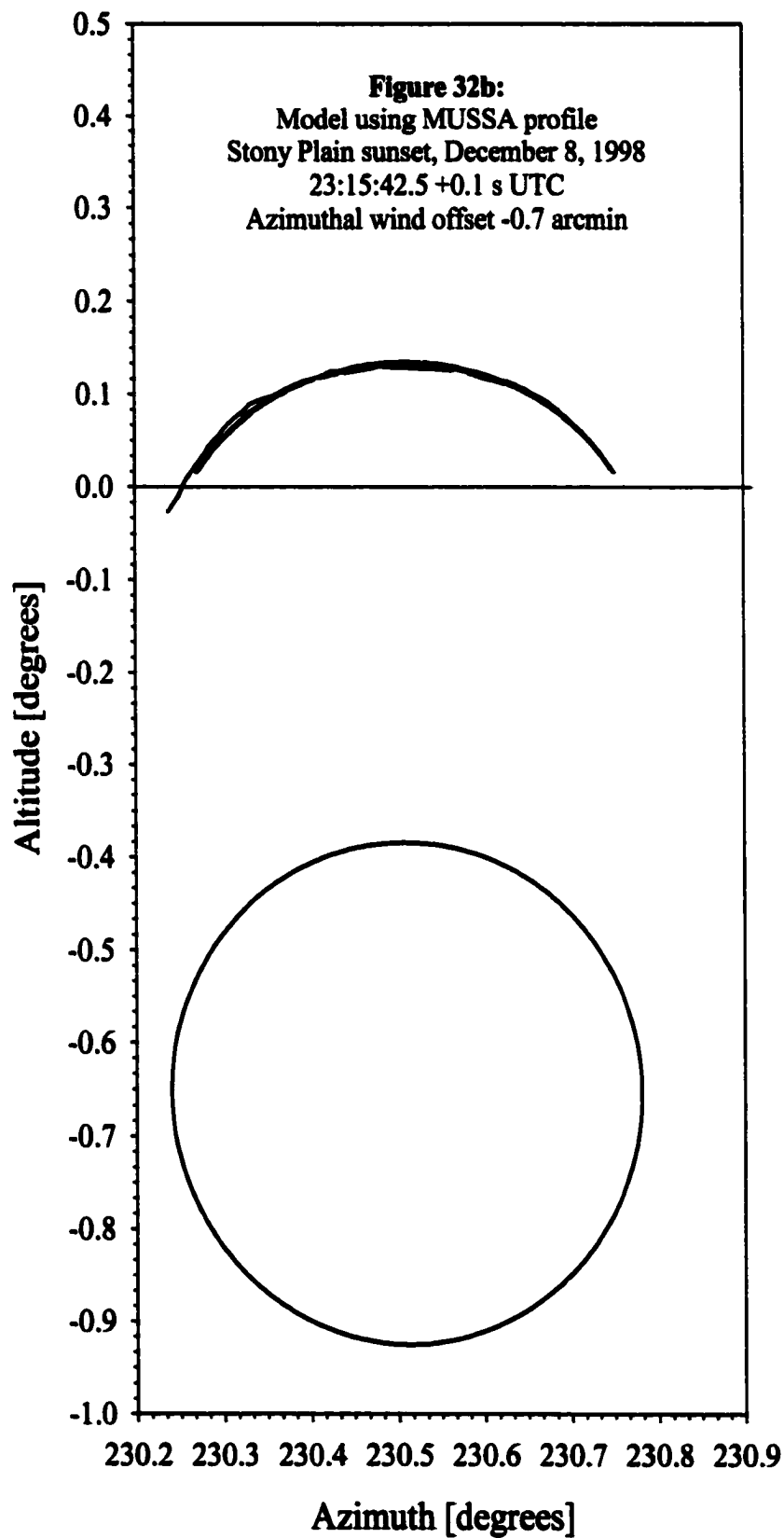


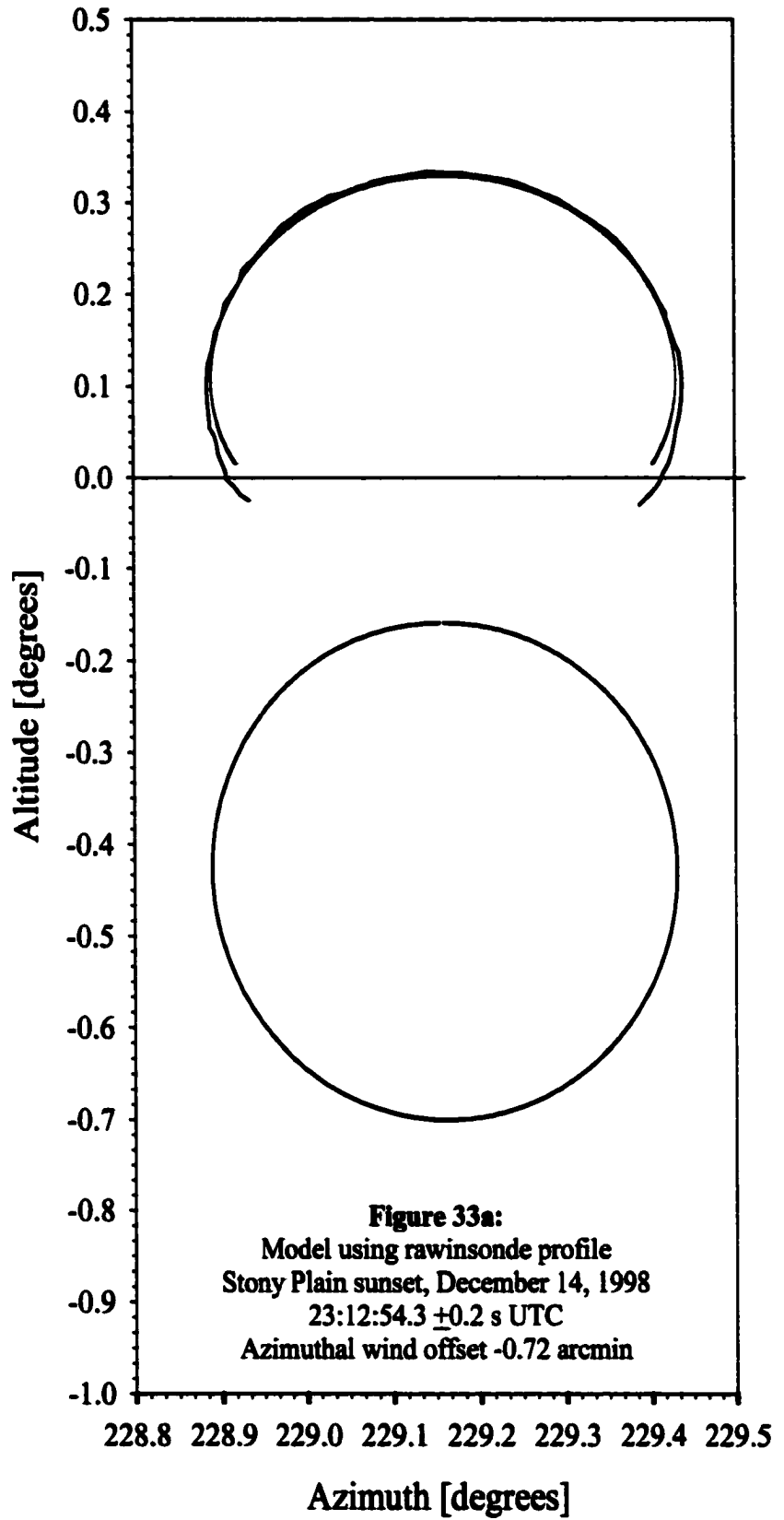


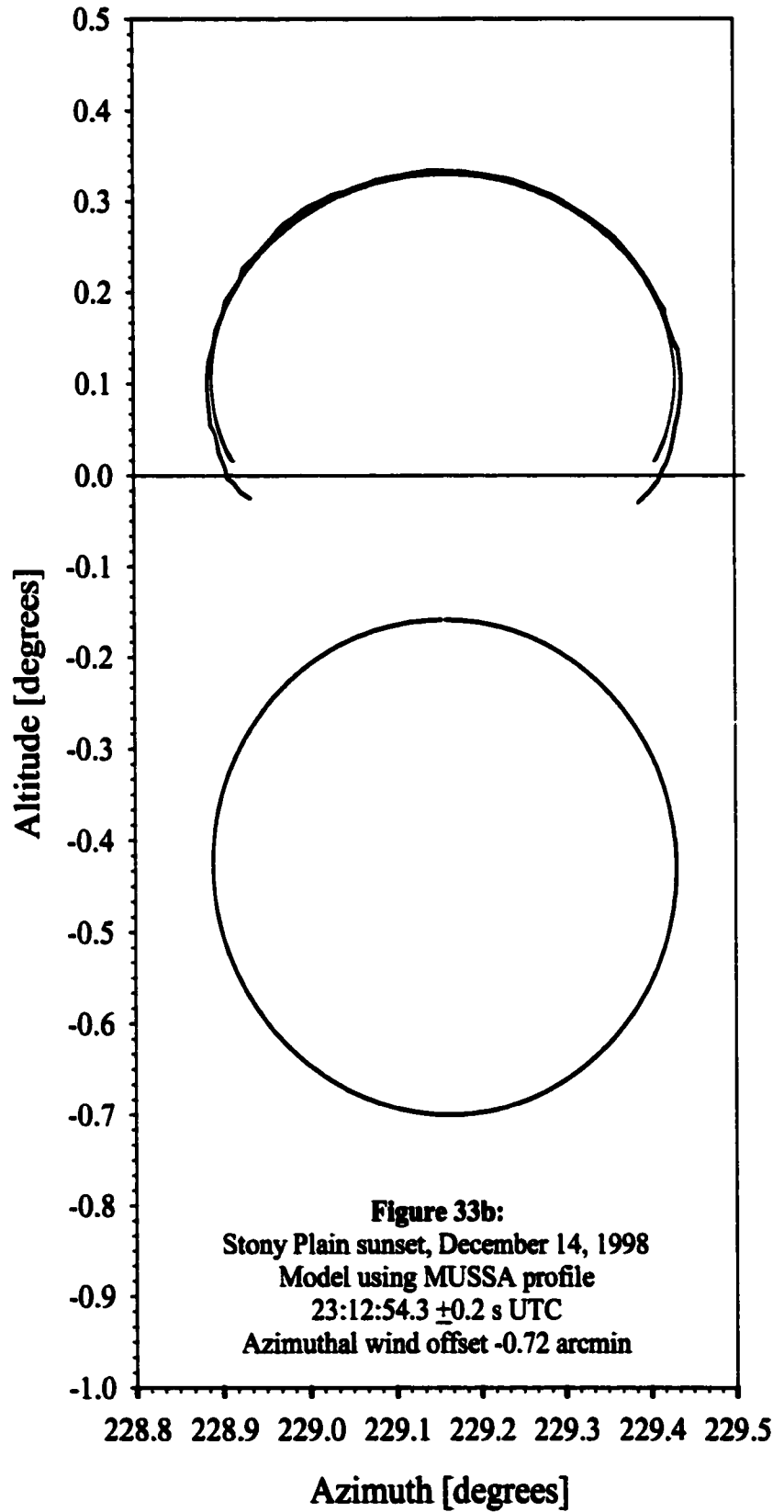


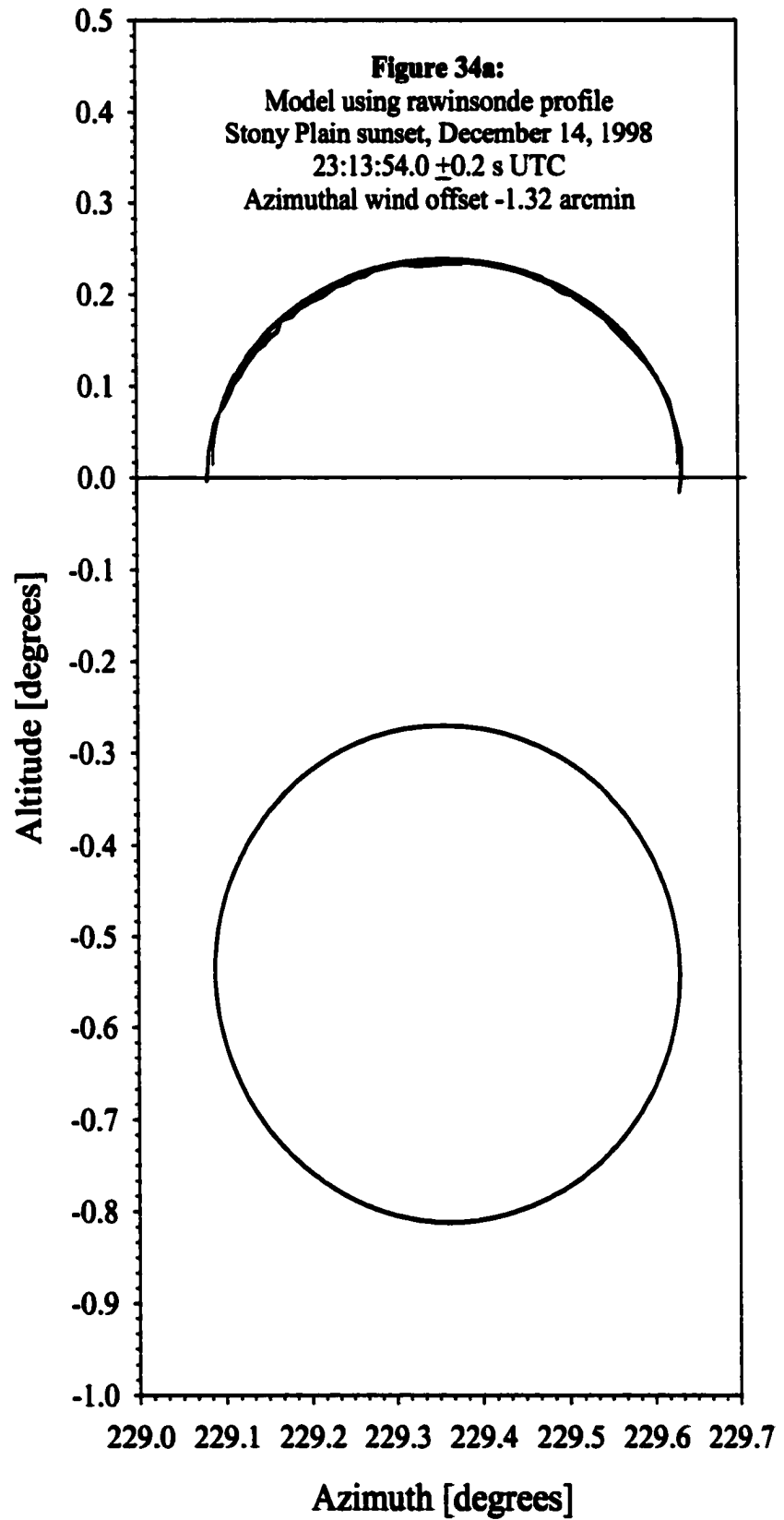


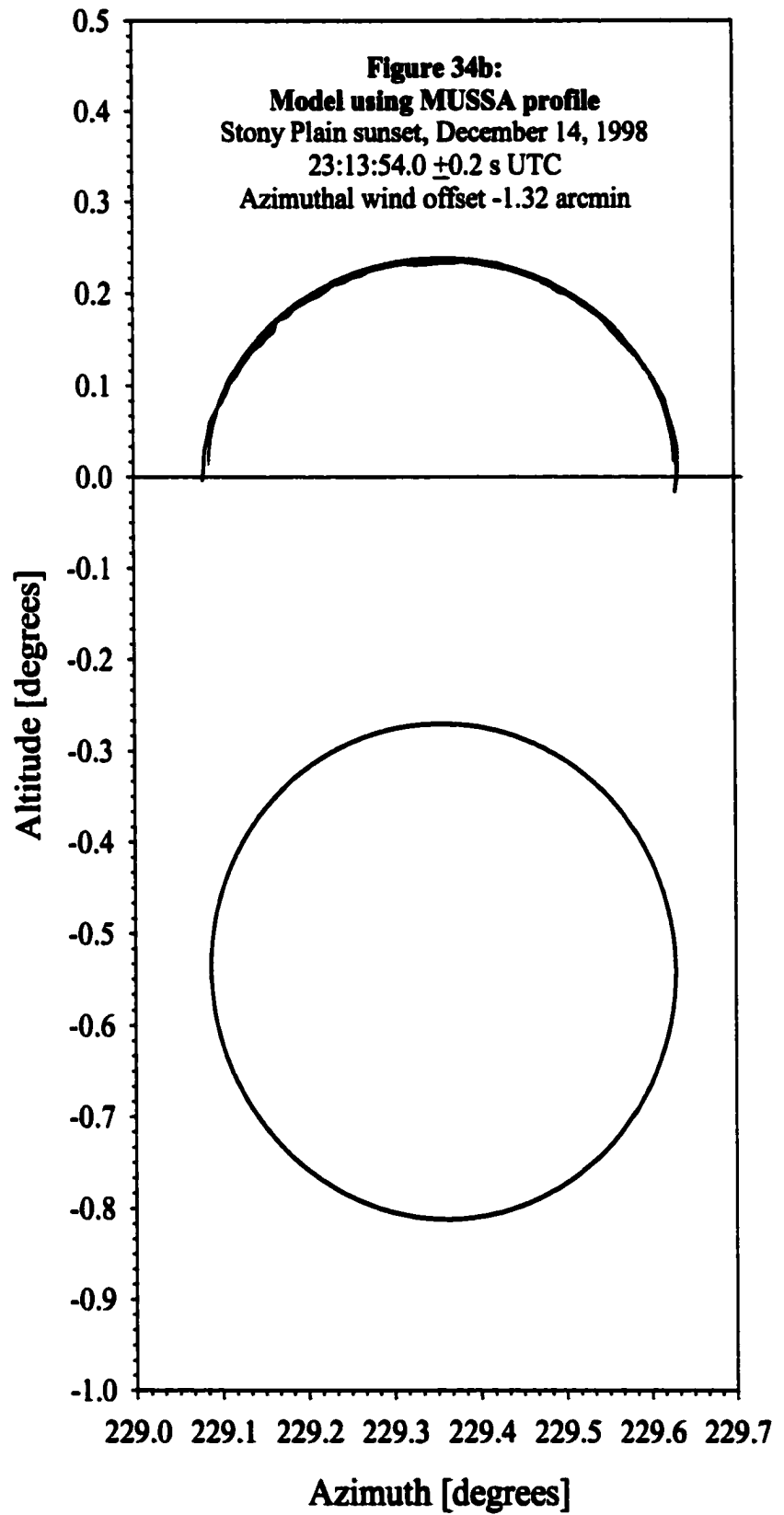


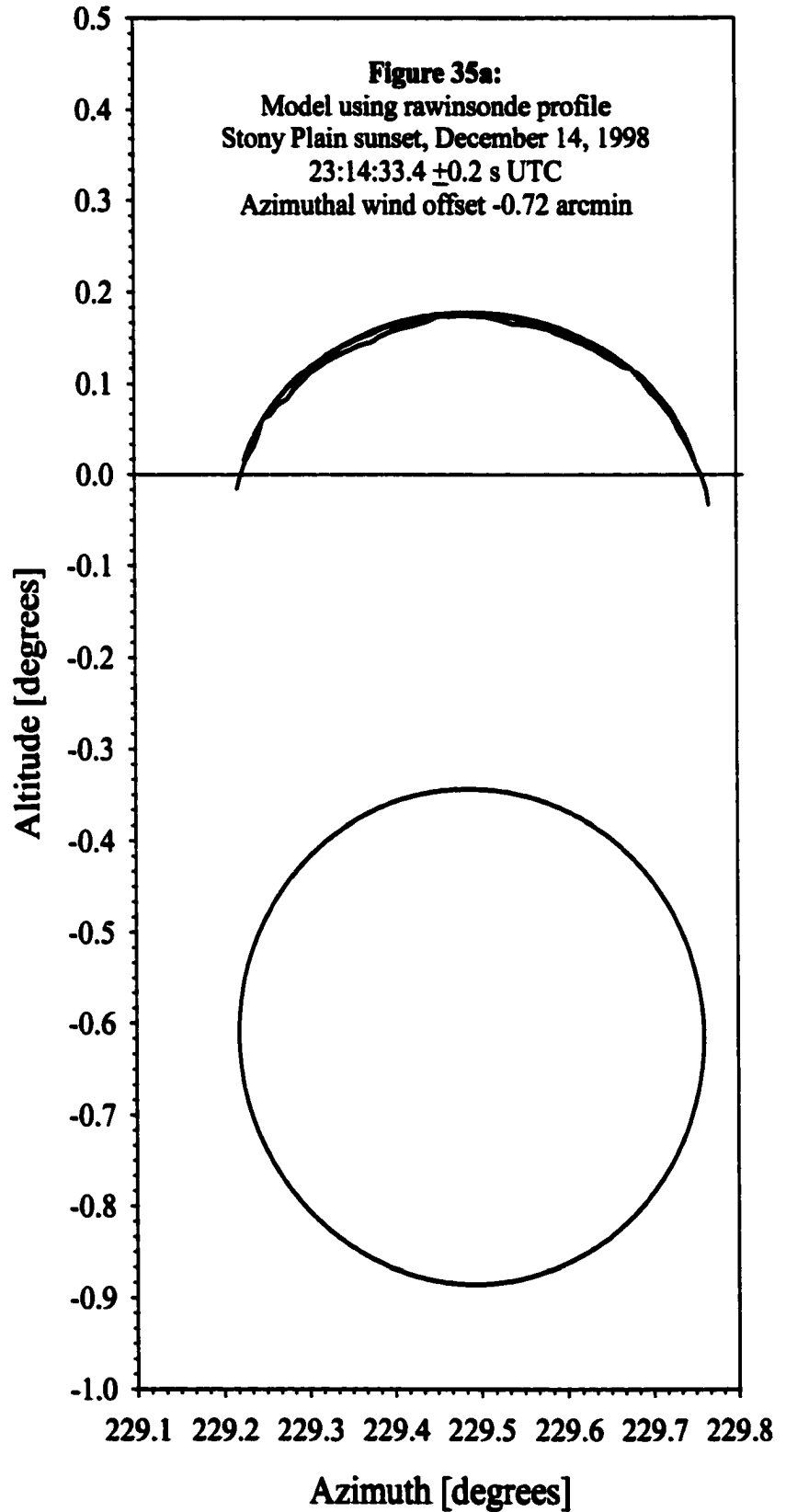


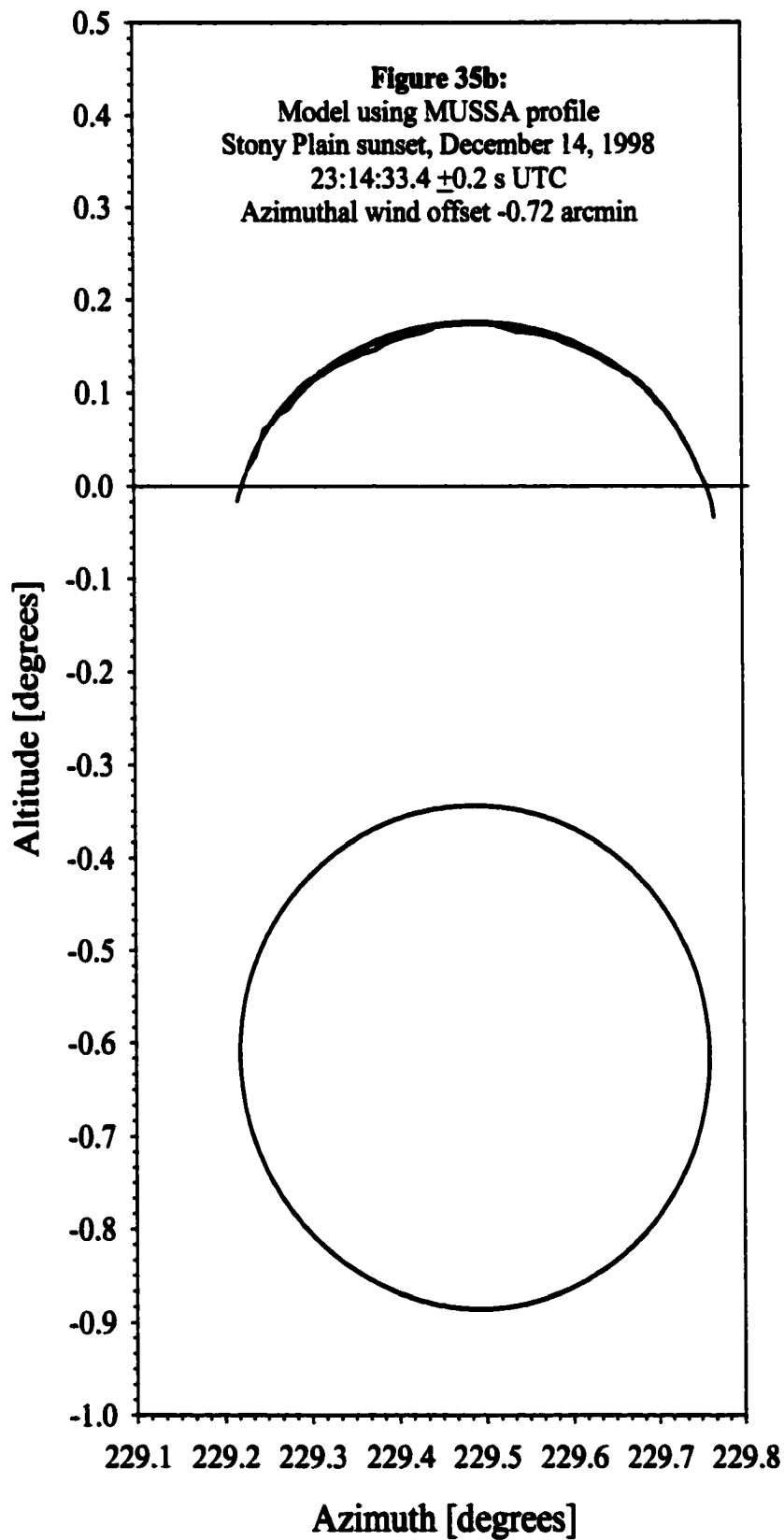


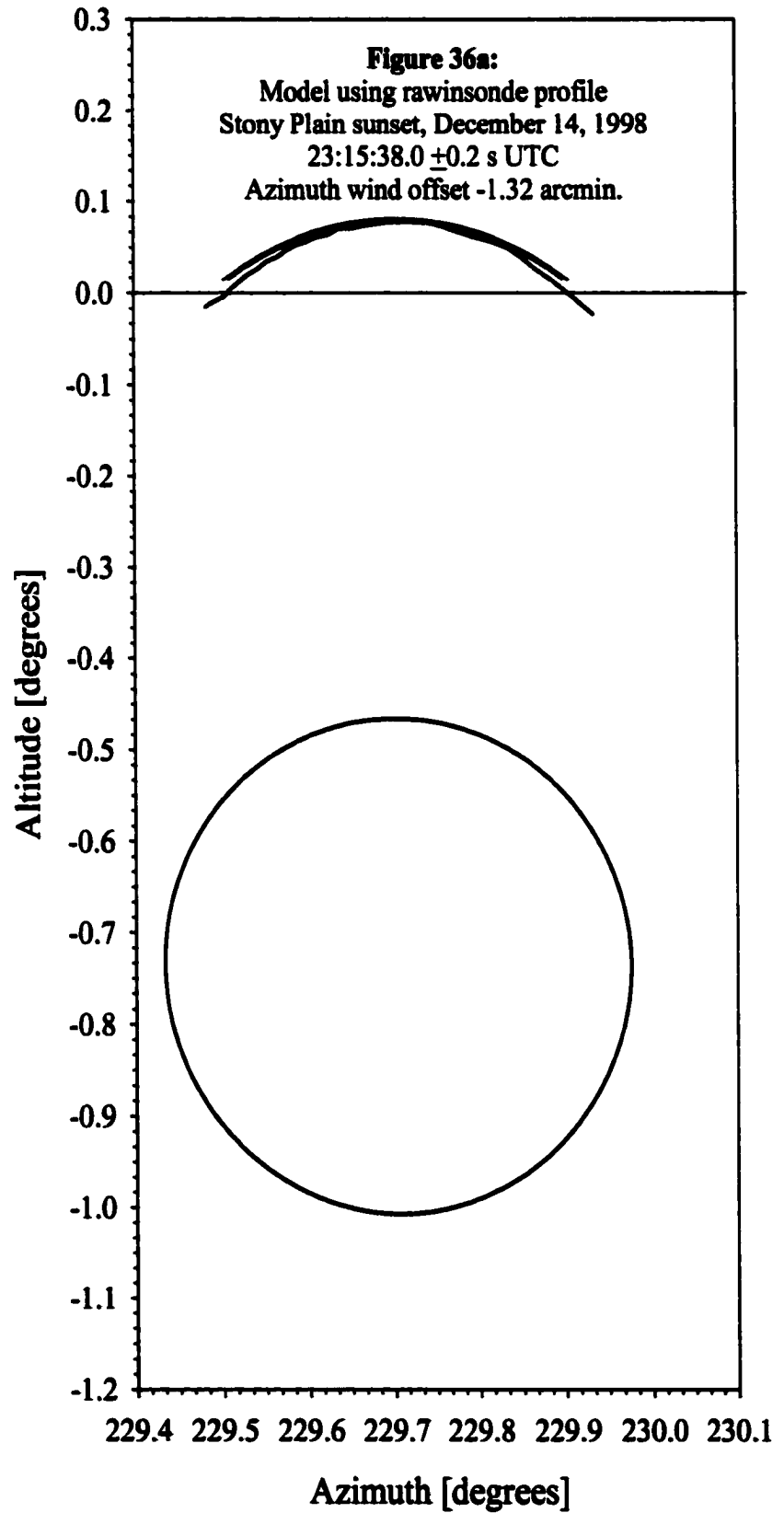


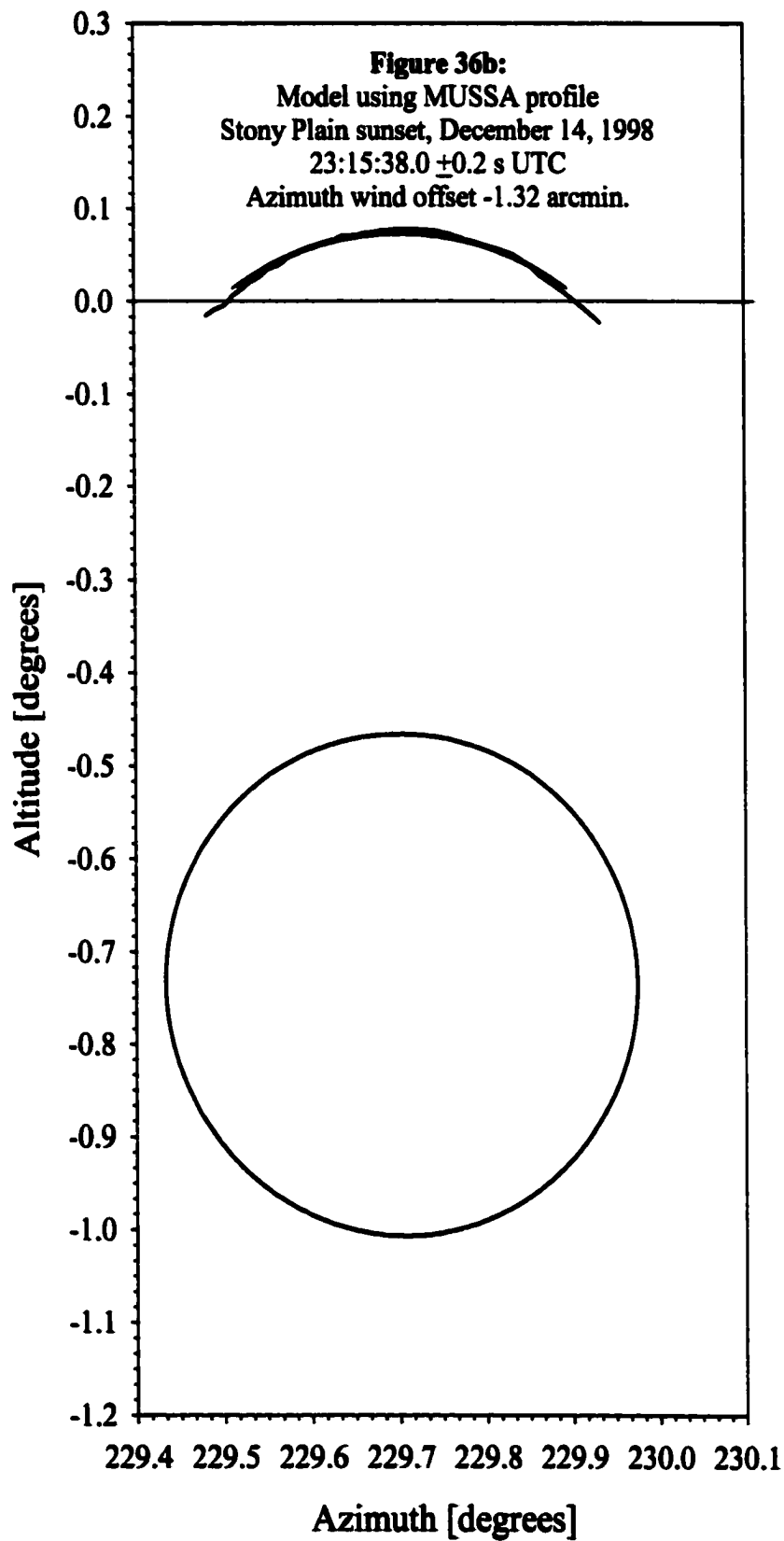


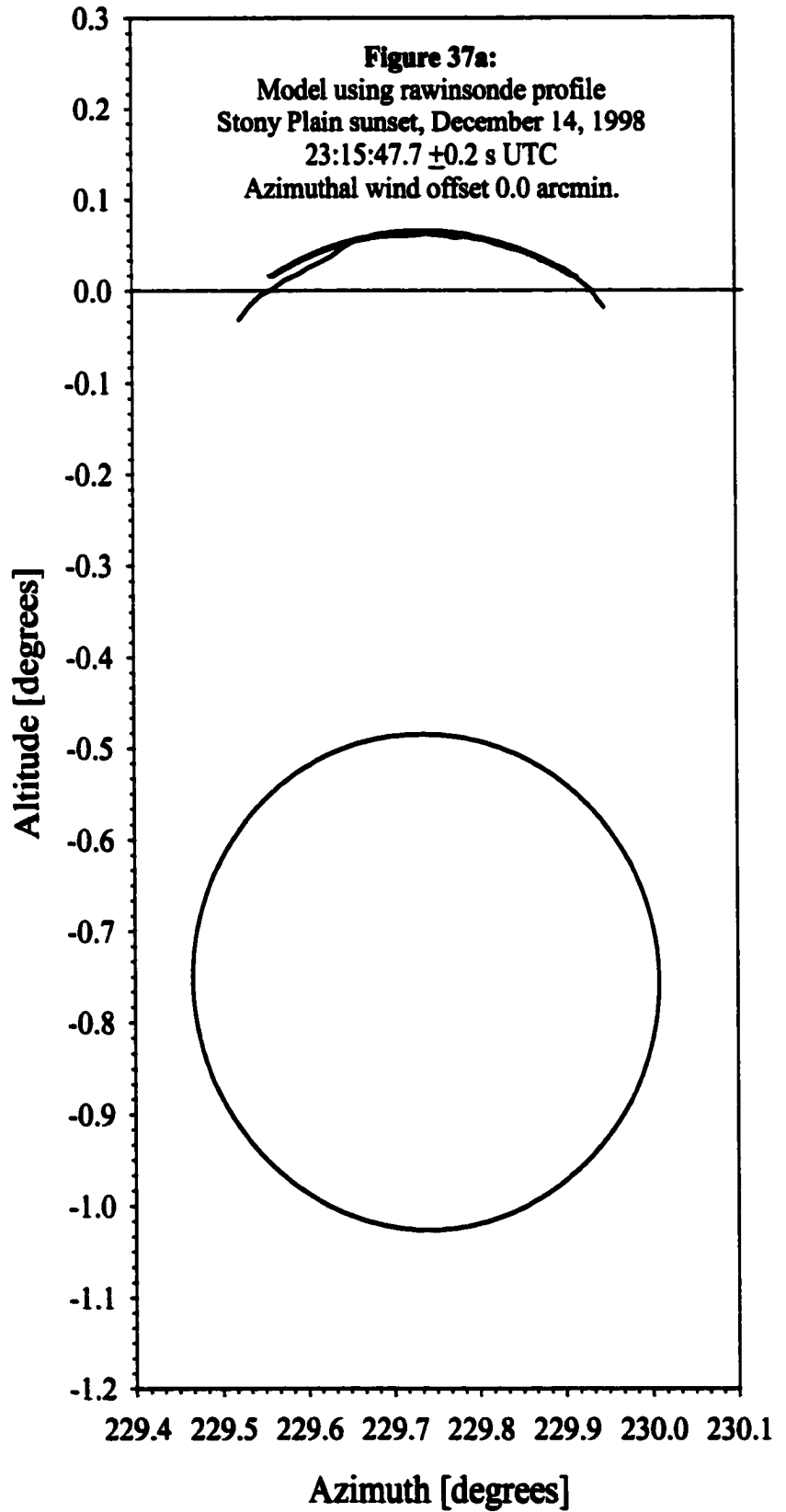


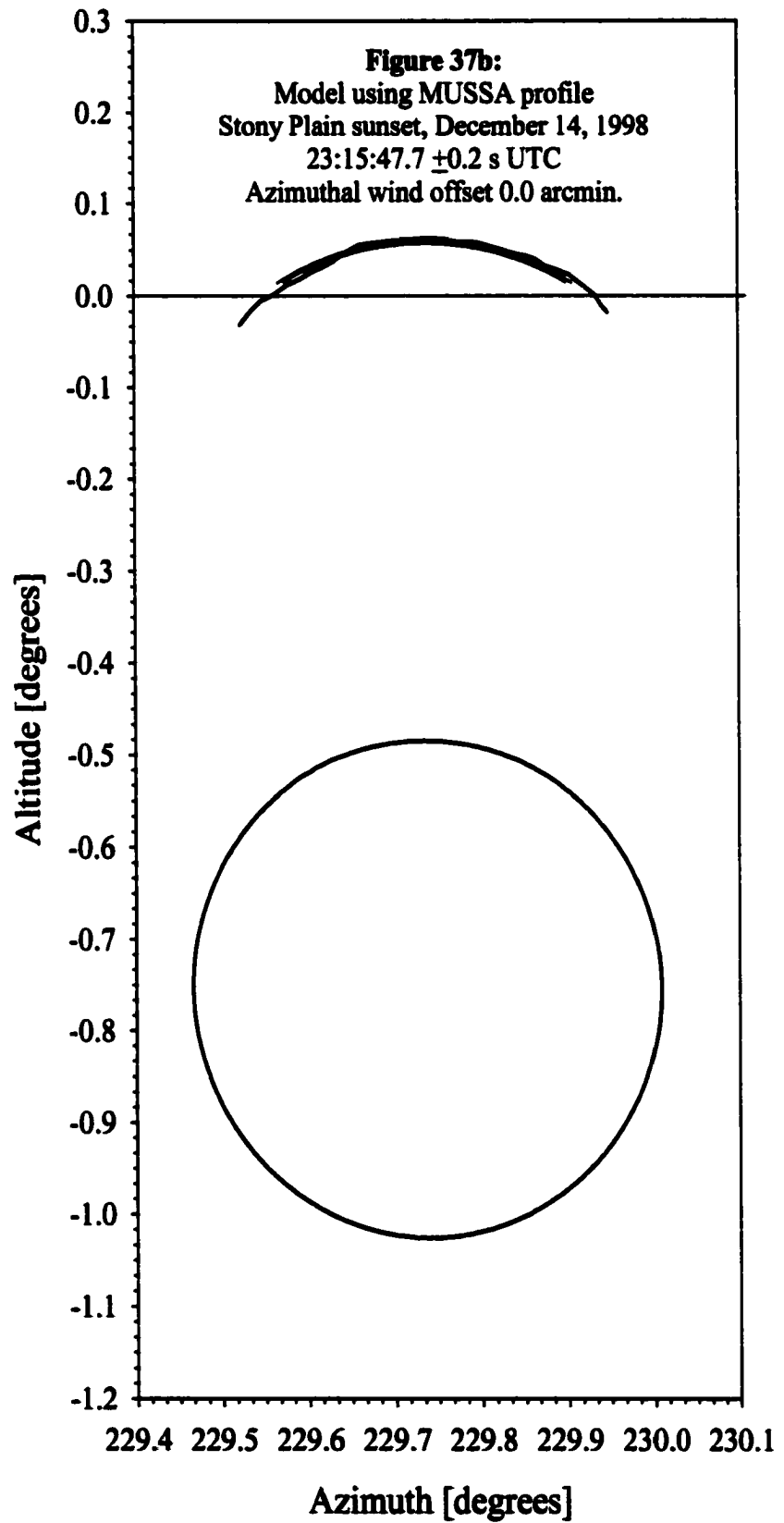


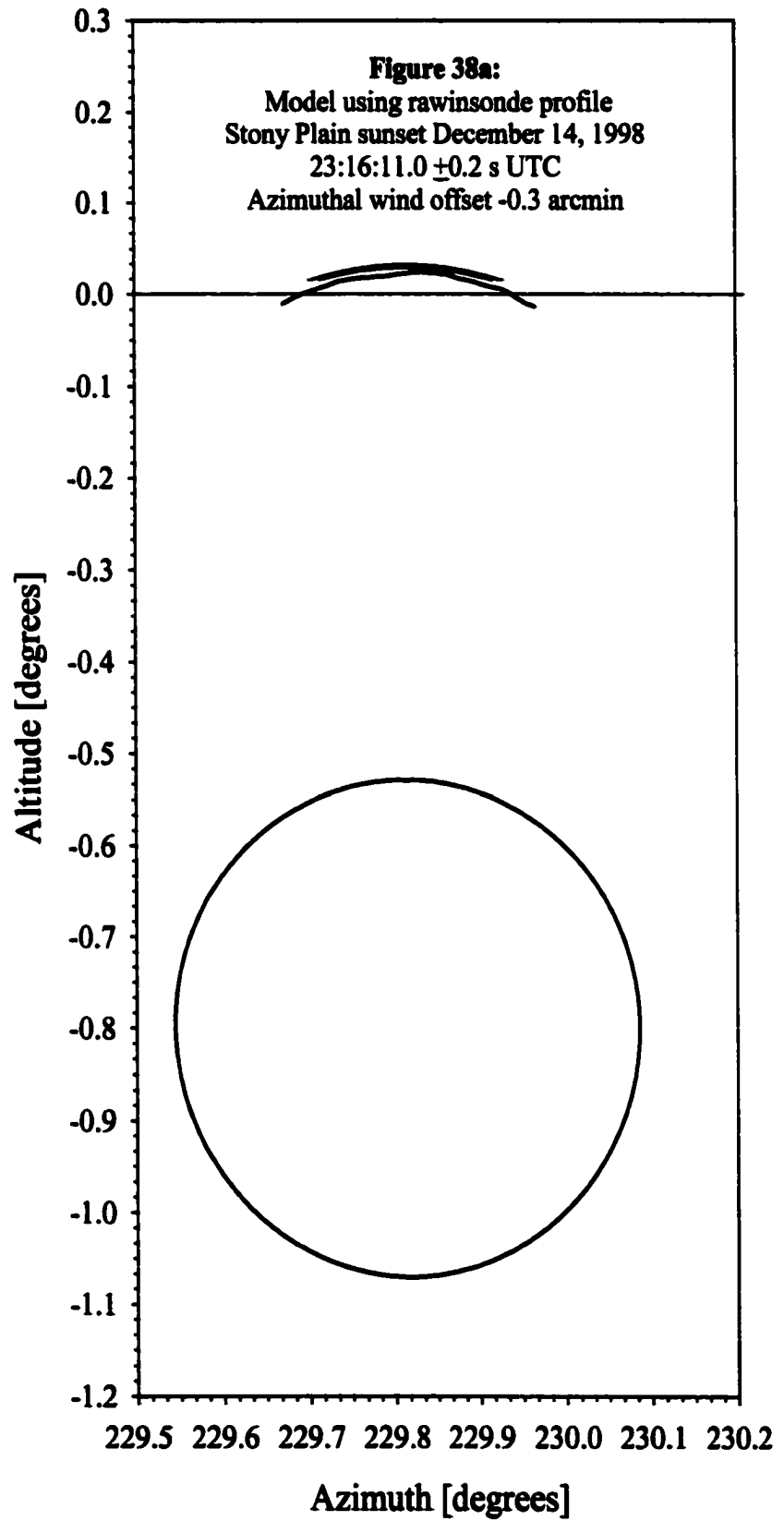


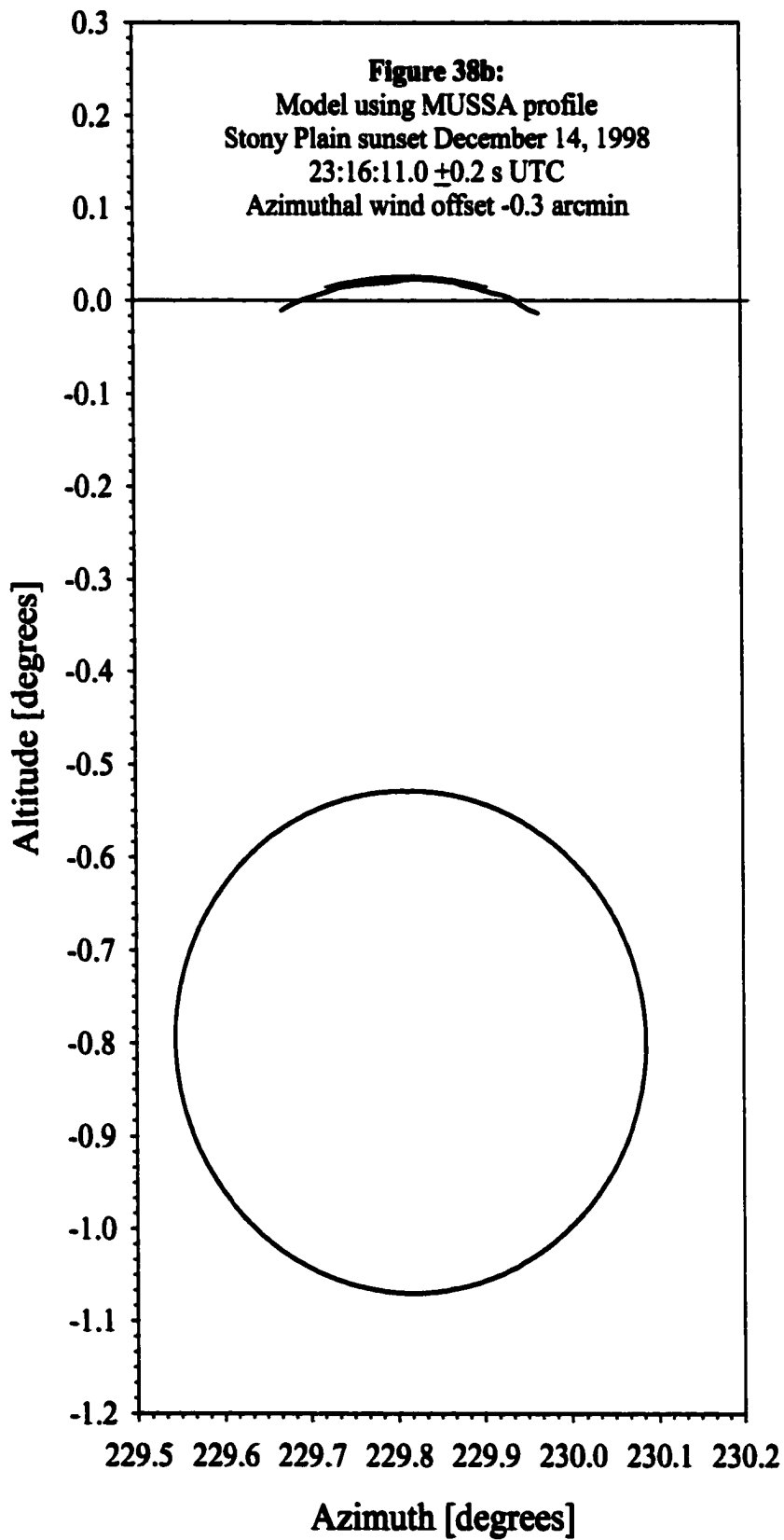


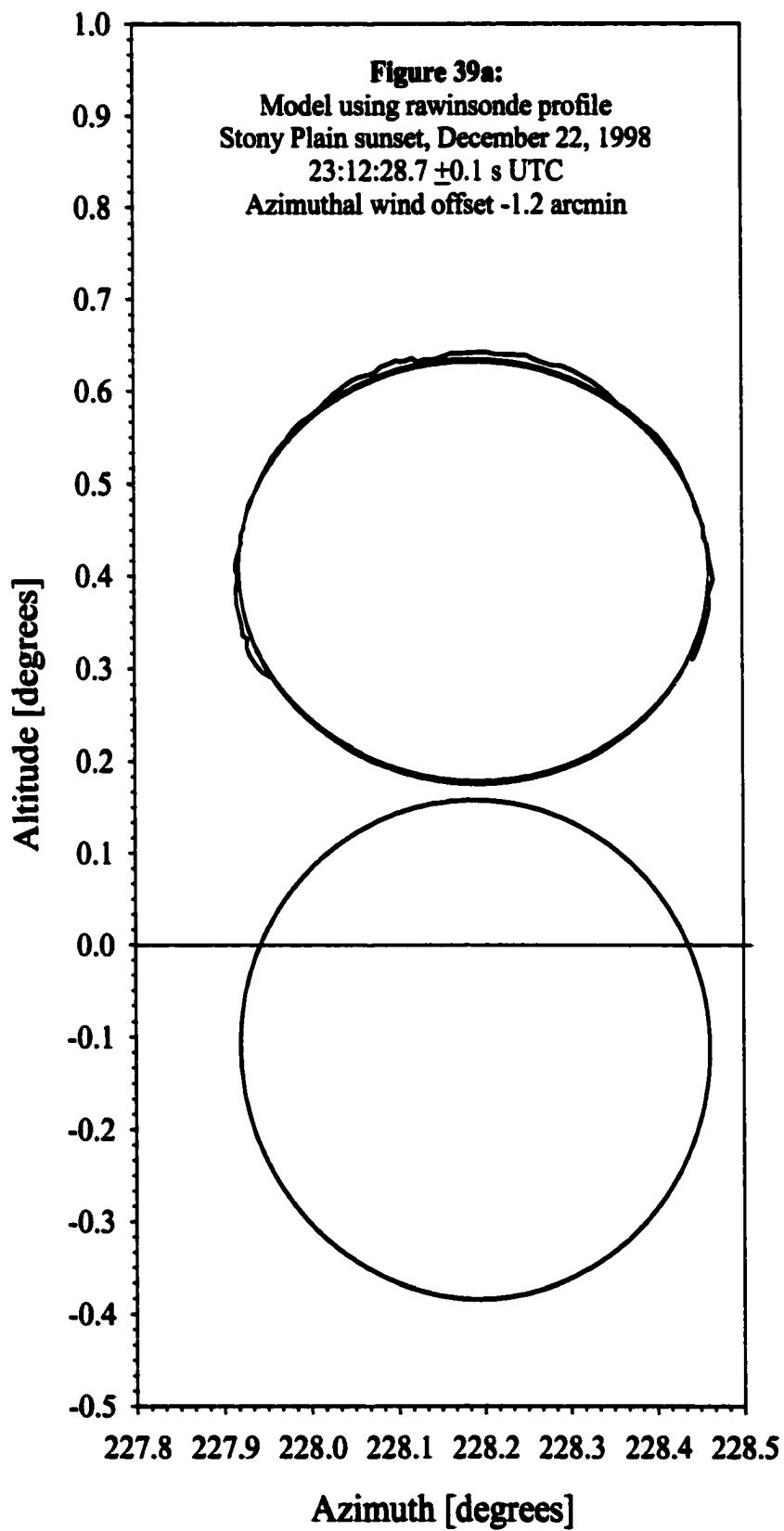


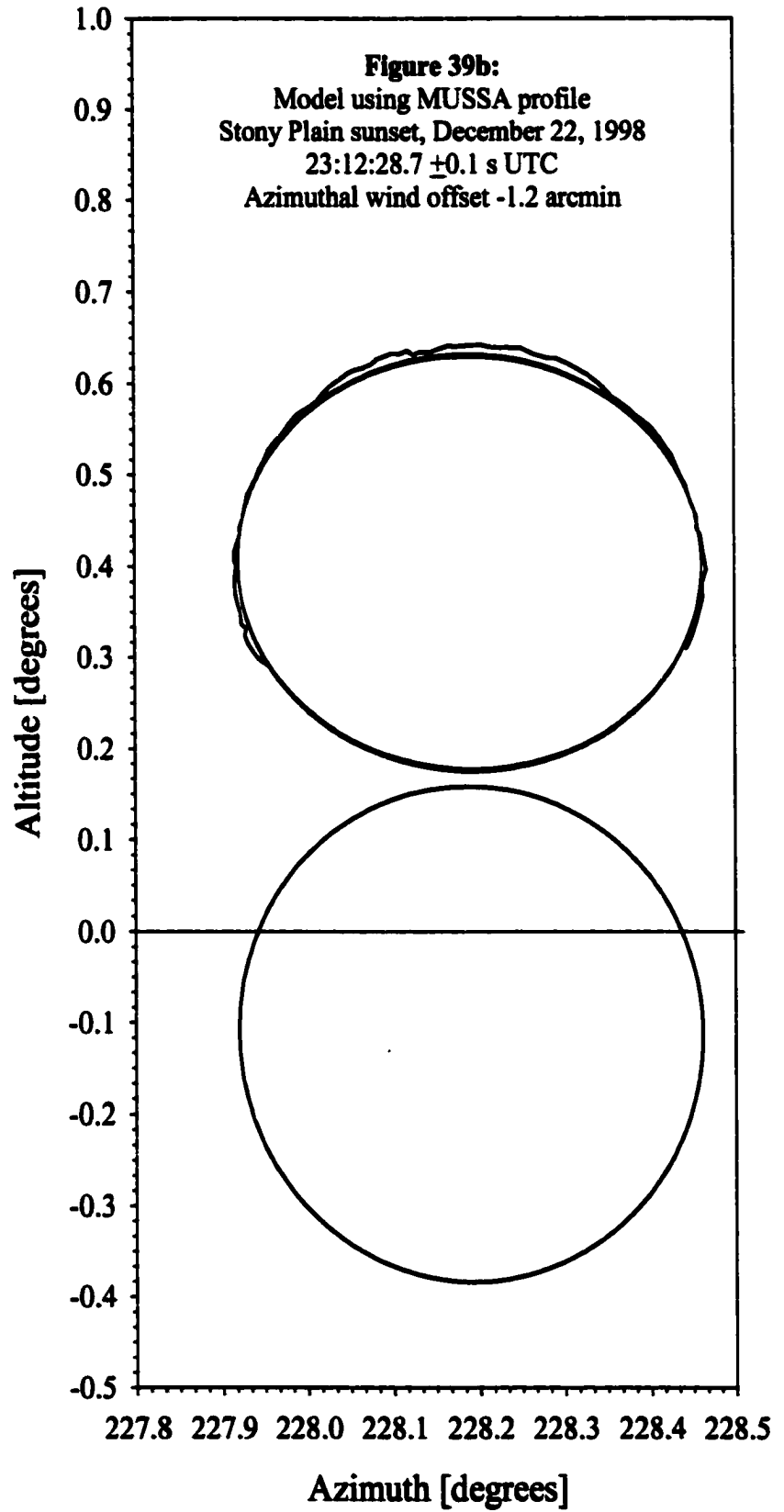


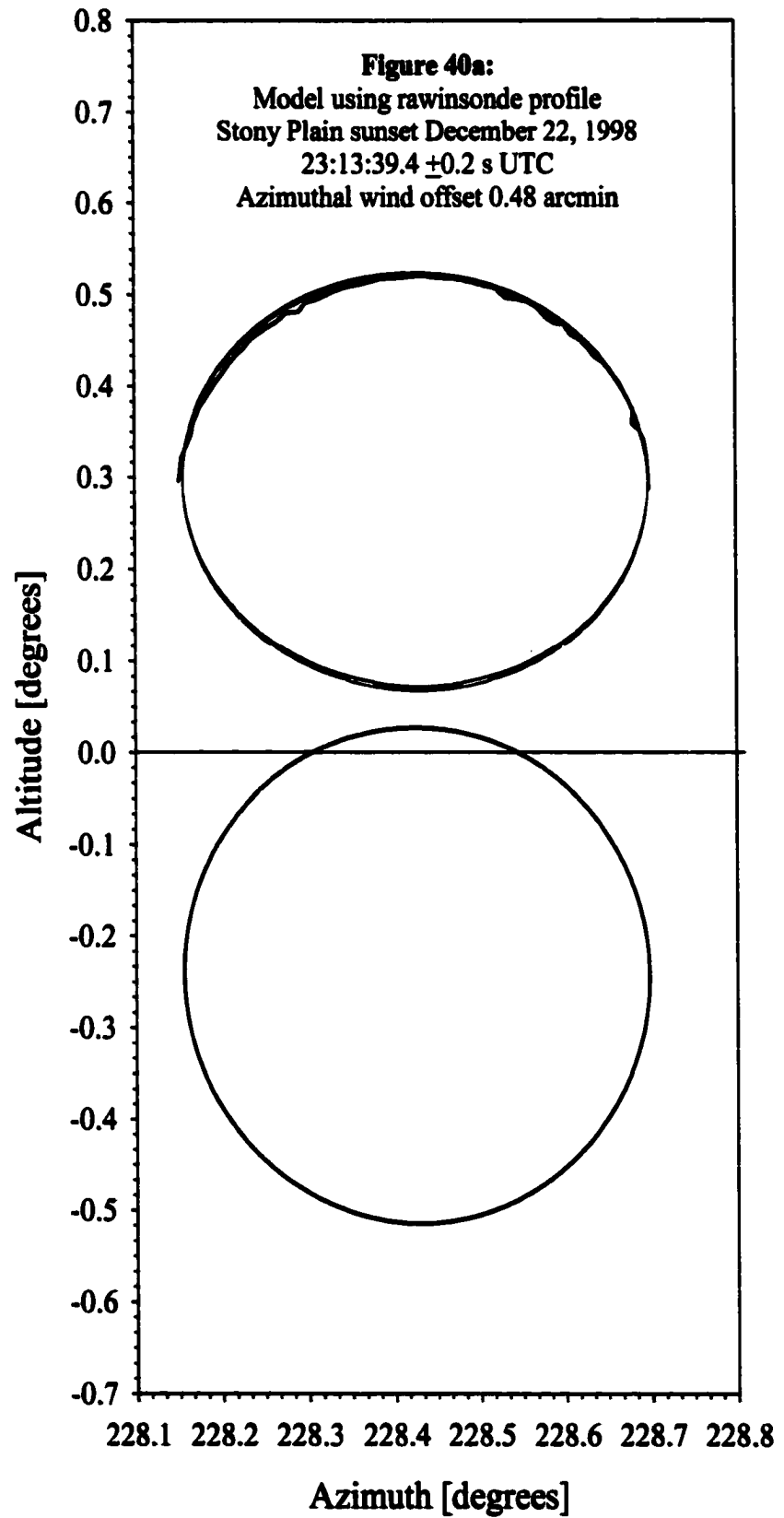


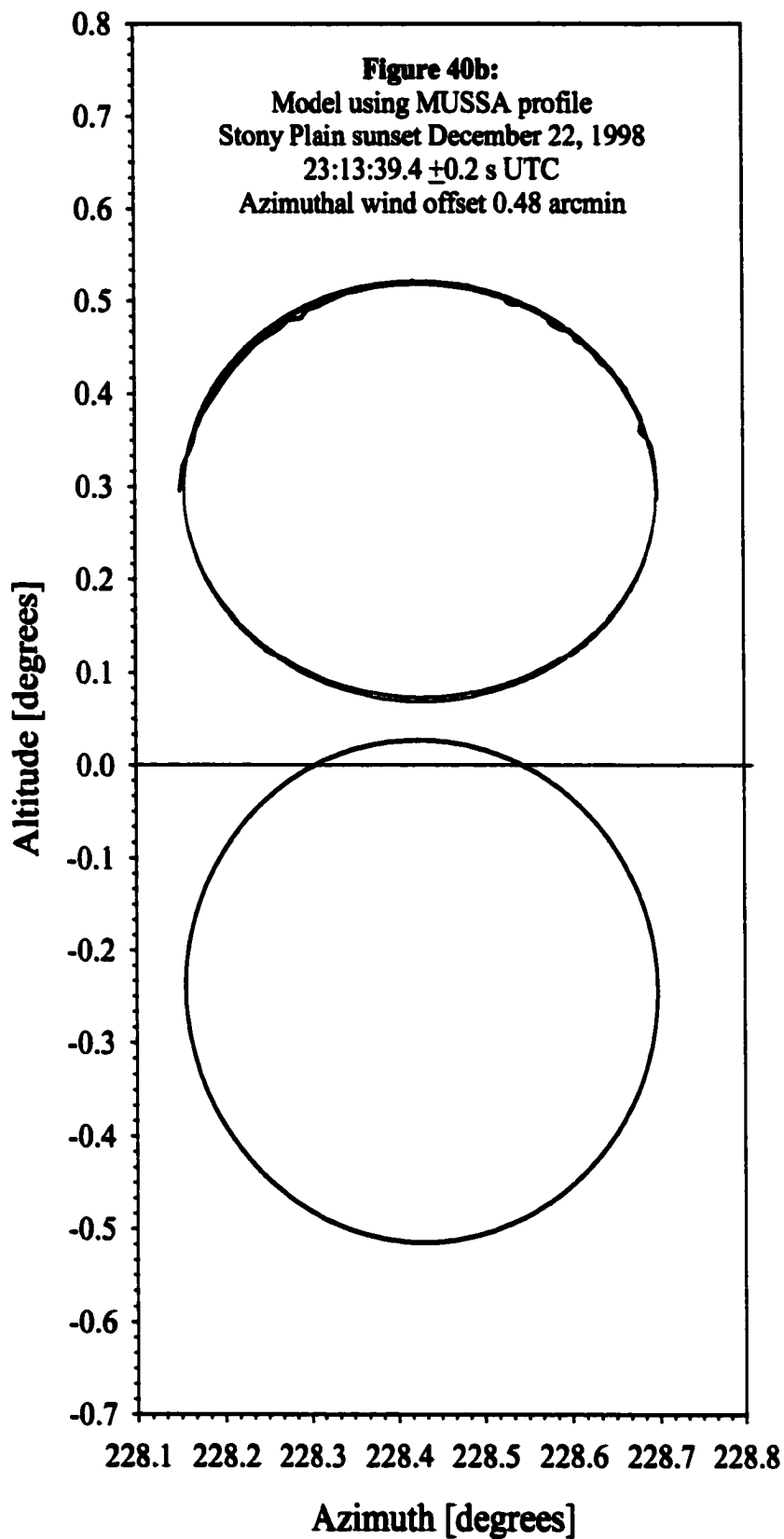


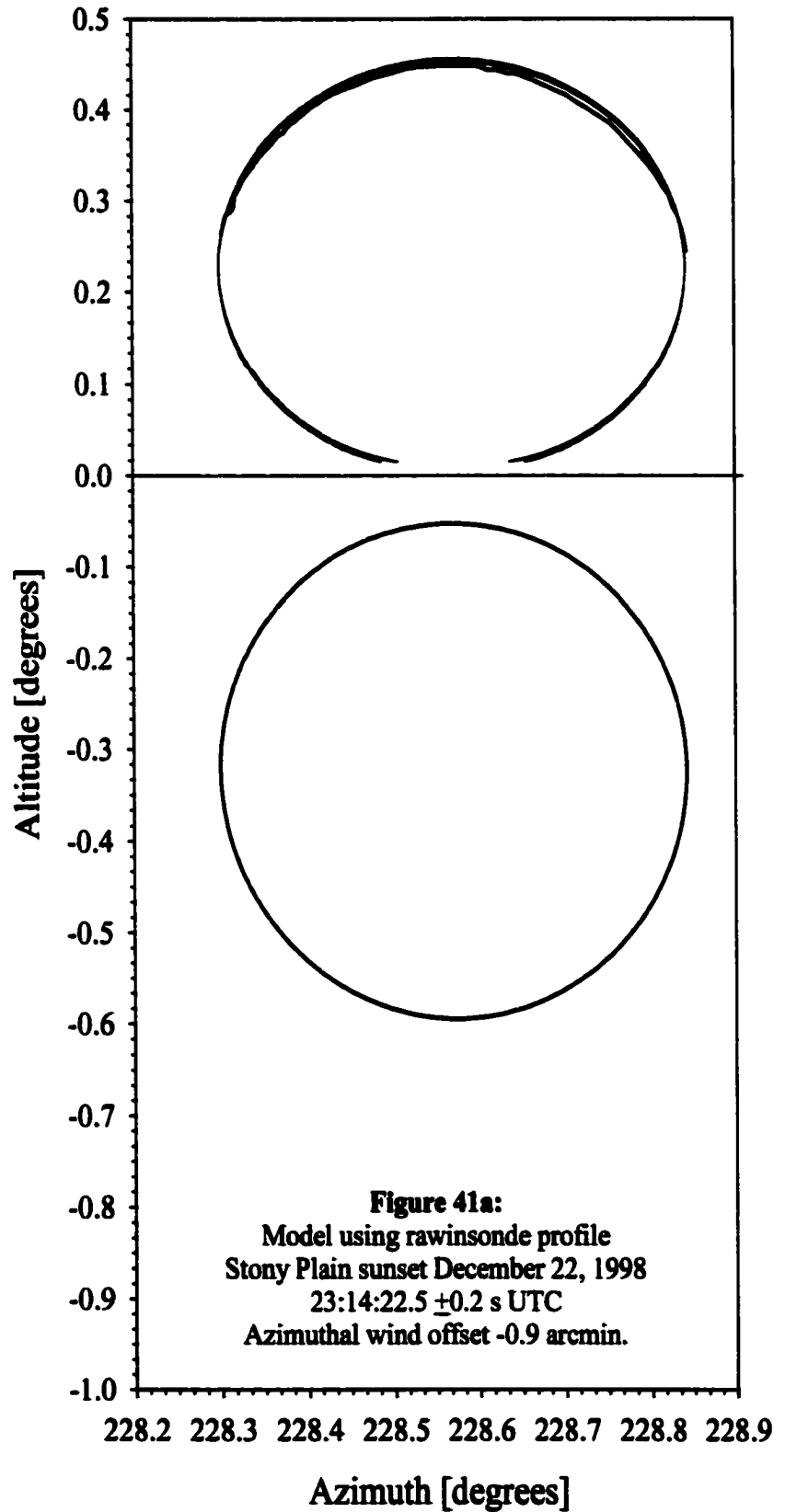


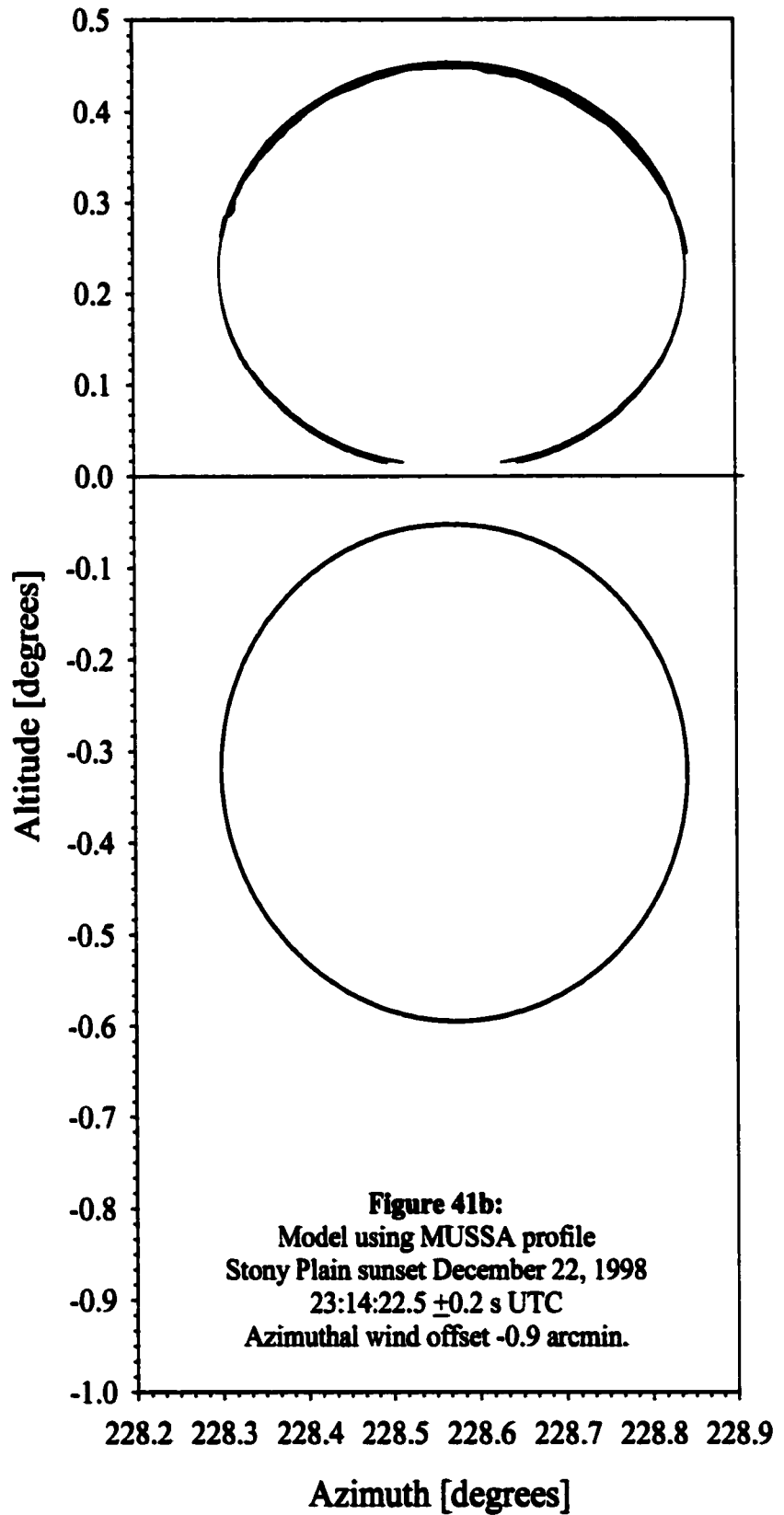


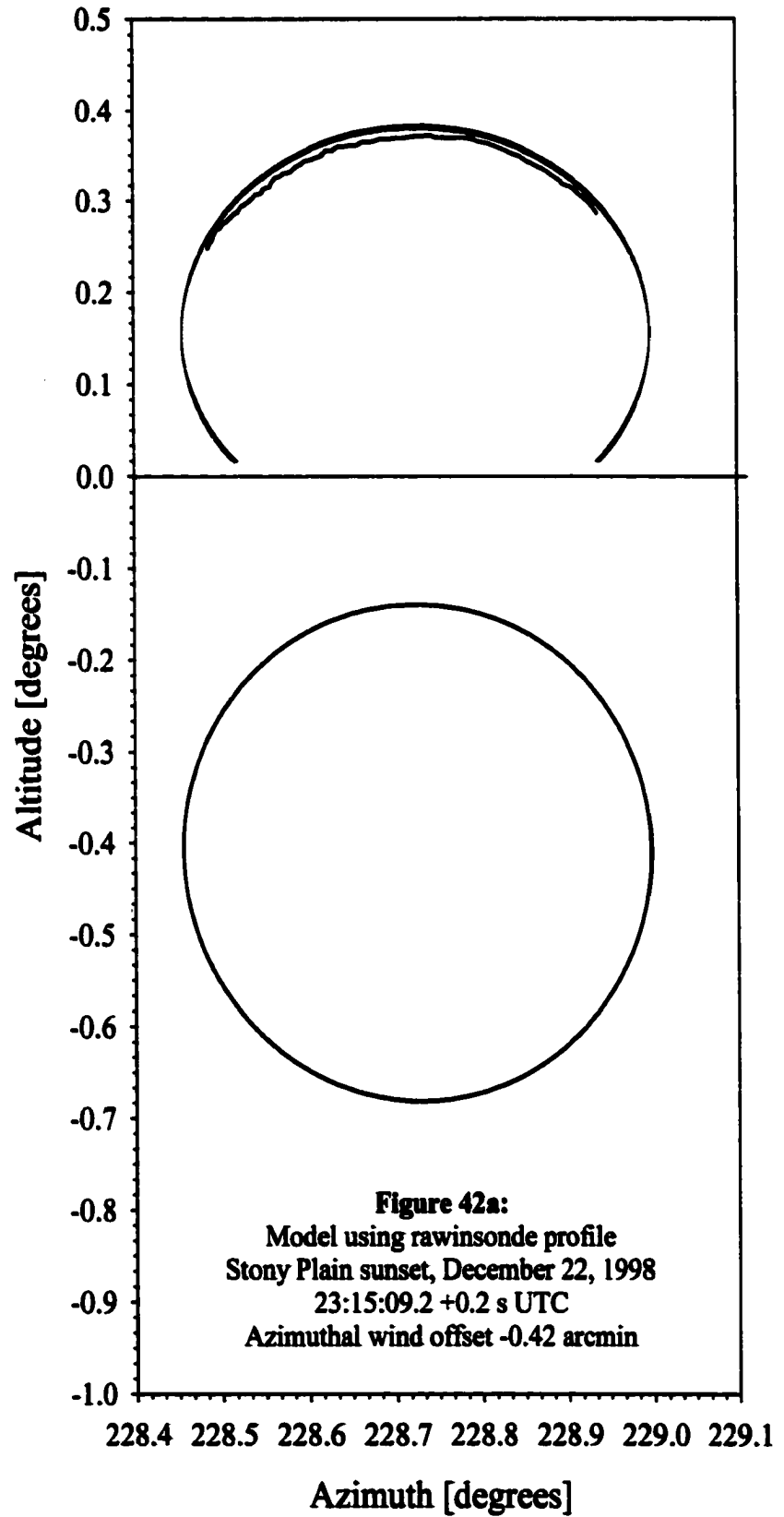


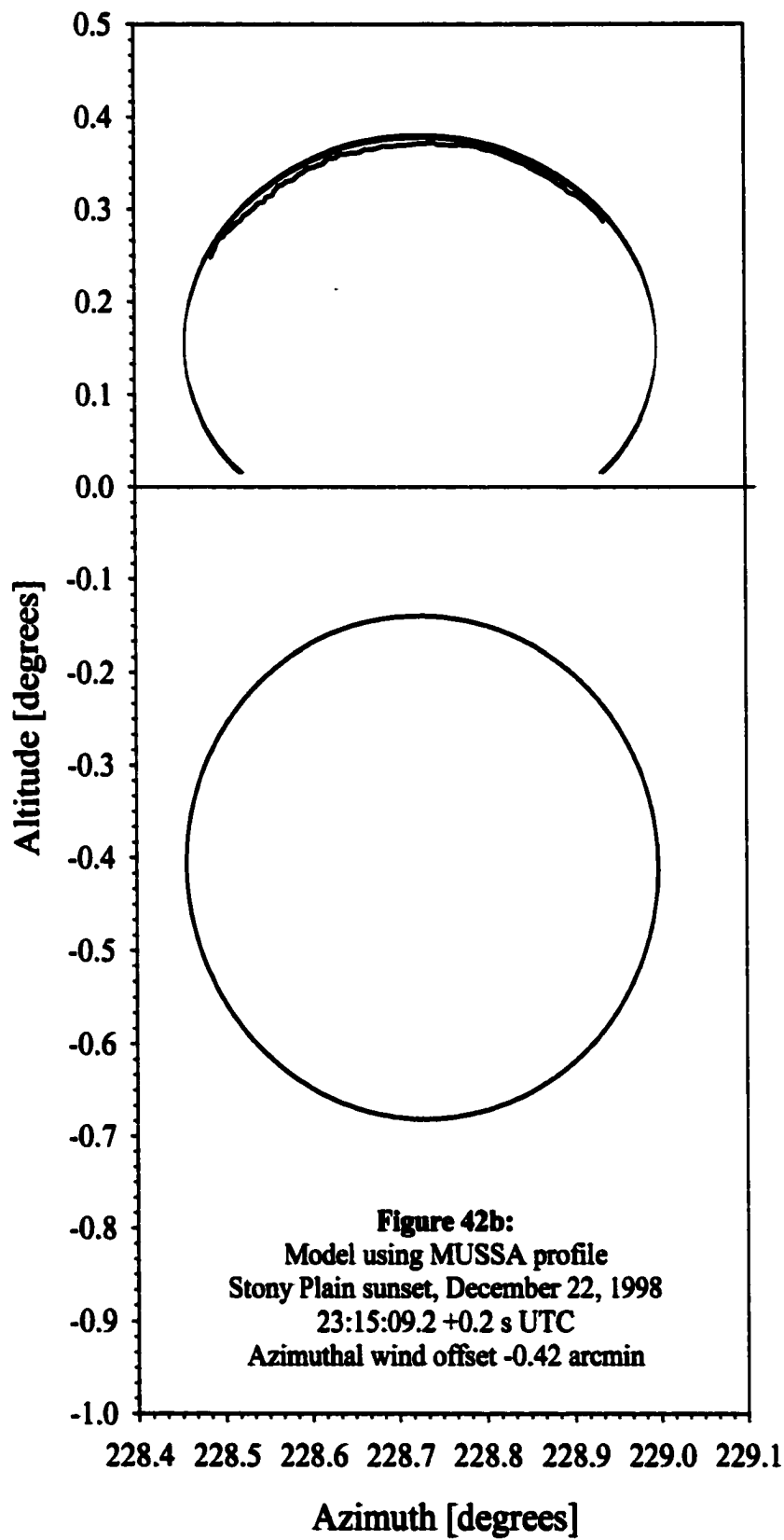


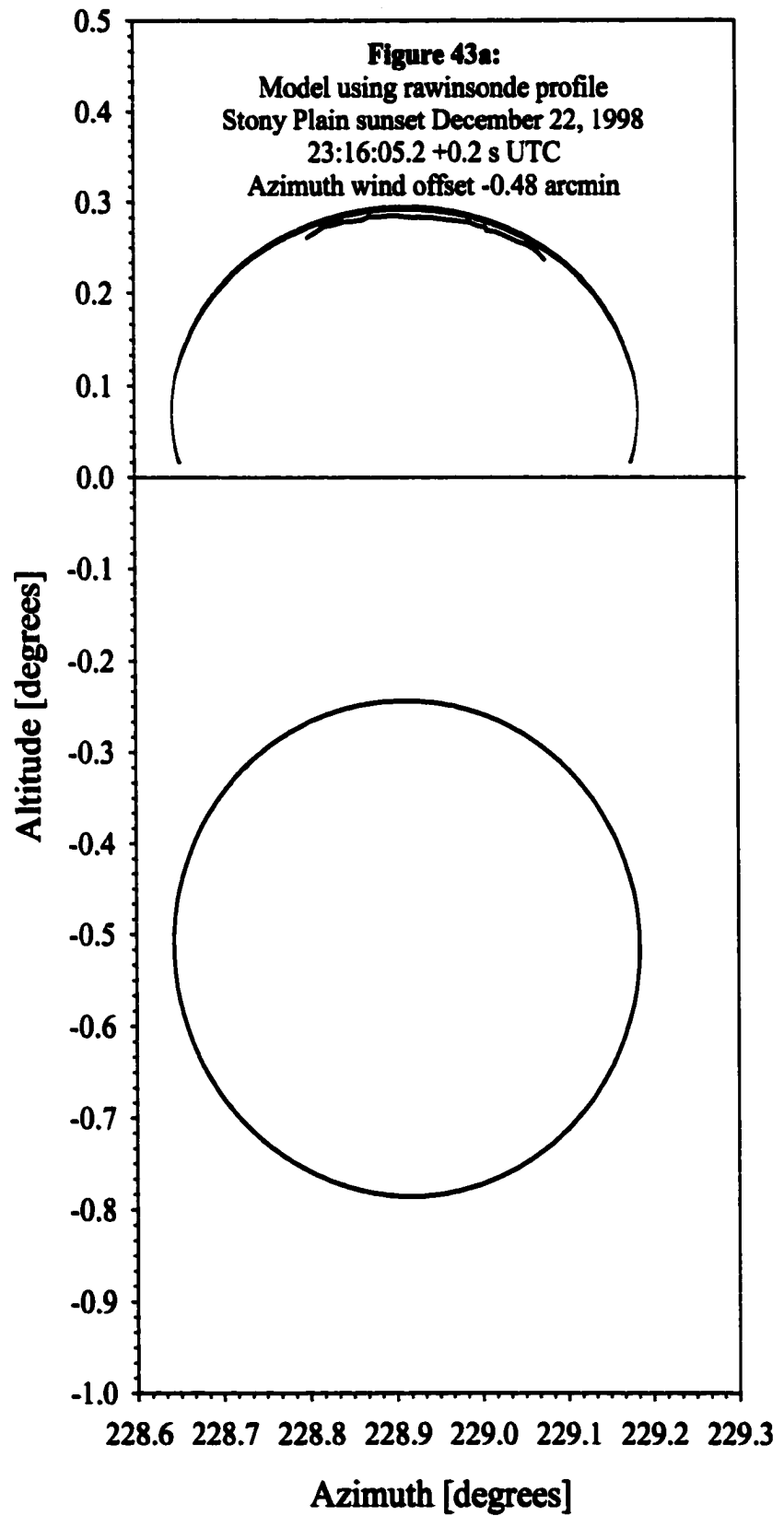


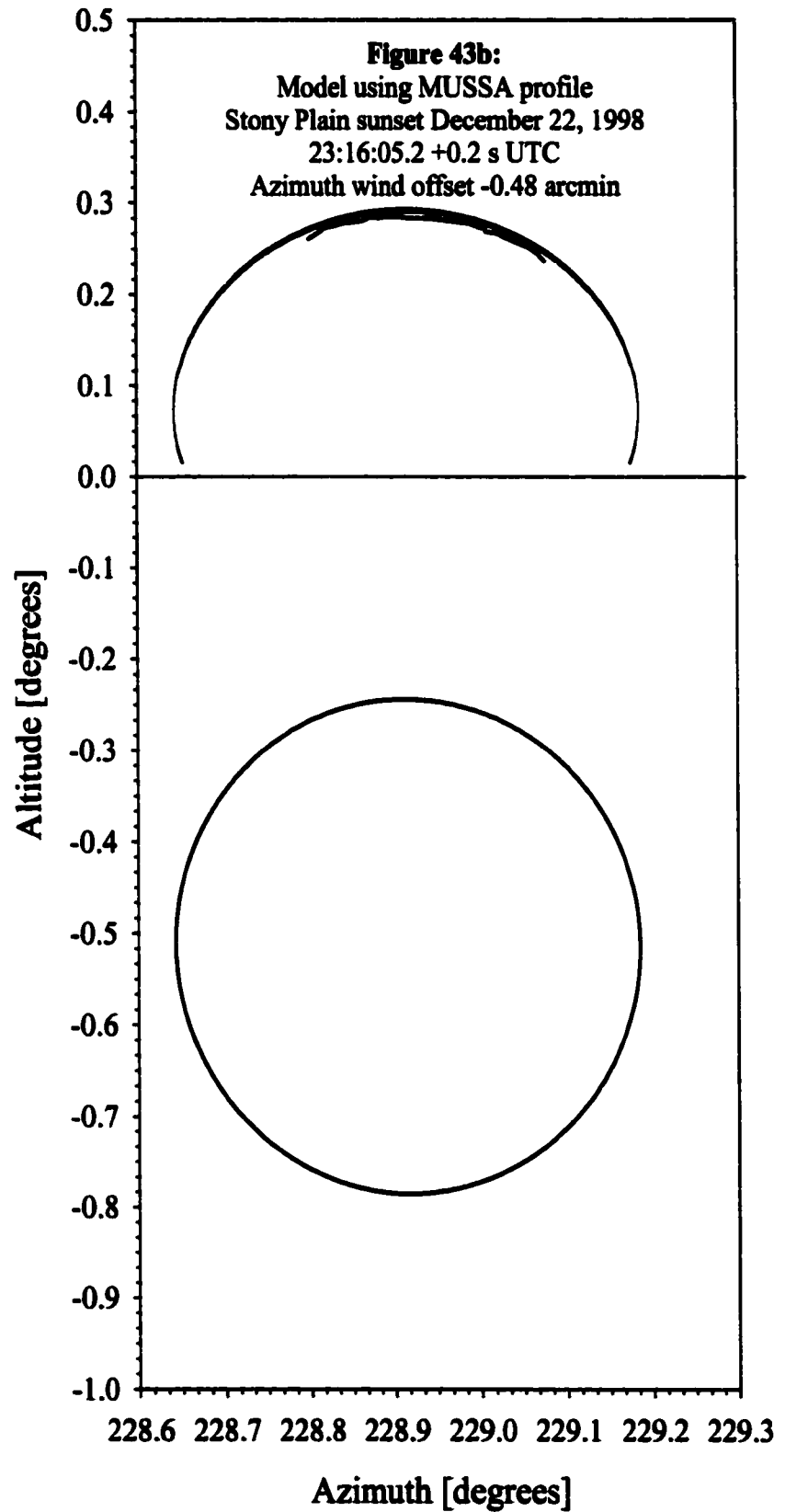












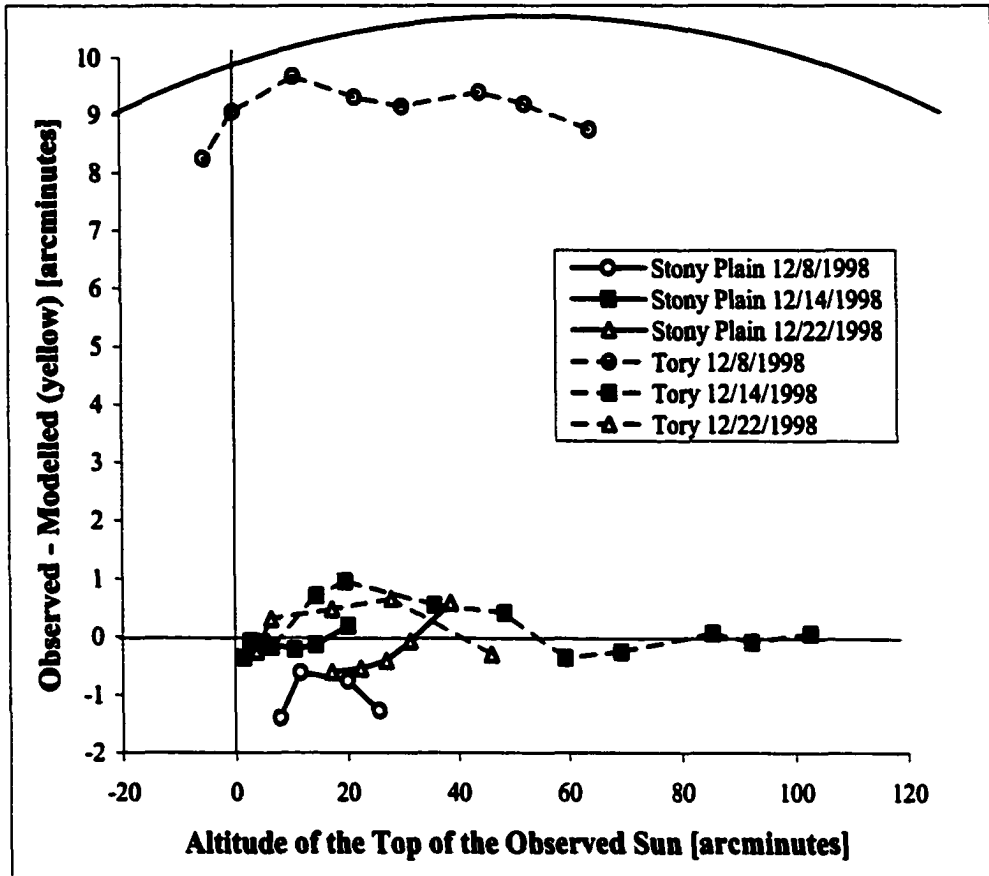


Figure 44: Observed refraction of the top of the Sun minus modelled refraction for yellow light from both Stony Plain and the H.M. Tory Building at the University of Alberta (dashed lines). The arc at the top of the graph is used for scale and represents the disk of the Sun ($D \sim 32$ arcminutes along the vertical scale).

increase in scintillation as the Sun approached the horizon. These timing errors translate into an error in zenith angle of between 6 and 17 arcseconds. This represents a range from 1 to 3 times the estimated resolution of the photogrammetric system. A comparison between the model and photogrammetric measurements (Stony Plain) can be seen in Figure 45 and 46.

5. Analysis

5.1 Estimating Uncertainty in the Refraction Model

To determine the uncertainty in the modelled refraction due to uncertainties in the meteorological measurements, a series of adjusted sounding files were produced and then used in the model. The instrument error specified by the manufacturer for the VIZ Mark II and Vaisala RS80 rawinsonde was used as adjustment coefficient for the sounding files. Assuming a normal distribution for the measurement uncertainties, a Monte Carlo routine was employed to determine the magnitude and sign of the error for the temperature, pressure and humidity measurements in the sounding. The error in the height of the RS80 sounding (in metres) was calculated from an empirical formula derived from experimental data in Antikainen and Kyvönen (1983):

$$|\Delta z| = -3.83 \ln(p) + 26.85, \quad (55)$$

where p is the pressure in hPa. No detailed height error analysis was found for the VIZ system. However, a value of ± 3 metres appears to represent the variation in height for daytime soundings at 800 hPa, and was used for the VIZ system (Schmidlin and Finger, 1987).

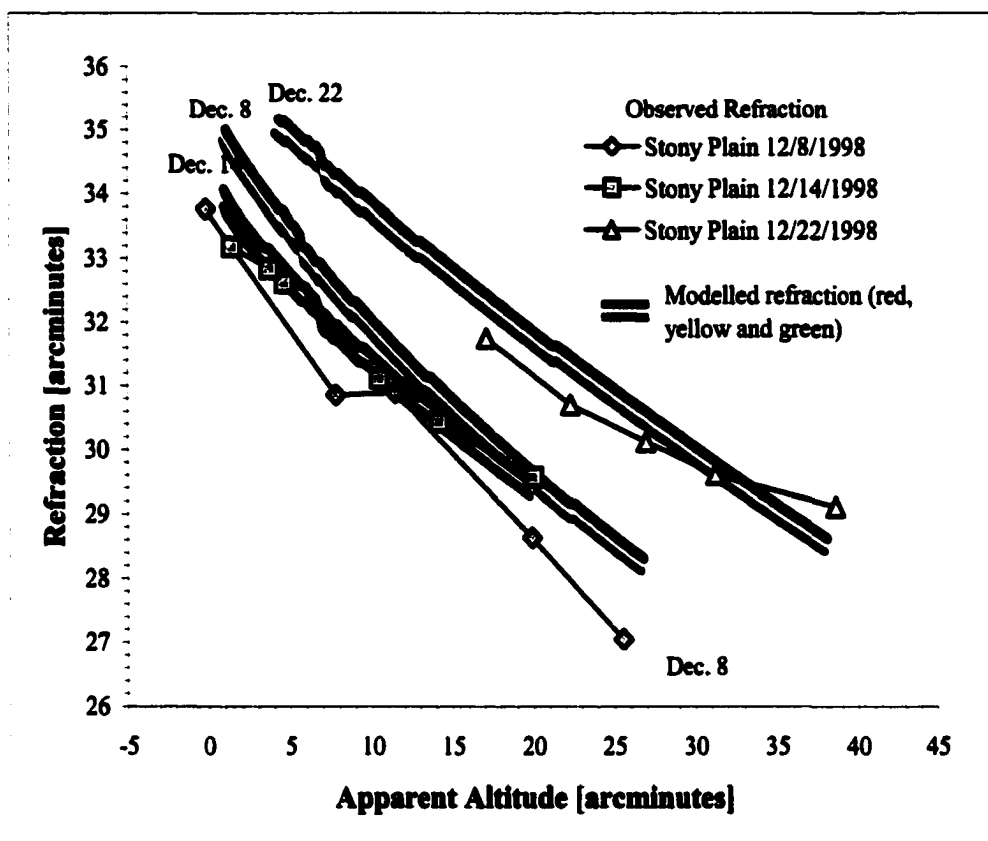


Figure 45: Comparison between photogrammetrically measured refraction from Stony Plain, and modelled refraction using rawinsonde data. Observed refraction was measured from the top of the solar image, while the modelled refraction was found from the full solar profile.

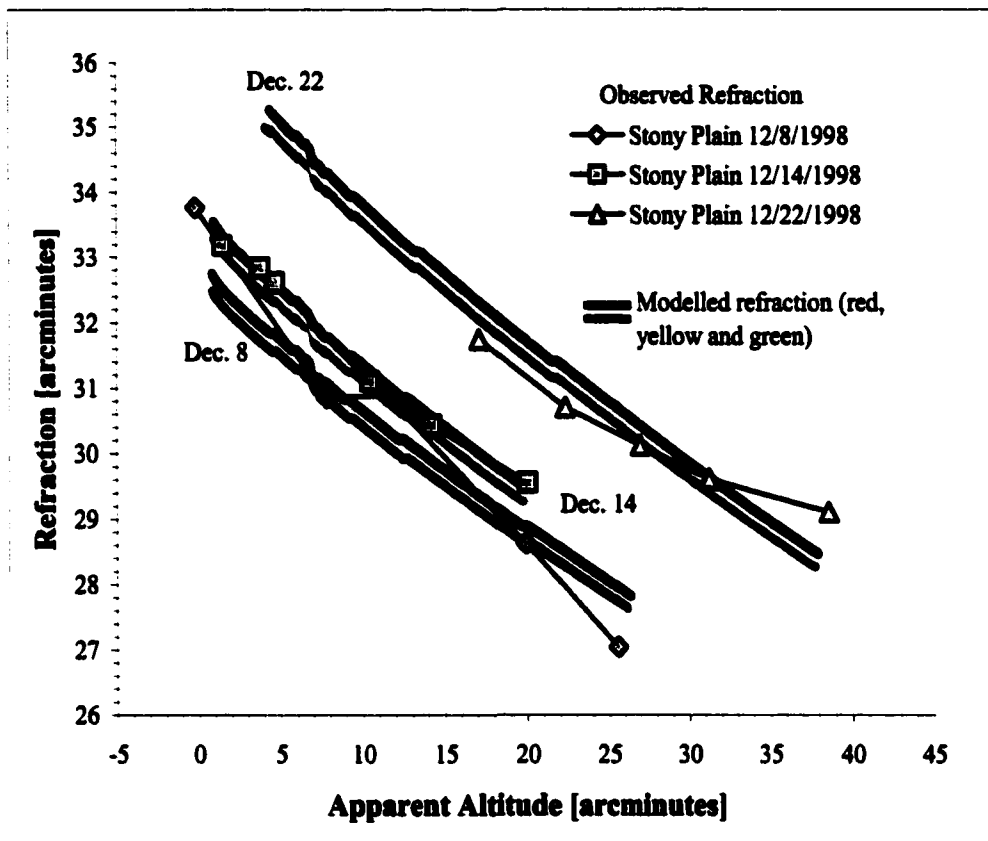


Figure 46: Comparison between photogrammetrically measured refraction from Stony Plain, and modelled refraction using a modified U.S. Standard Atmosphere. Observed refraction was measured from the top of the solar image, while the modelled refraction was found from the full solar profile. The U.S. Standard Atmosphere model shows small improvements over the rawinsonde model especially in the lowest altitude portion of the December 14 sunset and almost all of the December 8 sunset.

Since variations in the astronomical refraction are controlled by the lower part of the atmosphere (see Section 1 and Appendix H) the adjustments were done only to a height of 10 kilometres.

Ten adjusted files for the December 8, and 22, 1998 sounding were produced and inserted into the refraction model. The population standard deviations of the ten refraction values were then plotted against the altitude of the corresponding point on the profile of the geometric Sun (see Figures 47 and 48).

The maximum measurement error in timing the sunset photographs was estimated to be ± 0.2 seconds. The error in the altitude of the modelled geometric Sun due to timing δz_T can be estimated from the angular vertical rate of descent for the setting Sun. The zenith angle z can be found from the formula:

$$z = \cos^{-1}(\sin \delta \sin \phi + \cos \delta \cos \phi \cos H), \quad (56)$$

where δ is the declination of the Sun, ϕ is the geographic latitude and H is the hour angle. A numerical model was constructed using Equation 56 to determine the angular rate of descent when the Sun approached the horizon ($z = 90^\circ$). At the winter solstice ($\delta = -23^\circ 26'$) the vertical rate of descent for the geometric setting Sun is about $6.6''/s$. The actual observed descent rate will be less, since the amount of astronomical refraction increases with the zenith angle of the Sun. The measured descent rate for the three observed sunsets was $5.5''/s$ for both December 8 and 14 and $5.7''/s$ for December 22. The slightly greater value for the December 22 sunset appears to be due to the smaller zenith angle of the observed Sun. Therefore the maximum timing error of ± 0.2 s would produce a zenith angle error of $\pm 1''.1$.

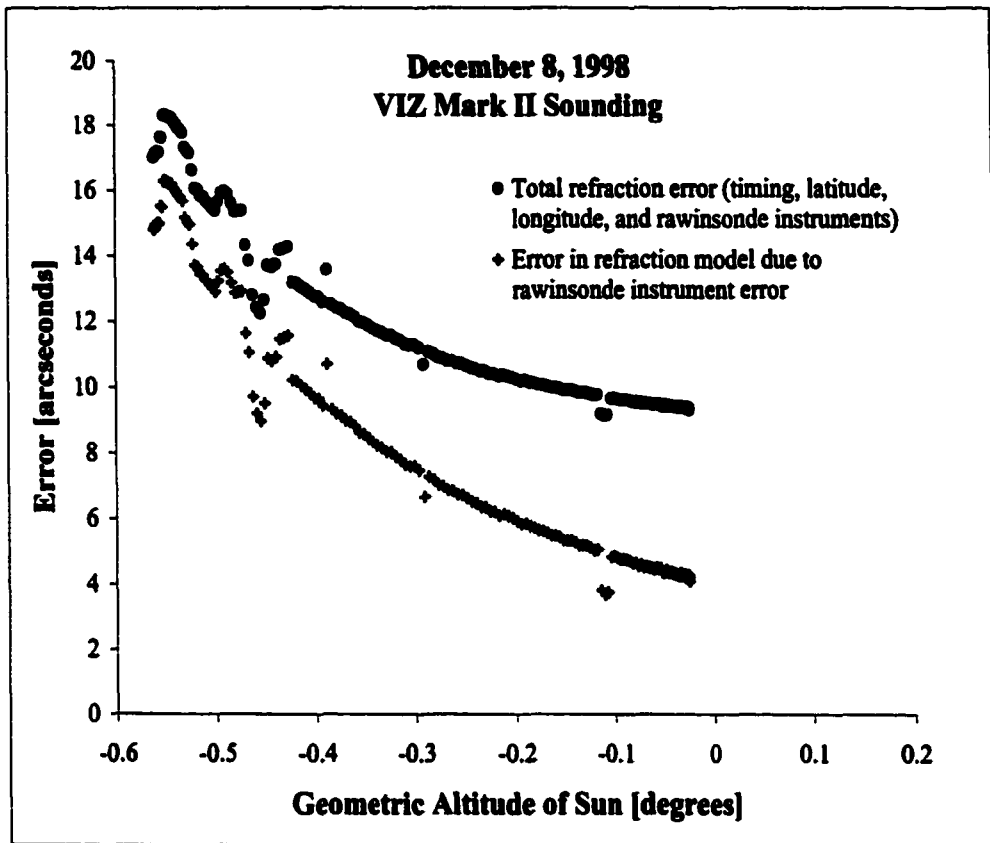


Figure 47: The error in the modelled refraction produced by instrument error in the December 8, 1998 VIZ Mark II rawinsonde. The total error includes errors produced by uncertainties in latitude, longitude and exposure timing. The geometric altitude of the Sun was used in the abscissa since the apparent altitude is variable due to the modelling error.

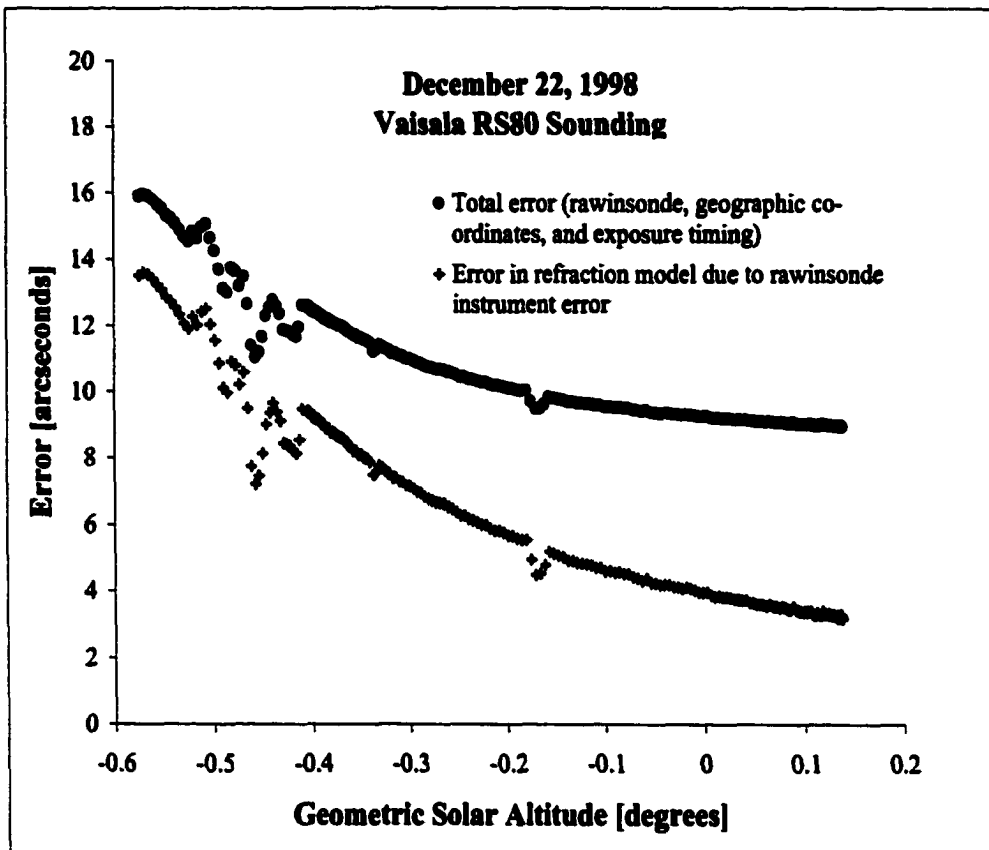


Figure 48: The error in the modelled refraction produced by instrument error in the December 22, 1998 Vaisala RS80 rawinsonde. The total error includes errors produced by uncertainties in latitude, longitude and exposure timing. The geometric altitude of the Sun was used in the abscissa since the apparent altitude is variable due to the modelling error.

The azimuthal error due to timing uncertainty δA_T was found in a similar fashion using the formula for azimuth A :

$$A = \cos^{-1} \left(\frac{\sin \delta - \cos z \sin \phi}{\sin z \cos \phi} \right). \quad (57)$$

Since the effects from astronomical refraction on azimuth of the Sun are negligible, this equation is more representative of the expected behavior. At the winter solstice the Sun is moving at an azimuthal rate of 12.0 "/s when $z = 90^\circ$. Therefore a timing error of ± 0.2 seconds would produce an azimuthal error of $\pm 2".4$.

The estimated error in latitude and longitude for the Stony Plain site was $\pm 9"$ in latitude and $\pm 13"$ in longitude. The elevation of the observing site was assumed to be accurate to less than a metre and therefore, was not considered significant since the Sun is very distant. The error in the cosine of the zenith angle due to uncertainties in latitude and longitude, $\delta \cos z_L$, is found through an error propagation performed on Equation 56 (Taylor, 1982), and produces the formula:

$$\delta \cos z_L = \left\{ \left[(\sin \delta \cos \phi - \cos \delta \sin \phi \cos H) \delta \phi \right]^2 + \left[-\cos \delta \cos \phi \sin H \delta H \right]^2 \right\}^{1/2}, \quad (58)$$

where the error in the solar declination is assumed to be negligible and $\delta \phi$ is the uncertainty in the latitude. The error in the azimuth due to uncertainties in latitude and longitude is determined from an error propagation through Equation 57 producing the formula:

$$\delta \cos A_{L(z=90^\circ)} = \left[(\tan \phi \delta z)^2 + \left(\frac{\delta \phi \sin \phi \sin \delta}{\cos^2 \phi} \right)^2 \right]^{1/2}, \quad (59)$$

where the uncertainty in the Hour Angle δH , is approximately equivalent to the uncertainty in the longitude. Placing the Sun near the horizon on the winter solstice

produces an uncertainty of $\pm 8''.3$ for the zenith angle and $\pm 14''.0$ for the azimuth, as seen from the Stony Plain site.

The total error in the zenith angle can be found from the formula:

$$\delta z_{Total} = \sqrt{\delta z_M^2 + \delta z_T^2 + \delta z_L^2}. \quad (60)$$

The total refraction error as a function of geometric altitude of the Sun can be seen in Figure 47 and 48. The total azimuthal error due to timing error and the error in latitude and longitude is found from the formula

$$\delta A_{Total} = \sqrt{\delta A_T^2 + \delta A_L^2}, \quad (61)$$

which gives a value of $\pm 14''.2$.

Error bars derived from Equations 60 and 61 when placed on Figures 29a to 43a would be about the same size as the lines of the graph, and therefore have not been included. The maximum zenith angle error of $18''$, when the image is very close to the astronomical horizon would translate to 0.7 mm error bars at the scale of Figures 29a to 43a. At zenith angles less than $89^\circ.7$ the error bars would be about 0.4 mm high. It should also be noted that the latitude and longitude error appears to dominate the error until the Sun is very close to the astronomical horizon.

5.2 Using Significant and Mandatory Levels: An Operational Refraction Model

Access to the Environment Canada RS80 fine-scale sounding files (10-second data intervals) is restricted to special requests. These data files are not usually archived by Environment Canada. Large archives of sounding are made available

online in the form of significant and mandatory levels (National Climate Data Center, 2000). Therefore, it is of practical interest to examine the accuracy of the model when using the more commonly available sounding data.

The significant and mandatory sounding files for the three sunsets were downloaded and the model was then run using exposure times that showed the bottom of the Sun very near or just below the observed horizon. This ensured that the comparison was complete down to the point of greatest observed refraction. A comparison between the fine scale model results and the significant and mandatory model results appears in Figure 49. It is apparent from the graph that the difference between the results is insignificant for the December 8 and 22 events. The mean difference is $+3.7 \pm 1.0$ arcseconds for December 8 and -3.6 ± 0.7 arcseconds for December 22. This is below the uncertainty of the model and the experiment (see section 5.1), and would suggest that the use of significant and mandatory files introduce no significant additional error in these events. However, the difference in refraction produced by the two sounding files appears to be larger for the December 14 event. As the Sun approaches the horizon, the difference approaches 15 arcseconds. This is still smaller than the maximum error displayed in Figure 48 and may therefore be considered insignificant. As mentioned in Section 3.6.4, the objective of the significant levels is to ensure an interpolated accuracy of 1°C for the mandatory levels. Therefore, it is not unreasonable to suggest that the increased difference observed for the December 14 sunset is a result of how close the significant levels bring the interpolation to within this specified criterion.

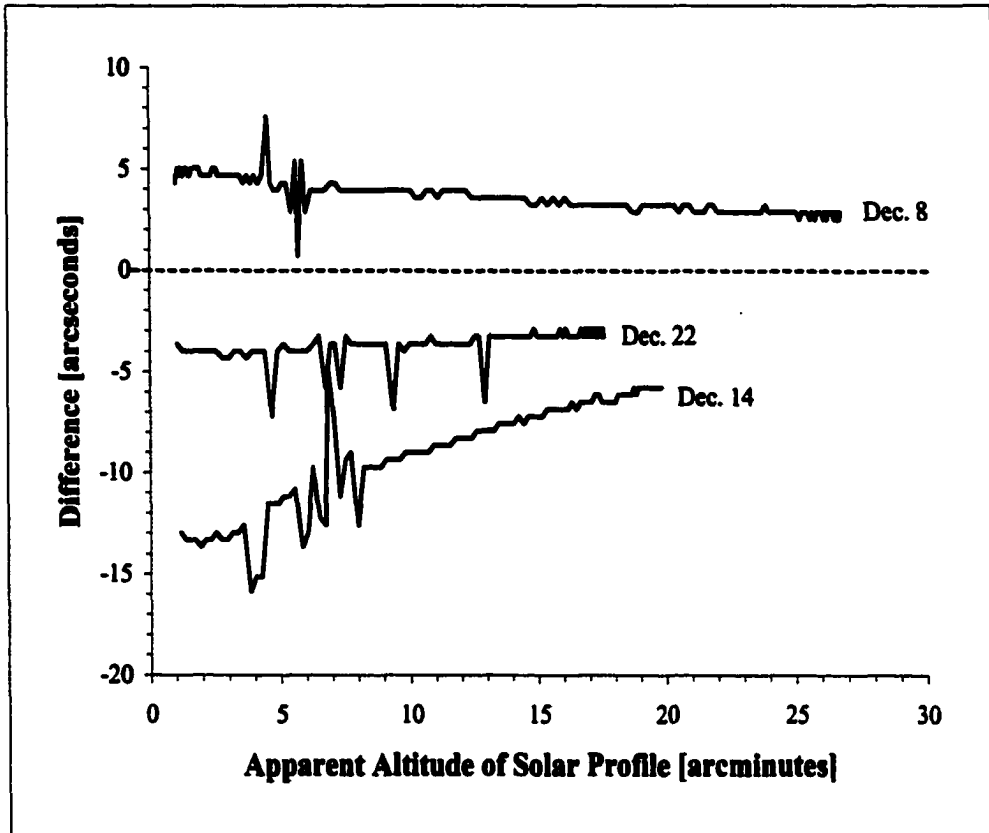


Figure 49: Comparison of the refraction produced by the model using the fine scale sounding file and the significant and mandatory file. The difference is equal to the significant and mandatory modelled refraction minus the fine scale modelled refraction.

More data would need to be collected over a wider range of atmospheric conditions before any general statement could be made about the utility of these simplified sounding files. However, the results suggest that the use of the significant and mandatory files may be appropriate for sunset refraction estimates.

5.3 Using a Modified U.S. Standard Atmosphere (MUSSA) in the Refraction Model

It was originally felt that the rawinsonde profiles would produce the highest accuracy in the refraction model since they are measuring the actual atmosphere rather than using an idealized model. To test this assumption, the results from the astronomical refraction model using the rawinsonde data were compared with the refraction produced by a modified U.S. Standard Atmosphere (MUSSA).

The U.S. Standard Atmosphere was developed in 1962 as an idealized, steady-state representation of the Earth's atmosphere from the surface to 1000 km (United States Government Printing Office, 1976). This atmospheric model is a time-averaged structure of the atmosphere as a function of height only (Wallace and Hobbs, 1977).

In this experiment, the tropospheric temperature gradient was -0.00649 Km^{-1} , the lower stratosphere was isothermal and the middle stratosphere had a warming of 0.00099 Km^{-1} . The height of the troposphere varies both geographically and seasonally, and was set to the value measured by the rawinsonde. As mentioned in the literature review, the effect the tropopause has on astronomical refraction is considerably less than the accuracy of this experiment. The start of the middle

stratosphere was set at a height of 20 km. Since both the pressure and humidity profiles are assumed to have minimal effect on the astronomical refraction, their rawinsonde profiles were used as a matter of convenience. The measured surface temperature at the time of the launch of the rawinsonde was used as the initial temperature and the rest of the profile was calculated from the above gradients.

The astronomical refraction model was then run for all the exposure times. The results appear in Figures 29b through 43b. A root mean square comparison between the observed astronomical refraction and the results from the two different astronomical refraction models (MUSSA and rawinsonde) appears in Table 5.

Date of Sunset	RMS [arcmin.] Rawinsonde	RMS [arcmin.] MUSSA
December 8, 1998	1.22	0.51
December 14, 1998	0.25	0.14
December 22, 1998	0.53	0.50

Table 5: Comparison of the root mean square difference between the observed and modelled refraction. The first second column is rms of the rawindsonde meteorological model and the third column is the rms of the Modified U.S. Standard Atmosphere (MUSSA) meteorological model.

From this analysis it is apparent that the use of a Modified U.S. Standard Atmosphere produces the same or better results than the rawinsonde. This is most likely due to instrument error in the rawinsonde, as outlined in Section 4.2.1. Therefore, present rawinsonde technology may be of insufficient accuracy to improve the modelling of astronomical refraction near the horizon. Since the uncertainty in the density gradient was dominated by the uncertainty in the measured temperature, more accurate temperature measurements would appear to

be necessary before rawinsondes could be used to improve refraction modelling. As discussed, some improvement may be possible through careful correction of known rawinsonde errors such as thermal lag. Currently, the Vaisala RS80 is not corrected for thermal lag since this error is not considered significant for forecasting purposes. However, the next model (Vaisala RS90) will have a faster temperature sensor (0.2 second lag at 1000 hPa and 6 ms⁻¹ airflow) (Paukkunen, 2000).

This also strongly suggests that the inverse solution to astronomical refraction may have limited usefulness. For the inverse solution, the measured astronomical refraction is used to determine the temperature profile of the atmosphere. In this sense, astronomical refraction could be used as a remote sensing technique. However, it appears that the model using a MUSSA profile produces a better fit with the observed astronomical refraction than the refraction model using the actual sounding. Therefore, the results suggest that an inverse solution to the observed refraction may simply produce no better than a MUSSA profile.

One of the more obvious differences between the MUSSA and rawinsonde profiles is the relative smoothness of the MUSSA temperature profile. To try to determine what in the MUSSA data was causing the improved performance, a simple smoothing function was applied to the rawinsonde temperature data. A running mean with a three-point filter was applied to the December 14 and 22 rawinsonde temperature data. Since the December 8 data had very irregular vertical spacing, this smoothing function produced a very spurious profile and was therefore not used. The resulting astronomical refraction for the December 14 and

22 sunsets showed an improvement of a few arcseconds. This appears to support the notion that some of the error may be due to temperature sensor noise.

The choice of a different filter size or smoothing function would require careful justification according to meteorological and instrumentation characteristics and shall be left to future investigations.

5.4 The Horizontal Temperature Gradient and Model Sensitivity

From both the Tory building and the Stony Plain measurements, it is apparent that the greatest discrepancy between modelled and observed refraction occurred on December 8, 1998. As mentioned in Section 3.4, it was posited that a strong horizontal temperature gradient might produce a relatively large discrepancy between the modelled and the observed refraction.

In order to examine the possible links between a horizontal temperature gradient and the behavior of the refraction model, a set of surface temperature time series was obtained from weather stations near Stony Plain (see Figures 50 to 53). It is apparent from these plots that there existed a significant horizontal temperature gradient on the date of December 8. To further illustrate the December 8 temperature gradient an additional station was obtained (Highvale, Alberta).

In order to explore the possible effects of the December 8 temperature gradient on the refraction model the temperature profile of the sounding was adjusted and the model run again. Since the sunlight came from the southwest, it was assumed that the rays near the surface would have passed through the warmer air in the direction of Highvale. Therefore, the temperature profile of the boundary

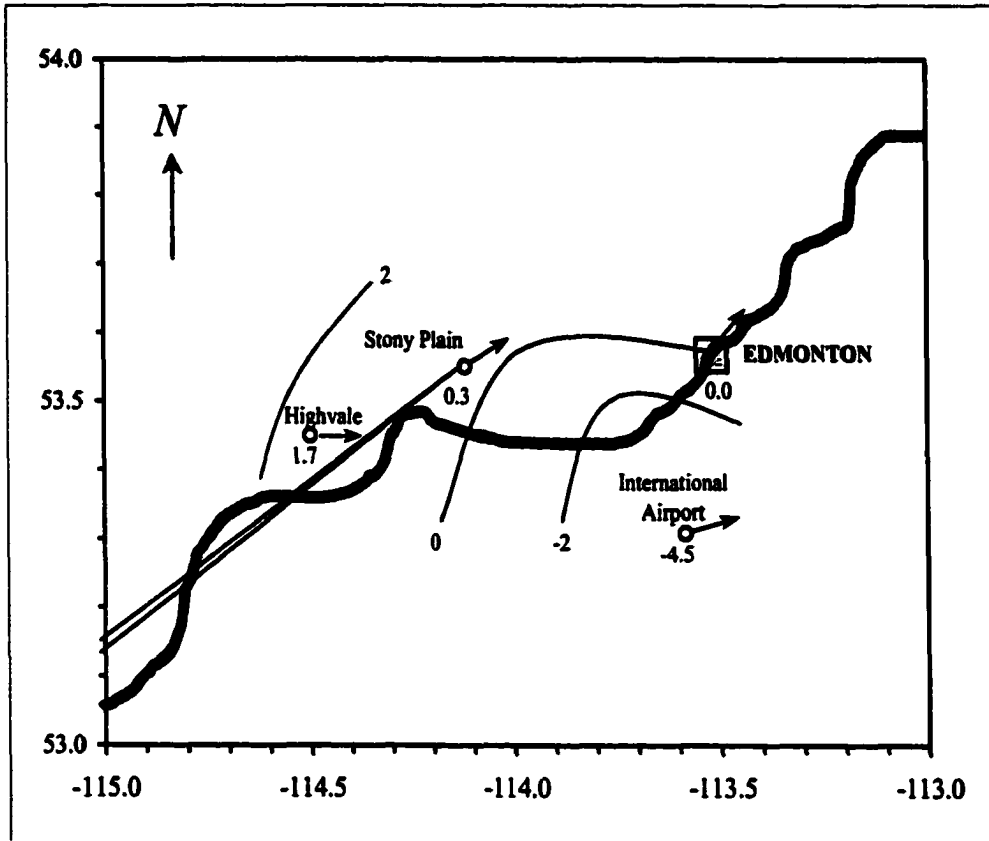
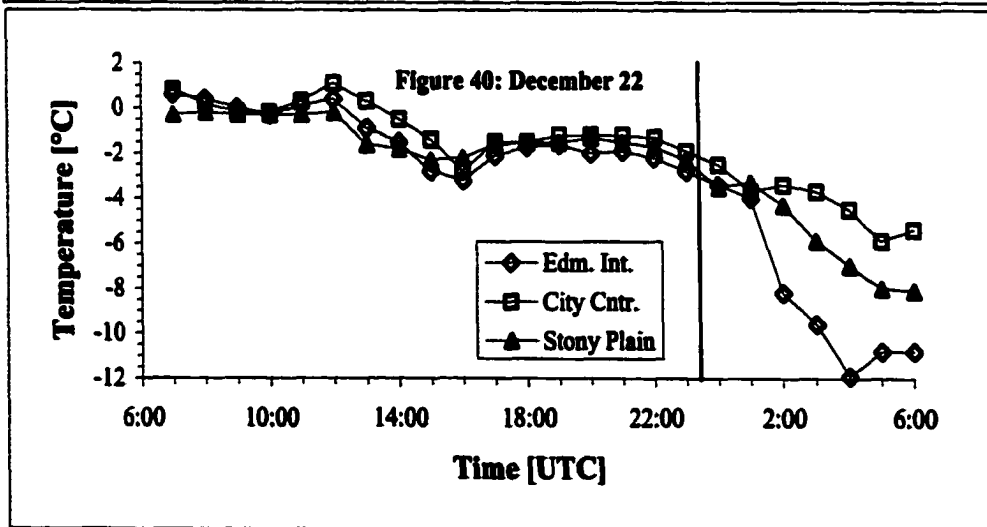
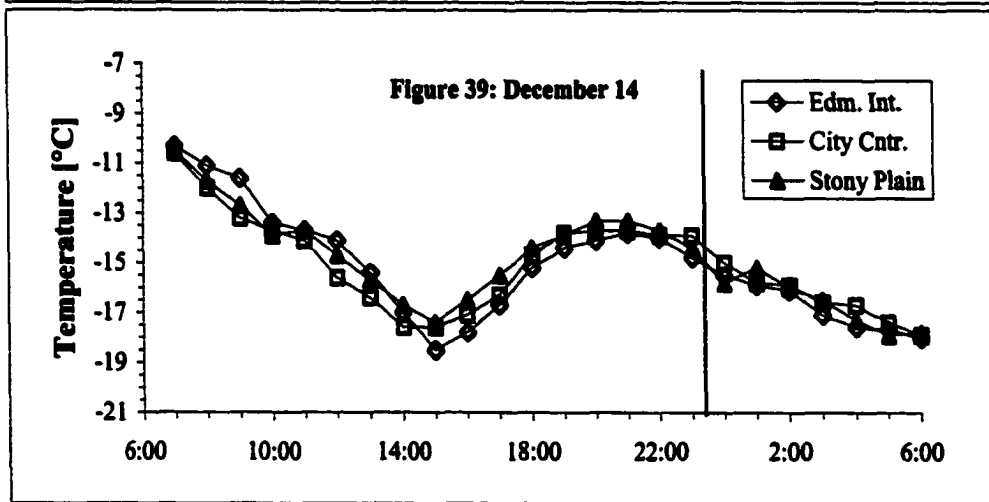
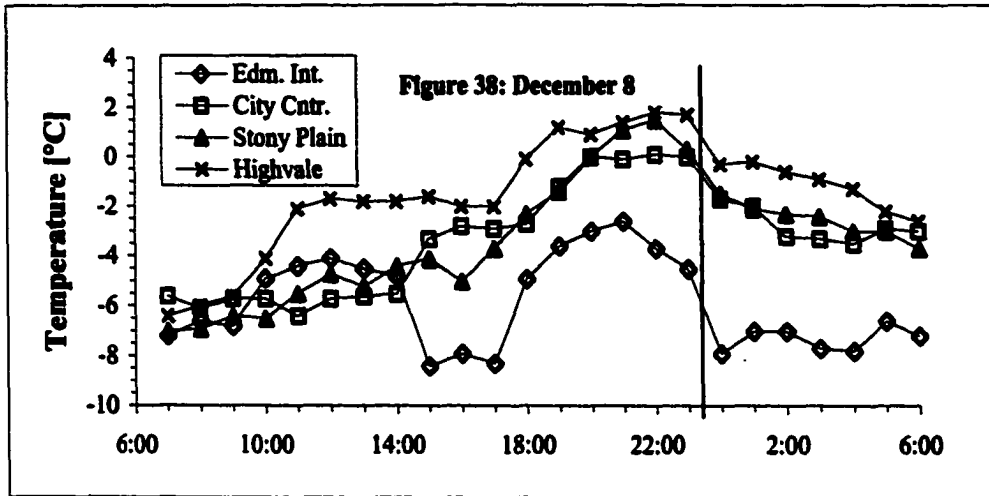


Figure 50: Horizontal temperature distribution for December 8, 1998 at 23:00 UTC. Graph axes are latitude and longitude. Surface temperatures in °C are printed below stations. The contours were drawn by hand. The straight lines from Stony Plain are the azimuthal range of the setting Sun (i.e. from the first to the last photograph). The location of the North Saskatchewan River (grey band) is only approximate. Arrows indicate mean hourly wind direction at 23:00 U.T.C.. The average hourly wind speed for the four stations was 3.2 ms^{-1} .



Figures 51 to 53: Surface temperature time series. Vertical line is the time of sunset.

layer experienced by the light ray to the southwest of Stony Plain was likely warmer than the Stony Plain sounding. From Figure 51 it appears the surface temperature at the time of the sunset increased by 1.4°C between Stony Plain and Highvale, a distance of about 30-km. However, the light ray path increases in height as it moves away from the observer. A plot of the light ray path and the topography below the ray appears in Figure 54.

Since the vertical temperature gradient at each point along the path is unknown, any adjustment to the sounding data must be very approximate. Nonetheless, the general behavior of the refraction (i.e. increase or decrease with temperature) can be revealed and may provide some direction for further study.

Assuming a linear temperature gradient between Stony Plain and Highvale and taking into account the increasing height of the light ray path, a first guess of +0.5°C for the surface value adjustment and +0.2°C to the second level (52 m above the surface) seemed reasonable. Three other model runs were performed with the adjustments doubled each time. Placing the adjusted sounding into the model produced a change in the refraction in a direction towards the observed values (see Figure 55). The actual discrepancy between the photographic altitude and modelled altitude of the Sun ($\lambda = 580 \text{ nm}$) was also plotted. This shows that the difference between the adjusted model results and the actual observed refraction is approximately minimized with a change in surface temperature of +2.0°C and +0.8°C at the next level.

This conclusion is somewhat complicated by the fact that on this day the Stony Plain Upper Air Station was training new technicians and using a VIZ

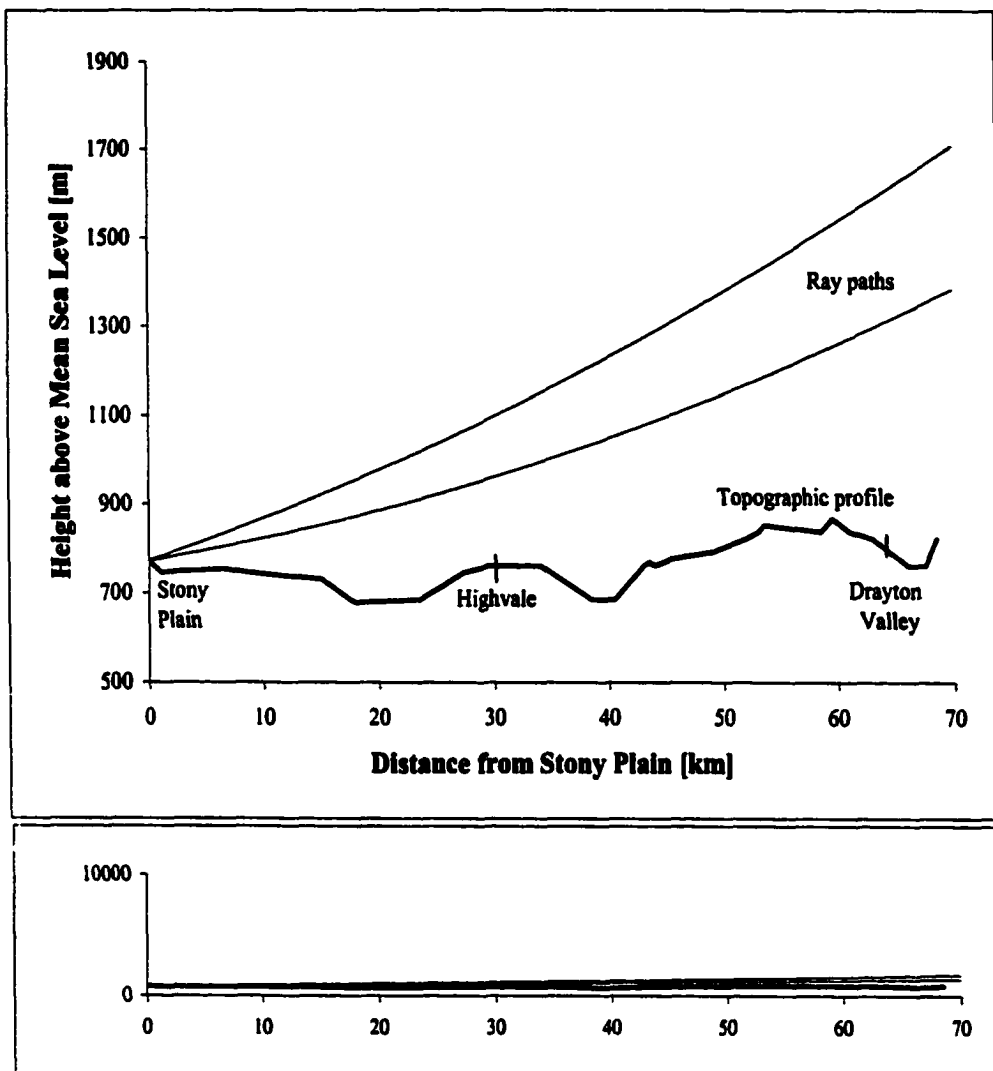


Figure 54: Ray path for December 8 1998 sunset (23:12:34.5 UTC) with respect to the mean sea level topography under the ray path. The two ray paths represent the top and bottom of the solar profile (i.e. maximum and minimum altitude). The upward curvature of the rays is an artifact of the projection of the surface of the Earth onto a Cartesian reference frame. The lower graph shows the same plot with equal scaling in the vertical and the horizontal and gives a sense of the actual ray path.

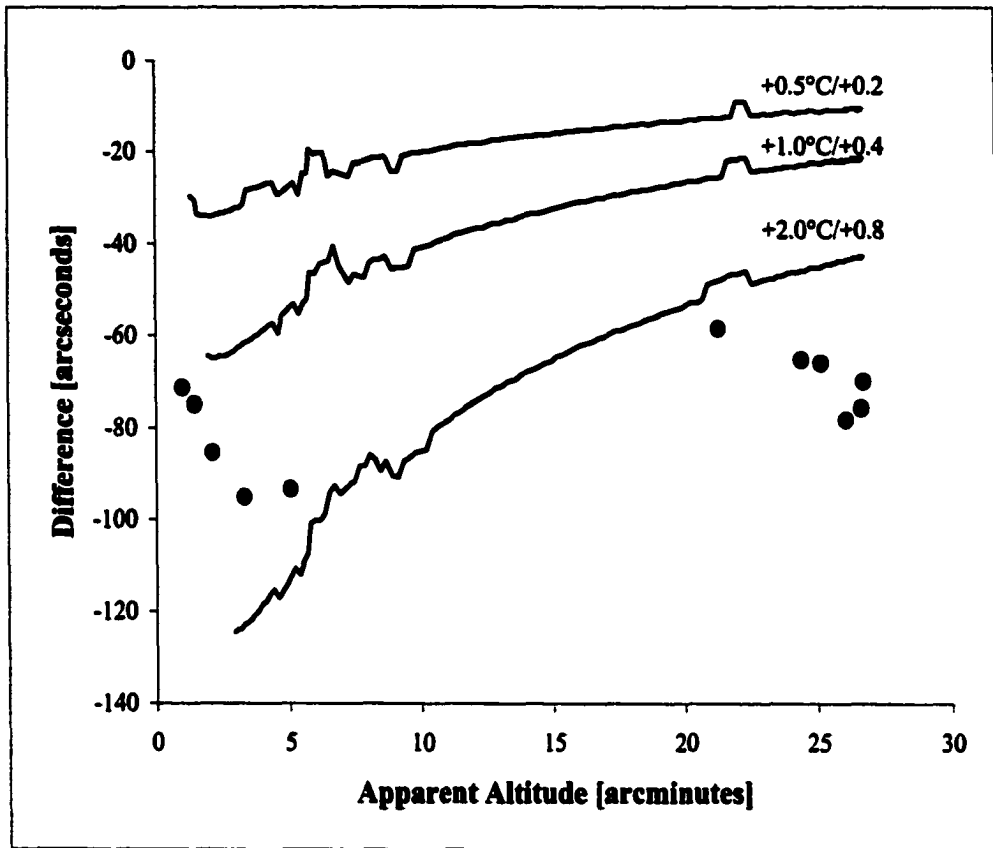


Figure 55: The difference between the December 8 modelled refraction with and without adjustments made to the surface temperature and the second level (52 m). A negative difference indicates a decrease in altitude of the model output and an improvement in the model. Temperature labels on the graph lines indicate the temperature change at the surface and the second level respectively. The points represent the difference between the measured altitude of the photographed sunset and the apparent altitude of the corresponding unadjusted modelled image points at the same azimuth as the point on the photograph. All model runs were done with yellow light ($\lambda = 580 \text{ nm}$).

rawinsonde that had coarser vertical resolution. As mentioned in Section 4.2.1, many of these old instruments were defective and were subsequently rejected prior to launch. Although difficult to substantiate, there is a distinct possibility that the December 8 instrument may have been faulty, thus producing erroneous model results. This notion is also supported by the improvement in the model results when a MUSSA profile was applied.

Future tests of the refraction model under significant horizontal temperature gradient conditions should be done with the current rawinsonde model. As well, the existence of a strong horizontal temperature gradient suggests the atmosphere will no longer be spherically symmetric. Therefore, the preceding analysis can only be considered crude at best. To fully explore the effects of a horizontal temperature gradient on the modelled refraction a full three-dimensional model of the atmosphere and a corresponding refraction model would need to be constructed.

5.5 Comparison of Refraction Model with Pulkovo Refraction Tables

The 'Refraction Tables of the Pulkovo Observatory' (1930, 1956, and 1985) is one of the most widely utilized sources for estimating astronomical refraction (Mahan, 1962, Green, 1985). The tables are based on an empirical method requiring the input of the apparent zenith angle, surface meteorological data, the wavelength of light, and the latitude and elevation of the observing station. Earlier versions of the tables (Pulkovo, 1930) required the input of the time of day and the time of year. This correction appeared to produce only a slight difference in the final computed value and was later dropped from the tables.

A comparison between the modelled results and the Pulkovo estimates can be seen in Figures 56a to 58a (rawinsonde profiles used in the model) and Figures 56b to 58b (MUSSA profiles). From a visual examination of these results it is apparent that the present refraction model using both a rawinsonde and MUSSA profile produces better results than the Pulkovo Tables for December 14 and 22. For the December 8 sunset event, the Pulkovo Tables appear to produce better results than the rawinsonde below 20 arcminutes altitude. However, the rate of change of the refraction with respect to altitude for the Pulkovo Tables does not appear to follow the observed refraction, while the rawinsonde modelled refraction trend appears to be parallel to the observed refraction trend yet offset by a nearly constant amount. The December 8 modelled refraction using a MUSSA profile produces a better fit than the Pulkovo Tables. A more quantitative measure of the difference in accuracy between the present refraction model and the Pulkovo Refraction Tables can be seen in Table 6.

Date of Sunset	RMS Observed – Model (rawinsonde) [arcminutes]	RMS Observed – Model (MUSSA) [arcminutes]	RMS Observed – Pulkovo [arcminutes]
12/08/1998	1.22	0.51	0.83
12/14/1998	0.25	0.14	0.24
12/22/1998	0.53	0.50	0.81

Table 6: An RMS comparison of present refraction model (yellow light, rawinsonde and MUSSA profiles) and the Pulkovo tables with respect to the observed astronomical refraction from Stony Plain.

The refraction produced by the Pulkovo Tables for the December 8 sunset was adjusted by changing the surface temperature (see Figures 56a to 58a). The

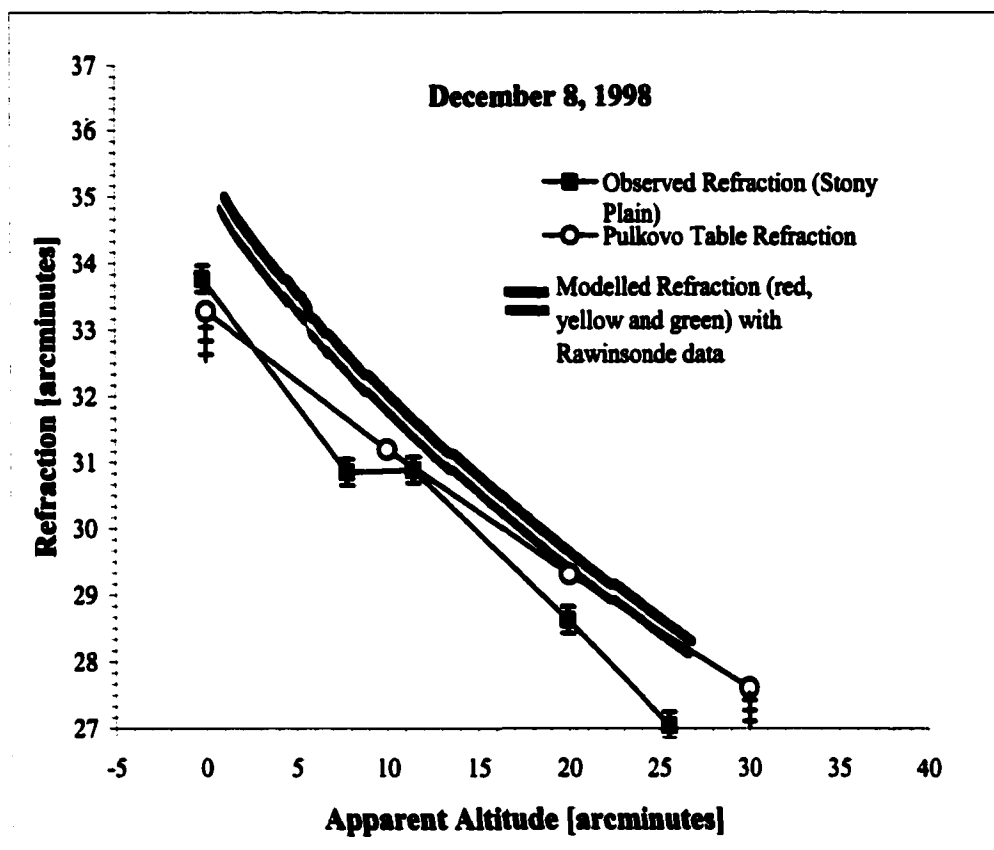


Figure 56a: Comparison of Pulkovo Table refraction, modelled refraction and observed refraction for December 8, 1998 sunset. The crosses represent the Pulkovo Table refraction values with surface temperature adjusted by +1.0 +2.0 +3.0 °C from an original value of -0.1°C, with the greatest temperature change at the bottom. The model used an unadjusted temperature profile based on the rawinsonde data. Error bars on the observed refraction values are derived from exposure timing error (about 1") errors in geographic coordinates (about 8") and theodolite (about 6") and photogrammetric errors (about 6")

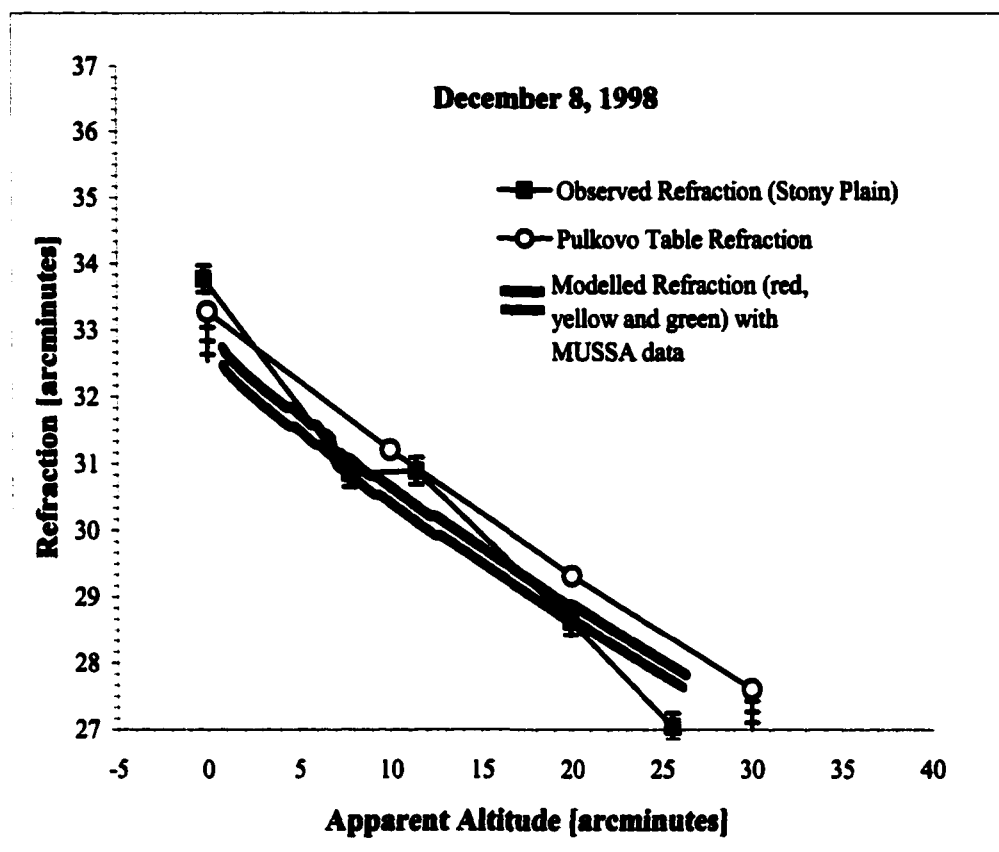


Figure 56b: Comparison of Pulkovo Table refraction, modelled refraction using a Modified U.S. Standard Atmosphere (MUSSA) and observed refraction for December 8, 1998 sunset.

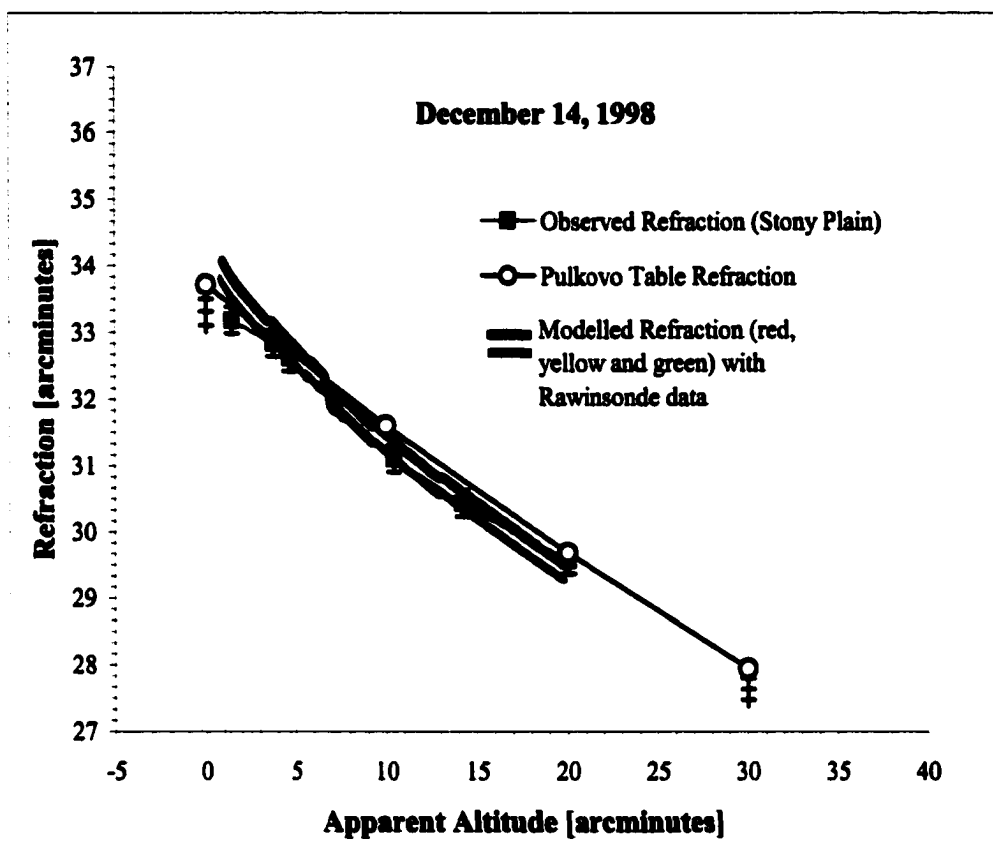


Figure 57a: Comparison of Pulkovo Table refraction, modelled refraction and observed refraction for December 14, 1998 sunset. The crosses represent the Pulkovo Table refraction values with surface temperature adjusted by +1.0 +2.0 +3.0 °C from an original value of -2.4°C, with the greatest temperature change at the bottom. The model used an unadjusted temperature profile based on the rawinsonde data.

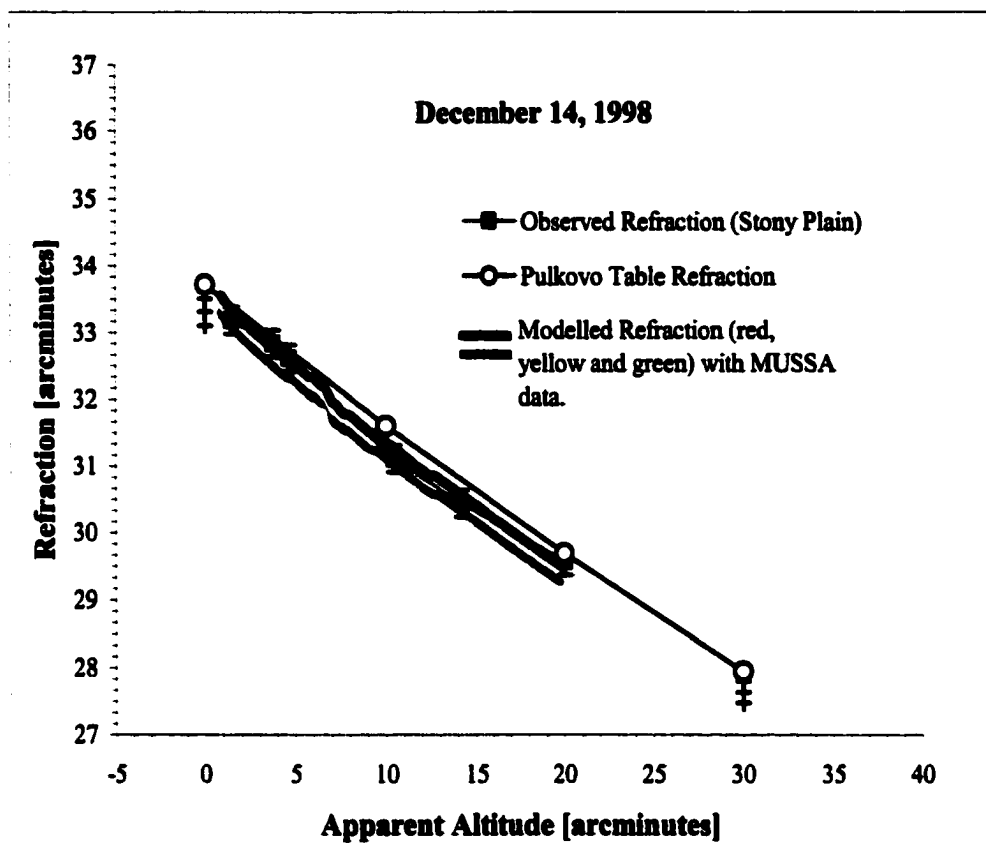


Figure 57b: Comparison of Pulkovo Table refraction, modelled refraction using a Modified U.S. Standard Atmosphere (MUSSA) and observed refraction for December 14, 1998 sunset.

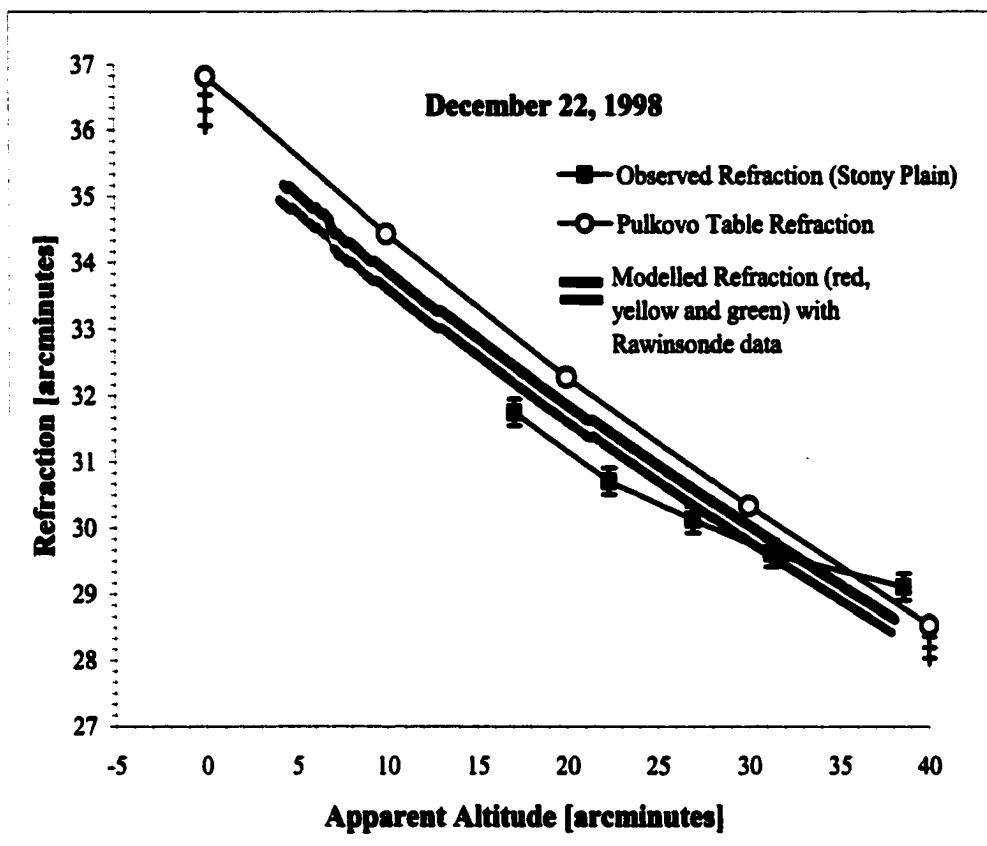


Figure 58a: Comparison of Pulkovo Table refraction, modelled refraction and observed refraction for December 22, 1998 sunset. The crosses represent the Pulkovo Table refraction values with surface temperature adjusted by +1.0 +2.0 +3.0 °C from an original value of -14.3°C, with the greatest temperature change at the bottom. The model used an unadjusted temperature profile based on the rawinsonde data.

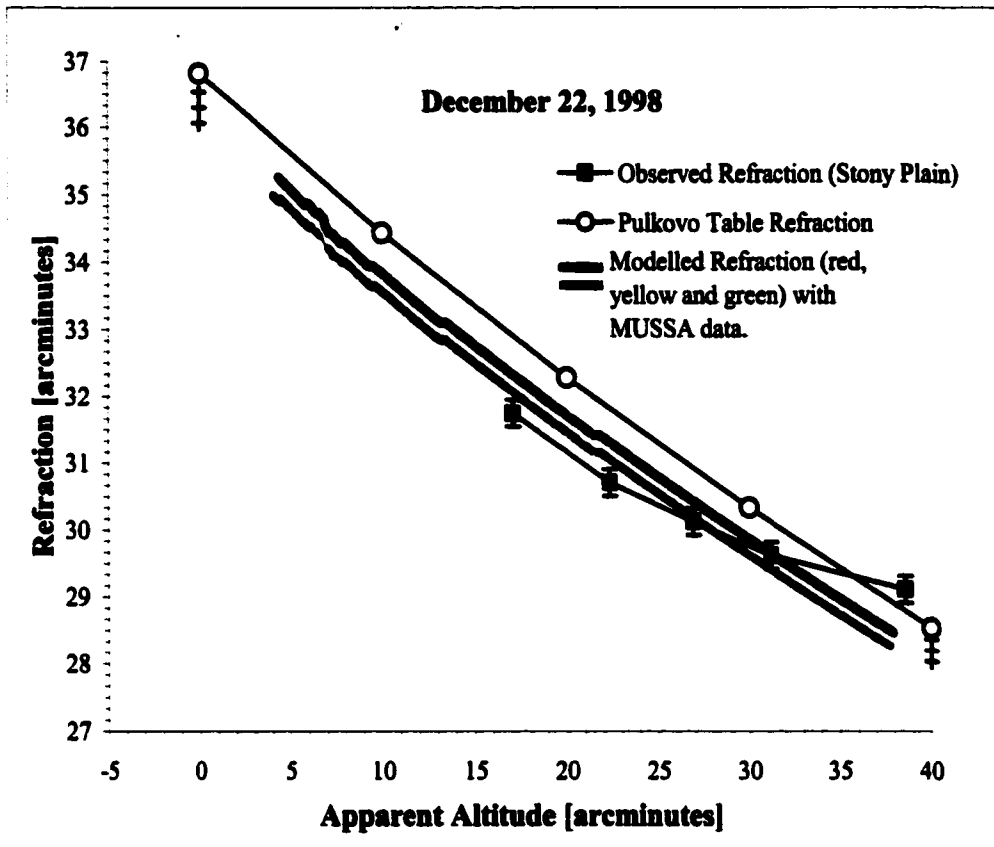


Figure 58b: Comparison of Pulkovo Table refraction, modelled refraction using a Modified U.S. Standard Atmosphere (MUSSA) and observed refraction for December 22, 1998 sunset.

surface temperature was adjusted by +1.0, +2.0 and +3.0°C and the refraction recalculated. From a visual examination of the graphs it appears that an increase in the surface temperature generally leads to an improvement in the performance of the Pulkovo Tables.

6. Conclusions

The improved performance of the MUSSA profile over the rawinsonde model suggests the rawinsonde data may not be accurate enough to produce an improved refraction model. These results raise the possibility that the rawinsonde temperature profile may be inadequate for detailed high zenith angle refraction modelling. However, careful correction and calibration of the rawinsonde instruments may help this situation. To continue this study, significant attention would need to be placed on the accuracy of the sounding data, especially near the surface where the greatest effects on astronomical refraction occur (see Appendix H). As mentioned previously, the common practice is to use the temperature from the nearest surface station as the first data point in the sounding. Unless the surface station and rawinsonde sensor are compared before each launch, it is impossible to know if any bias exists between the two instruments. A first step in correcting this situation would be to record the surface temperature as measured by the rawinsonde as well as the surface station. Care must also be taken to ensure that the rawinsonde temperature sensor has reached equilibrium before launch. As mentioned in Schwartz and Doswell (1991) and Mahesh et al (1997), the thermal lag of the sensor may be complicated by a quick release of the rawinsonde from a

heated or air-conditioned assembly shelter. During the current experiment at the Stony Plain Upper Air Station, the author observed a very quick release from the shelter on one occasion, however the date was not recorded.

The somewhat poorer results for the December 8 event and the discussions in Section 5.4, suggest that to improve the model, a significant effort may have to be undertaken to measure and incorporate the horizontal temperature distribution. The results of the temperature profile adjustments done on the December 8 sounding would further suggest that knowledge of the horizontal temperature distribution might improve the performance of the refraction model under conditions of substantial horizontal temperature gradients. The passage of a synoptic scale front may also imply that the assumption of a spherically symmetric atmosphere may no longer be valid. However, the use of an old and possibly degraded VIZ rawinsonde during the December 8 sunset has also reduced the confidence in this particular atmospheric data set.

The agreement between the Tory rooftop measurements and the December 14 and 22 results also suggest the model is valid over a relatively large geographical area (about 25 km) when the horizontal temperature distribution is homogeneous. It is also interesting to note that the two sites were at slightly different elevations – the Tory building being 45 metres lower. Therefore, it also appears that small differences in elevation did not appear to be a major factor during these particular sunsets. Consequently, it may not be necessary for observers to be stationed at the same location as the rawinsonde.

The use of significant and mandatory level sounding files in the model also appears to be promising. However, the effectiveness of the model with the significant and mandatory files would need to be tested more thoroughly by comparing modelled and observed refraction using a much larger sample of sunsets. Sunrises should be included since the morning boundary layer is much more complex after the formation of the nocturnal inversion. As well, the amount and quality of any required horizontal temperature data should also be investigated. This would be necessary in order to determine the minimum amount of information necessary, both vertical and horizontal, to produce an accurate refraction model output under the expected range of conditions. As mentioned earlier, the potential conflict between the temperature as measured by the rawinsonde and the surface station would also need to be addressed.

The potential for extracting temperature profiles from refraction measurements was not explored in this study. The possibility of extracting atmospheric soundings from refraction measurements is not great. If a MUSSA profile produces better model results than actual sounding data, it is assumed that the reverse solution (a temperature profile extracted from refraction measurements) would produce nothing better than a MUSSA profile.

Finally, the results suggest that the refraction model using a MUSSA profile produced better agreement with the observed refraction than the Pulkovo Refraction Tables. A root mean square analysis of the three sunsets shows a 37% to 42% improvement in the agreement between MUSSA model and the observed refraction compared to Pulkovo Tables and the observed values. Therefore, the

results suggest that the employment of a raytracing refraction model using a simple MUSSA profile should give better sunset astronomical refraction values than the Pulkovo Tables. Since the MUSSA profile requires only a surface temperature, the use of the refraction model is not restricted to sites with access to a rawinsonde. Therefore, the model may be more universally applicable than the Pulkovo Tables in predicting sunset refraction values.

7. Discussion

The use of photogrammetric techniques to extract observed refraction values appeared to be effective, although the time between the event and data reduction is rather lengthy. The major source of this delay is the time necessary to process the film, digitize the image and then calculate the object co-ordinates. This time delay could be greatly reduced through the employment of a photogrammetrically calibrated digital camera, which would eliminate the need for chemical processing and digital scanning. However, the cost of a digital camera capable of the necessary magnification and resolution may be prohibitive to those with limited funding. Quick and accurate measurements can also be obtained using a self-leveling theodolite. These instruments are capable of measuring only one point on the solar disk at a time.

Future research could involve the following components.

1. The refraction model could be significantly modified to incorporate zenith angles greater than 90° and horizontal gradients of temperature, pressure and humidity. The assumption of an isothermal layer for each increment of the raytracing model

could also be relaxed by making the temperature profile linear in each layer. This may help eliminate the appearance of total internal reflection when the ray is very nearly horizontal.

2. A larger sample of sunrise and sunset events should be sought. This would be useful in the examination of such things as the utility of significant and mandatory sounding files in the refraction model; the influence of horizontal temperature gradients on the accuracy of the model and a better comparison between the model and the Pulkovo Refraction Tables.

3. Improvements should be sought in the accuracy of the rawinsonde temperature data – especially near the surface. The next generation of Vaisala rawinsondes (RS90) will have a faster response time temperature sensor (0.2 s at 1000 hPa and air flow of 6 ms⁻¹)(Personal communication, Ari Paukkunen, 2000)

4. The model could be adjusted to simulate refraction events in the atmospheres of other planets.

APPENDIX A

CALCULATION OF THE REFRACTIVE INDEX OF AIR

The density of the air determines its index of refraction. The density of the air at a given temperature and pressure is a function of its constituents. The two most variable constituents in the Earth's atmosphere are water vapor and carbon dioxide. The following method developed by Ciddor (1996) determines the refractive index of air from the temperature, pressure, humidity and carbon dioxide content.

The refractive index ($n - 1$) is found from the equation (Ciddor, 1996):

$$n - 1 = (\rho_d / \rho_{std}) (n_{std} - 1) + (\rho_w / \rho_w) (n_w - 1), \quad (A1)$$

where ρ_d is the density of the dry component of air, ρ_{std} is the density of standard air (15°C, 101,325 Pa, 0% R.H. and CO₂ of 450 ppm), n_{std} is the refractive index of standard air, ρ_w is the density of the vapor component of air, ρ_w is the density of pure water vapor (20 °C, 1333 Pa) and n_w is the refractive index of pure water vapor at 20 °C and 1333 Pa.

The sounding provides only relative humidity and the refractive index formula requires vapor pressure. The vapor pressure was found from the relative humidity and temperature provided by the sounding. The saturation vapor pressure (in Pa) over liquid water e_s , was found from the empirical formula (Lowe, 1976):

$$e_s = (s_0 + T(s_1 + T(s_2 + T(s_3 + T(s_4 + T(s_5 + s_6 T)))))), \quad (A2)$$

where T is the temperature in degrees Kelvin and the constants are:

$$\begin{aligned}
s_0 &= 6.984505294 \times 10^5 \text{ Pa} \\
s_1 &= -1.88903931 \times 10^4 \text{ PaK}^{-1} \\
s_2 &= 2.133357675 \times 10^2 \text{ PaK}^{-2} \\
s_3 &= -1.288580973 \times 10^0 \text{ PaK}^{-3} \\
s_4 &= 4.393587233 \times 10^{-3} \text{ PaK}^{-4} \\
s_5 &= -8.023923082 \times 10^{-6} \text{ PaK}^{-5} \\
s_6 &= 6.136820929 \times 10^{-9} \text{ PaK}^{-6}
\end{aligned} \tag{A3}$$

The refractive index of standard air n_{air} (15 °C, 101,325 Pa, 0% R.H. and 450 ppm of CO₂) is then calculated from the formula (Ciddor, 1996):

$$10^8(n_{\text{air}} - 1) = k_1/(k_0 - \sigma^2) + k_3/(k_2 - \sigma^2), \tag{A4}$$

where σ is the wave number of light (reciprocal of the vacuum wavelength in μm), and the constants are:

$$\begin{aligned}
k_0 &= 2.380185 \times 10^2 \mu\text{m}^{-2} \\
k_1 &= 5.792105 \times 10^6 \mu\text{m}^{-2} \\
k_2 &= 5.7362 \times 10^1 \mu\text{m}^{-2} \\
k_3 &= 1.67917 \times 10^5 \mu\text{m}^{-2}
\end{aligned} \tag{A5}$$

The refractive index for water vapor under standard conditions (20°C, 1333 Pa) is then found from:

$$10^8(n_{\text{ws}} - 1) = c_f(w_0 + w_1\sigma^2 + w_2\sigma^4 + w_3\sigma^6), \tag{A6}$$

where c_f is an empirical correction factor found by fitting the calculations to the measurements, and the constants are:

$$\begin{aligned}
w_0 &= 2.95235 \times 10^2 \mu\text{m}^{-2} \\
w_1 &= 2.6422 \times 10^0 \mu\text{m}^{-2} \\
w_2 &= -3.2380 \times 10^{-6} \mu\text{m}^{-4} \\
w_3 &= 4.028 \times 10^{-9} \mu\text{m}^{-6}
\end{aligned} \tag{A7}$$

Next the compressibility of air Z must be found. This value represents the departure from ideal gas behavior and is calculated from the formula (Ciddor, 1996):

$$Z = 1 - (p_0/T_0) \left[a_0 + a_1 T_C + a_2 T_C^2 + (b_0 + b_1 T_C) x_w + (c_0 + c_1 T_C) x_w^2 \right] + (p/T_K)^2 (d + e x_w^2) \quad (A8)$$

where T_C is the temperature in degrees Celsius, $T_0 = 288.15$ K, $p_0 = 101,325$ Pa, and x_w is the mole fraction of water vapor and is set to zero. The remaining constants are:

$$\begin{aligned} a_0 &= 1.58123 \times 10^{-6} \text{ KPa}^{-1} \\ a_1 &= -2.9331 \times 10^{-8} \text{ Pa}^{-1} \\ a_2 &= 1.1043 \times 10^{-10} \text{ KPa}^{-1} \\ b_0 &= 4.028 \times 10^{-9} \text{ KPa}^{-1} \\ b_1 &= -2.051 \times 10^{-8} \text{ Pa}^{-1} \\ c_0 &= 1.9898 \times 10^{-4} \text{ KPa}^{-1} \\ c_1 &= -2.376 \times 10^{-6} \text{ Pa}^{-1} \\ d &= 1.83 \times 10^{-11} \text{ K}^2 \text{ Pa}^{-2} \\ e &= -7.65 \times 10^{-9} \text{ K}^2 \text{ Pa}^{-2} \end{aligned} \quad (A9)$$

The compressibility factor for pure water vapor is now calculated from equation (A8) by setting $T = 293.15$ K, $p = 101,325$ Pa, and $x_w = 1$.

The densities of dry standard air ρ_{air} and standard water vapor ρ_w are then computed using the general formula (Ciddor, 1996) (with the corresponding values of Z):

$$\rho = (pM_a/ZRT) \left[1 - x_w (1 - M_w/M_a) \right], \quad (A10)$$

where p is the atmospheric pressure (Pa), R is the universal gas constant ($8.314510 \text{ Jmol}^{-1}\text{K}^{-1}$), T is the air temperature (K), M_w is the molar mass of water vapor ($0.018015 \text{ kgmol}^{-1}$) and M_a is the molar mass of dry air (kgmol^{-1}), found from the equation:

$$M_a = 10^{-3} [28.9635 + 12.011 \times 10^{-6} (x_c - 400)], \quad (\text{A11})$$

where x_c is the concentration of CO₂ (in ppm), was recommended to be approximately 450 ppm (Ciddor, 1996).

The compressibility of moist air from the sounding (i.e. experimental conditions) is now found from equation (A8). The molar fraction of water vapor in moist air x_w is determined from the equation:

$$x_w = \frac{fhe_s}{p}, \quad (\text{A12})$$

where h is the fractional relative humidity (between 0 and 1), e_s is the saturation vapor pressure (in Pa) and is found from equation (A2), p is the atmospheric pressure from the sounding, and f is the enhancement factor for water vapor in air. The enhancement factor is used to compensate for departures from ideal gas behavior and is found from the formula (Giacomo, 1982):

$$f = \alpha + \beta p + \gamma T_c^2, \quad (\text{A13})$$

where the constants are:

$$\begin{aligned} \alpha &= 1.00062 \\ \beta &= 3.14 \times 10^{-9} \text{ Pa}^{-1} \\ \gamma &= 5.6 \times 10^{-7} \text{ }^\circ\text{C}^{-2} \end{aligned} \quad (\text{A14})$$

The density of the dry component ($M_w = 0$) of the moist air ρ_a can now be computed from equation (A10):

$$\rho_a = \frac{pM_a(1-x_w)}{ZRT}, \quad (\text{A14})$$

where p is the atmospheric pressure and Z is the compressibility determined from the sounding data.

Similarly, the density of the water vapor component of the air can be computed from equation (A10)

$$\rho_w = \frac{pM_w x_w}{ZRT}. \quad (\text{A15})$$

Finally, the index of refraction can be found from the formula (A1).

APPENDIX B

DERIVATION OF THE FUNDAMENTAL ASTRONOMICAL REFRACTION EQUATIONS

In this appendix the fundamental principles of refraction will be outlined and then applied to atmospheric refraction in a spherically symmetric atmosphere. The final following derivation is an elaboration of the derivation of the atmospheric refraction formula in a spherically symmetric atmosphere given by Bruton (1996).

B.1 Introduction to the Geometrical Optics of Refraction

The astronomical refraction model used in this thesis is based on geometrical optics. In geometrical optics it is assumed that when a light ray encounters an interface, it separates into refracted and reflected components. The four basic principles of geometrical optics are (Valasek, 1949, Hecht, 1990).

- 1) The assumption of rectilinear propagation of light in a homogeneous medium (i.e. light rays).
- 2) The laws of reflection:
 - a. The angle of reflection is equal to the angle of incidence.
 - b. The reflected ray lies in the plane of incidence. The plane of incidence is the plane defined by the incident ray and the normal to the surface at the point of contact of the ray.

3) The laws of refraction:

a. The ratio of the sine of the angle of incidence to the sine of the angle of refraction is equal to a constant (Snell's Law of Refraction).

b. The refracted ray lies in the plane of incidence.

4) All light rays are independent. This overlooks all diffraction and interference effects, which in the case of astronomical refraction can be assumed to be insignificant.

Hero of Alexandria first proposed the *variation principle* sometime between 150 B.C. and 250 A.D. (Hecht, 1990). This principle as applied to the process of reflection states that the path taken by a reflected beam of light must have the shortest possible length, which directly leads to the first law of reflection. In 1657, Pierre de Fermat reformulated the principle and applied it to the process of refraction. His *principle of least time* states that the actual path between two fixed points taken by a beam of light is the one that is traversed in the least time.

Using Figure B1 it can be shown that the time t required to travel from point S to point P is given by the formula (Hecht, 1990):

$$t = \frac{\overline{SO}}{v_i} + \frac{\overline{OP}}{v_t}, \quad (\text{B1})$$

where v_i is the velocity of the incident light ray and v_t is the velocity of the transmitted light ray. Using the Pythagorean relationship Equation B1 can be rewritten as:

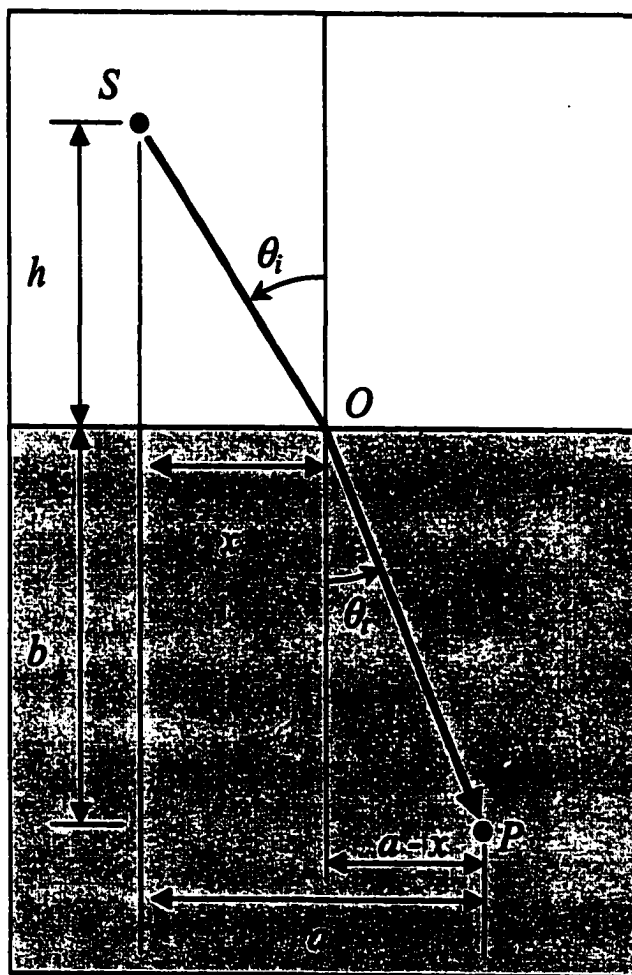


Figure B1: A schematic diagram used to illustrate the derivation of the refraction formula according to Fermat's Principle of least time (adapted from Hecht, 1990).

$$t = \frac{(h^2 + x^2)^{1/2}}{v_i} + \frac{[b^2 + (a-x)^2]^{1/2}}{v_t}. \quad (\text{B2})$$

A variation in x shifts point O , thereby changing the path taken by the ray between S to P . To find the minimum of t with respect to variations in x the derivative of Equation B2 is set to zero, that is:

$$\frac{\partial t}{\partial x} = \frac{x}{v_i(h^2 + x^2)^{1/2}} + \frac{-(a-x)}{v_t[b^2 + (a-x)^2]^{1/2}} = 0. \quad (\text{B3})$$

Now the equations for the sine of the two angles:

$$\sin \theta_i = \frac{x}{(h^2 + x^2)^{1/2}}, \quad \text{and} \quad \sin \theta_t = \frac{(a-x)}{[b^2 + (a-x)^2]^{1/2}}, \quad (\text{B4})$$

can be used to simplify Equation B3, leaving the expression:

$$\frac{\sin \theta_i}{v_i} = \frac{\sin \theta_t}{v_t}. \quad (\text{B5})$$

Since $v_i/v_t = n_t/n_i$, then Equation B5 can now be written as the more familiar expression for Snell's Law:

$$\frac{\sin \theta_i}{n_i} = \frac{\sin \theta_t}{n_t}. \quad (\text{B6})$$

B.2 Introduction to Refraction in a Spherically Symmetric Atmosphere

If a light ray traverses a discretely stratified medium the travel time will then be the sum of the individual path length times:

$$t = \sum_{j=1}^m s_j / v_j, \quad (\text{B7})$$

where s_j and v_j are the path length and velocity of light associated with the j th layer. According to Huygens' principle (Hecht, 1990), $v_j/v_i = n_i/n_j$, and Equation B5 can be written in the more useful form:

$$t = \frac{1}{c} \sum_{j=1}^m n_j s_j, \quad (\text{B8})$$

where n_j is the index of refraction of the j th layer. This summation (omitting the factor $1/c$) is known as the Optical Path Length (*OPL*) while the spatial path length is simply the summation of the values of s_j . In a medium with a continuous refractive index gradient such as the atmosphere, Equation B7 can be written in integral form, becoming:

$$OPL = \int_s^p n(s) ds. \quad (\text{B9})$$

In the case of the Earth's atmosphere, assumed to be spherically symmetric, Equation B8 can be written:

$$OPL = \int n(r) ds, \quad (\text{B10})$$

where r is the radius vector in spherical co-ordinates, taken from the centre of the Earth. The more modern and complete version of Fermat's principle states that the optical path length is stationary, corresponding to a function with a minimum, maximum or point of inflection (Hecht, 1990).

Considering the propagation of a light ray through a spherically symmetrical atmosphere and applying the Pythagorean relationship with co-ordinates r and θ (see Figure B2) produces the result:

$$ds = \sqrt{r^2 d\theta^2 + dr^2} = dr \sqrt{r^2 \dot{\theta}^2 + 1}, \quad (\text{B11})$$

where:

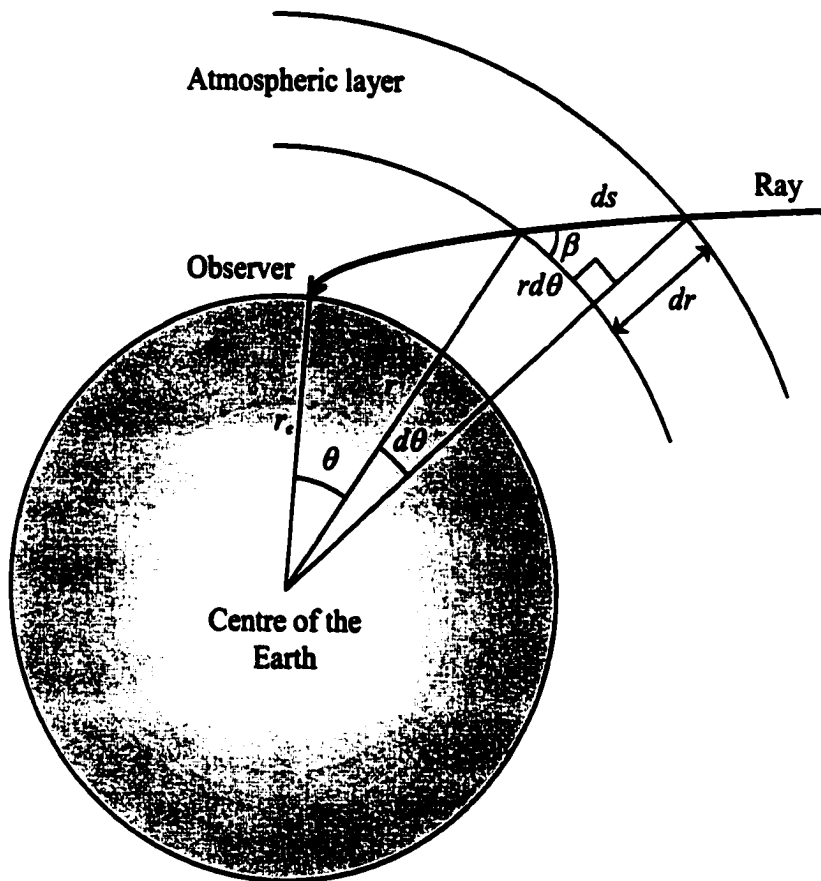


Figure B2: Atmospheric refraction in a spherically symmetrical atmosphere.

$$OPL = \int n(r) \sqrt{r^2 \dot{\theta}^2 + 1} dr = \int f(r, \theta, \dot{\theta}) dr. \quad (B13)$$

According to Fermat's principle the *OPL* through the atmosphere should be a stationary value (a minimum). However this path is unknown and only the starting and ending points are fixed. In a situation where an extreme must be found from an integral, the calculus of variations can be used (Arfken, 1968, Weisstein, 2000). At a stationary point: $\delta OPL = 0$ and from Equation B13

$$\delta OPL = \int \left[\frac{\partial f}{\partial \theta} \delta \theta + \frac{\partial f}{\partial \dot{\theta}} \frac{d(\delta \theta)}{dr} \right] dr. \quad (B14)$$

The second term can be integrated by parts¹ using

$$\begin{aligned} u &= \frac{\partial f}{\partial \dot{\theta}}, & dv &= d(\delta \theta) \\ du &= \frac{d}{dr} \left(\frac{\partial f}{\partial \dot{\theta}} \right) dr, & v &= \delta \theta \end{aligned} \quad (B15)$$

giving the result:

$$\int \frac{\partial f}{\partial \dot{\theta}} \frac{d(\delta \theta)}{dr} dr = \left[\frac{\partial f}{\partial \dot{\theta}} \delta \theta \right]_{r_1}^{r_2} - \int_{r_1}^{r_2} \delta \theta \frac{d}{dr} \left(\frac{\partial f}{\partial \dot{\theta}} \right) dr. \quad (B16)$$

Equation B16 is combined with B14 giving:

$$\delta OPL = \left[\frac{\partial f}{\partial \dot{\theta}} \delta \theta \right]_{r_1}^{r_2} + \int_{r_1}^{r_2} \frac{\partial f}{\partial \theta} \delta \theta - \delta \theta \frac{d}{dr} \left(\frac{\partial f}{\partial \dot{\theta}} \right) dr. \quad (B17)$$

Since the path is changing and not the end points: $\delta \theta(r_1) = \delta \theta(r_2) = 0$ and Equation

B17 becomes:

¹ Integration by parts:

$$\begin{aligned} d(uv) &= u dv + v du \\ \int d(uv) &= uv = \int u dv + \int v du \\ \int u dv &= uv - \int v du \end{aligned}$$

$$\delta OPL = \int_{r_1}^{r_2} \left[\frac{\partial f}{\partial \theta} - \frac{d}{dr} \left(\frac{\partial f}{\partial \dot{\theta}} \right) \right] \delta \theta dr. \quad (\text{B18})$$

Since at the stationary points $\delta OPL = 0$, then

$$\frac{\partial f}{\partial \theta} - \frac{d}{dr} \left(\frac{\partial f}{\partial \dot{\theta}} \right) = 0. \quad (\text{B19})$$

This is known as the Euler or Euler-Lagrange equation (Arfken, 1968, Weisstein, 2000). By combining Equations B13, and B19 the following result can be derived:

$$\frac{\partial f}{\partial \dot{\theta}} = \frac{n(r)r^2\dot{\theta}}{\sqrt{r^2\dot{\theta}^2 + 1}}. \quad (\text{B20})$$

The substitution of Equation B12 into B20 gives:

$$\frac{\partial f}{\partial \dot{\theta}} = \frac{n(r)r \cot \beta}{\sqrt{\cot^2 \beta + 1}}. \quad (\text{B21})$$

Since θ is ignorable (Bruton, 1996), from Equation B19 it follows that Equation B21 must be equal to a constant. Using the trigonometric relationships:

$$\cot^2 \beta + 1 = \frac{1}{\sin^2 \beta}, \quad \text{and} \quad \cot \beta = \frac{\cos \beta}{\sin \beta}, \quad (\text{B22})$$

Equation B21 can now be written:

$$nr \cos \beta = n_0 r_0 \cos \beta_0 = \text{constant}, \quad (\text{B23})$$

where n_0 , r_0 , and β_0 are the initial values. If a ray-tracing model uses a time-reversed scheme (as used in the present thesis) with the light ray starting at the observer, then these values will be for the observer's location. Equation B23 is called Snell's Law for spherical geometry.

The ray path can be better represented in terms of r and θ . In order to convert Equation B23 to spatial co-ordinates (r, θ) , the angle β must be eliminated.

Equation B23 can be re-arranged into the form:

$$\cos \beta = \frac{n_0 r_0}{nr} \cos \beta_0. \quad (\text{B24})$$

Equation B24 can be substituted into the trigonometric relationship:

$$\sin \beta = \pm \sqrt{1 - \cos^2 \beta}, \quad (\text{B25})$$

giving the expression:

$$\sin \beta = \pm \frac{\sqrt{n^2 r^2 - n_0^2 r_0^2 \cos^2 \beta_0}}{nr}. \quad (\text{B26})$$

Equation B24 and B26 can be substituted into B12 producing:

$$\frac{dr}{d\theta} = \frac{r}{\cot \beta} = \frac{r \sin \beta}{\cos \beta} = \pm r \sqrt{\left(\frac{nr}{n_0 r_0 \cos \beta_0} \right)^2 - 1}. \quad (\text{B27})$$

Bruton (1996) determined that for computational purposes it is easier to solve a second order differential equation than try to determine the sign of Equation B27.

The second order differential equation was found by applying the Chain Rule:

$$\frac{d^2 r}{d\theta^2} = \frac{d}{d\theta} \left(\frac{dr}{d\theta} \right) = \frac{d}{dr} \left(\frac{dr}{d\theta} \right) \cdot \frac{dr}{d\theta}, \quad (\text{B28})$$

to Equation B27 which gives the equation:

$$\frac{d^2 r}{d\theta^2} = r \left[r^2 n \left(\frac{r \frac{dn}{dr} + 2n}{(n_0 r_0 \cos \beta_0)^2} \right) - 1 \right], \quad (\text{B29})$$

which will now be further simplified through the application of a curvature scheme.

B.3 Derivation of the Ray Curvature Equation

The curvature κ of a ray at any point can be described by the expression (Bruton, 1996):

$$\kappa = \left| \frac{d\phi}{ds} \right|, \quad (\text{B30})$$

where ϕ is the angle between a line tangent to the ray and a line parallel to a fixed reference axis (for example the x-axis of a Cartesian coordinate frame), and s is arc length (see Figure B3).

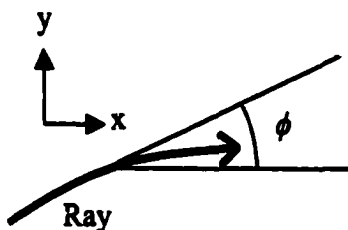


Figure B3: The angle ϕ is measured with respect to the direction of the x-axis.

In the Cartesian coordinate frame of Figure B3:

$$\tan \phi = \frac{dy}{dx}, \quad (\text{B31})$$

and:

$$ds^2 = dx^2 + dy^2. \quad (\text{B32})$$

Taking the derivative of Equation B31:

$$\sec^2 \phi \frac{d\phi}{dx} = \frac{d^2y}{dx^2}, \quad (\text{B33})$$

which can be rewritten as:

$$(1 + \tan^2 \phi) \frac{d\phi}{dx} = \frac{d^2 y}{dx^2}, \quad (\text{B34})$$

then rearranged to yield:

$$\frac{d\phi}{dx} = \frac{\frac{d^2 y}{dx^2}}{1 + \left(\frac{dy}{dx}\right)^2}. \quad (\text{B35})$$

Now Equation B30 can be rewritten as:

$$\kappa = \left| \frac{d\phi/dx}{ds/dx} \right|, \quad (\text{B36})$$

where the denominator is derived from Equation B32:

$$ds/dx = \left[1 + (dy/dx)^2 \right]^{1/2}, \quad (\text{B37})$$

and Equation B35 is substituted in the numerator giving:

$$\kappa = \left| \frac{d^2 y/dx^2}{\left[1 + (dy/dx)^2 \right]^{3/2}} \right|. \quad (\text{B38})$$

Since the refraction model uses polar co-ordinates (r, θ) , Equation B38 must be transformed into polar co-ordinates by applying the transformations:

$$x = r \cos \theta \quad \text{and} \quad y = r \sin \theta, \quad (\text{B39})$$

where r is the distance from the centre of the Earth to the end of the ray and θ is the angle between lines from the centre of the Earth to the beginning and end of the ray. Taking the differentials of B39 and substituting the results into Equations B31 and B32 gives:

$$\tan \phi = \frac{\sin \theta \frac{dr}{d\theta} + r \cos \theta}{\cos \theta \frac{dr}{d\theta} - r \sin \theta}, \quad (\text{B40})$$

and:

$$ds^2 = dr^2 + r^2 d\theta^2. \quad (\text{B41})$$

Taking the derivative of Equation B40 and applying the identity:

$$\sec^2 \phi = (\tan^2 \phi + 1), \quad (\text{B42})$$

gives:

$$\frac{d\phi}{d\theta} = \frac{2\left(\frac{dr}{d\theta}\right)^2 - r \frac{d^2r}{d\theta^2} + r^2}{\left(\frac{dr}{d\theta}\right)^2 + r^2}. \quad (\text{B43})$$

From Equation B41 we can derive:

$$\frac{ds}{d\theta} = \left[\left(\frac{dr}{d\theta}\right)^2 + r^2 \right]^{1/2}. \quad (\text{B44})$$

Equation B30 can be rewritten as:

$$\kappa = \frac{\left| \frac{d\phi}{d\theta} \right|}{\left| \frac{ds}{d\theta} \right|}. \quad (\text{B45})$$

Equations B43 and B44 can be substituted into Equation B45 giving:

$$\kappa = \frac{r^2 + 2\left(\frac{dr}{d\theta}\right)^2 - r \frac{d^2r}{d\theta^2}}{\left[\left(\frac{dr}{d\theta}\right)^2 + r^2 \right]^{3/2}}. \quad (\text{B46})$$

Substituting Equations B27 and B29 into Equation B46 and simplifying gives:

$$\kappa = -\frac{n_0 r_0 \cos \beta_0}{r n^2} \frac{dn}{dr}. \quad (\text{B47})$$

Finally, placing the equation for Snell's Law for spherical geometry (Equation B23) into Equation B47 gives:

$$\kappa = -\frac{\cos \beta}{n} \frac{dn}{dr}, \quad (\text{B48})$$

which can be used in a difference formulation for numerical ray tracing through the atmosphere.

APPENDIX C

REFRACTION MODEL FORTRAN 77 CODE (DIGITAL COMPILER)

C1. Table of Contents

The following section numbers and titles appear in the code of the model and are intended to make the program more understandable.

1.0 Variables and Arrays

2.0. Initial Input and Constants

2.1 Date and Time Input

2.2 Constants

3.0 Geographic Co-ordinates

3.1 Conversion of Geographic Co-ordinates from DDMSS to Decimal Degrees

3.2.1 Co-ordinates of Apartment Building Observing Site

3.2.2 Co-ordinates of Tory Building Observing Site

3.2.3 Co-ordinates of Stony Plain Upper Air Station

4.0 Calculation of Solar Co-ordinates (links to subroutines)

4.1 Julian Date Conversion Subroutine

4.2. Equatorial Co-ordinates of the Sun Subroutine

4.3 Sidereal Time Conversion Subroutine

4.4 Horizon Coordinate Conversion Subroutine

4.5 Solar Parallax Subroutine

4.6 Solar Semi-diameter Subroutine

5.0 Production of Solar Profile Co-ordinates

6.0 Diagnostic Routines for Celestial Co-ordinates

7.0 Reading the Rawinsonde Files

7.1 Reading the U.S. Standard Atmosphere (if chosen)

7.2 Reading Selected Fine Scale Sounding Files (if chosen)

7.3 Conversion to SI Units

8.0 Bomford's Terrestrial Refraction Formula

9.0 Ray Travel Increment

10.0 Input of Wavelength of Light

11.0 Atmospheric Carbon Dioxide

12.0 Computing Standard Index of Refraction

12.1 Computing Standard Index of Refraction of Dry Air

12.2 Computing Standard Index of Refraction of Water Vapor

12.3 Computing Compressibility of Standard Dry Air

12.4 Computing Compressibility of Water Vapor

12.5 Computing Molar Mass of Dry Air

12.6 Computing the Density of Standard Dry Air and Water Vapor

12.7 Test Program to Compute Index of Refraction (a debugging tool).

14.0 Refraction Do Loop for Disk of the Sun

15.0 Ray Tracing Routine

15.1 Computing the Thickness of the Atmospheric Layers

15.2 Computing the Altitude Dependence of θ (ray travel increment).

- 15.3 Computing the Index of Refraction at the Top of the Layer
- 15.4 Finding the Curvature of the Ray through the Layer
- 15.5 Computing the Complement of the Incident Angle (η)
- 15.6 Testing for Total Internal Reflection
- 15.7 Finding the Angle γ ('Sweep' angle of the Ray)
- 15.8 Finding θ (The angular distance traveled by the ray in polar co-ordinates)
- 15.9 The End of the Ray Tracing Do Loop (i.e. the ray passes into the next layer)
 - 15.9.1 Ray Path Data (optional)
- 15.10 Altitude of the Sun and Miss-Angle of the Ray When the Ray Exits Atmosphere
- 15.11 Writing Data to Output Files

Subroutines

- 1.0 Date Format Conversion**
- 2.0 Time Format Conversion**
- 3.0 Conversion to Julian Date**
 - 3.1 Checking for February
 - 3.2 Checking for Pre-Gregorian Period Dates
 - 3.3 Calculating Julian Date
- 4.0 Geocentric Solar Co-ordinates**
 - 4.1 Geometric Mean Longitude

4.2 Mean Anomaly**4.3 Eccentricity of Earth's Orbit****4.4 Sun's Equation of Centre****4.5 Sun's True Longitude and True Anomaly****4.6 Solar Radius Vector****4.7 Correction for Nutation and Aberration****4.8 Obliquity of the Ecliptic****4.9 Celestial Co-ordinates of the Sun****5.0 Local Sidereal Time****5.1 Julian Date Conversion****5.2 Finding Greenwich Sidereal Time (GST)****5.2.1 GST in Revolutions****5.2.2 GST in Hours****5.3 Computing Local Sidereal Time (LST)****6.0 Conversion from Equatorial to Horizon Co-ordinates****6.1 Conversion of Right Ascension to Hour Angle****6.2 Computation of Altitude and Azimuth****7.0 Computation of Diurnal Parallax****8.0 The Index of Refraction****9.0 The Compressibility of Air****10.0 Saturation Vapor Pressure**

```

*-----*
*                REFRACTION MODEL                *
*                Russell D. Sampson                *
*                Started: April 30, 1998            *
*                Preliminary Model completed:      *
*                September 14, 1998                *
*                Final version completed April,     *
*                2000                               *
*-----*

*-----*
* 1.0 VARIABLES AND ARRAYS.                       *
*-----*
* Double precision is used extensively throughout *
* this model since the changes in angle due to   *
* refraction from one increment to the next are *
* extremely small. One increment is only 0.0001 *
* degree in geographic distance (about 11 DM    *
* path length).                                  *
*-----*

*
* PROGRAM REFRACTION
*
* IMPLICIT DOUBLEPRECISION (A - H, O - Z), INTEGER (I - N)
* DOUBLE PRECISION TMIN(900), TSEC(900), P(900),
* + VIRT(900), DPD(900), DLRATE(900), ASRATE(900), ZGPM(900),
* + TEMP(900), RH(900), SUNY(1000), PA(900), TK(900), FRH(900),
* + SUNK(1000), DJDATE(200), OUTPUT(500,6), Z(900), SCALEH(900),
* + PATH1(500,2), PATH2(500,2), DANGLE(1000,2)
*
* CHARACTER*12 FILENAME
* CHARACTER*12 FILENAME2
*
*-----*
* 2.0 INITIAL INPUT.
*-----*
*
* 5 PRINT*, '*****'
* PRINT*, ' '
* PRINT*, ' REFRACTION MODEL'
* PRINT*, ' '
* PRINT*, ' Russell D. Sampson'
* PRINT*, ' University of Alberta, April, 2000'
* PRINT*, ' '
*
*-----*
* If diagnostics are required for the astronomical components of
* the model then make IDIAG = 1. Diagnostics are located near the
* end of the programme in section 6.0.
*-----*
*
* IDIAG = 1
*
* OPEN (UNIT=25,FILE='D:\Russ2\Refraction\ -sun2.txt')
* OPEN (UNIT=26,FILE='D:\Russ2\Refraction\ -sun.txt')
* OPEN (UNIT=29,FILE='D:\Russ2\Refraction\ -path.txt')
*
*-----*
* 2.1 INITIAL ANGLE, DATE and TIME INPUT.
*-----*
*
* PRINT*, 'Do you want to use the default date and time?'
* PRINT*, 'Enter 1 for "YES" or 0 for "NO".'
*
* READ*, IYESNO
*
* PRINT*, ' '
* PRINT*, 'Do you want to set the initial angle (beta)?'
* PRINT*, 'Enter 1 for "YES" or 0 for "NO".'
*
* READ*, IBETAYESNO
*
* IF (IBETAYESNO.EQ.1) THEN

```

```

PRINT*, 'Enter initial angle for Beta in double precision
+ (decimal degrees)'
PRINT*, 'Example 1.0D00 for 1 degree'
PRINT*, ' '
READ*, BETANO3

ENDIF
*
IF (IYESNO.EQ.1) THEN
DATE = 19981214.0D+00
TIME = 230000.0D+00
CALL DATEFORM(DATE, YR, DMON, DAY)
CALL TIMEFORM(TIME, HR, DMIN, SEC)
PRINT*, ' '
PRINT*, ' '
PRINT 6, IDINT(DMON), IDINT(DAY), IDINT(YR)
6 FORMAT (18X, 'Date: ', I2, '/', I2, '/', I4, ' UTC')
PRINT*, ' '
PRINT 7, IDINT(HR), IDINT(DMIN), SEC
7 FORMAT (18X, 'Time: ', I2, ':', I2, ':', F4.1, ' UTC')
PRINT*, ' '
*
ELSE
10 PRINT*, 'Enter the date of the sunrise or sunset event
+(YYYYMMDD)'
PRINT*, 'NOTE: use double precision notation
+(ex: 19980601.0D00).'
READ*, DATE
PRINT*, ' '
PRINT*, 'Enter time in UTC (HHMMSS.S)'
PRINT*, 'NOTE: use double precision notation.
+(ex: 120210.0D00)'
READ*, TIME
PRINT*, ' '
CALL DATEFORM(DATE, YR, DMON, DAY)
CALL TIMEFORM(TIME, HR, DMIN, SEC)
PRINT*, 'Is the following date and time correct?'
PRINT*, ' '
PRINT 20, IDINT(DMON), IDINT(DAY), IDINT(YR)
20 FORMAT (4X, 'Date: ', I2, '/', I2, '/', I4)
PRINT 30, IDINT(HR), IDINT(DMIN), SEC
30 FORMAT (4X, 'Time: ', I2, ':', I2, ':', F4.1, ' UTC')
PRINT*, ' '
PRINT*, 'Enter 1 to continue and 0 to start again.'
READ*, IYESNO
IF (IYESNO.EQ.0) THEN
GO TO 10
ENDIF
ENDIF
*
-----*
* 2.2 CONSTANTS *
* *
* GEORAD is the mean radius of the Earth in meters, PI is pi. *
* *
*-----*
*
PI = 3.1415926535897932D+00
GEORAD = 6.371004D+06
SUMREFRACT = 0.0D0
*
-----*
*3.0 GEOGRAPHIC COORDINATES. *
*-----*
*
PRINT*, 'Which geographic coordinates?'
PRINT*, ' '
PRINT*, 'Enter 0 to enter a new Lat/Long, 1 for Sask. Dr.'
PRINT*, 'or 2 for Tory roof-top or 3 for Stony Plain.'
PRINT*, ' '
*

```

```

READ*, ILATLONG
*   ILATLONG = 3
*
PRINT*, 'Do you want to use the default elevation of the
+observer?'
PRINT*, ' '
PRINT*, 'The default elevation is 0 meters above the surface.'
PRINT*, ' '
PRINT*, 'Enter 0 to enter a new elevation, 1 for the default'
PRINT*, ' '
*
READ*, IELEV
*
IF (IELEV.EQ.0) THEN
  PRINT*, 'Enter elevation of observer in meters.'
  PRINT*, 'Using double precision notation (ex: 7.88D+02)'
  READ*, ELEV
ELSE
  ELEV = 7.726D+02
ENDIF
*
PRINT*, ' '
PRINT 35, ELEV
35 FORMAT (5X,'Geometric elevation = ',F9.2,1X,'geopotential metres')
*
IF (ILATLONG.EQ.0) THEN
  PRINT*, 'Do you want to use decimal degrees or DDMSS?'
  PRINT*, 'Enter 1 for decimal and 0 for DDMSS.'
  READ*, IDECORDMS
  IF (IDECORDMS.EQ.1) THEN
    PRINT*, 'Enter Latitude in decimal degrees.'
    READ*, DLAT
    PRINT*, 'Enter Longitude in decimal degrees.'
    READ*, DLONG
  *
  *-----*
  * 3.1 Conversion of DLAT and DLONG. from DDMSS to Decimal Degrees. *
  *-----*
  *
  ELSEIF (IDECORDMS.EQ.0) THEN
65   PRINT*, 'Enter Latitude in DDMSS.SS.'
      PRINT*, 'NOTE: use double precision notation.'
      PRINT*, ' '
      READ*, DLAT
      PRINT*, 'Enter Longitude in DDMSS.SS.'
      PRINT*, 'NOTE: use double precision notation.'
      PRINT*, ' '
      READ*, DLONG
      PRINT*, 'Enter Elevation in meters'
      PRINT*, 'NOTE: use double precision notation.'
      PRINT*, ' '
      READ*, ELEV
  *
      PRINT*, 'Latitude = ', DLAT
      PRINT*, 'Longitude = ', DLONG
      PRINT*, 'Elevation = ', ELEV
      PRINT*, 'Is this correct?'
      PRINT*, 'Enter 1 for "yes" and 0 for "no"'
      READ*, IYESNO
      IF (IYESNO.EQ.0) THEN
        GO TO 65
      ENDIF
      DLATDEG = DINT(DLAT/1.0D+04)
      DLATMIN = DINT((DLAT - DLATDEG*1.0D+04)/1.0D+02)
      DLATSEC = DLAT - DLATMIN*1.0D+02 - DLATDEG*1.0D+04
      DLAT = DLATDEG + (DLATMIN/6.0D+01) + (DLATSEC/3.6D+03)
      DLONGDEG = DINT(DLONG/1.0D+04)
      DLONGMIN = DINT((DLONG - DLONGDEG*1.0D+04)/1.0D+02)
      DLONGSEC = DLONG - DLONGMIN*1.0D+02 - DLONGDEG*1.0D+04
      DLONG = DLONGDEG + (DLONGMIN/6.0D+01) + (DLONGSEC/3.6D+03)
      DLAT = DLAT*2.0D+00*PI/3.6D+02

```

```

          DLONG = DLONG+2.0D+00*PI/3.6D+02
        ENDIF
*
*-----*
* 3.2.1 Coordinates for the Apartment Building *
* 9947 Saskatchewan Dr. *
* Edmonton, Alberta, Canada *
* EVEL is an average elevation between the two observing sites. *
*-----*
*
      ELSEIF (ILATLONG.EQ.1) THEN
        DLAT = 5.352599D+01*2.0D+00*PI/3.6D+02
        DLONG = 1.1348732D+02*2.0D+00*PI/3.6D+02
      ENDIF
*
*-----*
* 3.2.2 Coordinates for Tory Building roof top *
* University of Alberta, Edmonton, Alberta, Canada *
*-----*
*
      IF (ILATLONG.EQ.2) THEN
        DLAT = 5.35281D+01*2.0D+00*PI/3.6D+02
        DLONG = 1.135194D+02*2.0D+00*PI/3.6D+02
        ELEV = 7.28D+02
        PRINT*, 'YOU HAVE CHOOSEN TORY'
      ENDIF
*
*-----*
* 3.2.3 Coordinates for Stony Plain Upper Air Station *
*-----*
*
      IF (ILATLONG.EQ.3) THEN
        DLAT = 5.354694D+01*2.0D+00*PI/3.6D+02
        DLONG = 1.1410667D+02*2.0D+00*PI/3.6D+02
        ELEV = 7.726D+02
        PRINT*, ' '
        PRINT*, 'YOU HAVE CHOOSEN STONY PLAIN UPPER AIR STATION'
      ENDIF
*
*-----*
* 4.0 CALCULATION OF COORDINATES FOR THE SUN. *
* *
* 4.1 JULIAN subroutine is used to find the Julian date. *
* *
* 4.2 SOLAR subroutine is used to find the equatorial coordinates of *
* the Sun (i.e. its right ascension and declination) *
* *
* 4.3 SIDEREAL subroutine is used to find the local sidereal time. *
* *
* 4.4 HORIZON subroutine is used to find the horizontal coordinates *
* of the Sun (i.e. its altitude and azimuth) *
* *
* 4.5 PARALLAX subroutine is used to find the diurnal parallax of *
* the Sun. *
* *
* 4.6 S is the semidiameter of the Sun. *
*-----*
*
      CALL JULIAN(DMON, YR, DAY, HR, DMIN, SEC, DJD)
*
      CALL SOLAR(T, DJD, DL, PI, DM, e, C, THETA, DNU,
+ SOLRAD, DOMEDA, THETAAPP, EPSILON, RA, DEC, QUADRA,
+ QUADTHETA, RADEG, DECDEG, RAHR, RAMIN, RASEC, DECD, DECM,
+ DECS)
*
      CALL SIDEREAL(DJDO, YR, DMON, DAY, A, B, THETANO, TNO, GST, DLST,
+ HR, DMIN, SEC, DLONG, PI)
*
      CALL HORIZON(H, DLST, PI, RA, DEC, DLAT, ALT, AZ)

```

```

*
CALL PARALLAX(SOLRAD, GEORAD, ALT, DPAR)
*
PRINT*, ' '
PRINT 75, ALT*1.8D02/PI
75  FORMAT (4X, 'Altitude of Geometric Sun = ', F7.3, ' degrees')
*
S = 4.65241D-03/(SOLRAD/1.4959787D+11)
*
-----*
* 5.0 PRODUCING DATA POINTS DEFINING THE SOLAR DISC [radians]. *
-----*
*
DEGRES = 1.0D+00
*
RES = DEGRES*PI/1.8D+02
L = 1
DO 80 ANGLE = 0.0D00, PI, RES
    SUNX(L) = S*DSIN(ANGLE)
    SUNY(L) = ALT + S*DCOS(ANGLE)
    L = L + 1
80  CONTINUE
*
LSUN = L - 1
*
-----*
* 6.0 FULL DIAGNOSTICS OF CELESTIAL COMPONENT OF MODEL. *
-----*
*
IF (IDIAG.EQ.1) THEN
    PRINT*, '-----'
    PRINT*, '    Diagnostic Analysis of Celestial Algorithms'
    PRINT*, ' '
    PRINT*, 'Julian Date = ', DJD
    PRINT*, 'Solar celestial coordinates:'
    PRINT 90, IDINT(RAHR), IDINT(RAMIN), RASEC
    90  FORMAT (1X, 'RA = ', I2'h ', I2'm ', I2,F5.2,'s')
    PRINT 100, IDINT(DECLD), IDINT(DECLM), DECS
    100  FORMAT (1X, 'dec = ', I3'd ', I2,m ', I2,F5.2,'s')
    PRINT*, ' '
    *
    DLONG2 = DLONG*360.0/(2.0*PI)
    DLONGMIN = (DLONG2 - DINT(DLONG2))*6.0D1
    DLONGSEC = (DLONGMIN - DINT(DLONGMIN))*6.0D1
    IF (DLONG2.LT.0.0D0) THEN
        DLONGMIN = DLONGMIN*(-1.0D0)
        DLONGSEC = DLONGSEC*(-1.0D0)
    ENDIF
    PRINT 101, IDINT(DLONG2), IDINT(DLONGMIN), DLONGSEC
    101  FORMAT (1X, 'Longitude: ', I4,'d ', I2,'m ', F5.2,'s')
    *
    DLAT2 = DLAT*360.0/(2.0*PI)
    DLATMIN = (DLAT2 - DINT(DLAT2))*6.0D1
    DLATSEC = (DLATMIN - DINT(DLATMIN))*6.0D1
    IF (DLAT2.LT.0.0D0) THEN
        DLATMIN = DLATMIN*(-1.0D0)
        DLATSEC = DLATSEC*(-1.0D0)
    ENDIF
    PRINT 102, IDINT(DLAT2), IDINT(DLATMIN), DLATSEC
    102  FORMAT (1X, 'Latitude: ', I3,'d ', I2,'m ', F5.2,'s')
    *
    GSTMIN = (GST - DINT(GST))*6.0D1
    GSTSEC = (GSTMIN - DINT(GSTMIN))*6.0D1
    PRINT 103, IDINT(GST), IDINT(GSTMIN), GSTSEC
    103  FORMAT (1X, 'Greenwich Sidereal Time: ', I2,'h ', I2,'m ',
    +F5.2,'s ')
    *
    DLSTMIN = (DLST - DINT(DLST))*6.0D1
    DLSTSEC = (DLSTMIN - DINT(DLSTMIN))*6.0D1
    PRINT 104, IDINT(DLST), IDINT(DLSTMIN), DLSTSEC
    104  FORMAT (1X, 'Local Sidereal Time: ', I2,'h ', I2,'m ',

```



```

*
+F5.2,'s ')
*
      H2 = H*360.0/(2.0*PI+1.5D1)
      HMIN = (H2 - DINT(H2))*6.0D1
      HSEC = (HMIN - DINT(HMIN))*6.0D1
      IF (H2.LT.0.0D0) THEN
          HMIN = HMIN*(-1.0D0)
          HSEC = HSEC*(-1.0D0)
      ENDIF
      PRINT 105, IDINT(H2), IDINT(HMIN), HSEC
105  FORMAT (1X, 'Hour angle: ',I4,'h ',I2,'m ',F5.2,'s')
*
      DAL2 = ALT*360.0/(2.0*PI)
      DAL2MIN = (DAL2 - DINT(DAL2))*6.0D1
      DAL2SEC = (DAL2MIN - DINT(DAL2MIN))*6.0D1
      IF (DAL2.LT.0.0D0.AND.DAL2.GT.-1.0D0) THEN
          DAL2MIN = DAL2MIN*(-1.0D0)
          DAL2SEC = DAL2SEC*(-1.0D0)
      PRINT 106, IDINT(DAL2), IDINT(DAL2MIN), DAL2SEC
106  FORMAT (1X, 'Altitude of the Centre of the Sun: -',I2,
+d ',I2,'m ',F5.2,'s')
      ELSEIF (DAL2.LT.-1.0D0) THEN
          DAL2MIN = DAL2MIN*(-1.0D0)
          DAL2SEC = DAL2SEC*(-1.0D0)
      PRINT 107, IDINT(DAL2), IDINT(DAL2MIN), DAL2SEC
107  FORMAT (1X, 'Altitude of the Centre of the Sun: ',I3,
+d ',I2,'m ',F5.2,'s')
      ELSEIF (DAL2.GT.0.0D0) THEN
      PRINT 108, IDINT(DAL2), IDINT(DAL2MIN), DAL2SEC
108  FORMAT (1X, 'Altitude of the Centre of the Sun: ',I3,
+d ',I2,'m ',F5.2,'s')
      ENDIF
*
      DAZ2 = AZ*360.0/(2.0*PI)
      DAZMIN = (DAZ2 - DINT(DAZ2))*6.0D1
      DAZSEC = (DAZMIN - DINT(DAZMIN))*6.0D1
      IF (DAZ2.LT.0.0D0) THEN
          DAZMIN = DLZMIN*(-1.0D0)
          DAZSEC = DLZSEC*(-1.0D0)
      ENDIF
      PRINT 109, IDINT(DAZ2), IDINT(DAZMIN), DAZSEC
109  FORMAT (1X, 'Azimuth of the Centre of the Sun: ',I3,'d ',
+I2,'m ',F5.2,'s')
*
      PRINT 110, (DPAR*3.6D2/(2.0D0*PI))*3.6D3
110  FORMAT (1X, 'Diurnal Parallax (arcsec.): ',F4.2,'s')
*
      SMIN = 6.0D01*(S*3.6D2)/(2.0D0*PI)
      SSEC = (SMIN - DINT(SMIN))*6.0D01
      PRINT 111, IDINT(SMIN), SSEC
111  FORMAT (1X, 'Semi-diameter of Sun: 0.0d ',I2,'m ',F5.2,'s')
      PRINT*, ' '
      PRINT*, '-----'
      ENDIF
*
      PRINT*, 'Continue with the run?'
      PRINT*, ' '
      PRINT*, 'Enter 2, to start again, 1 to continue and 0 to stop.'
      READ*, IYESNO
*
      IF (IYESNO.EQ.0) THEN
          PRINT*, ' '
          PRINT*, 'Model run has been terminated.'
          PRINT*, ' '
          STOP
      ELSEIF (IYESNO.EQ.2) THEN
          GO TO 5
      ENDIF
*
*-----*
*7.0  READING THE UPPER AIR SOUNDING FILES  *

```

```

*
* The fine scale sounding files contain the following:
*
* Time [DMIN,sec], pressure [hPa], height [gpm],
* Temperature [C], Relative Humidity, Virtual Temperature [C],
* Dew Point Depression [C] Lapse Rate [C/km], Ascension Rate
* [DM/s]
*
* The fine scale sounding files are in:
*
* C:\Program Files\DevStudio\MyProjects\refraction1\*.txt
*
*-----*
*
PRINT*, 'Do you want the refraction values for each layer?'
PRINT*, ' '
PRINT*, 'Enter 1 for yes and 0 for no'
READ*, LAYERR
PRINT*, ' '
PRINT*, 'Do you want to use a specified sounding or'
PRINT*, 'the U.S. Standard Atmosphere?'
PRINT*, ' '
PRINT*, 'Enter 1 for specified sounding or 0 for U.S.
+Standard Atmosphere'
READ*, IATM
IF (IATM.EQ.0) THEN
PRINT*, ' '
*
*-----*
* 7.1 This is a test atmosphere such as the U.S. Standard
* Atmosphere.
*-----*
*
OPEN (UNIT=24,FILE='C:\Program Files\DevStudio\MyProjects\
+refraction1\atm2.txt',STATUS='OLD')
*
DO 120 I=1,10
READ (24,*,END=120) TMIN(I), TSEC(I), P(I), ZGPM(I),
+TEMP(I), RH(I), VIRT(I), DPD(I), DLRATE(I), ASRATE(I)
120 CONTINUE
ENDIF
*
*-----*
* 7.2 The following opens the fine scale sounding files.
*-----*
*
IF (IATM.EQ.1) THEN
PRINT*, 'What is the file name of the sounding?'
PRINT*, ' '
READ (*,'(A)') FILENAME
OPEN (21,FILE=FILENAME)
DO 130 I=1,1000
READ (21,*,END=145) TMIN(I), TSEC(I), P(I), ZGPM(I),
+TEMP(I), RH(I), DPD(I)
130 CONTINUE
ENDIF
*
IF (ELEV.LT.ZGPM(1)) THEN
PRINT*, 'Elevation of observer is less than surface
+of sounding'
PRINT*, 'The model shall assume the elevation of the
+observer is equal to the surface of the sounding'
ELEV = ZGPM(1)
ENDIF
*
*-----*
* 7.3 Conversion of the atmospheric profile to SI units (K, Pa),
* fractional relative humidity and geopotential metres to geometric*
* metres. Conversion of geopotential metres to geometric
*

```

```

*      metres was accomplished by a third degree polynomial derived from*
*      the formula for geopotential height in Iribarne and Godson,      *
*      (1981) Atmospheric Thermodynamics, Second Edition, D. Reidel    *
*      Pub., pp. 259. NOTE: THIS IS LATITUDE SPECIFIC.                  *
*
*      Constants AAA1, AAA2, are for the formula to convert geometric   *
*      metres to geopotential meters (Iribarne, and Godson). G0 is the  *
*      mean sea level gravitational acceleration, while G450 is the     *
*      value at 45 degrees north latitude. These values are used inside *
*      the refraction routine (section 15.2)
*-----*
145  AA1 = 5.23658D-14
      AA2 = 1.566195D-07
      AA3 = -7.08293D-04
      AA4 = -8.2D-03
*
      AAA1 = 2.59D-03
      AAA2 = 3.14D-07
      G0 = 9.80665D+00
      G450 = 9.80616D+00
*
*-----*
*      The following formula is the first and second term of the      *
*      integrated equation from Iribarne and Godson. The result is used *
*      in section 15.2.
*-----*
*
      CONST01 = (G450/G0)*(1.0D0 - AAA1*DCOS(2.0D0*DLAT))
*
      DO 150 I=1, 900
          PA(I) = P(I)*1.0D+02
          TK(I) = TEMP(I) + 2.7315D+02
          FRH(I) = RH(I)/1.0D+02
          Z(I) = ZGPM(I) + AA1*ZGPM(I)**3.0D0 + AA2*ZGPM(I)**2.0D0 +
+AA3*ZGPM(I) + AA4
*
          IF (TMIN(I).EQ.999.0D00) THEN
              GO TO 152
          ENDIF
150  CONTINUE
*
152  DO 155 I=1, 900
          IF (PA(I+1).EQ.0.0D00) THEN
              GO TO 160
          ENDIF
          SCALEH(I) = (ZGPM(I) - ZGPM(I+1))/DLOG(PA(I)/PA(I+1))
155  CONTINUE
*
*-----*
*8.0 Bomford's empirical formula for determining the horizontal      *
*      refraction (the altitude of the astronomical horizon due to     *
*      atmospheric refraction). SURFLAP is the surface temp. gradient. *
*-----*
*
160  SURFLAP = (TK(2) - TK(1))/(Z(2) - Z(1))
*
      DHORIZON = (7.91E-01*P(1)/(TK(1)*TK(1)))*(3.42D-02 + SURFLAP)
*
      PRINT*, ' '
      PRINT 165, DHORIZON*1.8D+02/PI
165  FORMAT (5X,'Terrestrial refraction = ',F7.4,' degrees')
*
*-----*
*9.0 SELECTION OF RAY TRAVEL INCREMENT.
*
*      This angle is taken from the centre of the Earth. If this value *
*      needs to be changed then change DTHETADEG.
*-----*
*
      DTHETADEG = 1.0D-03
      DTHETA = DTHETADEG*PI/1.8D+02

```

```

*
*-----*
* 10.0 WAVELENGTH OF LIGHT. *
*
*   A wavelength of 633 nm is orange-red or 660 nm is red. These *
*   was choosen as a close representation of the sunrise *
*   or sunset colouration. NOTE: Cidor's equations use *
*   micrometers.(0.001*nm) To change the wavelength reset *
*   WAVELENGTH. YELLOW = 580, GREEN = 530, BLUE = 470 *
*-----*
*
PRINT*, ' '
PRINT*, 'Enter wavelength of light in nanometers [nm]. '
PRINT*, ' Red 660, Yellow 580, Green 530, Blue 470'
PRINT*, ' '
PRINT*, '      Example: 6.60D+02 for 660 nm'
READ*, WAVELENGTH

*
WAVENUMBER = 1.0D00/(WAVELENGTH*1.0D-03)
*
*-----*
* 11.0 ATMOSPHERIC CARBON DIOXIDE *
*
*   The default concentration is 450 ppm. To change the *
*   concentration reset the value of CO2. *
*-----*
*
CO2 = 4.5D+02
*
*-----*
* 12.0 COMPUTING STANDARD INDEX OF REFRACTION. *
*
*   From: Ciddor's equations (1), (2) and (3). *
*
*   Now compute the index of refraction at standard *
*   conditions for Carbon Dioxide. Standard conditions are: *
*   T = 15 C, p = 1013.25 kPa, 0% RH, and 450 ppm of Carbon *
*   Dioxide. This only has to be done once. *
*-----*
*
*   List of constants from Appendix A of Ciddor. *
*-----*
*
DK0 = 2.380185D+02
DK1 = 5.792105D+06
DK2 = 5.7362D+01
DK3 = 1.67917D+05
*
*-----*
* 12.1 STANDARD INDEX OF REFRACTION OF DRY AIR *
*-----*
*
DNSTANDRYAIR = (DK1/(DK0 - WAVENUMBER**2.0D00)) +
+ (DK3/(DK2 - WAVENUMBER**2.0D00))
*
*
IF (CO2.EQ.4.5D+02) THEN
DNCO2 = DNSTANDRYAIR
ELSE
DNCO2 = (DNSTANDRYAIR/1.0D+08) *
+ (1.0D00 + 0.534D-06*(CO2 - 4.5D+02))
ENDIF
*
*-----*
* 12.2 INDEX OF REFRACTION FOR STANDARD VAPOR. *
*
*   NOTE: This step was left out of Ciddor's instruction list *
*   on page 1572. *
*-----*
*

```

```

* List of constants found in Appendix A of Cidor. *
*-----*
CF = 1.022D+00
W0 = 2.95235D+02
W1 = 2.6422D+00
W2 = -3.238D-02
W3 = 4.028D-03
*
DNVAPOR = (CF*(W0 + W1*(WAVENUMBER**2.0D00) +
+ W2*(WAVENUMBER**4.0D00) + W3*(WAVENUMBER**6.0D00)))
*
*-----*
* 12.3 COMPUTING COMPRESSIBILITY OF STANDARD DRY AIR AND VAPOR. *
*-----*
* Now compute the compressibility of dry air setting T = 288.15 K, *
* p = 101 325 Pa, and water content = 0. This is Ciddor's eqn. 12.*
* Since there are two separate calculations of the compressibility *
* the computation is done in a separate subroutine (COMPRESS). If *
* a fixed concentration of Carbon Dioxide is used then this *
* calculation is only done once. *
*-----*
*
DRYTEMP = 2.8815D+02
DRYPRESS = 1.01325D+05
DRYMOIST = 0.0D+00
*
CALL COMPRESSIBILITY (COMPRESSDRY, DRYTEMP, DRYPRESS, DRYMOIST)
*
*-----*
* 12.4 THE COMPRESSIBILITY OF PURE WATER VAPOR: *
*-----*
*
WETTEMP = 2.9315D+02
WETPRESS = 1.333D+03
DMOISTA = 1.0D+00
*
CALL COMPRESSIBILITY (COMPRESSWET, WETTEMP, WETPRESS, DMOISTA)
*
*-----*
* 12.5 THE MOLAR MASS OF DRY AIR WITH CO2 IN PPM: *
*-----*
*
DMOLEMASSA = 1.0D-03*(2.89635D+01 + 1.2011D-05*(CO2 - 4.0D+02))
*
*-----*
* 12.6 THE DENSITY OF STANDARD DRY AIR AND WATER VAPOR. *
*-----*
*
R = 8.31451D+00
DMOLEMASSW = 1.8015D-02
DRYDENSITY = DRYPRESS*DMOLEMASSA/(COMPRESSDRY*R*DRYTEMP)
WETDENSITY = WETPRESS*DMOLEMASSW/(COMPRESSWET*R*WETTEMP)
*
*-----*
* 12.7 TEST PROGRAM TO COMPUTE INDEX OF REFRACTION *
*-----*
*
TKA = 293.15D00
PAA = 101325.0D00
FRHA = 0.3D00
*
CALL REFINDEX (TKA, PAA, FRHA,
+ WAVENUMBER, CO2, DNCO2, DNVAPOR, COMPRESSDRY, COMPRESSWET,
+ DRYDENSITY, WETDENSITY, R, DMOLEMASSA, DMOLEMASSW, TESTINDEX)
*
*-----*
*****

```

```

*          R A Y T R A C I N G   R O U T I N E
*****
*-----*
*
*          NOTE: This is a time reversed ray tracing so the
*          rays are traced from the observer out to the Sun.
*
* 14.0 DO LOOP FOR DISC OF THE SUN
*
* This DO LOOP asks the model to raytrace a series of rays that
* will eventually make up the disc of the Sun. SUNDEG is the
* altitude of a point on the profile of the Sun. REFGUESS is the
* initial guess of the model as to the amount of refraction. If
* the point on the Sun is at an altitude greater than 10 degrees
* then a formula from Green, R., Spherical Astronomy is used
* (the first part of the IF statement. If the Sun is below
* this value then a formula from the Astronomical
* Almanac is used in the "ELSE" component of the IF statement
* (1992, page B62).
*-----*
*
PRINT*, ' '
PRINT*, '+++++++ Please stand by. ++++++'
PRINT*, '+++++++ The model is working.+++++++'
PRINT*, ' '
DO 455 L=1, LSUN
*
      IF (SUNY(L).LT.8.73D-02) THEN
          SUNDEG = SUNY(L)*1.8D+02/PI
          REFGUESS = (PA(1)/1.0D2)*(0.1594D00 + 1.96D-02*SUNDEG +
+          2.0D-5*SUNDEG*SUNDEG)/(TK(1)*
+          (1.0D+00 + 5.05D-01*SUNDEG + 8.45D-02*SUNDEG*SUNDEG))
          REFGUESS = REFGUESS*PI/1.8D02
      ELSE
          REFGUESS = 60.29D00*DTAN((PI/2.0D0) - SUNY(L)) -
+          6.688D-02*((DTAN((PI/2.0D0) - SUNY(L)))*3.0D00)
          REFGUESS = REFGUESS*2.0D00*PI/1.296D+06
      ENDIF
*
*-----*
*          SUMTHETA is the sum of the incremental angle theta and represents*
*          the total angular distance the ray has travelled with respect to *
*          the centre of the Earth. BETANO is the initial angle of the ray.*
*-----*
*
      SUMTHETA = 0.0D00
      BETANO = REFGUESS + SUNY(L)
      BETAL = REFGUESS + SUNY(L)
      IF (IBETAYESNO.EQ.1) THEN
          BETANO = PI*BETANO3/1.8D02
      ENDIF
*
*-----*
*          If the formula estimates a negative altitude then the
*          programme assumes a zero angle for the intitial incident
*          angle. Otherwise the ray would be sent into the ground.
*-----*
*
      IF (BETANO.LT.0.0D+00) THEN
          BETANO = 0.0D+00
      ENDIF
*
*
      RAD = GEORAD + ELEV
      I = 1
      JN = 0
      NN = 1
      IZ = 1
      K = 1

```

```

*
*-----*
* 15.0 RAY TRACING ROUTINE *
*
* The next DO LOOP traces a series of rays through the modeled *
* atmosphere until the exiting ray 'strikes' the target portion *
* of the Sun. Its CONTINUE statement is found around line number *
* 740. If the adjusted ray has a negative initial angle, *
* then the initial angle is set to zero. If this repeats itself, *
* then it is obvious the ray will not converge on the *
* Sun and the program exits the DO LOOP. *
* This is a code "4" in the last column of the output file. *
*-----*
*
* DO 350 K=1, 100
*
*-----*
* Find the refractive index at the elevation of the observer. *
*-----*
*
* IF (ELEV.EQ.Z(1)) THEN
* CALL REFINDEX (TK(1), PA(1), FRH(1),
+ WAVENUMBER, CO2, DNCO2, DNVAPOR, COMPRESSDRY,
+ COMPRESSWET, DRYDENSITY, WETDENSITY, R, DMOLEMASSA,
+ DMOLEMASSW, SURFRINDEX)
* ELSE
*
* I = 1
*-----*
* This equation does a linear interpolation of the temperature *
* and relative humidity between the sounding measurements to find *
* the temperature and humidity at the elevation of the observer. *
* NOTE: continued interpolation for the rest of the ray path is *
* done in a later portion of the programme. *
*-----*
*
* DNEWTEMP = (TK(I) + ((ELEV - Z(I))/(Z(I+1) -
+ Z(I))) * (TK(I+1) - TK(I)))
*
* DNEWRH = FRH(I) + ((ELEV - Z(I))/
+ (Z(I+1) - Z(I)))*(FRH(I+1) - FRH(I))
*
*-----*
* The following routine calculates the scale height between *
* the sounding measurements and then interpolates the value of *
* pressure between the sounding using this scale height. This *
* calculation is for the observer's elevation only. *
*-----*
*
* DNEWP = PA(I)*DEXP((ELEV - ZGPM(I))/SCALEH(I))
*
* CALL REFINDEX (DNEWTEMP, DNEWP,
+ DNEWRH, WAVENUMBER, CO2, DNCO2, DNVAPOR,
+ COMPRESSDRY, COMPRESSWET, DRYDENSITY, WETDENSITY,
+ R, DMOLEMASSA, DMOLEMASSW, SURFRINDEX)
*
* ENDIF
*
* IF (BETANO.LE.0.0D+00) THEN
* BETANO = 0.0D+00
* IZ = IZ + 1
* IF (IZ.EQ.3) THEN
* KODE = 4
* GO TO 400
*
* ENDIF
*
* ENDIF
*
* BETA = BETANO
* BETANO2 = BETANO
*
*-----*

```

```

*      This DO WHILE Loop does the actual ray-tracing of a single *
*      ray through the modeled atmosphere. The loop ends just *
*      after the GO TO 170 statement around line number 1000. ZN is *
*      the height above sea-level and 7.85D+04 is the limit of the *
*      sample and test atmospheres used in the model. The IF *
*      statement can be activated if the number of layers for each *
*      ray is required (this is a good diagnostic) *
*-----*
*
*      IF (ZN.GE.7.95D+04) THEN
*      PRINT*, 'NUMBER OF LAYERS = ', LAYNUM
*      ENDIF
*
170      DO WHILE (ZN.LT.7.95D+04)
*-----*
* 15.1 COMPUTING THE THICKNESS OF THE ATMOSPHERIC LAYER THROUGH *
* WHICH THE RAY PASSES AT THE INCREMENTAL ANGLE DTHETA. *
*-----*
*
*      JN = JN + 1
*      LAYNUM = JN
*-----*
*      RADH is the distance from the centre of the Earth to the end *
* of the ray traveling through an increment of DTHETA. *
*-----*
*
*      RADH = RAD*DCOS(BETA)/DCOS(BETA + DTHETA)
*      ZN = RADH - GEORAD
*      IF (JN.EQ.2) THEN
*      ZNO = ZN
*      ENDIF
*      THICK = RADH - RAD
*
*-----*
* 15.2 THE VALUE OF DTHETA CHANGES WITH ALTITUDE. *
* This is done in order to reduce the computational time. It *
* is assumed that the amount of refraction will be very minor *
* at very high altitudes. *
*-----*
*
*      IF (ZN.GT.4.0D+04) THEN
*      DTHETA = 1.74532925199D-04
*      ENDIF
*
*-----*
*      If the ray has crossed a sounding data level then the next *
* level must be used for interpolation. *
*-----*
*
*      IF (ZN.GT.Z(I+1)) THEN
*      I = I + 1
*      ENDIF
*
*-----*
*      The next IF statement does a simple interpolation *
* of the sounding data to find the values at the *
* end of each ray segment. The pressure is interpolated *
* using the exponential pressure relation. The height ZN *
* is converted to gpm from a formulation in Iribarne and *
* Godson, Atmospheric Thermodynamics, page 159. To reduce *
* computation time, the variables are declared outside the *
* refraction routine. *
*-----*
*
*      IF (ZN.GE.Z(I).AND.ZN.LT.Z(I+1)) THEN
*
*      DNEWTEMP = (TK(I) + ((ZN - Z(I))/(Z(I+1) - Z(I)))
+      * (TK(I+1) - TK(I)))
*
*      ZNGPM = CONST01*(ZN - (5.0D-01*AAA2*ZN**2.0D0))

```



```

DNEWP = PA(I)*DEXP((ZNGPM-ZGPM(I))/SCALEH(I))
*
+
DNEWRH = FRH(I) + ((ZN - Z(I))/
(Z(I+1) - Z(I)))*(FRH(I+1) - FRH(I))
*
-----*
* The following IF statement can be activated if the complete *
* interpolated pressure file needs to be examined. It can also *
* be easily modified to include the temperature and humidity. *
*-----*
*
IF (L.EQ.2) THEN
*
WRITE (29,171) DNEWP, ZN, ZNGPM
*171 FORMAT (1X, F15.9, 2X, F15.9, 2X, F15.9)
*
ENDIF
*
-----*
* 15.3 CALCULATE THE INDEX OF REFRACTION AT THE TOP OF THE LAYER. *
*-----*
*
CALL REFINDEX (DNEWTEMP, DNEWP, DNEWRH, WAVENUMBER,
+ CO2, DNCO2, DNVAPOR, COMPRESSDRY, COMPRESSWET,
+ DRYDENSITY, WETDENSITY, R, DMOLEMASSA, DMOLEMASSW,
+ RINDEX)
*
-----*
* Calculation of the cosine of the critical angle (the angle *
* necessary for total internal reflections). *
*-----*
*
CRITICAL = RINDEX/SURFRINDEX
*
-----*
* 15.4 FINDING THE CURVATURE OF THE RAY THROUGH THE LAYER. *
*-----*
* Equation 19 in Bruton. *
*
NOTE: since the curvature coefficient is used only in the *
equation to find the angle eta, and in that equation it is *
divided by 2, this simple division is done in the initial *
curvature equation and thus cancels the 2 used to find *
the mean refraction, thus reducing the number of *
computations. *
*
NOTE: the derivation of the curvature equation already *
includes Snell's Law. *
*-----*
*
COSBETA = DCOS(BETA)
CURVE = -1.0D00*COSBETA*(RINDEX-SURFRINDEX)/(THICK*
+ (SURFRINDEX+RINDEX))
*
-----*
* 15.5 FINDING ANGLE ETA. *
*-----*
* This is the complement of the incident angle (i.e. 90 - i ) *
* at the top of the layer and the bottom of the next layer. *
* This is equation (29) in Bruton. *
*
NOTE: CETAI is used to reduce the number of *
computations in the model. *
*-----*
*
CETA1 = RAD/RADH
*
COSETA = CETA1*COSBETA + CURVE*(RADH -
+ ((RAD*RAD)/RADH))
*
-----*

```

```

* 15.6 TESTING FOR TOTAL INTERNAL REFLECTION.
*
* The following IF statement tests for total internal
* reflection. This is done by seeing if the critical angle
* is achieved at the angle eta.
*
* In a horizontally homogeneous atmosphere, this implies that
* the ray hits the ground and the horizon will be seen at the
* initial angle beta. A reflected ray is a code 2 in the
* output file. To find the distance to the visible refracted
* horizon, the value of SUMTHETA is
* doubled since it is assumed that the reflected ray will
* retrace its path to the ground.
*-----

```

```

*
*       IF (COSETA.GE.CRITICAL) THEN
*           KOE = 2
*           WRITE (25,210) (AZ*1.8D+02/PI) +
210      +(SUNK(L)*1.8D+02/PI), SUNY(L)*1.8D+02/PI, K, KOE, BETA1*1.8D2/PI,
*           +SUMTHETA*6.36D+03
*           FORMAT (1X,F9.4,2X,F7.4,13X,I3,2X,I2,2X,F7.4,2X,
*           +F5.1)
*
*           GO TO 450
*-----

```

```

* The following print statements are diagnostics that can be
* activated when necessary by moving them above the GO TO 450
* statement.
*-----

```

```

*
*       PRINT*, 'COSETA = ', COSETA
*       PRINT*, 'ZN [m]= ', ZN
*       PRINT*, 'Z (I) = ', Z(I)
*       PRINT*, 'GEORAD = ', GEORAD
*       PRINT*, 'RAD = ', RAD
*       PRINT*, 'RADH = ', RADH
*       PRINT*, 'L [SOLAR DISC NUMBER] = ', L
*       PRINT*, 'K [RAY TRIAL NUMBER] = ', K
*       PRINT*, 'JN [NUMBER OF LAYERS] = ', JN
*       PRINT*, 'I [SOUNDING LAYER NUMBER] = ', I
*       PRINT*, 'TK(I) = ', TK(I)
*       PRINT*, 'SURFRINDEX = ', SURFRINDEX
*       PRINT*, 'RINDEX = ', RINDEX
*       PRINT*, 'REFGUESS = ', REFGUESS
*       PRINT*, 'SUNY(1) = ', SUNY(1)
*       PRINT*, 'DNEWP = ', DNEWP
*       PRINT*, 'PA(I) = ', PA(I)
*       PRINT*, 'CURVATURE = ', CURVE
*       STOP
*       ENDIF
*-----

```

```

* 15.7 FINDING ANGLE GAMMA.
*
* This is the angle produced by the curving ray and can be
* considered the sector of a circle. The following IF
* statement is included to print a statement if the cosine
* of eta is > 1 or < -1. This diagnostic is used to help
* ensure any modifications do not damage the routine.
*-----

```

```

*
*       IF (COSETA.GT.1.0D00.OR.COSETA.LT.-1.0D00) THEN
*           PRINT*, ' '
*           PRINT*, 'WARNING! Cos(eta) greater than 1 or less
210      +than -1'
*           PRINT*, ' '
*           PRINT*, 'COSETA = ', COSETA
*           PRINT*, 'ZN [m]= ', ZN
*           PRINT*, 'L [SOLAR DISC NUMBER] = ', L

```

```

PRINT*, 'K [RAY TRIAL NUMBER] = ', K
PRINT*, 'JN [NUMBER OF LAYERS] = ', JN
PRINT*, 'I [SOUNDING LAYER NUMBER] = ', I
PRINT*, 'TK(I) = ', TK(I)
PRINT*, 'SURFRINDEX = ', SURFRINDEX
PRINT*, 'RINDEX = ', RINDEX
PRINT*, 'REFGUESS = ', REFGUESS
PRINT*, 'SUNY(1) = ', SUNY(1)
PRINT*, 'DNEWP = ', DNEWP
PRINT*, 'CURVATURE = ', CURVE
STOP
ENDIF
ETA = DACOS(COSETA)
TANGAMMA = (COSETA - (CETA1 * COSBETA))/(DSIN(ETA) +
+ (CETA1*DSIN(BETA)))
GAMMA = DATAN(TANGAMMA)*2.0D00
*
*-----*
* 15.8 FINDING THE THETA DUE TO CURVATURE AND THE SUM OF THETA. *
*-----*
* This is the angular distance traveled in polar coordinates. *
* This is greater than the initial value of theta due to the *
* curvature of the light ray. See Equation (31) in Bruton. *
*-----*
*
CTHETA = ETA - BETA + GAMMA
REFRACT = CTHETA + DACOS(COSBETA) - DACOS(COSETA)
REFRACT = 180.0D0*REFRACT/PI
SUMREFRACT = SUMREFRACT + REFRACT
*
*-----*
* Summation of angular distance theta. *
*-----*
*
SUMTHETA = SUMTHETA + CTHETA
*
*-----*
* If the ray has travelled a distance of 1500 km then it is *
* assumed that this ray is 'forbidden'. The raytrace is *
* terminated and the programme moves on to the next point on *
* the solar disc. This is recorded as a code "3" in the final *
* column of the output file. In essence, this is the same as *
* a total internal reflection and in a horizontally homogeneous *
* atmosphere should occur rarely, if ever. *
*-----*
*
IF (SUMTHETA.GT.2.5D-01) THEN
*
KODE = 3
WRITE (25,230) (AZ*1.8D+02/PI) +
+ (SUNX(L)*1.8D+02/PI), SUNY(L)*1.8D+02/PI, K, KODE, BETA1*1.8D2/PI
230 FORMAT (1X,F9.4,2X,F7.4,13X,I3,2X,I2,2X,F7.4)
*
GO TO 450
ENDIF
*
*-----*
* 15.9 THE END OF THE RAY TRACING DO LOOP *
*-----*
* This is the end of the ray tracing DO loop. The ray will *
* now pass into the next atmospheric layer and the final value *
* of eta will now become the initial angle beta and the index *
* of refraction at the top of the layer will now become the *
* index at the bottom of the layer, and the height of the *
* top of the previous segment of the ray (RADH) becomes the *
* height of the bottom of the new segment of the ray. *
*-----*
*
DISTANCE = SUMTHETA*6.371D+06
BETA = ETA
SURFRINDEX = RINDEX

```

```

RAD = RADH
IF (RAD.GT.6371.826D03.AND.RAD.LT.6371.827D03) THEN
  HEIGHT50 = RAD
  THETA50 = SUMTHETA
ENDIF
*
*-----*
* 15.9.1 RAY PATH DATA *
*
* The following IF statement can be activated if the user *
* wants to obtain the ray path of the sunlight through the *
* atmosphere. The output is the linear distance along the *
* Earth's surface and the height in metres above sea level. *
* The output is in D:\Russ2\refraction\path.txt *
* The other IF statement is activated when the user wants *
* the incremental refraction at each level. If REFRACT is *
* is changed to SUMREFRACT then the cumulative refraction at *
* each level is written to the file. *
*-----*
*
* IF (SUMTHETA.LT.0.017D0.AND.SUNX(L).LT.0.01D0) THEN
* WRITE (29,231) (SUMTHETA*3.6D2/(2.0D0*PI))*
* 111.292D0, RAD - GEORAD
*231  FORMAT (1X,F8.3,2X,F7.1)
* ENDF
*
* IF (LAYERR.EQ.1) THEN
232  WRITE (29, 232) ZN - 7.72D02, REFRACT
* 232  FORMAT (1X,F10.3,2X,F12.10)
* ENDF
*
* ENDDO
*
* LAYERS = JN
* TOP = ZN
*
*-----*
* 15.10 ALTITUDE AND ERROR OF THE SUN AT THE EXIT POINT. *
*
* Find the altitude of the Sun from the point the ray leaves *
* the atmosphere. *
*-----*
*
* SUNALT = SUMTHETA + SUNY(L)
*
*-----*
*
* Now check to see how close the ray comes to the Sun. *
*-----*
*
* ERROR = ETA - SUNALT
*
*-----*
*
* Check to see if the ray is within the tolerance range *
* (+/-0.1 arcmin) If not, apply a small adjustment to *
* the initial angle Beta, reset the initial conditions *
* and try again. *
*-----*
*
* IF (ERROR.LT.3.0D-05.AND.ERROR.GT.-3.0D-05.AND.
+BETANO.LT.3.0D-05) THEN
  GO TO 400
* ELSEIF (ERROR.LT.3.0D-05.AND.ERROR.GT.-3.0D-05) THEN
  GO TO 400
* ELSEIF (BETANO.LE.0.0D00) THEN
  GO TO 400
* ELSE
  I = 1
  JN = 0
  RAD = GEORAD + ELEV
  ZN = 0.0D00

```

```

DTHETA = DTHETADEG*PI/1.8D+02
SUMTHETA = 0.0D00
*
IF (BETANO.LT.ERROR) THEN
  ERROR = BETANO
  IF (BETANO.LT.3.0D-05) THEN
    GO TO 400
  ENDIF
ENDIF
*
BETANO = BETANO - ERROR*5.0D-01
*
ENDIF
*
-----*
* This CONTINUE statement ends the incremental search routine *
* for each series of trial rays. The DO loop ends when the *
* ray hits the Sun at the designated location. *
*-----*
*
IF (LAYERR.EQ.1) THEN
  PRINT*, 'REFRACTION DATA IN FILE -PATH'
  PRINT*, 'Beta(0) = ', 1.8D2*BETANO2/PI
  STOP
ENDIF
350 CONTINUE
*
-----*
* 15.11 WRITING DATA TO OUTPUT FILE AND END STATEMENTS *
*
* The codes are "5" for a ray that is below the horizon and *
* code "1" for a successful hit. *
*-----*
*
400 IF (BETANO.LE.0.0D0) THEN
  KODE = 5
  WRITE (25,405) (AZ*1.8D+02/PI) + (SUNX(L)*1.8D+02/PI),
+ SUNY(L)*1.8D+02/PI, K, KODE, BETA1*1.8D2/PI
405 FORMAT (1X,F9.4,2X,F7.4,13X,I3,2X,I2,2X,F7.4)
  WRITE (25,406) (AZ*1.8D+02/PI) + (SUNX(L)*(-1.8D+02/PI)),
+ SUNY(L)*1.8D+02/PI, K, KODE, BETA1*1.8D2/PI
406 FORMAT (1X,F9.4,2X,F7.4,13X,I3,2X,I2,2X,F7.4)
  ELSE
  KODE = 1
  WRITE (25,410) (AZ*1.8D+02/PI) + (SUNX(L)*1.8D+02/PI),
+ SUNY(L)*1.8D+02/PI, BETANO*1.8D+02/PI, K, KODE,
+ BETA1*1.8D2/PI
410 FORMAT (1X,F9.4,2X,F7.4,2X,F9.4,2X,I3,2X,I2,2X,F7.4)
  WRITE (25,420) (AZ*1.8D+02/PI) + (SUNX(L)*(-1.8D+02/PI)),
+ SUNY(L)*1.8D+02/PI, BETANO*1.8D+02/PI, K, KODE,
+ BETA1*1.8D2/PI
420 FORMAT (1X,F9.4,2X,F7.4,2X,F9.4,2X,I3,2X,I2,2X,F7.4)
  ENDIF
*
*-----*
*
* The following statements place the altitude and azimuth data into*
* an ordered array suitable for outline tracing in most plotting *
* software. Some minor adjustment of the order of the data *
* still needs to be done in the spread sheet. *
*-----*
*
450 OUTPUT(L,1) = (AZ*1.8D+02/PI) + (SUNX(L)*1.8D+02/PI)
  OUTPUT(L+LSUN,1) = (AZ*1.8D+02/PI) + (SUNX(L)*(-1.8D+02/PI))
  OUTPUT(L,2) = SUNY(L)*1.8D+02/PI
  OUTPUT(L+LSUN,2) = SUNY(L)*1.8D+02/PI
*
IF (KODE.EQ.1) THEN
  OUTPUT(L,3) = BETANO*1.8D+02/PI
  OUTPUT(L+LSUN,3) = BETANO*1.8D+02/PI

```

```

ENDIF
*
OUTPUT(L,4) = BETA1*1.8D+02/PI
OUTPUT(L+LSUN,4) = BETA1*1.8D+02/PI
*
-----*
*       This CONTINUE statement ends the incremental construction   *
*       of the solar image.                                         *
*-----*
*
455  CONTINUE
*
-----*
*       The following DO LOOP writes the alt. and az. data into a file. *
*       Geometric Azimuth, Geometric Altitude, Model Refraction, USNO  *
*       Refraction.                                                 *
*-----*
*
DO 470 L=1, LSUN*2
    WRITE (26,460) OUTPUT(L,1), OUTPUT(L,2), OUTPUT(L,3),
+OUTPUT(L,4)
460  FORMAT (1X,F9.4,2X,F7.4,2X,F7.4,2X,F7.4)
    IF (L.EQ.LSUN*2) THEN
        WRITE (26,460) OUTPUT (1,1), OUTPUT (1,2),
+OUTPUT (1,3), OUTPUT (1,4)
    ENDIF
470  CONTINUE
*
480  PRINT*, 'Another run?'
    PRINT*, 'Enter 1 for "YES" or 0 for "NO"'
    READ*, IYESNO
    IF (IYESNO.EQ.1) THEN
        GO TO 5
    ENDIF
    PRINT*, ' '
    PRINT*, '       Data in: D:russ2\refraction\ -sun.txt'
    PRINT*, ' '
END
*
-----*
*                               S U B R O U T I N E S
*-----*
*-----*
*-----*
*-----*
*-----*
* 1. FORMAT CONVERSION OF DATE FROM YYYYMMDD to YYYY, MM, DD.      *
*-----*
SUBROUTINE DATEFORM(DDATE, YR, DMON, DAY)
DOUBLEPRECISION DDATE, YR, DMON, DAY
*
YR = DINT(DDATE/1.0D+04)
DMON = DINT((DDATE - (YR*1.0D+04))/1.0D+02)
DAY = DINT(DDATE - (YR*1.0D+04) - (DMON*1.0D+02))
*
RETURN
END
*
-----*
*-----*
*-----*
*-----*
*-----*
* 2. FORMAT CONVERSION OF TIME FROM HHMMSS.S TO HH, MM, SS.S      *
*-----*
*-----*
SUBROUTINE TIMEFORM(DTIME, HR, DMIN, SEC)
DOUBLEPRECISION DTIME, HR, DMIN, SEC
*
HR = DINT(DTIME/1.0D+04)
DMIN = DINT((DTIME - (HR*1.0D+04))/1.0D+02)
SEC = (DTIME - (HR*1.0D+04) - (DMIN*1.0D+02))
*

```

```

RETURN
END
*
*****
*-----*
*3. CONVERSION TO JULIAN DATE *
*
* (from Meeus, J. (1988), Astronomical Formulae for Calculators, *
* forth Edition, Willmann-Bell Pub.) *
*-----*
*
SUBROUTINE JULIAN(DDMON, DYR, DDAY, DHR, DDMIN, DSEC, DDJD)
DOUBLEPRECISION DDMON, DYR, DDAY, DHR, DDMIN, DSEC, DA, DB, DDJD
*
*-----*
* 3.1 Checking for February *
* (which has an extra day on a leap year). *
*-----*
IF (DDMON.LE.2.0D+00) THEN
  DYR = DYR - 1.0D+00
  DDMON = DDMON + 1.2D+01
ENDIF
*
*-----*
* 3.2 Checking for Pre-Gregorian period dates. Adjustment for *
* post Gregorian dates. *
*-----*
IF ((DYR + (DDMON/10.0) + (DDAY/1000.0)).GT.1582.1015) THEN
  DA = DINT(DYR/1.0D+02)
  DB = 2.0D+00 - DA + DINT(DA/4.0D+00)
ENDIF
*
*-----*
* 3.3 Calculation of Julian Date. *
*-----*
*
DDJD = DINT(3.6525D+02 * DYR) + DINT(3.06001D+01 *
+ (DDMON + 1.0D+00)) + DDAY + DHR/2.4D+01 + DDMIN/1.44D+03 +
+ DSEC/8.64D+04 + 1.7209945D+06
IF ((DYR + (DDMON/10.0) + (DDAY/1000.0)).GT.1582.1015) THEN
  DDJD = DDJD + DB
ENDIF
*
RETURN
END
*
*****
*-----*
* 4.0 GEOCENTRIC SOLAR COORDINATES (Meeus, 1988). *
*-----*
*
SUBROUTINE SOLAR(T, DJD, DL, PI, DM, e, C, THETA, DNU,
+ SOLRAD, DOMEDA, THETAAPP, EPSILON, RA, DEC, QUADRA,
+ QUADTHETA, RADEG, DECDEG, RAHR, RAMIN, RASEC, DECD, DECM,
+ DECS)
*
IMPLICIT DOUBLEPRECISION (A - H, O - Z)
*
T = (DJD - 2.41502D+06)/3.6525D+04
*
*-----*
* 4.1 Geometric Mean Longitude (w.r.t. mean equinox) *
*-----*
*
DL = 2.7969668D+02 + (3.600076892D+04 * T) +
+ (3.025D-04 * (T**2.0D+00))
DL = DL - (DINT(DL/3.6D+02)*3.6D+02)
DL = (DL * 2.0D+00 * PI)/ 3.6D+02
*

```

```

*-----*
* 4.2 Mean Anomaly (fictitious Sun in a circular orbit) *
*-----*
*
  DM = 3.5847583D+02 + (3.599904975D+04 * T) - 1.5D-04 * (T**2.0D+00)
+   - (3.3D-06 * (T**3.0D+00))
  DM = DM - (DINT(DM/3.6D+02)*3.6D+02)
  DM = (DM * 2.0D+00 * PI) / 3.6D+02
*
*-----*
* 4.3 Eccentricity of Earth's Orbit. *
*-----*
*
  e = 1.675104D-02 - (4.18D-05 * T) - (1.26D-07*(T**2.0D+00))
*
*-----*
* 4.4 The Sun's Equation of Centre. *
*-----*
*
  C = (1.91946D+00 - (4.798D-03 * T) - 1.4D-05 * (T**2.0D+00)) *
+   DSIN(DM) + (2.0094D-02 - 1.0D-04 * T) * DSIN(2.0D+00 * DM) +
+   2.93D-04 * DSIN(3.0D+00 * DM)
  C = (C * 2.0D+00 * PI) / 3.6D+02
*
*-----*
* 4.5 The Sun's True Longitude (Theta) and True Anomaly (DNU). *
*-----*
*
  THETA = DL + C
  DNU = DM + C
*
*-----*
* 4.6 The Solar Radius Vector (in AUs). *
*-----*
*
  SOLRAD = (1.0000002D+00 * (1.0D+00 - e**2.0D+00))/
+   (1.0D+00 + e * DCOS(DNU))
*
*-----*
* 4.7 Corrections for Nutation and Aberration. Nutation is the small *
* short period variations in the precession of the Earth's axis of *
* rotation. This is mostly caused by the gravitational pull of *
* the Moon. Aberration is the small displacement in observed *
* position caused by the finite speed of light from the object *
* coupled with the motion of the Earth through space. *
*-----*
*
  DOMEDA = 2.5918D+02 - 1.934142D+03 * T
  DOMEDA = (DOMEDA * 2.0D+00 * PI) / 3.6D+02
  THETAAPP = (THETA/(2.0D+00*PI))*3.6D+02 - 5.96D-03 -
+   4.79D-03 * DSIN(DOMEDA)
  THETAAPP = (THETAAPP * 2.0D+00 * PI) / 3.6D+02
*
*-----*
* 4.8 Obliquity of the ecliptic. (i.e. the tilt of the Earth's axis) *
*-----*
*
  EPSILON = 2.3452294D+01 - (1.30125D-02 * T) - (1.64D-06 *
+   (T**2.0D+00)) + (5.03D-07*(T**3.0D+00)) +
+   (2.56D-03 * DCOS(DOMEDA))
  EPSILON = (EPSILON * 2.0D+00 * PI) / 3.6D+02
*
*-----*
* 4.9 Celestial Coordinates of the Sun. *
*-----*
*
  RA = DATAN(DCOS(EPSILON)*DTAN(THETAAPP))
  DEC = DASIN(DSIN(EPSILON)*DSIN(THETAAPP))
*
  IF (RA.LT.0.0D00) THEN
    RA = RA + 2.0D+00*PI

```



```

ENDIF
*
QUADRA = IDINT(RA/(PI/2.0D+00))
QUADTHETA = IDINT(THETAAPP/(PI/2.0D+00))
RA = ((QUADTHETA - QUADRA)*PI/2.0D+00) + RA
RADEG = (RA/(2.0D00*PI))*360.0D00
DECDEG = (DEC/(2.0D00*PI))*360.0D00
RAHR = DINT(RADEG/15.0D00)
RAMIN = DINT((RADEG - RAHR*15.0D00)*4.0D00)
RASEC = (RADEG - RAHR*15.0D00 - RAMIN/4.0D00)*240.0D00
DECD = DINT(DECDEG)
DECM = DINT((DECDEG - DECD)*60.0D00)
*
IF (DECD.LT.0.0D00) THEN
    DECM = DECM*(-1.0D00)
ENDIF
*
IF (DECD.LT.0.0D00) THEN
    DECS = (DECDEG - DECD + (DECM/60.0D00))*(-3600.0D00)
ELSEIF (DECD.GE.0.0D00) THEN
    DECS = (DECDEG - DECD - (DECM/60.0D00))*3600.0D00
ENDIF
*
RETURN
END
*
*****
*
*-----*
* 5.0 LOCAL SIDEREAL TIME (DLST), From Meeus, Jean (1988), *
* Astronomical Formulae for Calculators, Willmann-Bell Inc., *
* Pages 39-41. *
*-----*
*
SUBROUTINE SIDEREAL(DJDO, YR, DMON, DAY, A, B, THETANO, TNO, GST,
+ DLST, HR, DMIN, SEC, DLONG, PI)
DOUBLEPRECISION DJDO, YR, DMON, DAY, A, B, THETANO, TNO, GST, DLST,
+ HR, DMIN, SEC, DLONG, PI
*
*-----*
* 5.1 Finding Julian Date. *
*-----*
*
DJDO = DINT(3.6525D+02 * YR) + DINT(3.06001D+01 *
+ (DMON + 1.0D+00)) + DAY + 1.7209945D+06
*
IF ((YR + (DMON/10.0) + (DAY/1000.0)).GT.1582.1015) THEN
    A = DINT(YR/1.0D+02)
    B = 2.0D+00 - A + DINT(A/4.0D+00)
    DJDO = DJDO + B
ENDIF
*
*-----*
* 5.2 Finding Greenwich Sidereal Time (GST). *
*-----*
* 5.2.1 GST in Revolutions. *
*-----*
*
TNO = (DJDO - 2.41502D+06)/3.6525D+04
THETANO = 6.6460656D+00 + (2.400051262D+03 * TNO) + (2.581D-05 *
+ (TNO ** 2.0D+00))
THETANO = THETANO/2.4D+01
*
*-----*
* 5.2.2 GST in Hours. *
*-----*
*
GST = ((THETANO - IDINT(THETANO)) * 2.4D+01) + ((HR +
+ DMIN/6.0D+01 + SEC/3.6D+03) * 1.002737908D+00)
*
IF (GST.GT.2.4D+01) THEN

```

```

      GST = GST - 2.4D+01
    ELSEIF (GST.LT.0.0D+00) THEN
      GST = GST + 2.4D+01
    ENDIF
*
*-----*
* 5.3 Computing Local Sideral Time (DLST). *
*-----*
*
  DLST = GST - ((DLONG*3.6D+02/(2.0D+00*PI))/1.5D+01)
*
  IF (DLST.LT.0.0D+00) THEN
    DLST = DLST + 2.4D+01
  ENDIF
*
  RETURN
  END
*
*****
*-----*
* 6.0 CONVERSION FROM EQUATORIAL COORDINATES TO HORIZON COORDINATES. *
*-----*
*
  SUBROUTINE HORIZON(H, DLST, PI, RA, DEC, DLAT, ALT, AZ)
  DOUBLEPRECISION H, DLST, PI, RA, DEC, DLAT, ALT, AZ
*
*-----*
* 6.1 Conversion of Right Ascension to Hour Angle. *
*-----*
*
  H = (DLST/2.4D+01)*2.0D+00*PI - RA
*
  IF (H.GT.2.0D+00*PI) THEN
    H = H - 2.0D+00*PI
  ENDIF
*
  IF (H.LT.0) THEN
    H = H + 2.0D+00*PI
  ENDIF
*
*-----*
* 6.2 Computation of Altitude and Azimuth. *
*-----*
*
  ALT = DASIN(DSIN(DEC)*DSIN(DLAT) + DCOS(DEC)*DCOS(DLAT)*DCOS(H))
  AZ = DACOS((DSIN(DEC) - DSIN(DLAT)*DSIN(ALT))/
+          (DCOS(DLAT)*DCOS(ALT)))
*
  IF (H.GT.0.0.AND.H.LT.PI) THEN
    AZ = 2.0D+00*PI - AZ
  ENDIF
*
  RETURN
  END
*
*****
*-----*
* 7.0 COMPUTATION OF DIURNAL PARALLAX (HORIZONTAL PARALLAX). *
*-----*
*
  SUBROUTINE PARALLAX(SOLRAD, GEORAD, ALT, DPAR)
  DOUBLEPRECISION SOLRAD, GEORAD, ALT, DPAR
*
  SOLRAD = SOLRAD * 1.4959787D+11
  SOLRAD = DSQRT(GEORAD**2.0D+00 + SOLRAD**2.0D+00 -
+ 2.0D+00*GEORAD*SOLRAD*DSIN(ALT))
  DPAR = (GEORAD/SOLRAD)*DCOS(ALT)
*
  RETURN

```

```

END
*
*****
*
*-----*
* 8.0 INDEX OF REFRACTION. *
* *
* Computation of the index of refraction: From Ciddor, Philip E. *
* (1996), Refractive index of air: new equations for the visible *
* and near infrared, Applied Optics, 35, 1566. *
* *
* NOTE: The STEP numbers used in this subroutine are from Ciddor's *
* paper. *
*-----*
*
SUBROUTINE REFINDEX (TEMP, P, RH, WAVENUMBER,
+ CO2, DNCO2, DNVAPOR, COMPRESSDRY, COMPRESSWET,
+ DRYDENSITY, WETDENSITY, R, DMOLEMASSA, DMOLEMASSW, DRINDEX)
*
IMPLICIT DOUBLEPRECISION (A - H, O - Z)
*
*-----*
* Original data file has T in [C], p in [hPa], and RH in [%]. All *
* values transfered to this subroutine are in SI units [K, Pa] and *
* humidity is fractional. *
* *
* STEP 1. (Cidor page 1572) *
*-----*
*
CALL SATVAPORPRESSURE (TEMP, SVP)
*
*-----*
* At this point it is convenient to compute the enhancement factor,*
* (ENHANCF), vapor pressure (VAPORPRESSURE), and the molar *
* fraction of water (MOLEFRAC). *
*-----*
*
VAPORPRESSURE = RH*SVP
*
ALPHA = 1.00062D+00
BETA = 3.14D-08
GAMMA = 5.6D-07
*
ENHANCF = ALPHA + BETA*P +
+(GAMMA*((TEMP-2.7315D+02)**2.0D+00))
*
DMOLEFRAC = ENHANCF*VAPORPRESSURE/P
*
*-----*
* STEP 2 TO 6 ARE DONE OUTSIDE SUBROUTINE (SEE SECTION 18 IN *
* MAIN PROGRAM). This is done in order to reduce the number of *
* calculations done in the the subroutine. *
* *
* STEP 7. *
* Compute the compressibility of the moist air under experimental *
* conditions. *
*-----*
*
CALL COMPRESSIBILITY (COMPRESS, TEMP, P, DMOLEFRAC)
*
*-----*
* STEP 8. *
* Compute the denisty of the dry component of the moist air. *
*-----*
*
DRYDENSITYB = P*DMOLEMASSA*(1.0D+00 - DMOLEFRAC)/
+ (COMPRESS*R*TEMP)
*
*-----*
* STEP 9. *

```

```

*      Compute the density of the water vapor component.      *
*-----*
*      WETDENSITYB = P*DMOLEMASSW*DMOLEFRAC/(COMPRESS*R*TEMP)
*-----*
* STEP 10.
*      And finally, compute the index of refraction.
*-----*
*      DRINDEX = 1.0D+00+(((DRYDENSITYB/DRYDENSITY)*DNCO2 +
+ (WETDENSITYB/WETDENSITY)*DNVAPOR)/1.0D08)
*      DENSITYBB = DRYDENSITYB + WETDENSITYB
*
*      RETURN
*      END
*
*****
*-----*
* 9.0 THE COMPRESSIBILITY OF AIR.
*-----*
*
*      SUBROUTINE COMPRESSIBILITY (DCOMPRESS, TK, PRESS, DMOIST)
*
*      IMPLICIT DOUBLEPRECISION (A-H, O-Z)
*
*-----*
*      List of constants from Cidor, Appendix A.
*-----*
*
*      A0 = 1.58123D-06
*      A1 = -2.9331D-08
*      A2 = 1.1043D-10
*      B0 = 5.707D-06
*      B1 = -2.051D-08
*      C0 = 1.9898D-04
*      C1 = -2.376D-06
*      D = 1.83D-11
*      E = -7.65D-09
*
*      TC = TK - 2.7315D+02
*
*-----*
*      NOTE: the following equation mixes units of temperature (K and C).
*-----*
*
*      DCOMPRESS = 1.0D+00 - (PRESS/TK)*(A0 + A1*TC + A2*(TC*TC) +
+ (B0 + B1*TC)*DMOIST + (C0 + C1*TC)*(DMOIST**2.0D+00)) +
+ ((PRESS/TK)**2.0D00)*(D + E*(DMOIST**2.0D00))
*
*      RETURN
*      END
*****
*-----*
* 10.0 SATURATION VAPOR PRESSURE.
*-----*
*
*      This subroutine calculates the saturated vapor pressure SVP at a
*      given temperature T in degrees Kelvin. [K = C + 273.15 K] The
*      second formula is over ice and in this program will be used when
*      the air temperature goes below -40 C.
*-----*
*
*      SUBROUTINE SATVAPORPRESSURE (T, SVP)
*
*      IMPLICIT DOUBLEPRECISION (A - H, O - Z)
*
*-----*
*      The IF statement is used to determine the vapor pressure over
*      ice, but because the sky is assumed to be clear there will be

```

```

*      little or no ice crystals in the air, so it is ignored.      *
*      Also there needs to be a weighting function added in order for *
*      the vap. pres. to be continuous, otherwise the vertical density *
*      distribution becomes radically discontinuous (i.e. density      *
*      increases with height).                                       *
*
*      IF (T.GT.233.15D00) THEN
*
*      Lowe, Paul R., (1976), An Approximating Polynomial for the
*      Computation of Saturation Vapor Pressure,
*      Journal of Applied Meteorology, 16, 100-103
*-----*
*
*      A0 = 6.984505294D+03
*      A1 = -1.889039310D+02
*      A2 = 2.133357675D+00
*      A3 = -1.288580973D-02
*      A4 = 4.393587233D-05
*      A5 = -8.023923082D-08
*      A6 = 6.136820929D-11
*
*      SVP = A0 + T*(A1 + T*(A2 + T*(A3 + T*(A4 + T*(A5 + A6*T))))
*      SVP = SVP*1.0D02
*
*-----*
*      NOTE: THE FOLLOWING ROUTINE IS THE INACTIVE ICE COMPONENT
*
*      From Cidor.
*
*      SVP = 1.0D+01**((-2.6635D+03/T) + 1.2537D+01)
*-----*
*
*      RETURN
*      END
*****

```

APPENDIX D

**PRECISION AND ACCURACY OF THE BOMFORD TERRESTRIAL
REFRACTION FORMULA**

The light from the horizon reference markers (i.e. the treetops) must pass through the atmosphere before reaching the theodolite. Consequently, the light also undergoes refraction. In this case the deflection is called terrestrial refraction. The amount of terrestrial refraction (in radians) is determined by the formula (Bomford, 1980):

$$R_t = \frac{kd}{r_e}, \quad (D1)$$

where d [m] is the distance, r_e is the radius of the Earth [m] and k is the refraction coefficient of the light ray found, through the expression

$$k = \frac{252p}{T^2} \left(0.0342 + \frac{dT}{dz} \right), \quad (D2)$$

where p is the barometric pressure in millibars, T is the surface temperature [K] and dT/dz is the vertical temperature gradient in degrees per metre (positive for an inversion).

Before this equation could be used with confidence, its precision and accuracy was evaluated. The accuracy of the terrestrial refraction calculations was tested using a fixed reference target. A smokestack from the Keephills Power Plant could be seen easily from the Stony Plain site and was chosen as a standard reference target. The zenith angle of the top of the stack was measured at the beginning and end of each observing session.

The geographic coordinates of the stack are $53^{\circ} 26' 52''.3$ N, $114^{\circ} 27' 02''.4$ W while the height is 138. m, and the elevation of the base is $752. \pm 1.$ m (Bolton, 1999). From a 1:50 000 topographic map, the approximate geographic coordinates of the observing site were found to be $53^{\circ} 32' 49''$ N, $114^{\circ} 06' 24''$ W. The barometer elevation at the Stony Plain Environmental Monitoring Station is $766. \pm 1.$ m (Funston, 1999) and the height of theodolite above the barometer was measured to be 6.6 ± 0.1 m. The distance between the stations was taken off the topographic map and found to be $25,300. \pm 100.$ m. The measured value of the altitude appears in Table D1 along with the estimated value from Bomford's formula (1980).

Using the data in Table D1, the mean uncorrected altitude of the Keepphills stack is $10' 44''.0$ with a sample standard deviation of $21''.2$, while the mean corrected altitude (i.e. unrefracted) is $09' 24''.5$ with a sample standard deviation of $5''.8$. From a series of four measurements of the stack taken within a span of a few minutes using the Kern theodolite, the measurement error (repeatability) was found to be $\pm 5''.3$. The standard deviation of the corrected values is very close to the measurement error (see Figure D1). This suggests that Bomford's terrestrial refraction formulae produces precise corrections. In other words, after the refraction corrections are applied, the uncertainty in the altitude of a fixed reference marker measured on different days and under different meteorological conditions is similar to the measurement error of the instrument and observer.

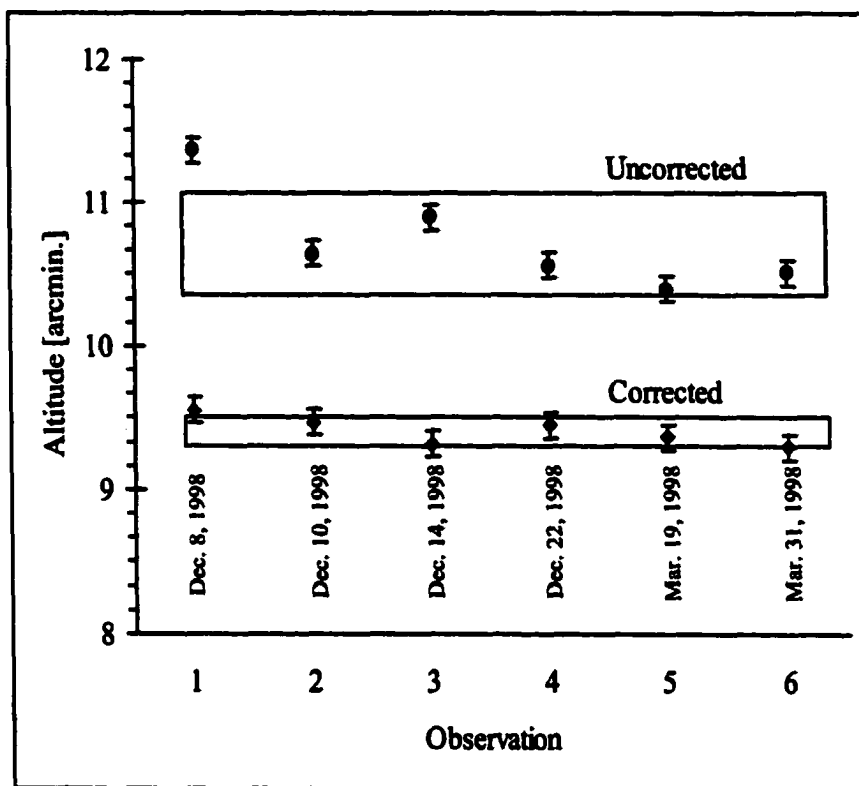


Figure D1: Altitude measurements of the Keephills smoke stack - corrected and uncorrected for terrestrial refraction. The error bars are the standard deviation of a series of consecutive observations taken on a specific day and represent the measurement uncertainty due to instrument and observer error. The boxes are the total uncertainty envelopes centred on the mean and having widths equal to the sample standard deviation of all six days of measurements.

Date	T [°C]	p [hPa]	$\Delta T/\Delta z$ [°Cm ⁻¹]	Observed Altitude [° ' "]	Corrected Altitude [° ' "]
Dec. 8, 1998	-0.5	924.6	0.008	00 11 22	00 09 33
Dec. 10, 1998	6.0	918.0	-0.005	00 10 39	00 09 28
Dec. 14, 1998	-2.5	931.3	0.002	00 10 54	00 09 19
Dec. 22, 1998	-14.3	934.3	-0.011	00 10 34	00 09 27
Mar. 19, 1999	2.0	933.0	-0.010	00 10 24	00 09 22
Mar. 31, 1999	-1.0	926.0	-0.006	00 10 31	00 09 18

Table D1: Observed altitude of the top of the Keephills stack and corrected values from Bomford's terrestrial refraction formula. Observed values are averages of at least two measurements. The first column is the surface temperature and the second is the surface station pressure. The fourth column is the vertical temperature gradient at the surface, as measured by the afternoon rawinsonde from Stony Plain.

The precision produced by the terrestrial refraction correction formula therefore appears to be satisfactory. However, its accuracy must also be verified. An independent estimate of the geometric (i.e. unrefracted) altitude a of the Keephills smokestack is calculated from the formula:

$$a = 90^\circ - \cos^{-1} \left(\frac{r_2^2 + d^2 - r_1^2}{2dr_2} \right), \quad (\text{D3})$$

where r_1 is the distance from the top of the smokestack to the centre of the Earth (the mean radius of the Earth is 6 371 004 m) and r_2 is the distance from the theodolite station to the centre of the Earth, and d is the distance between the smokestack and the theodolite (25 300 ±100m). Equation D3 yields a geometric altitude of 09' 7".7 a difference of 16".8 from the mean corrected altitude of 09' 24".5. This suggests the accuracy may be less than the estimated accuracy of the theodolite measurements (about 6"). However, before passing judgement, the

uncertainty produced by error propagation through Equation D3 must first be estimated.

To estimate the uncertainty in the calculation of the geometric altitude δa , an error propagation analysis (Taylor, 1982) of Equation D3 produces the expressions:

$$\delta \cos a = \left\{ \left[\left(\frac{-r_1^2}{dr_2} \right) \delta r_1 \right]^2 + \left[\left(\frac{r_2^2 - r_1^2}{2d^2 r_2} - \frac{1}{2r_2} \right) \delta d \right]^2 + \left[\left(\frac{d^2 - r_1^2}{2dr_2^2} - \frac{1}{2d} \right) \delta r_1 \right]^2 \right\}^{1/2}, \quad (D4)$$

and:

$$\delta a = \frac{-1}{\sqrt{1 - \cos a}} \delta \cos a, \quad (D5)$$

where δr_1 , δr_2 and δd are the uncertainties in the values (no correction was made for the oblate shape of the Earth). Equations D4 and D5 produce an uncertainty of $\pm 12''.7$. The calculated value of δa , has the highest sensitivity to changes in the values of the uncertainties in the two radii (δr_1 , δr_2). This result suggests that Bomford's formulation is not only precise but also accurate since the range in values due to the uncertainty calculated from Equation D3 overlap the range in values from the uncertainty of the observed altitude of the smoke stack, once corrected for terrestrial refraction (see Table D2).

Method	Altitude	Uncertainty
Geometric (Equation D3)	09' 07".7	12".7
Theodolite (corrected for terrestrial refraction)	09' 24".5	05".8

Table D2: Altitude of Keephills smokestack as found by geometric method and as measured by theodolite with corrections for refraction. Uncertainties for the geometric method are calculated from Equations D4 and D5. Uncertainty in the theodolite method is determined from the standard deviation of total corrected observations.

To determine the sensitivity of Bomford's equation to errors in its coefficients, an error propagation analysis was performed on the equation. The general form of the error propagation formula (Taylor, 1982) for Bomford's equation is:

$$\delta R_t = \left\{ \left[\delta d \frac{\partial R_t}{\partial d} \right]^2 + \left[\delta p \frac{\partial R_t}{\partial p} \right]^2 + \left[\delta T \frac{\partial R_t}{\partial T} \right]^2 + \left[\delta \left(\frac{dT}{dz} \right) \frac{\partial R_t}{\partial \left(\frac{dT}{dz} \right)} \right]^2 \right\}^{\frac{1}{2}}, \quad (D6)$$

where δd is the uncertainty in the distance (determined earlier to be about 300 m), δp is the uncertainty in the atmospheric pressure (estimated to be about 2. mb), δT is the uncertainty in the surface temperature (about 1.0 K) and $\delta(dT/dz)$ the uncertainty in the vertical temperature gradient. The terms in Equation D6 are:

$$\frac{\partial R_t}{\partial d} = \frac{252p}{r_e T^2} \left(0.0342 + \frac{dT}{dz} \right), \quad (D7)$$

$$\frac{\partial R_t}{\partial p} = \frac{252d}{r_e T^2} \left(0.0342 + \frac{dT}{dz} \right), \quad (D8)$$

$$\frac{\partial R_t}{\partial T} = -\frac{504dp}{r_e T^3} \left(0.0342 + \frac{dT}{dz} \right), \quad (D9)$$

and:

$$\frac{\partial R_t}{\partial \left(\frac{dT}{dz} \right)} = \frac{252dp}{r_e T^2}. \quad (D10)$$

In Equation D6, the uncertainty in the surface vertical temperature gradient can be estimated from the assumption that:

$$\frac{dT}{dz} \cong \frac{\Delta T}{\Delta z}, \quad (\text{D11})$$

and therefore

$$\delta \frac{dT}{dz} \cong \left[\left(\frac{\delta \Delta T}{\Delta z} \right)^2 + \left(\delta \Delta h \frac{\Delta T}{\Delta z} \right)^2 \right]^{\frac{1}{2}}, \quad (\text{D12})$$

where ΔT is the change in temperature over a height of Δz and is estimated using the surface measurements and the first measurement after release of the sounding. The measurement error from a Vaisala RS80 radiosonde is ± 0.2 K for temperature, ± 0.1 hPa for pressure (Vaisala online technical specifications, 1999) and about ± 1.0 m for height at 900 hPa (Antikainen and Hyvönen, 1983).

The uncertainty in the surface vertical temperature gradient was calculated from Equation D12 for each date using surface and rawinsonde data. Theodolite measurements of the smokestack on March 19 and 31, 1999 were taken three to four hours before the rawinsonde launch. It was assumed that the surface vertical temperature profile would not have changed significantly between the time of these observations and the rawinsonde launch. On March 19 and 31 the weather was cool and clear with a moderate wind, which suggests a relatively stable air mass. At that time of year sunset does not take place until 2.5 to 2.9 hours after the rawinsonde launch. Therefore, the nocturnal surface inversion would probably not have started before the launch of the rawinsonde (Stull, 1988). The error

propagation for Bomford's formula can now be performed and the results appear in Table D3.

Date [m/d/y]	$\delta(dT/dz)$ [$\pm^{\circ}\text{Cm}^{-1}$]	δR_t [\pm'']
12/08/98	0.0054	1.9
12/10/98*	0.0005	0.9
12/14/98	0.0059	1.9
12/22/98	0.0050	1.6
03/19/99	0.0004	0.7
03/31/99*	0.0003	0.9

Table D3: Uncertainties in the surface vertical temperature gradient and the terrestrial refraction R_t . Those dates marked with an asterisk used the 850 hPa mandatory level to determine the surface vertical temperature gradient. The average uncertainty in the gradient is $\pm 0.0035^{\circ}\text{Cm}^{-1}$.

Over a distance of 2500 m between the observer and the target, the average uncertainty in the terrestrial refraction is $\pm 1''.3$, about five times smaller than the estimated resolution of the photogrammetric system (approximately $6''$). The combined uncertainty due to errors in the terrestrial refraction and measurement errors in the zenith angle of the treetops $\delta Z'$ can be found from:

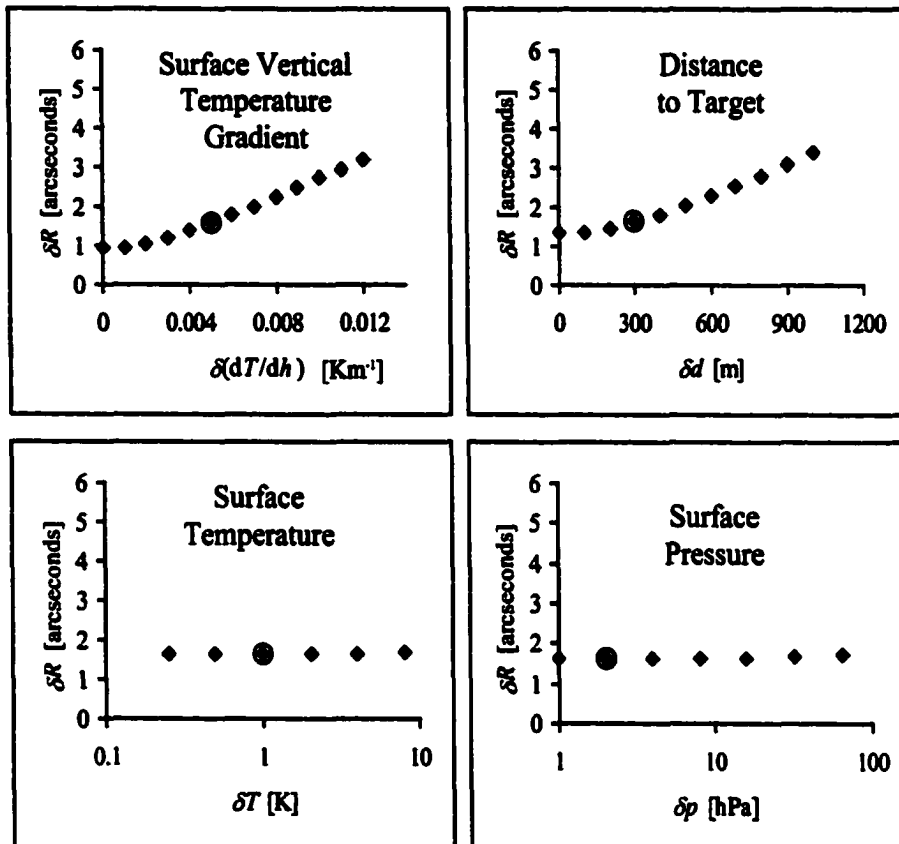
$$\delta Z' = \sqrt{\delta R_t^2 + \delta Z^2}, \quad (\text{D13})$$

where δZ is the estimated measurement error of the zenith angle of the treetops (6".0) and this results in a $\delta z'$ of 6".1. This is only a 2 percent increase in the uncertainty in the estimated measurement error of the zenith angle of the treetops and can therefore be ignored.

In order to explore the potential uncertainties in Bomford's method, a sensitivity analysis was performed on Equation D6. In this analysis, the parameters of the error propagation equation for terrestrial refraction were while the other uncertainties were kept fixed. It was apparent that the uncertainty in terrestrial refraction was most sensitive to the distance between the observer and the target and the surface vertical temperature gradient. However, an error in excess of ± 900 metres in the target distance would be necessary to produce a propagated uncertainty of half of the resolution of the photogrammetric system. The error in the surface vertical temperature gradient would need to be greater than $\pm 0.011^\circ\text{Cm}^{-1}$ to produce a propagated uncertainty in the terrestrial refraction of half of the resolution of the photogrammetric system (see Figures D2 to D5).

Conclusions

After applying the Bomford formula (1980) for terrestrial refraction, a reduction in the sample standard deviation of the altitude observations of the Keephills smokestack from 21".2 to 5".8 was observed. Since the standard deviation of the corrected observation is now about as large as the measurement error of the theodolite (about 6") it appears reasonable to conclude that the Bomford formula produces precise altitude values.



Figures D2, D3, D4 and D5: Sensitivity analysis of the terrestrial refraction error propagation formula (Equation D6). The uncertainty in the terrestrial refraction δR is plotted against the uncertainties in individual parameters from Bomford's terrestrial refraction equation (the ordinates in the temperature and the pressure graphs are logarithmic). In each plot, one uncertainty parameter is altered while all others are held fixed at their most likely values. The uncertainty is apparently most sensitive to errors in the target distance measurement and the measurement of the surface vertical temperature gradient.

APPENDIX E**FORTRAN CODE FOR 3x3 MATRIX INVERSION**

Based on Press, W.H., et al. (1992)

```

*-----*
*
*           M A T R I X   I N V E R S I O N   C A L C U L A T O R
*
*           Russell D. Sampson, October 28, 1999
*
* FROM: Press, W.H. et al. (1992), Numerical Recipes in FORTRAN,
*
* Cambridge University Press, pp. 963 (see pages 27-31)
*
*
* This program, calculates the inverse matrix using the Gauss-
* Jordan Elimination method with full pivoting. For an
* introduction to the Gauss Elimination method see Etter: FORTRAN
* With Numerical Methods for Engineers and Scientists (page 492).
*
* This program was specifically written for photogrammetric
* applications. It attempts to invert the omega-phi-kappa
* rotation matrix. Therefore, it is set up to invert only a three
* by three matrix.
*-----*
*
* PROGRAM MATRIXINVERSION
*
* INTEGER N, I, J, M, NP, MP
* REAL C(3,3), D(3,3)
* CHARACTER*20 MATRIX
*
* PRINT*, '++++++ 3 BY 3 MATRIX INVERSION ROUTINE ++++++'
* PRINT*, 'Using the Gauss-Jordan Elimination Method with'
* PRINT*, 'full pivoting. (Numerical Recipes pages 27-31)'
* PRINT*, ' '
*
* NP = 50
* MP = 50
*-----*
*
* Now we read the matrix file and place the elements into the
* array A(NP,NP).
*-----*
*
* PRINT*, 'What is the file name of the matrix to be inverted?'
* READ(*,'(a)') MATRIX
* OPEN (10,FILE=MATRIX)
* PRINT*, ' '
*
* READ (10,*) N
* DO 2 I=1,N
*   READ (10,*) (C(I,J),J=1,N)
2 CONTINUE
*
*-----*
*
* Now we read the identity matrix file and place the elements
* into the array B(NP,MP).
*-----*
*
* OPEN (UNIT=11, FILE='D:\Russ2\Photogrammetry\Photogrammetry\
* +inversmx\inversmx\identity.txt',STATUS='OLD')
* READ (11,*) M
* DO 3 I=1,N
*   READ (11,*) (D(I,J),J=1,M)
3 CONTINUE
*
* CALL GAUSSJ(C,N,NP,D,M,MP)
*
* PRINT*, 'The Inverse Matrix is '
* PRINT*, ' '
* DO 5 I=1,N
*   PRINT 4, D(I,1), D(I,2), D(I,3)
4   FORMAT (1X,F14.10,2X,F14.10,2X,F14.10)
5 CONTINUE

```

```

*
*   OPEN (UNIT=12,FILE='D:\Russ2\Photogrammetry\Photogrammetry\
+inversmx\inversmx\inv.tmp')
*
*   DO 8 I=1,N
*       WRITE (12,7) D(I,1), D(I,2), D(I,3)
7       FORMAT (1X,F14.10,2X,F14.10,2X,F14.10)
8       CONTINUE
*
*   PRINT*, ' '
*   PRINT*, 'Output is contained in D:\Russ2\Photogrammetry\
+Photogrammetry\inversmx\inversmx\inv.tmp'
*   PRINT*, ' '
*
*   END
*
*-----*
*   M A T R I X   I N V E R S I O N   S U B R O U T I N E   *
*-----*
*
*   SUBROUTINE GAUSSJ(A,N,NP,B,M,MP)
*
*-----*
*   A is the input matrix A(1:N,1:N) stored in an array of physical *
*   dimensions NP by NP. B is an input matrix B(1:N,1:M) containing *
*   the M right-hand side vectors, stored in an array of physical *
*   dimensions NP by MP. On output A(1:N,1:N) is replaced by its *
*   matrix inverse and B(1:N,1:M) is replaced by the corresponding *
*   set of solution vectors.
*-----*
*
*   INTEGER M,MP,N,NP,NMAX
*   REAL A(3,3), B(3,3)
*   PARAMETER (NMAX=50)
*
*-----*
*   NMAX is the largest anticipated value of N.
*-----*
*
*   INTEGER I,ICOL,IROW,J,K,L,LL,INDXC(NMAX),INDXR(NMAX),IPIV(NMAX)
*
*-----*
*   Integer arrays INDXC, INDXR and IPIV are used for bookkeeping of *
*   the pivoting.
*-----*
*
*   REAL BIG, DUM, PIVINV
*
*   DO 11 J=1,N
*       IPIV(J) = 0
11  ENDDO
*
*   DO 22 I=1,N
*
*-----*
*   This the main do loop over the columns to be reduced
*-----*
*
*   BIG = 0
*   DO 13 J=1,N
*
*-----*
*   This is the outer loop of the search for a pivot element.
*-----*
*
*   IF (IPIV(J).NE.1) THEN
*       DO 12 K=1,N
*           IF (IPIV(K).EQ.0) THEN
*               IF (ABS(A(J,K)).GE.BIG) THEN

```

```

                BIG = ABS(A(J,K))
                IROW = J
                ICOL = K
            ENDIF
        ELSE IF (IPIV(K).GT.1) THEN
            PAUSE 'Singular matrix in GAUSSJ!'
        ENDIF
12          ENDDO
        ENDIF
13      ENDDO
*
*          IPIV(ICOL) = IPIV(ICOL) + 1
*
*-----*
*   We now have the pivot element, so we interchange rows, if needed,
*   to put the pivot element on the diagonal. The columns are not
*   physically interchanged, only relabled:
*
*   INDXC(I), the column of the ith pivot element, is the ith column
*   that is reduced, while INDXR(I) is the row in which that
*   pivot element was originally located. If INDXR(I) is not equal
*   to INDXC(I) there is an implied column interchange. With this
*   form of bookkeeping, the solution b's will end up in the correct
*   order, and the inverse matrix will be scrambled by columns
*-----*
*
*          IF (IROW.NE.ICOL) THEN
*              DO 14 L=1, N
*                  DUM = A(IROW,L)
*                  A(IROW,L) = A(ICOL,L)
*                  A(ICOL,L) = DUM
14          ENDDO
*              DO 15 L=1, M
*                  DUM = B(IROW,L)
*                  B(IROW,L) = B(ICOL,L)
*                  B(ICOL,L) = DUM
15          ENDDO
*          ENDIF
*
*          INDXR(I) = IROW
*          INDXC(I) = ICOL
*
*-----*
*   We are now ready to divide the pivot row by the pivot element,
*   located at IROW and ICOL.
*-----*
*
*          IF (A(ICOL,ICOL).EQ.0) PAUSE 'Singular matrix in GAUSSJ'
*          PIVINV = 1./A(ICOL,ICOL)
*          A(ICOL,ICOL) = 1
*          DO 16 L=1, N
*              A(ICOL,L) = A(ICOL,L) * PIVINV
16          ENDDO
*          DO 17 L=1, M
*              B(ICOL,L) = B(ICOL,L) * PIVINV
17          ENDDO
*
*-----*
*   Now we reduce the rows - except for the pivot point, of course.
*-----*
*
*          DO 21 LL=1, N
*              IF (LL.NE.ICOL) THEN
*                  DUM = A(LL,ICOL)
*                  A(LL,ICOL) = 0
*                  DO 18 L=1, N
*                      A(LL,L) = A(LL,L) - A(ICOL,L) * DUM
18          ENDDO
*                  DO 19 L=1, M
*                      B(LL,L) = B(LL,L) - B(ICOL,L) * DUM

```

```

19             ENDDO
             ENDIF
21         ENDDO
22     ENDDO
*
*-----*
*   This is the end of the main loop over columns of the reduction. *
*   It only remains to unscramble the solution in view of the column *
*   interchanges. We do this by interchanging pairs of columns in *
*   the reverse order the permutation was built up.
*-----*
*
DO 24 L=N, 1, -1
    IF (INDXR(1).NE.INDXC(1)) THEN
        DO 23 K=1, N
            DUM = A(K,INDXR(1))
            A(K,INDXR(1)) = A(K,INDXC(1))
            A(K,INDXC(1)) = DUM
23         ENDDO
        ENDIF
24     ENDDO
    RETURN
END
*-----*

```

APPENDIX F**TREETOP AND REFERENCE TARGET DATA**

Table F1: The zenith angle measurements of the reference targets visible from the Stony Plain weather station observation deck. The first column is the target designation (the smokestack is located at the Keephills Power Plant while the tower is a distant transmission tower). The second column is the date of the measurements. The third is the instrument used; 'WH' for Wild Heerbrugg theodolite and 'K' for Kern E-2 theodolite). The next twelve columns are the individual zenith angle measurements in degrees, arcminutes and arcseconds while the last three columns are the final computed zenith angles. The Kern E-2 had a self-leveling feature that made telescope reversal unnecessary.

Target	Date	Instr.	1		2		3		4		°	"	"
			°	"	°	"	°	"	°	"			
STACK	08-Dec-98	WH	90	8 0	90	8 0	270	30 42.0	270	30 48.0	89	48	37.5
STACK	08-Dec-98	WH	90	8 42	90	8 42	270	30 0.0	270	30 0.0	89	49	21.0
STACK	14-Dec-98	WH	90	8 30	90	8 24	270	30 0.0	270	30 0.0	89	49	13.5
STACK	14-Dec-98	WH	90	8 24	90	8 30	270	30 18.0	270	30 12.0	89	49	6.0
STACK	22-Dec-98	WH	90	8 54	90	8 48	270	30 0.0	270	30 0.0	89	49	25.5
STACK	22-Dec-98	WH	90	8 18	90	8 12	270	30 12.0	270	30 18.0	89	49	0.0
STACK	19-Mar-99	K	89	49 33	89	49 34	270	10 23.0	270	10 26.0	89	49	34.5
STACK	19-Mar-99	K	89	49 28	89	49 29	270	10 17.0	270	10 16.0	89	49	36.0
STACK	31-Mar-99	K	270	10 26	270	10 32	270	10 32.0	270	10 34.0	89	49	29.0
TOWER	19-Mar-99	K	90	0 56	90	0 56	269	58 54.0	269	58 50.0	90	1	2.0
TOWER	19-Mar-99	K	90	1 4	90	1 7	269	58 58.0	269	58 54.0	90	1	4.8
TOWER	31-Mar-99	K	269	59 18	269	59 12	269	59 16.0	269	59 19.0	90	0	43.7
8	31-Mar-99	K	269	58 27	269	58 20	269	58 20	269	58 21	90	1	38.0
9	31-Mar-99	K	269	57 53	269	57 48	269	57 55	269	57 53	90	2	7.7
9a	31-Mar-99	K	269	58 39	269	58 30	269	58 40	269	58 40	90	1	22.8
9b	31-Mar-99	K	269	58 38	269	58 41	269	58 39	269	58 40	90	1	20.5
9c	31-Mar-99	K	269	58 31	269	58 34	269	58 37	269	58 32	90	1	26.5
10	31-Mar-99	K	269	58 32	269	58 33	269	58 30	269	58 36	90	1	27.3
10a	31-Mar-99	K	269	57 57	269	58 2	269	58 4	269	58 4	90	1	58.3
11	19-Mar-99	K	90	2 2	90	1 56					90	1	59.0
11	31-Mar-99	K	269	58 8	269	58 10	269	58 6	269	58 9	90	1	51.8

Table F1

Target	Date	Instr.	1		2		3		4		°	'	"	
			°	'	°	'	°	'	°	'				
11a	19-Mar-99	K	90	1	59	1	56				90	1	57.5	
12	22-Dec-98	WH	90	20	30	20	24	270	18	0	270	18	6	12.0
12	19-Mar-99	K	90	1	21	1	16	269	58	42	269	58	44	17.8
12a	19-Mar-99	K	90	1	16	1	11							13.5
14	19-Mar-99	K	90	0	42	0	45	269	59	11	269	59	9	46.8
14a	19-Mar-99	K	90	1	8	1	13							10.5
14b	19-Mar-99	K	90	1	18	1	19							18.5
15	19-Mar-99	K	90	0	39	0	44	269	59	12	269	59	15	44.0
15.5	14-Dec-98	WH	90	20	18	20	18	270	18	12	270	18	6	4.5
15.5	19-Mar-99	K	90	1	9	1	10							9.5
15c	19-Mar-99	K	90	1	18	1	19							18.5
15d	19-Mar-99	K	90	1	21	1	22							21.5
16	10-Dec-98	WH	90	18	54	18	48	270	19	54	270	20	0	27.0
16	14-Dec-98	WH	90	18	54	18	54	270	19	48	270	19	48	33.0
16	22-Dec-98	WH	90	19	0	18	54	270	19	36	270	19	30	42.0
16	19-Mar-99	K	89	59	36	59	35	270	0	14	270	0	14	40.8
16a	19-Mar-99	K	90	1	36	1	40							38.0
16b	19-Mar-99	K	90	0	58	1	3							0.5
16.5	19-Mar-99	K	90	1	42	1	39	269	58	22	269	58	29	37.5
17	10-Dec-98	WH	90	19	30	19	36	270	19	18	270	19	6	10.5
17	14-Dec-98	WH	90	19	30	19	24	270	19	0	270	19	0	13.5
17	22-Dec-98	WH	90	19	36	19	30	270	18	54	270	18	54	19.5
17	19-Mar-99	K	90	0	20	0	20	269	59	34	269	59	37	22.2

Table F1

Target	Date	Instr.	1		2		3		4		°	"	°	"	
			°	"	°	"	°	"	°	"					
17a	19-Mar-99	K	90	0	90	0					90	0	28.5		
17b	19-Mar-99	K	90	1	90	1					90	1	6.5		
18	10-Dec-98	WH	90	20	90	20	270	18	30	270	18	30	90	0	46.5
18	14-Dec-98	WH	90	20	90	20	270	18	36	270	18	30	90	0	43.5
18	19-Mar-99	K	90	0	90	0	269	58	57	269	59	2	90	0	58.8
19a	19-Mar-99	K	90	1	90	1	269	57	59	269	58	0	90	1	55.5
20	19-Mar-99	K	90	0	90	0	269	59	25	269	59	26	90	0	25.8
20a	19-Mar-99	K	90	1	90	1							90	1	15.5
20b	19-Mar-99	K	90	0	90	0							90	0	37.5
21	19-Mar-99	K	90	0	90	0	269	59	39	269	59	43	90	0	21.2
22	19-Mar-99	K	89	59	89	59	270	0	7	270	0	10	89	59	49.5
22b	19-Mar-99	K	90	0	90	0							90	0	47.0
23	19-Mar-99	K	90	0	90	0	269	59	59	269	59	52	90	0	3.5
24	19-Mar-99	K	90	1	90	1	269	58	52	269	58	47	90	1	7.8
26	19-Mar-99	K	90	1	90	1	269	58	17	269	58	19	90	1	45.5

Table F1

APPENDIX G**SOUNDING FILES FOR DECEMBER 8, 14, AND 22, 1998**

A Vaisala RS80 rawinsonde instrument produced the sounding files of December 14 and 18. Only the boundary layer is printed from these large files. The sounding file for December 8, 1998 was produced by a VIZ rawinsonde and is shown in its entirety. The last two rows of data for each sounding file were added to represent the higher layers of the atmosphere. These higher layers were not measured, but taken from the U.S. Standard Atmosphere (U.S. Government Printing Office, 1976). Plots of the soundings can be seen in Figures G1 through G6.

December 8, 1998 23:15 UTC (VIZ Rawinsonde)

Time [min.]	Time [sec.]	<i>p</i> [hPa]	<i>z</i> [gpm]	<i>T</i> [°C]	RH [%]	T-T _d [°C]
0	0	924.6	766	-0.5	77.0	3.5
0	5	918.7	818	-0.1	46.4	10.2
0	55	886.8	1101	1.0	35.9	13.6
5	58	724.1	2688	-13.2	65.7	5.0
7	52	672.1	3251	-17.2	55.6	6.8
8	32	659.5	3393	-17.9	37.6	11.1
13	28	525.0	5052	-31.9	20.3	15.2
18	28	415.3	6658	-46.3	24.9	11.5
20	25	381.0	7225	-51.4	26.9	10.3
20	48	374.9	7329	-52.1	27.2	10.1
21	8	369.3	7427	-52.0	27.2	10.1
21	29	362.9	7541	-49.7	26.7	10.6
23	25	326.5	8230	-51.8	24.7	10.9
24	48	307.5	8619	-50.2	23.9	11.3
25	29	298.3	8818	-51.1	23.4	11.3
27	37	272.3	9413	-48.5	21.7	12.2
28	25	261.0	9692	-50.4	21.3	12.1
30	1	243.6	10145	-47.3	20.0	13.0
33	28	209.4	11148	-46.7	16.7	14.4
35	4	195.6	11598	-49.1	16.0	14.4
35	58	189.8	11795	-47.8	15.6	14.7
37	12	181.3	12097	-49.3	15.3	14.7
40	20	159.2	12949	-48.1	14.3	15.4
40	49	156.0	13085	-45.6	14.0	15.9
41	33	151.1	13300	-44.2	13.5	16.5
42	53	140.6	13777	-48.0	12.9	16.1
43	25	137.2	13938	-48.2	12.9	16.1
43	44	135.2	14039	-46.6	12.7	16.5
45	40	125.2	14546	-46.6	12.1	16.8
50	40	101.5	15930	-50.4	11.6	16.4
51	32	97.8	16167	-50.7	11.6	16.4
52	36	93.4	16468	-48.2	11.4	16.9
55	0	83.3	17217	-52.0	11.3	16.3
60	0	66.0	18728	-50.8	11.1	16.7
63	53	54.6	19961	-51.0	10.9	16.7
64	28	53.1	20146	-49.5	10.8	17.1
66	52	47.2	20913	-50.1	10.6	17.1

December 8, 1998 23:15 UTC (VIZ Rawinsonde)

Time [min.]	Time [sec.]	<i>p</i> [hPa]	<i>z</i> [gpm]	<i>T</i> [°C]	RH [%]	T-T_d [°C]
68	5	44.6	21290	-48.7	10.5	17.4
71	1	38.4	22269	-51.0	10.4	17.1
72	58	34.9	22894	-49.2	10.3	17.5
74	48	31.8	23494	-50.2	10.2	17.4
79	48	25.0	25103	-45.3	9.6	18.7
81	25	22.7	25747	-47.2	9.4	18.5
83	8	20.9	26284	-45.7	9.3	18.8
88	9	16.2	27994	-46.0	9.0	19.1
93	9	12.5	29682	-45.8	8.7	19.3
98	8	9.5	31558	-46.9	8.6	19.2
100	53	8.2	32507	-46.1	8.6	19.3
103	8	7.3	33230	-49.6	8.6	18.6
106	32	6.2	34302	-51.4	8.7	18.1
109	28	5.5	35159	-56.2	8.9	17.0
		1.0	47000	-3.0	1.0	
		0.01	80000	-93.0	1.0	

December 14, 1998 23:15 UTC (Vaisala RS80 Rawinsonde)

Time [min.]	Time [sec.]	<i>p</i> [hPa]	<i>z</i> [gpm]	<i>T</i> [°C]	RH [%]	<i>T_d</i> [°C]
0	0	931.3	766	-2.5	30	-17.7
0	10	925.7	814	-2.4	33	-16.5
0	20	919.9	865	-2.8	34	-16.5
0	30	913.8	917	-3.2	34	-16.9
0	40	907.6	971	-3.6	35	-16.9
0	50	901.4	1025	-4.0	35	-17.2
1	0	895.9	1073	-4.4	35	-17.6
1	10	890.5	1121	-4.9	36	-17.7
1	20	885.3	1167	-5.3	37	-17.7
1	30	879.9	1215	-5.7	38	-17.8
1	40	874.1	1266	-6.2	39	-17.9
1	50	868.4	1318	-6.7	40	-18.1
2	0	862.2	1373	-7.2	41	-18.2
2	10	857.4	1417	-7.6	42	-18.3
2	20	852.6	1460	-8.0	43	-18.4
2	30	847.8	1504	-8.5	44	-18.6
2	40	843.1	1548	-8.9	45	-18.7
2	50	837.9	1595	-9.3	45	-19.1
3	0	832.6	1644	-9.7	46	-19.2
3	10	828.2	1685	-10.1	47	-19.3
3	20	823.5	1728	-10.5	47	-19.7
3	30	818.7	1774	-10.9	46	-20.3
3	40	813.8	1820	-11.2	44	-21.1
3	50	808.8	1867	-11.4	40	-22.3
4	0	804.1	1912	-11.6	36	-23.7
4	10	798.8	1963	-11.7	29	-26.2
4	20	793.4	2015	-11.8	25	-27.9
4	30	788.1	2065	-12.0	22	-29.5
4	40	783.0	2116	-12.2	20	-30.7
4	50	777.8	2166	-12.4	17	-32.5
5	0	772.5	2218	-12.6	13	-35.4
5	10	767.6	2267	-12.8	12	-36.4
5	20	762.8	2315	-13.2	12	-36.7
5	30	757.8	2365	-13.6	12	-37.1
5	40	752.6	2417	-14.0	13	-36.6
5	50	747.5	2469	-14.4	13	-36.9
6	0	742.7	2517	-14.8	14	-36.5

December 22, 1998 23:15 UTC (Vaisala RS80 Rawinsonde)

Time [min.]	Time [sec.]	<i>p</i> [hPa]	<i>z</i> [gpm]	<i>T</i> [°C]	RH [%]	<i>T-T_d</i> [°C]
0	0	934.3	766	-14.3	70.0	-18.6
0	10	927.3	823	-14.9	41.0	-25.3
0	20	921.9	868	-15.1	41.0	-25.4
0	30	916.5	912	-15.5	42.0	-25.5
0	40	911.4	954	-15.9	43.0	-25.7
0	50	905.8	1000	-16.2	44.0	-25.7
1	0	899.9	1050	-16.5	43.0	-26.2
1	10	894.0	1099	-16.9	44.0	-26.3
1	20	888.1	1149	-17.3	44.0	-26.7
1	30	882.0	1200	-17.7	43.0	-27.3
1	40	876.2	1249	-17.6	42.0	-27.5
1	50	870.7	1297	-17.8	41.0	-27.9
2	0	865.0	1346	-18.2	41.0	-28.3
2	10	859.3	1395	-18.5	42.0	-28.3
2	20	853.9	1442	-18.7	42.0	-28.5
2	30	848.7	1488	-18.9	38.0	-29.7
2	40	843.7	1531	-19.1	32.0	-31.7
2	50	838.6	1577	-19.2	25.0	-34.4
3	0	833.5	1622	-19.3	16.0	-38.9
3	10	828.4	1668	-19.4	13.0	-41.0
3	20	823.1	1715	-19.6	15.0	-39.8
3	30	817.9	1762	-19.9	16.0	-39.4
3	40	813.0	1807	-20.1	18.0	-38.4
3	50	808.0	1852	-20.4	29.0	-33.9
4	0	802.9	1899	-20.8	34.0	-32.6
4	10	797.2	1951	-21.2	35.0	-32.7
4	20	791.6	2004	-21.6	37.0	-32.5
4	30	786.4	2052	-22.0	40.0	-32.0
4	40	781.2	2101	-22.4	43.0	-31.6
4	50	776.3	2147	-22.7	45.0	-31.4
5	0	771.2	2196	-23.0	46.0	-31.5
5	10	765.9	2246	-23.4	46.0	-31.9
5	20	760.7	2296	-23.7	44.0	-32.6
5	30	755.4	2347	-24.0	42.0	-33.4
5	40	749.8	2401	-24.3	41.0	-33.9
5	50	744.4	2454	-24.7	41.0	-34.2
6	0	738.6	2511	-25.1	41.0	-34.6
6	10	733.0	2566	-25.4	34.0	-36.8

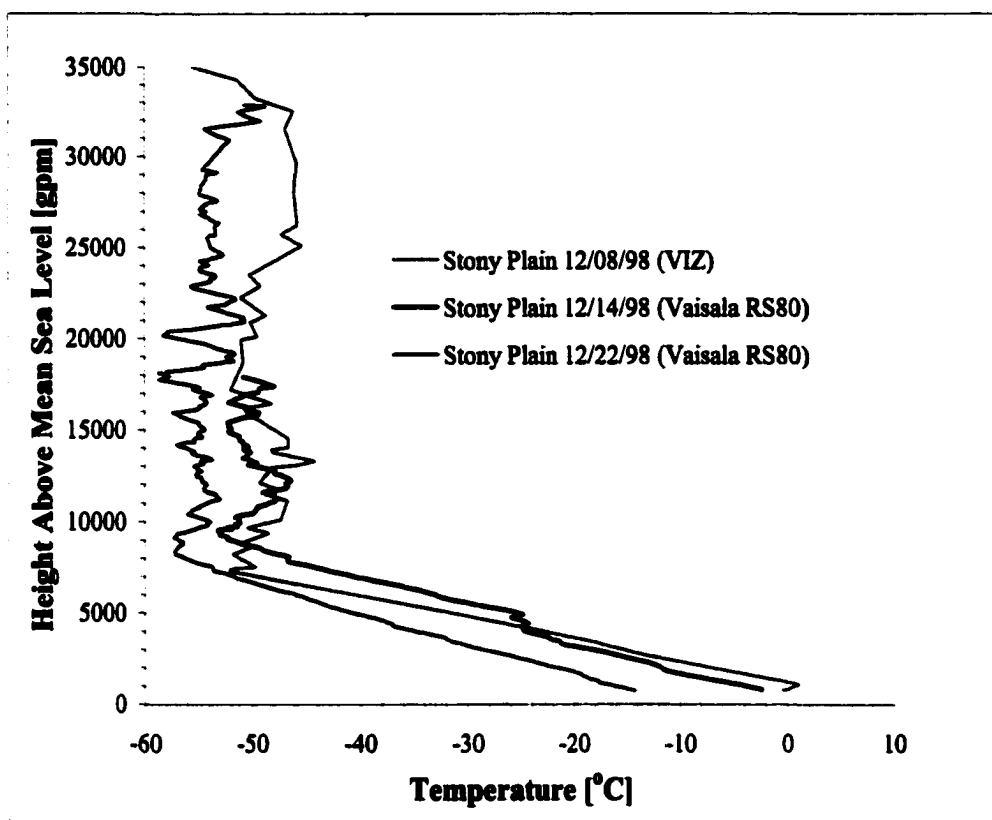


Figure G1: The temperature profile from the 23:15 UTC rawinsonde files for the sunset refraction experiments.

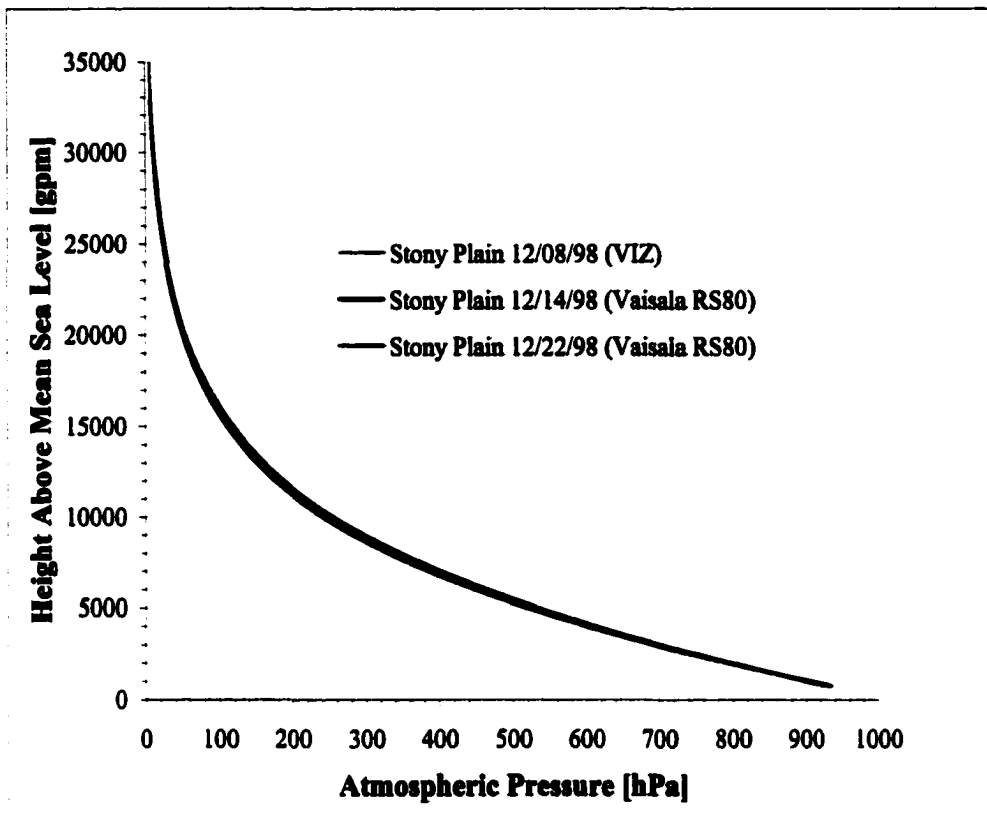


Figure G2: The atmospheric pressure profile from the 23:15 UTC rawinsonde files for the sunset refraction experiments.

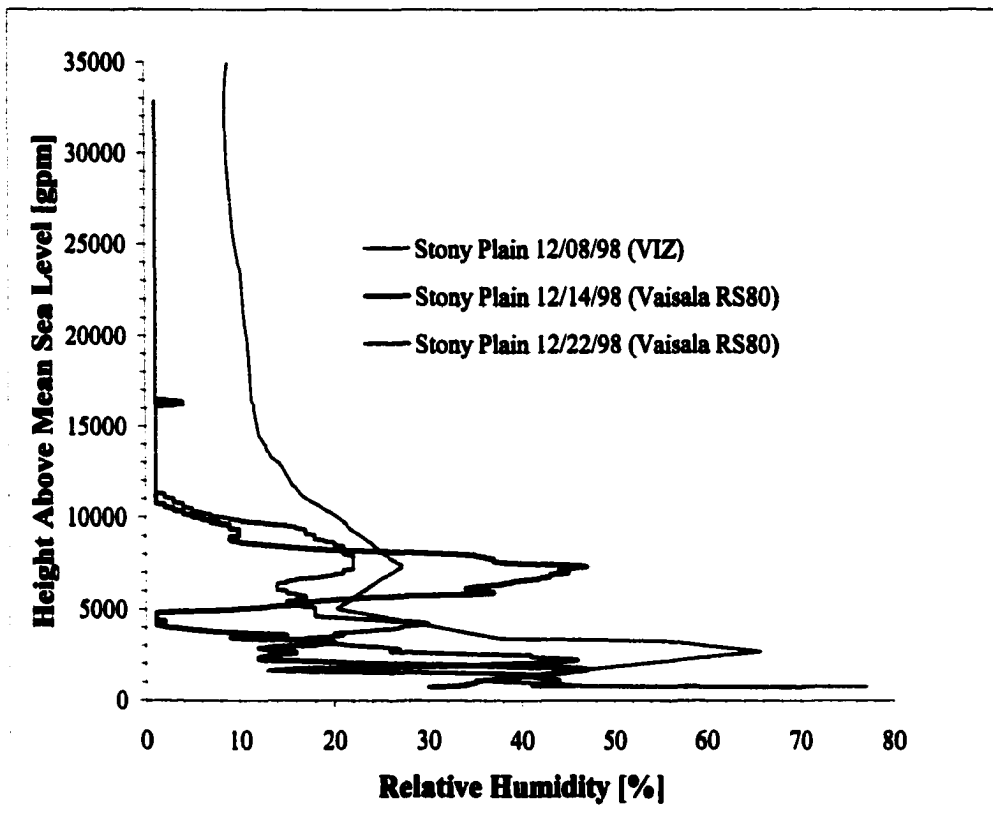


Figure G3: The relative humidity profile from the 23:15 UTC rawinsonde files for the sunset refraction experiments.

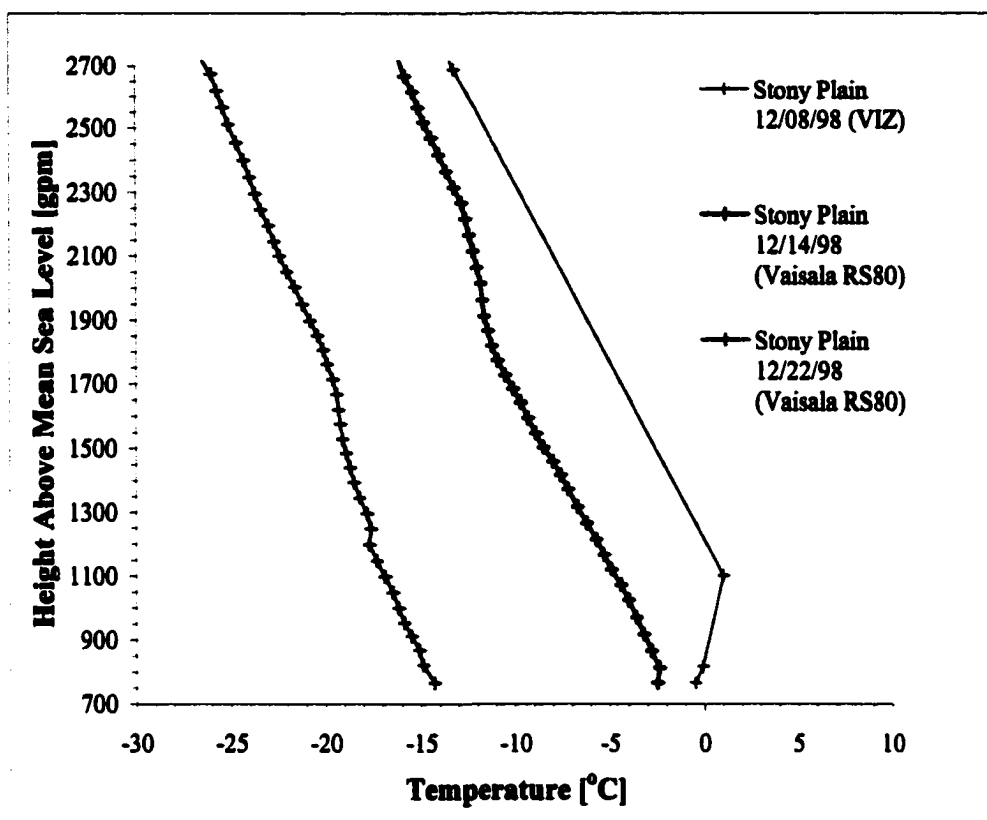


Figure G4: The planetary boundary layer temperature profile from the 23:15 UTC rawinsonde files for the sunset refraction experiments.

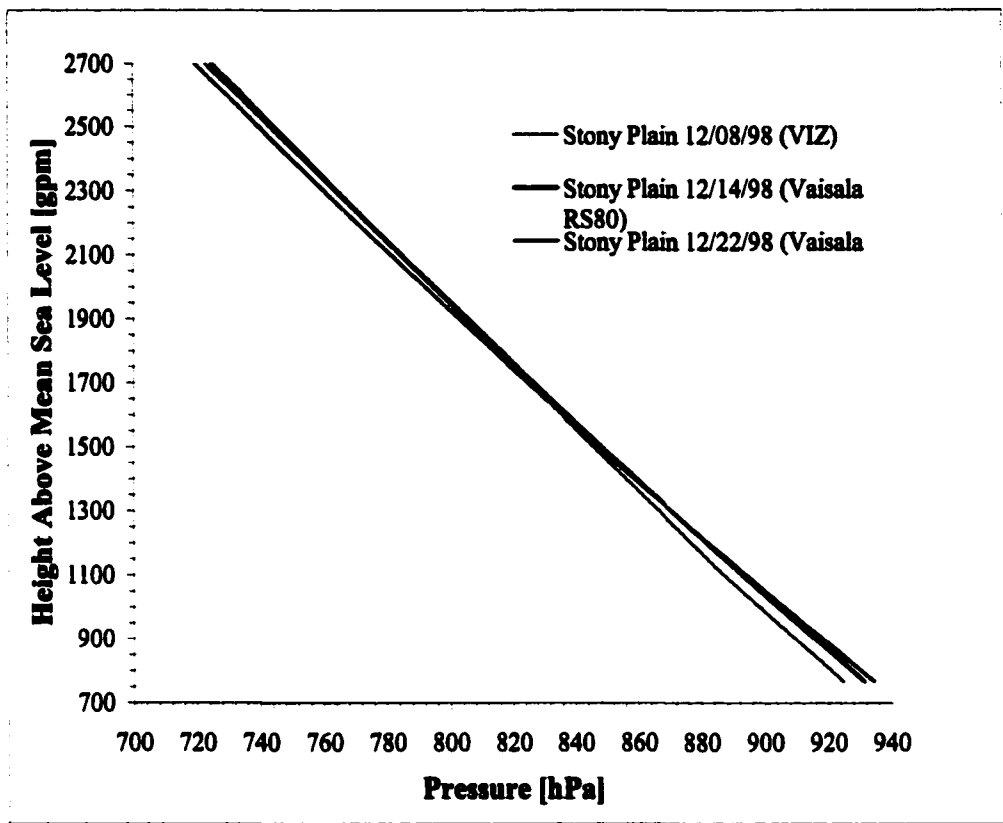


Figure G5: The planetary boundary layer atmospheric pressure profile from the 23:15 UTC rawinsonde files for the sunset refraction experiments.

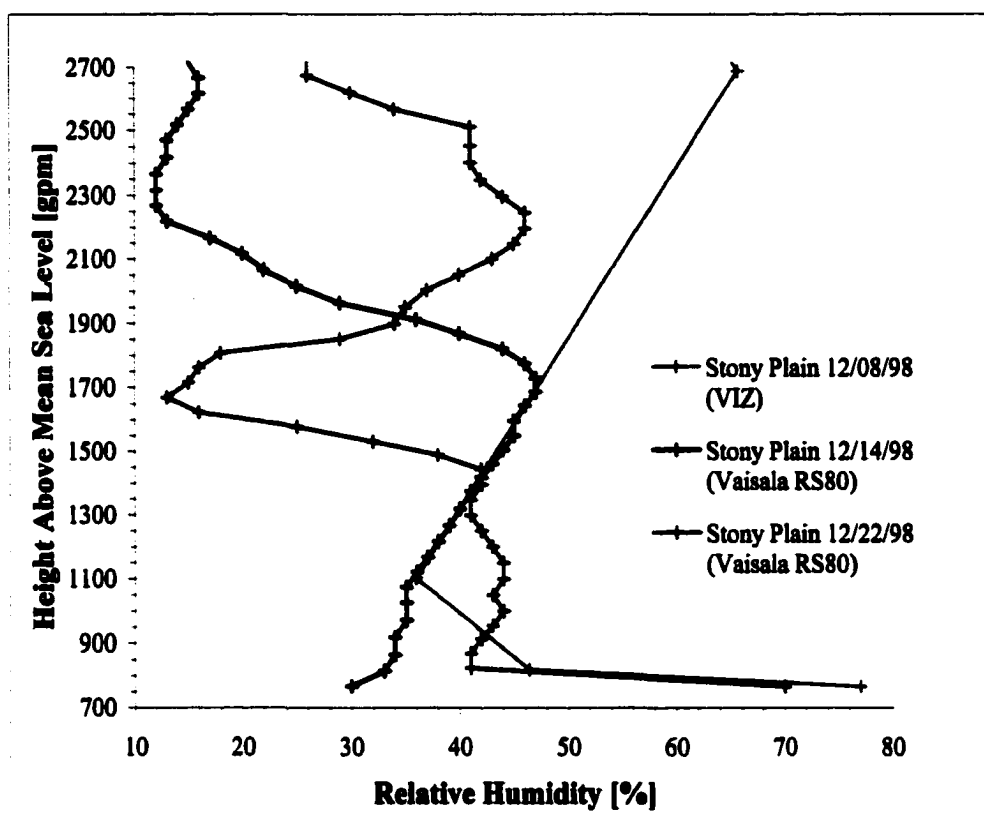


Figure G6: The planetary boundary layer relative humidity profile from the 23:15 UTC rawinsonde files for the sunset refraction experiments.

APPENDIX H

REFRACTION AS A FUNCTION OF DEPTH IN THE ATMOSPHERE

As outlined in Chapter 3, the astronomical refraction varies with depth in the atmosphere. The greatest contribution to the refraction occurs in the lower atmosphere. In order to investigate this effect more thoroughly, a quantitative analysis was performed using with the 23:15 UT December 14, 1998 sounding from Stony Plain. The incremental refraction R'_i at the i th layer was determined from

$$R'_i = \beta_i - \mu_i + \theta_i, \quad (\text{H1})$$

where β , μ and θ are defined in Chapter 3, Section 2.2. The incremental refraction R'_i is plotted in Figure H1. It is apparent from this graph that the maximum incremental refraction occurs near the surface and is about an order of magnitude greater than at the top of the sounding (about 20 km). In Figure H1, the layer thicknesses are not perfectly uniform since the model establishes the thickness from a fixed value of θ (see Chapter 3, Section 2). If the model was revised to consider fixed layer thicknesses or fixed layer masses the details of Figure H1 would change, but the qualitative result would be the same.

As the ray progresses through the atmosphere, a summation of the incremental refraction for each layer is performed. This summation determines the astronomical refraction accumulated from the top down to a particular level in the atmosphere. We shall call this the "cumulative absolute refraction" level j or R_j . Since the model uses a time-reversed scheme, R_j was found from

$$R_j = R_0 - \sum_{i=0}^j R'_i, \quad (\text{H2})$$

where the subscript i designates the atmospheric level (with $i = 0$ at the surface), j is the level of interest and R_0 is the cumulative absolute refraction observed at the surface. Rays were launched from the observer at zenith angles of $89^\circ.95$, $89^\circ.5$ and 85° . This is the zenith angle z_0 at which a point source (e.g. a star) would appear to an observer at the surface ($z_0 = 90^\circ - \beta_0$). All simulations used red light with a wavelength of $660 \mu\text{m}$ for the test ray. The cumulative absolute refraction is plotted in Figure H2.

The cumulative absolute refraction (Equation H2) was then divided by R_0 to give a cumulative fractional refraction at each level (see Figure H3). A table of the cumulative absolute and cumulative fractional refraction at 30, 10, 1, 0.1 and 0.01 km appears in Tables H1 and H2.

Height Above Station [gpm]	Cumulative Absolute R_j [$^\circ$] $\beta_0 = 0^\circ.05$	Cumulative Absolute R_j [$^\circ$] $\beta_0 = 0^\circ.5$	Cumulative Absolute R_j [$^\circ$] $\beta_0 = 5^\circ$
30 000	0.0020	0.0020	0.0015
10 000	0.0690	0.0683	0.0409
1 000	0.3683	0.3538	0.1415
100	0.4870	0.4421	0.1557
10	0.5335	0.4579	0.1574

Table H1: The cumulative absolute refraction at five heights above the Stony Plain station. The angle β_0 is the initial launch angle of the ray in the model. It is the altitude ($90^\circ - z_0$) of the incoming ray as observed at the surface.

Height Above Station [gpm]	Cumulative Fractional Refraction $\beta_0 = 0^\circ.05$	Cumulative Fractional Refraction $\beta_0 = 0^\circ.5$	Cumulative Fractional Refraction $\beta_0 = 5^\circ$
30 000	0.004	0.004	0.010
10 000	0.126	0.149	0.260
1 000	0.670	0.769	0.898
100	0.886	0.960	0.988
10	0.971	0.995	0.998

Table H2: As for Table H1 but for cumulative fractional refraction at five heights above the station.

It is apparent from graphs H1 to H3 and Tables H1 and H2, that when the initial launch angle of the light ray at the surface is very close to the horizon (i.e. very small β_0) the influence of the lower atmosphere is greatest. For example, when $\beta_0 = 0^\circ.05$, the lowest 100 metres of the atmosphere produces 11 percent of the refraction (about 2.8 arcminutes). However, it is also apparent that the upper atmosphere still makes a significant contribution to the total astronomical refraction. In Table H1, the atmosphere above 1 kilometre contributes 67 percent of the total refraction when $\beta_0 = 0^\circ.05$, and almost 90 percent when $\beta_0 = 5^\circ$.

Therefore, it appears that the atmosphere's contribution to astronomical refraction depends on the initial launch angle of the model (i.e. the apparent altitude of the celestial object). However, anomalous refraction phenomena such as the Novaya Zemlya mirage (Lehn, 1979), strongly suggest that the contribution of the lower atmosphere to the total observed astronomical refraction can vary over a large range. The present analysis uses atmospheric profiles that are apparently well mixed in the planetary boundary layer. Surface inversion layers or superadiabatic conditions could likely produce significantly different results, such as inferior or superior mirages with much of the refraction occurring near the surface.

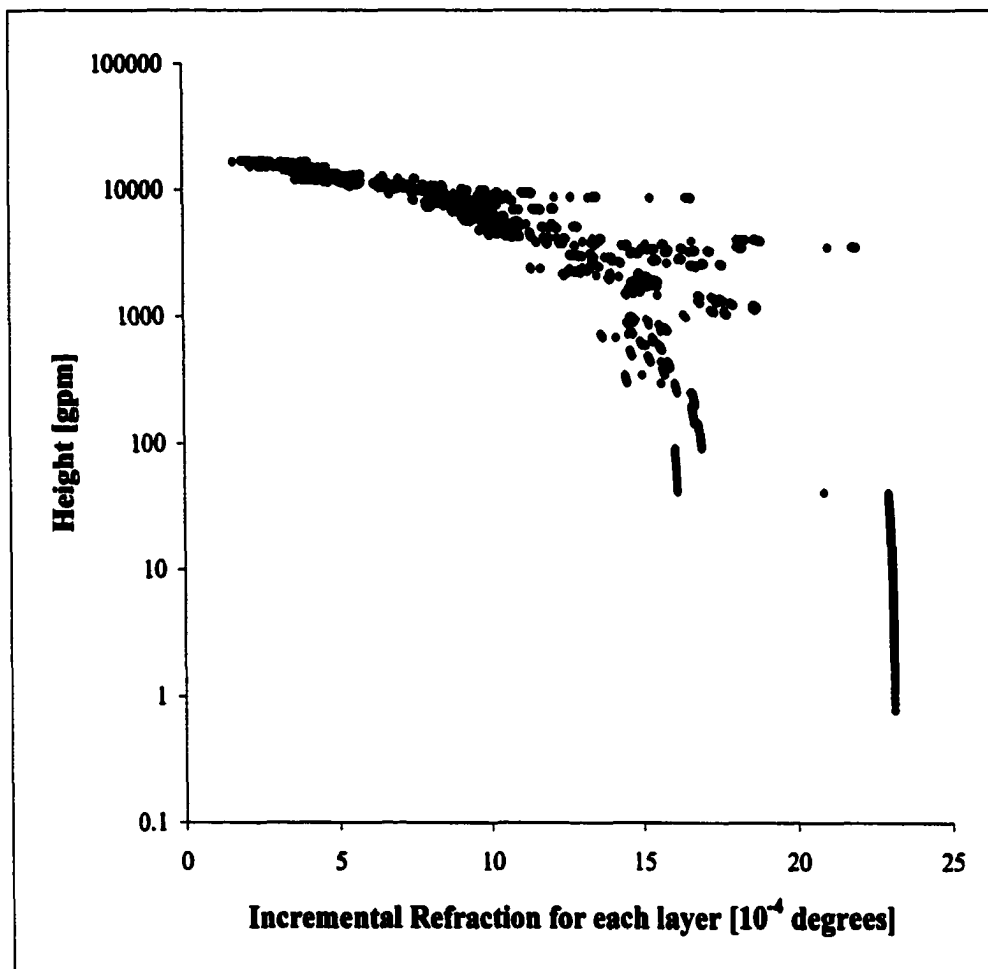


Figure H1: The incremental astronomical refraction values for each layer. The initial ray angle was set to $0^\circ.05$ ($z = 89^\circ.95$), wavelength $660 \mu\text{m}$ (red) and the December 14, 1998, 23:15 UT sounding was used. It should be noted that due to the scale compression each point near the top of the sounding represents a sounding layer which is actually comprised of many points. An example of this effect can be seen in the layer at the bottom of the sounding (between a height of 0 and 50 metres above the station).

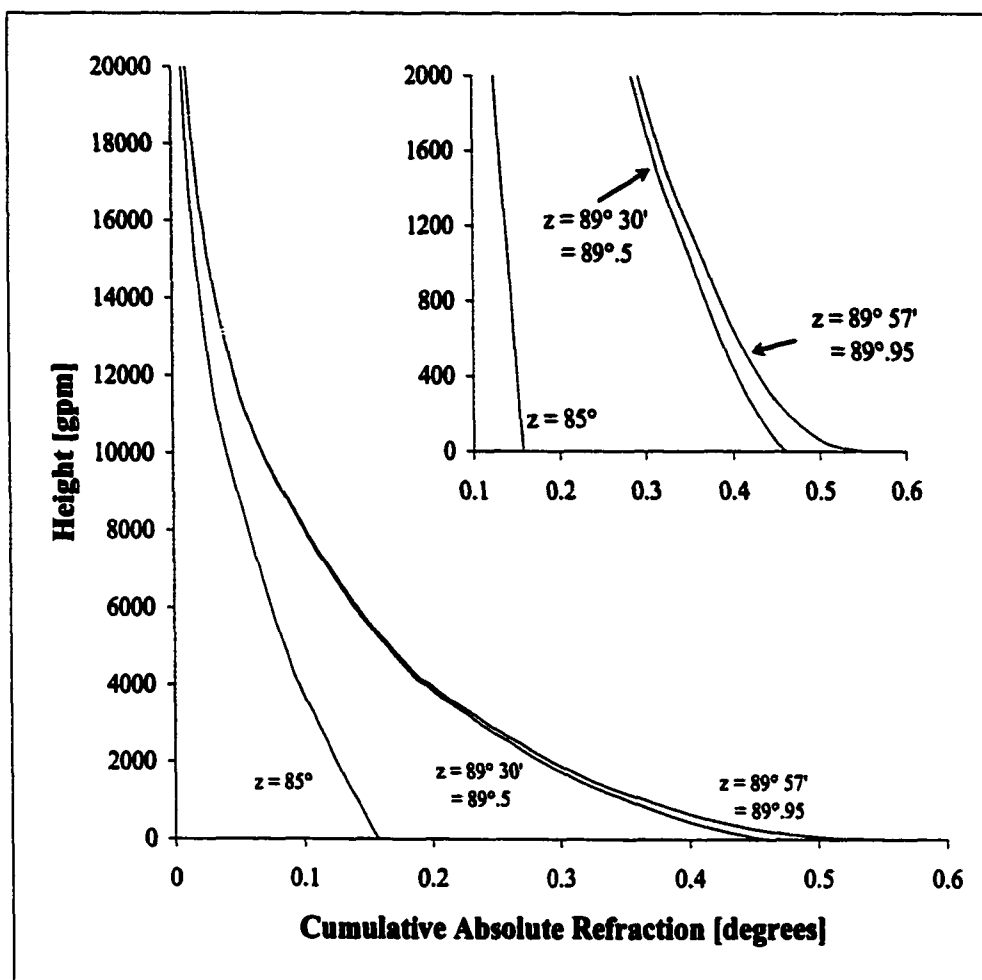


Figure H2: The cumulative absolute astronomical refraction with respect to height. The three curves are for three different values of the zenith angles of the ray at the surface (i.e. the initial angle in a time reversed ray tracing model). The December 14, 1998 sounding file and a wavelength of $660 \mu\text{m}$ (red light) were used as model input values. The insert shows a magnified view of the lowest 2000 gpm.

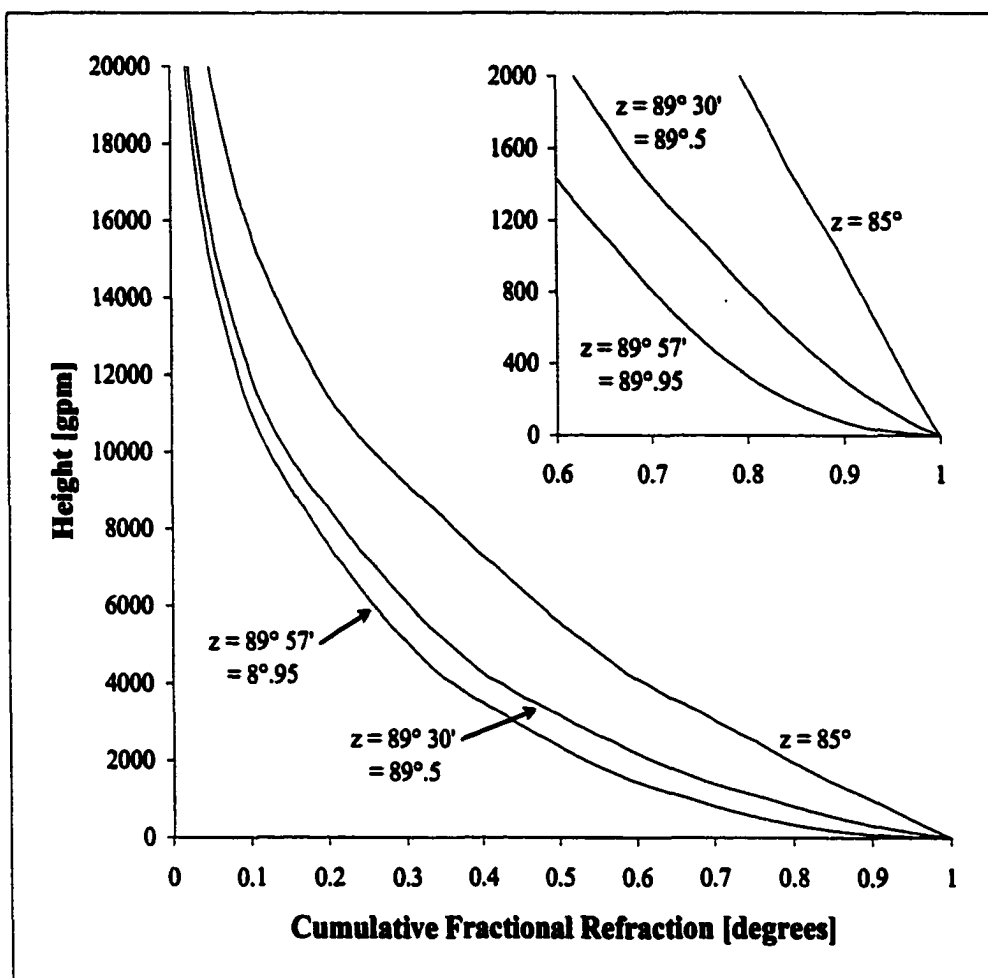


Figure H3: The cumulative fraction astronomical refraction as a function of height. The three curves are for three different input values of the zenith angles of the ray at the surface (i.e. the initial angle in a time reversed ray tracing model). The December 14, 1998 sounding file and a wavelength of $660 \mu\text{m}$ (red light) were used as model input values. The insert shows a magnified view of the lowest 2000 gpm.

References

- Ahlgren, J. R., 1997: *GeoClock 7.5 for Windows*, www.clark.net/pub/bblake/geoclock.
- Allan, C. W., 1973: *Astrophysical Quantities*, Athlone Press, London, 342 pp.
- Antikainen, V. and Hyvönen, V., 1983: The Accuracy of Vaisala RS 80 Radiosonde, Proceedings of the 5th Symposium on Meteorological Observations and Instrumentation, American Meteorological Society, April 11-15, 1983, Toronto, pages 134 – 140
- Arfken, George, 1968: *Mathematical Methods for Physicists*, Academic Press, New York, 704 pp.
- Arribas, S., et al, 1999: Differential Atmospheric Refraction in Integral-Field Spectroscopy; Effects and Corrections, *Astronomy and Astrophysics Supplement Series*, 136, 189 – 192
- Arya, S. P., 1988: *Introduction to Micrometeorology*, Academic Press, 307 pp.
- Beaubien, R. 1994: Personal Communication, Edmonton Office of Atmospheric Environment Services
- Bolton, J., 1999: Personal Communication, TransAlta Keephills Plant.
- Bomford, G., 1980: *Geodesy*, Forth Edition, Clarendon Press, Oxford, 855 pp.
- Brinker, R. C. and Wolf, P. R., 1984: *Elementary Surveying*, Harper D Row, New York, 608 pp.
- Brockington, M., 2000: Personal Communication, Bioware Corp. Edmonton.
- Bruton, D., 1996: *Optical Determination of Atmospheric Temperature Profiles*, Ph.D. thesis, Department of Physics, Texas A&M University,
- Carlsen, D., 2000: Personal Communication, Winnipeg Office of Meteorological Services of Canada, Environment Canada.
- Ciddor, P. E., 1996: Refractive index of air: new equations for the visible and infrared, *Applied Optics*, 35, 1566 – 1573.
- Clemence, G. M., 1951: Astronomical Refraction at Great Zenith Angles, *Astronomical Journal*, 56, 123 – 124.

Environment Canada, 1999: Climate Normals for Alberta,
http://www.cmc.ec.gc.ca/climate/normal/E_AL_WMO.HTM

Flesch, T. K. and Wilson, J. D., 1998: Wind and remnant tree sway in forest cutblocks. II. Relating measured tree sway to wind statistics, *Agricultural and forest Meteorology*, **93**, 243-258.

Fraser, A. B., 1975: The Green Flash and Clear Air Turbulence, *Atmosphere*, **13**, 1 – 10.

Friedman, R. M., 1989: *Appropriating the Weather, Vilhelm Bjerknes and the Construction of a Modern Meteorology*, Cornell University Press, Ithaca, 251 pp.

Funston, G., 1999: personal communications, Stony Plain Upper Air Station, Environment Canada.

Garfinkel, B., 1944: An Investigation in the Theory of Astronomical Refraction, *Astronomical Journal*, **50**, 169 - 179

Garfinkel, B., 1967: Astronomical Refraction in a Polytopic Atmosphere, *Astronomical Journal*, **72**, 235 – 234.

Giacomo, P., 1982: Equation for the Determination of the Density of Moist Air (1981), *Metrologia*, **18**, 33 – 40.

Grant, A. S. G., 1954: Notes on the Atmospheric Refraction Index in Canada from Aircraft Meteorological Soundings, *Transactions of the American Geophysical Union*, **35**, 508 – 510.

Green, M. G., 1985: *Spherical Astronomy*, Cambridge University Press, Cambridge, 520 pp.

Gubler, J., and Tytler, D., 1998: Differential Atmospheric Refraction and Limitations on the Relative Astrometric Accuracy of Large Telescopes, *Publications of the Astronomical Society of the Pacific*, **110**, 738 – 746.

Györi, L., 1993: Determination of Atmospheric Refraction from the distortion of the Sun's Disc, *Astronomy and Astrophysics*, **278**, 659 – 664.

Hagihara, Y., 1936: On the Theory of Astronomical Refraction, *Japanese Journal of Astronomy and Geophysics*, **14**, 1-17

Hecht, E., 1990: *Optics*, Addison-Wesley, Reading Mass., 676 pp.

Holton, J. R., 1979: *An Introduction to Atmospheric Dynamics*, Academic Press, Orlando FL, 391 pp.

- Humphreys, W. J., 1940: *Physics of the Air*, McGraw-Hill, New York, 676 pp.
- Iribarne, J. V. and Godson W. L., 1981: *Atmospheric Thermodynamics*, Reidel, Dordrecht, 259 pp.
- Karara, H. M., 1989: *Non-Topographic Photogrammetry*, second edition, American Society for Photogrammetry and Remote Sensing, 521 pp.
- Kepler, J. 1604: *Ad Vitellionem paralipomena, quibus astronomiae pars optica traditur*. Francfort, (De observatione Hollandorum in alto Septentrione), page 138 – 143
- Khrgian, A. Kh., 1959, *Meteorology a Historical Survey*, (Translated and edited by Ron Hardin), Israel Program for Scientific Translations, 387 pp.
- Kireev, S. V. and Sokolovskiy, S. V., 1994: Variations of Refraction Angles from Observations of the Moon from Space, *Applied Optics*, 33, 8402 – 8405
- Lane, D. J., 1998: *Earth Centred Universe, Planetarium and Telescope Control Software for Windows*, Nova Astronomics, Halifax, Canada (www.nova-astro.com).
- Lehn, W. H. and El-Arini, M. B., 1978: Computer-graphics analysis of atmospheric refraction, *Applied Optics*, 17, 3146 – 3151
- Lehn, W. H., 1979: The Novaya Zemlya effect: an arctic mirage, *Journal of the Optical Society of America*, 69, 776 – 781
- Lehn, W. H., 1985: A simple parabolic model for the optics of the atmospheric surface layer, *Applied Mathematical Modelling*, 9, 447 – 455.
- Lehn, W. H. 1994: Mirages with Atmospheric Gravity Waves, *Applied Optics*, 33, 4639 – 4643.
- Lehn, W. H., 1997: Analysis of an Infrared Mirage Sequence, *Applied Optics*, 36, 5217 – 5223.
- Lowe, P. R., 1976: An approximating polynomial for the computation of saturation Vapor Pressure, *Journal of Applied Meteorology*, 16, 100 – 103.
- Luers, J. K. and Eskridge, R. E., 1995: Temperature Corrections for the VIZ and Vaisala Radiosondes, *Journal of Applied Meteorology*, 34, 1241 – 1253.
- Lynch, D. K. and Livingston, W., 1995: *Color and Light in Nature*, Cambridge University Press, Cambridge, 254 pp.

- Mahan, A. I., 1962: Astronomical Refraction – Some History and Theories, Applied Optics, 1, 4, 497 – 511.**
- Mahesh, A., Walden, Von P., and Warren S. G., 1997: Radiosonde Temperature Measurements in Strong Inversions: Correction for Thermal Lag Based on an Experiment at the South Pole, Journal of Atmospheric and Oceanic Technology, 14, 45 – 53.**
- Meeus, J., 1988: Astronomical Formulae for Calculators, Willmann-Bell Inc., Richmond Virginia, 218 pp.**
- Menat, M., 1980: Atmospheric Phenomena before and during sunset, Applied Optics, 19, 3458 – 3468.**
- Mikkola, S., 1979: Calculating Astronomical Refraction by Means of Continued Fractions, Refractive Influences in Astrometry and Geodesy, Tengstrom, E. and Teleki, G (ed.) International Astronomical Union Symposium No. 89, 95 – 101.**
- Minnaert, M., 1993: Light and Color in the Outdoors, Springer-Verlag, New York, 417 pp.**
- National Aeronautic and Space Administration (NASA), 2000: Satellite Laser Ranging Technologies, http://ranier.oact.hq.nasa.gov/Sensors_page/Laser/SLR.html**
- National Climate Data Center, (NCDC), 2000, Online Upper Air Data, <http://raob.fsl.noaa.gov>**
- Noerdlinger, P. D., 1999: Atmospheric Refraction Effects in Earth Remote Sensing, ISPRS – Journal of Photogrammetry and Remote Sensing, 54, 360 – 373.**
- O’Connell, D. J. K., 1958: The Green Flash and Other Low Sun Phenomena, North Holland Publishing, Amsterdam, 192 pp.**
- O’Connor and Robertson, E. F., 2000: History of Mathematics Archive, University of St. Andrews Scotland, School of Mathematics, <http://www-history.mcs.st-andrews.ac.uk/history/Mathematicians/Cleomedes.html>**
- Oke, T. R., 1987: Boundary Layer Climates, Methuen & Co. Ltd., London, 435 pp.**
- Paukkinen, Ari, 2000, Personal Communications, Vaisala Oyj, Helsinki, Finland, ari.paukkinen@vaisala.com**
- Press, W. H. et al., 1992: Numerical Recipes in FORTRAN, Cambridge University Press, 963 pp.**

Poulkovo Observatory, (1931) Poulkovo Refraction Tables, third edition, Moscow Academy Press, Moscow, 22 pp.

Pulkovo Observatory, (1956) Refraction Tables of the Pulkovo Observatory, fourth edition, Academy of Sciences Press, Moscow, 32 pp.

Pulkovo Observatory, (1985) Refraction Tables of the Pulkovo Observatory, fifth edition, Nauka Publishing House, Leningrad, 48 pp.

Saastamoinen, J., 1979: On the Calculation of Refraction in Model Atmospheres, Refractive Influences in Astrometry and Geodesy, Tengstrom, E. and Teleki, G (ed.) International Astronomical Union Symposium, 89, 73 – 94.

Sampson, R., 1993, Atmospheric Refraction and Sunrise and Sunset, Sky & Telescope, 85, 96 – 97 (February)

Sampson, R. D., 1994: Atmospheric Refraction and its Effects on Sunrise and Sunset, Masters of Science Thesis, Department of Geography, University of Alberta.

Sampson, R. D., 1997: Atmospheric Refraction and its Effects on Sunrise and Sunset, in Light and Color in the Open Air, Vol. 4, 1997 OSA Technical Digest Series (Optical Society of America, Washington D.C., 1997), 45-47.

Sampson, R. D., 2000: Astronomical Refraction and the Equinox Sunrise, Journal of the Royal Astronomical Society of Canada, 94, 26-29.

Schaefer, B. E. and Liller, W., 1990: Refraction Near the Horizon, Publications of the Astronomical Society of the Pacific, 102, 796 – 805.

Schmidlin F. J., and Finger, F. G., 1987: Conclusions and Recommendations Resulting from the WMO International Radiosonde Intercomparison, Proceedings of the 6th Symposium on Meteorological Observations and Instrumentation, American Meteorological Society, January 12-16, 1987, New Orleans, 459 – 462.

Scion Corporation, 1999, Scion Image for Windows, Frederick, Maryland, <http://www.scioncorp.com/index.htm>

Sippican Inc., 1998, <http://www.sippican.com/pdf/mark2.pdf>

Smart, W. M. 1965, Spherical Astronomy, Cambridge University Press, Cambridge, 520 pp.

Smith, M. A., 1999: Ptolemy and the Foundations of Ancient Mathematical Optics: A Source Based Guided Study, Transactions of the American Philosophical Society, Vol. 89, Part 3, 172 pp.

- Smith, M. A., 1996: Ptolemy's Theory of Visual Perception; an English Translation of the *Optics*, Transactions of the American Philosophical Society, Vol. 86, Part 2, 300 pp.
- Stull, R. B., 1988: Introduction to Boundary Layer Meteorology, Kluwer Academic Publishers, Dordrecht Neth., 666 pp.
- Sugawa, C., 1955: On the Numerical Integration of Astronomical Refraction, Publications of the Astronomical Society of Japan, Nihon Temmon Gakkai Publications, 7, 163-175
- Swartz, B. E. and Doswell, C. A., 1991: North American Rawinsonde Observations: Problems, Concerns, and a Call to Action, Bulletin of the American Meteorological Society, 72, 1885 – 1896.
- Taylor, J. R., 1982: An Introduction to Error Analysis, University Science Books, Mill Valley California, 270 pp.
- Thom, A. A., 1958: An empirical investigation of atmospheric refraction, Empire Survey Review, XIV, 248 – 262.
- Thom, A. A., 1971: Megalithic Lunar Observatories, Clarendon Press, Oxford, 127 pp.
- Thomas, M. E. and Joseph, R. I., 1996: Astronomical Refraction, Johns Hopkins Applied Physics Laboratory (APL) Technical Digest, 17, 279 – 284.
- United States Naval Observatory, (USNO), 1999: Multiyear Interactive Computer Almanac (MICA), http://aa.usno.navy.mil/AA/data/docs/WebMICA_2.html.
- United States Government Printing Office, 1976: U.S. Standard Atmosphere, Washington, D.C. 227 pp.
- Vaisala product specifications (1998): <http://www.vaisala.fi/products.htm>
- Valasek, J., 1949: Introduction to Theoretical and Experimental Optics, Wiley & Sons, New York, 454 pp.
- Visser, S. W., 1956: The Novaya Zemlya Phenomenon, Proceedings, Koninklijke Nederlandse Akademie van Wetenschappen, Series B, Physical Sciences, 59, 375 – 385.
- Wallace, J. M. and Hobbs, P. V., 1977: Atmospheric Science, Academic Press, London, 467 pp.

Weast, R. C. (ed.), 1974: CRC Handbook of Chemistry and Physics, CRC Press, Cleveland, Ohio.

Weather Services Directorate, 1987: Manual of Upper Air Observations, Environment Canada, Atmospheric Environment Service,

Weisstein, Eric (Wolfram Research) 2000: Online Mathematics Encyclopedia, <http://mathworld.wolfram.com/Euler-LagrangeDifferentialEquation.html>

Wilson, J. D., 1999: personal communications, Department of Earth and Atmospheric Science, University of Alberta

Yan, H., 1996: A New Expression for Astronomical Refraction, The Astronomical Journal, **112**, 1312 – 1317.

Yan, H., 1998: Improvement of Astronomical Refraction by Mapping Function, Chinese Astronomy and Astrophysics, **22**, 487 – 496.

Yan, H. J. and Wang, G. L., 1999: Considerations of Atmospheric Refraction in Laser Ranging Data, Monthly Notices of the Royal Astronomical Society, **307**, 605 – 610.

Yatsenko, A. Yu, 1995: Exact Theory of Astronomical Refraction for the Real Atmosphere, Astronomy and Astrophysics Supplement Series, **111**, 579 – 586.

Young, A. T., Kattawar, G. W. and Parviainen, P., 1997: Sunset Science. I. The Mock Mirage, Applied Optics, **36**, 2689 – 2700.

Young, A. T., 1999: Green Flashes and Mirages, Optics & Photonics News, March, 31 – 37.

Zaba, Z., 1953: L'Orientation Astronomique dans L'Ancienne Egypte et la Precession de L'Axe du Monde, Editions de L'Academie Tchecoslovaque des Sciences, Prague, 74 pp.

Zahoor, A., 2000: Muslim Scientists and Islamic Civilization, <http://salam.muslimsonline.com/~azahoor/haitham.html>

CHAPTER 4: FINAL CONCLUSIONS AND SUGGESTIONS FOR FURTHER RESEARCH

1. Photogrammetry: Conclusions

The photogrammetric system appears to have provided the desired resolution of 0.1 arcminutes or better. Further improvements would require a flatbed scanner with higher resolution, more accurate reference target horizon coordinate values and higher accuracy in the focal length of the lens. However, due to scintillation of the high zenith angle solar disk, it appears that an improvement in the resolution of the photogrammetric system may not improve the accuracy of these particular measurements.

The Agfa Studio Scan II *si* colour flatbed scanner appears to be suitable for photogrammetry of this nature. To achieve the highest accuracy, correction formulae must be applied to compensate for linear and non-linear scanner distortions.

The Questar 3.5 inch telescopic lens showed no measurable distortion and was found to have a focal length of 1445.3 \pm 3.6mm (with object distance at infinity). The terrestrial calibration demonstrated that the image distance does not follow the simple lens formula. This was most likely due to the rather complex nature of the Questar Maksutov lens system, where the focus is achieved through the movement of the primary mirror. Therefore, the simple lens formula can not be used to determine the image distance in the Questar 3.5 inch telescopic lens.

1.1 Suggestions for Further Research into the Photogrammetric Utility of Flatbed Scanners

If flatbed scanners are to be used with confidence for photogrammetric purposes, it is important to explore the variability of the distortion during the life span of a particular machine. It would also be important to determine the distortion variability between numerous machines of the same and different designs. The scanner's sensitivity to thermal expansion could also be investigated further. The photogrammetric utility of high-resolution film scanners could also be explored. For example the Hewlett Packard PhotoSmart S20 shows great potential for photogrammetry with an increased optical resolution of 2400-ppi.

1.2 Suggestions for Further Research into the Photogrammetric Utility of the Questar 3.5-inch Telescopic Lens

Further research could be conducted to examine the focal length's sensitivity to ambient temperature and thermal expansion of the optics. Images of star fields could be taken under various ambient temperatures. The climate of Edmonton, Alberta is well suited for such a study since the nighttime temperatures can vary from about 20°C to -40°C. Other, more temperate climates would not present as large a temperature range. It would also be useful to measure the focal length and distortion values for other Questar 3.5-inch lenses.

2. Astronomical Refraction: Conclusions

Contrary to initial expectations, the best fit between the observed and the modelled astronomical refraction model occurred with the use of the MUSSA profile rather than the rawinsonde data. This suggests that until rawinsonde temperature sensors and data collection techniques improve, the use of these instrumental data may not significantly improve the results over the idealized atmosphere. However, the modelled astronomical refraction using either the rawinsonde or the MUSSA profiles showed better results when compared with the Pulkovo Refraction Tables. Since the MUSSA profile only requires the surface temperature, an observer equipped with this astronomical refraction model and accurate surface temperature data should be able to outperform the Pulkovo Refraction Tables under similar conditions to those observed during the experiment (i.e. a well mixed atmosphere). Since detailed and accurate vertical temperature profiles are expensive and difficult to obtain (requiring a rawinsonde or tower), this result appears to be promising. However, the experiment outlined in this thesis was restricted to a rather small sample of sunsets. Therefore, further data would need to be collected and analyzed, especially during nighttime and morning conditions when the boundary layer is more complex.

2.1 Suggestions for Further Research into the Use of the Astronomical Refraction Model

The introduction of the Vaisala RS90 rawinsonde with its improved temperature sensor may eliminate many of the barriers that have prevented

successful use of soundings in the astronomical refraction model. It is not known when the Meteorological Services of Canada will be adopting their use. The results of this study would suggest that more attention should be given to the correct launch procedures in order to prevent any temperature errors occurring immediately after launch. An instrumented tower near the launch site with calibrated temperature sensors could be used to check the performance of the rawinsonde. An application of a thermal lag time correction to the sounding data may also improve the model's performance.

From previous studies astronomical refraction at sunrise appears to be more complex than during sunset. Therefore, it is critical that this study be extended to include sunrises. However, unusual refraction events like the Novaya Zemlya solar mirage and the Chinese Lantern effect that appear to be most common during sunrise, suggest that a much more complete two dimensional atmospheric model would be necessary. In order to explore mirage effects frequently observed during sunrises, the atmospheric model should include gravity waves as suggested by Fraser (1975).

The large sunrise and sunset refraction data set collected in Sampson (1994) could also be used to increase the sample of events modelled with the MUSSA profile. This data set includes hourly surface temperatures collected at the time the refraction values were measured for sunrise or sunset.

Eventually, operational software could be developed that may include an atmospheric boundary layer model that could be used to produce accurate

astronomical refraction forecasts for any location on the surface of the Earth or even within or beyond the atmosphere.

References

Fraser, A. B., 1975: The Green Flash and Clear Air Turbulence, *Atmosphere*, 13, 1 – 10.

Sampson, R. D., 1994: Atmospheric Refraction and its Effects on Sunrise and Sunset, Masters of Science Thesis, Department of Geography, University of Alberta.